Imperial College London

Doctoral Thesis

Immune Reactions in Lymph Nodes and Ovarian Cancer

Author:
Sarah Johnson

Supervisor:
Prof. James E. Moore.Jr

A thesis submitted in fulfillment of the requirements for the degree of Doctor of Philosophy

in the

Department of Bioengineering

March 26, 2019

Abstract

During adaptive immune response, the lymph node (LN) volume may increase, but the impact on T cell (TC) trafficking and interaction are unknown. Lymphangiogenic LNs are associated with poor prognosis in cancer patients, in addition to presenting with impaired anti-tumour immune responses. Lymphatic vessels (LVs) can respond to lymph-born signalling molecules and secrete agents that can impact the response at the LN. Two studies were conducted to gain insight into immune response changes; first, in the LN due to LN swelling and second, in LVs of ovarian cancer patients.

The first study involved using an agent-based model to describe the TCs response to antigen presenting dendritic cells in the LN paracortex while modulating the paracortex swelling behaviour. The expression of TC receptor Sphingosine-1- phophate-1 receptor ($S1P_1r$) was also modulated and the effector TC response analysed under different swelling conditions. This showed that paracortical swelling can aid TC activation but can inhibit effector $CD8^+$ TCs production if the swelling occurs too early in the proliferative response. $S1P_1r$- mediated retention of newly differentiated effector TCs increased the effector TC response.

The second study investigated LV changes from ovarian cancer patients using immunohistochemistry to quantify LV inflammatory status, identify cancer-cell infiltration and analyse changes in miRNA expression. Patient relapse was associated with high LV inflammation away from the tumour site. In addition, several miRNA groups, including the let-7 family, may present as prognostic and therapeutic targets.

This research confirmed that LN swelling affects TC response to antigen and that retention of newly differentiated effector TCs can impact the immune response. In addition, LVs can undergo systemic changes that may contribute to or are a result of cancer progression. Therefore, targeting the timing of LN swelling, temporary effector TC retention and LVs offer new ways to manipulate the immune response at the LN.

Contents

Abstract **iii**

Declaration of Authorship **xi**

Copyright Declaration **xiii**

Acknowledgements **xvii**

1 Introduction to the lymphatics **1**

1.1 A brief history of the lymphatics 1

1.2 Current understanding of the lymphatic system 3

1.3 Contribution to maintenance of fluid homoeostasis in the body . 5

1.4 Lymphatics and immune response 8

1.4.1 Modelling TC behaviour in the LN 9

1.5 Structural cells of the lymph node and lymphatic vessels 11

1.6 Lymphatics and metastasis 13

1.7 Problem Definition 16

2 The impact of lymph node swelling on T cell response **21**

2.1 Introduction 21

2.1.1 Lymph node structure and cell transit 21

2.1.2 Cell mediated response 23

2.1.3 Stromal cells contribution to immune response 25

2.1.4 Types and Causes of Lymphandeopathy 27

2.1.5 Mechanisms of paracortical enlargement 28

2.1.6 Observed changes during paracortical enlargement 28

2.1.7 Previous work 30

2.1.8 Summary of aims 36

2.2 Methods 37

2.2.1 Geometry of a novel ABM model 37

Agent based modelling 37

Geometry 43

2.2.2 Model development and governing equations 44
Agents 44
Interactions 47
T cell exit and Sphingosine-1-Phosphate regulation 48
T cell recruitment 50
Stromal cells 51
Baseline motility and response simulations 52
2.2.3 Incorporating para-cortical enlargement 53
Estimating and applying volume change 53
Modulating T cell S1P1r expression and paracortical swelling 53
Summary of Key Assumptions 56
2.2.4 Global sensitivity analysis 58
Considering parameter uncertainty 58
Latin hypercube sampling 59
Model outputs 60
Analysing correlation 62
2.2.5 Model validation 64
Parameter tables 65
UML diagrams 68
2.3 Results 82
2.3.1 Overview 82
2.3.2 The model produced realistic baseline T cell motility 84
2.3.3 The model produced a realistic T cell response to agDCs . . 85
2.3.4 Paracortical expansion and T cell response 88
The effect of varying maximal paracortical swelling (V_{Max}) . 88
Varying T_{Mid} can counteract the effects of V_{Max}. 94
The conditional effects of varying Tmid 95
Factors that contribute to optimal paracortical expansion . 98
Parcortical swelling and T cell egress 99
Modulating effector T cell S1P1 receptor expression 101
2.3.5 Global sensitivity analysis results 104
2.3.6 Validation 112
Varying the initial proportion of cognate T cells 112
Varying the stimuli strength 115
Curtailing the stimuli duration 117
Removing S1P1r down-regulation on activated T cells . . . 119

2.4 Discussion 121
2.4.1 Retention of newly differentiated effector T cells, impacts the response more varying maximal swelling. 122
2.4.2 Paracortical swelling results in more initial TC activation. . 124
2.4.3 Paracortical swelling dynamics impact effector TC response. 125
2.4.4 Paracortical swelling impacted CD4+ and CD8+ TCs response distinctively 127
2.4.5 Increase in TC egress rates limit the TC response. 130
2.4.6 Validation and Limitations 131
Baseline stimulations 131
Replicating *in-vivo* experiments 132
Sensitivity analysis 133
Improving confidence in the model 133
Experimental limitations 134
2.4.7 Summary 137

3 Lymphatic vessel miRNA expression during ovarian cancer 139
3.1 Introduction 139
3.1.1 The lymphatic involvement in ovarian cancer 139
3.1.2 Lymphatic involvement in metastasis 140
Transport 140
Immunity 143
3.1.3 Micro RNA and dysregulation in cancer 144
3.1.4 Regulation of lymphatics by miRNA 149
3.1.5 Cancer-induced lymphatic miRNA expression change . . . 150
3.1.6 Therapeutic potential 152
3.1.7 Summary of the study goal 152
3.2 Methods 154
3.2.1 Sample collection 154
3.2.2 Vessel isolation 156
3.2.3 RNA extraction from the whole vessel 157
3.2.4 Using QPCR to quantify miRNA expression 158
3.2.5 Immunohistochemical Staining 161
3.2.6 Imaging and Image Processing 162
Summary of Experimental Design 163
3.2.7 Analysis techniques 164
Techniques to identify a stably expressed genes 164

Normalisation of miRNA expression 168
Statistical Analysis of differentially expressed miRNA . . . 168
3.3 Results 170
3.3.1 Overview 170
3.3.2 Imaging allowed quantification of cancer-infiltration status of macroscopically normal LV samples 171
LV state at time of surgery correlated to patient relapse. . . 175
LVs showed differential miRNA expression when inflamed or cancer-cell infiltrated 177
Principle component analysis results identified variation attributed to inflammation and cancer-infiltration. . 185
Pathway analysis showed dysregulated miRNA involvement in maintaining LV integrity 189
Analysis of LV miRNA expression in patients who relapsed 191
3.4 Discussion 192
3.4.1 Patient relapse is associated with highly inflamed LVs that show differential miRNA expression. 192
3.4.2 Dysregulated miRNA affect endothelial cell processes in ways that may be beneficial or detrimental in the LVs 193
3.4.3 Down-regulation of let-7 miRNA in inflamed LVs could altered LV permeability and immune responses. 196
3.4.4 Cancer-containing LVs show dysregulated miRNA involved maintaining LEC phenotypes 197
3.4.5 Dysregulated expression of miR-29a, miR-29b, miR-19a and miR-19b, may impact fibrosis pathways and the secretion of NO in LVs. 198
3.4.6 Several up-regulated miRNA in cancer containing and inflamed LVs target VEGF. 200
3.4.7 MicroRNA that target anti-apoptotic factor BCL-2 were up-regulated in cancer-containing LVs 201
3.4.8 Analysis of differentially expressed miRNA revealed common roles in KEGG pathways associated with LV structure and integrity. 202
3.4.9 Experimental limitations 203
3.4.10 Summary 205

4 Future work **207**

4.0.1 Key Contributions 207

4.0.2 Further investigate the use of inflammation and let-7 as a marker of prognosis 212

4.0.3 Confirm let-7 roles *in-vitro*, to assess therapeutic potential 212

4.0.4 Assess miRNA expression in LNs 213

4.0.5 Assess miRNA modulation that may inhibit VEGF expression in LECs 214

4.0.6 Assess permeability of inflamed EOC LV samples 215

4.0.7 Improve the model by incorporating fluid dynamics 215

4.0.8 Investigate whether facilitating LN stretch alters TC response.216

4.0.9 Modulate murine TC expression of S1P1r early on specific effector TCs. 217

4.0.10 Gain insight into the relationship between TC egress and LN swelling 219

4.0.11 Summary 220

A Supplementary Data for Chapter 2 **221**

B Supplementary Data for Chapter 3 **229**

B.1 Normalisation techniques 229

B.2 Imaging Results 231

B.2.1 Haematoxylin and Eosin Samples 231

B.2.2 Myeloperoxidase 232

B.2.3 Wilms Tumour-1 235

B.2.4 Pax-8 238

B.2.5 Podoplanin 241

B.2.6 Additional miRNA expression data 242

Bibliography **247**

Permissions Documents **291**

Declaration of Authorship

I, Sarah Johnson, declare that this thesis titled, "Immune Reactions in Lymph Nodes and Ovarian Cancer" and the work presented in it are my own. I confirm that:

- This work was done wholly or mainly while in candidature for a research degree at Imperial College London.
- Where any part of this thesis has previously been submitted for a degree or any other qualification at this University or any other institution, this has been clearly stated.
- Where I have consulted the published work of others, this is always clearly attributed.
- Where I have quoted from the work of others, the source is always given. With the exception of such quotations, this thesis is entirely my own work.
- I have acknowledged all main sources of help.
- Where the thesis is based on work done by myself jointly with others, I have made clear exactly what was done by others and what I have contributed myself.

Signed:

Date: 29/03/2019

Copyright Declaration

The copyright of this thesis rests with the author. Unless otherwise indicated, its contents are licensed under a Creative Commons Attribution-Non Commercial 4.0 International Licence (CC BY-NC). Under this licence, you may copy and redistribute the material in any medium or format. You may also create and distribute modified versions of the work. This is on the condition that: you credit the author and do not use it, or any derivative works, for a commercial purpose. When reusing or sharing this work, ensure you make the licence terms clear to others by naming the licence and linking to the licence text. Where a work has been adapted, you should indicate that the work has been changed and describe those changes. Please seek permission from the copyright holder for uses of this work that are not included in this licence or permitted under UK Copyright Law.

Dedicated to my Grandmother, 'Life will never be long enough'.

Acknowledgements

This work would not have been possible without the help and support from many others. First, I would like to express my deepest gratitude to my PhD advisor Prof. James Moore for his encouragement and understanding as well as his intellect and academic support.

I would like to thank Dr. Sanjukta Chakraborty for her help and guidance and for the in-valuable training that she provided both in the UK and Texas. I would also like to thank my current and former friends and colleagues in the Moore lab, Dr. John Wilson, Dr Samira Jamalian, Dr Mohammad Jafarnejad, Dr. Lowell Edgar and Willie Bonneuil. A special thankyou goes to Dr Jennifer Frattolin whose help and support has been invaluable these past few months. My gratitude goes to the faculty and staff at the Department of Bioengineering at Imperial College London, in particular, Kosta Rolev and Joel Eustaquio for going beyond their role in order to help me out. I'd also like to thank the members of the Hammersmith group led by Prof. Christina Fotopoulou, for their insight and help.

I'd like to thank my good friends Chris and Antoinette. Although both hundreds and thousands of miles away, together you managed to still support me and deal with my late and dramatic phone-calls. I'm not sure what I'd have done without you both supporting me through the last few years and I'm so grateful that we met.

Finally, I want to thank my family, my parents for their continued support and my sister who has grown into a caring young women who reminds me what is important. And thankyou of course, to my Grandmother, Flora Johnson, you were always my biggest fan, closest confident and first port-of-call. Although no longer here I know you'd be immensely proud of me, and I can only hope to live a life as fully and bravely as you did.

List of Abbreviations

agDC	Antigen Presenting Dendritic Cell
DC	Dendritic Cell
EC	Endothelial Cell
EMT	Epithelial-to-Mesenchymal Transition
EOC	Epithelial Ovarian Cancer
FRC	Fibroblastic Reticular Cell
HKG	House Keeping Gene
IHC	Immuno-Histo-Chemical
LCMV	Lymphocytic choriomeningitis virus
LEC	Lymphatic Endothelial Cell
LN	Lymph Node
LV	Lymphatic Vessel
MHC	Major Histocompatibility Complex
miRNA	Micro RNA
mRNA	Messenger RNA
NO	Nitric Oxide
OC	Ovarian Cancer
PDPN	Podoplanin
RA	Rheumatoid Arthritis
TC	T Cell
VEC	Vascular Endothelial Cell
VEGF	Vascular Endothelial Growth Factor

List of Figures

1.1 A historical painting of the lymphatic network. 2
1.2 A summary of the roles of the lymphatic system. 6
1.3 Two causes of secondary lymphoedema 7
1.4 Summary of current research regarding LN swelling and cell-mediated response. 17
1.5 Summary of current research regarding tumour draining lymphatic vessels, away from the tumour micro-environment. 19

2.1 The structure of the LN and the ABM geometry. 22
2.2 S1P_1r signalling contributes to three aspects of TC egress. 24
2.3 Visual interface of the ABM. 37
2.4 A class diagram displaying the underlying ABM structure. 39
2.5 A flow diagram of the setup processes in the model. 40
2.6 A flow diagram of the 'main' processes in the model. 41
2.7 The process of generating the model for batch simulations. 42
2.8 Modelling the stimulation of TCs by DCs. 46
2.9 Grouping the parameters of the model. 55
2.10 Applying a global sensitivity analysis. 61
2.11 An explanation of the correlation methods used in the study. . . . 63
2.12 UML diagram for 'UpdateTCs'. 68
2.13 UML diagram for 'UpdateTCsAgeing'. 68
2.14 UML diagram for 'RemoveTCsAgeing'. 69
2.15 UML diagram for 'SeeIfExit'. 69
2.16 UML diagram for 'RemoveTCExit'. 70
2.17 UML diagram for 'RemoveLinks'. 70
2.18 UML diagram for 'TCsMove'. 71
2.19 UML diagram for 'UpdateDCs'. 72
2.20 UML diagram for 'StimulateTCs'. 73

2.21 UML diagram for 'AgeDCs'. 73
2.22 UML diagram for 'BindTCs'. 74
2.23 UML diagram for 'UpdateCognateTCs'. 75
2.24 UML diagram for 'AddDCs'. 76
2.25 UML diagram for 'SeeIfActivated'. 77
2.26 UML diagram for 'Proliferation'. 78
2.27 UML diagram for 'SeeIfEffector' or 'SeeIfEffectorMemory. 79
2.28 UML diagram for 'AlterGrid'. 80
2.29 UML diagram for 'SetGeometry'. 81
2.30 Baseline TC motility. 84
2.31 Types of TCs in the paracortex following entry of agDCs. 86
2.32 TC trafficking rates. 87
2.33 Captured phases of TC trafficking and response to AgDC stimuli. 87
2.34 TC response over 11 days when V_{Max} was varied from 1 to 2·8. . . 89
2.35 The variation in TC subsets as V_{Max} was varied from 1 to 2·8. . . 89
2.36 Paracortex swelling and cognate TCs contact with DCs. 90
2.37 The relationship between the maximal swelling, TC-DC contact and TC response. 92
2.38 TC-DC contact is more important at larger swelling values. 93
2.39 Increasing T_{Mid} counteracts the loss in effector TCs with V_{Max} A. . 95
2.40 Further simulations showed that T_{mid} became more influential at higher values of V_{Max}. 97
2.41 Increasing T_{mid} to 12e4 changes optimal swelling from 1 to 1·8-fold. 98
2.42 variation of underlying model rules regarding egress and expansion. 100
2.43 Varying SP_{early} and thus retention of newly differentiated TCs. . . 103
2.44 Sample sensitive parameter identification. 105
2.45 TC responses *in-silico* and *in-vivo* when proportion of cognate TCs was varied. 114
2.46 TC responses *in-silico* and *in-vivo* when the DC stimuli is varied. . 116
2.47 TC responses *in-silico* and *in-vivo* when a stimuli is abruptly abolished. 118
2.48 TC responses *in-silico* and *in-vivo* when $S1P_1r$ down-regulation is inhibited. 120

2.49 A summary of the effect of modulating T_{mid} on the number of effector TCs exited at different maximal swelling. 127

3.1 The location of the EOC tumour and LVs. 141
3.2 Schematic describing steps in EOC metastasis to LVs. 142
3.3 Regulation of gene expression by miRNA. 147
3.4 Lymphatic vessel isolation technique. 156
3.5 Assessing RNA quality using absorbance. 157
3.6 Underlying principles of real time quantitative PCR. 160
3.7 Quantifying LV state by anti-body staining. 162
3.8 Experimental design for LV miRNA analysis. 163
3.9 Normalisation between arrays. 164
3.10 GeNorm identifies stably expressed genes. 165
3.11 Sample H & E vessel staining. 171
3.12 Staining of the lymphatic endothelium with podoplanin. 172
3.13 Sample staining of LV inflammatory marker. 172
3.14 Sample staining of positive control EOC tumour. 173
3.15 Sample LV Wilms-Tumour-1 staining. 173
3.16 Sample LV Pax8 staining. 174
3.17 Overlap was observed between differential expression of miRNA in inflamed LVs and in cancer-infiltrated LVs. 180
3.18 Normalised expression of miRNAs. 183
3.19 The results of a Principle Component Analysis. 188
3.20 Overlap in differential expression of miRNA in inflamed, cancer-infiltrated and relapse-associated LVs. 191
3.21 Dysregulated miRNA that affect TGF-β signalling in the LECs. . . 200
3.22 Dysregulated miRNA that target VEFG. 202

4.1 Key contributions and remaining unknowns regarding LN swelling. 209
4.2 Key contributions and remaining unknowns regarding draining LVs state in ovarian cancer. 211
4.3 A summary of molecular mechanisms that allow LN stromal cell stretch. 218

A.1 TC recruitment rate and TC to grid ratio whilst varying V_{Max}. . . . 221

A.2 Additional data when V_{Max} was varied with T_{mid}=10e4 TCs. 222
A.3 Contact between TC-DCs, and TC response with varying T_{mid} value and a large swelling. 223
A.4 Contact between TC-DCs and effector TCs exited with varying T_{mid}. 224
A.5 Increasing T_{mid} increases the TC to grid ratio earlier in the response. 224
A.6 At a low agDC application, effector TCs exited showed some correlation with TC-DC contact at larger swelling values. 224
A.7 When the DC stimuli was reduced, CD4+ TCs did not show all-or-nothing behaviour. 225
A.8 Further effects of reducing probability of TC cognition. 225
A.9 Individual simulation results when curtailing the stimuli. 226
A.10 Inhibition TC S1P1r expression at different maximal swellings. . . 227

B.1 Finding the optimal number of genes to normalise data. 229
B.2 A selection of H and E stained lymphatic vessel samples. Sample 6 shows signs of cryogenic damage but for the purpose of detecting cancer cell presence, maintenance of structure was sufficient. . 231
B.3 Inflammatory marker myeloperoxidase (MPO) and nuclear marker DAPI for samples 1 to 4. 232
B.4 Inflammatory marker myeloperoxidase (MPO) and nuclear marker DAPI for samples 5 to 8. 233
B.5 Inflammatory marker myeloperoxidase (MPO) and nuclear marker DAPI for samples 9,10 and controls 234
B.6 Cancer-cell marker Wilms-Tumour-1 (WT1) and nuclear marker DAPI for sample 1-4. 235
B.7 Cancer-cell marker Wilms-Tumour-1 (WT1) and nuclear marker DAPI for sample 5-8. 236
B.8 Cancer-cell marker Wilms-Tumour-1 (WT1) and nuclear marker DAPI for sample 9,10 and controls. 237
B.9 Cancer-cell marker Pax-8 and nuclear marker DAPI for sample 1-4. 238
B.10 Cancer-cell marker Pax-8 and nuclear marker DAPI for sample 5-8. 239
B.11 Cancer-cell marker Pax-8 and nuclear marker DAPI for sample 9,10 and controls. 240
B.12 Lymphatic endothelial cell marker Podoplanin (Green) 241

B.13Permission for reprint of Figure 2 in Chapter 3. 291
B.14Permission for use of data for Fig 1.24 in Chapter 2. 292
B.15Permission for use of data for Figure in Chapter 2. 292
B.16Permission for use of data for Fig 1.25 in Chapter 2. 293
B.17Permission for use of data from Figure 1.25 in Chapter 2. 293
B.18Permission for use of data for Fig 1.26 in Chapter 2. 293
B.19Permission for use of data from Figure 1.27 in Chapter 2. 294

List of Tables

2.1 Table of assumptions. 56
2.2 Assumption Table Part 2. 57
2.3 Parameters that were not varied in the global sensitivity analysis 65
2.4 Parameters varied in the global sensitivity analysis. 66
2.5 Parameters that significantly affected number of activated TCs. . 108
2.6 Parameters that significantly affected the number of activated TCs after increasing SP_{act}. 108
2.7 Parameters that significantly affected the number of effector TCs. 109
2.8 Parameters that significantly affected the number of effector TCs that exited the paracortex. 110
2.9 Parameters that significantly affected memory TCs number in the paracortex. 111
2.10 Parameters that significantly affected the number of memory TCs exited in the paracortex. 111

3.1 Summary of up-regulated and down-regulated miRNA in expression profiling studies relevant to ovarian cancer. 148
3.2 Samples collected from 10 patients undergoing primary debulking or interval debulking for advanced EOC. 155
3.3 Different methods were to identify stably expressed genes. 167
3.4 Pairwise HKG analysis 167
3.5 Single HKG analysis 167
3.6 Summary of the LV imaging results and clinical data. 175
3.7 Cohen's Kappa Coefficient for inner-agreement between different sample states (1=perfect agreement) and Fisher's exact test for identification of significant non-random association (p<0. 176

3.8 Assessment of clinical correlation between LVs presenting with high inflammation and those presenting with low inflammation (n=7), using Cohen's Kappa Coefficient for inner-agreement between different sample states (1=perfect agreement) and Fisher's exact test to identify significant non-random association between groups. 177
3.9 Differential expression of miRNA between LV groups. 179
3.10 The known function of the dysregulated-miRNA in cancer-infiltrated and/or inflamed LVs. 184
3.11 The contribution of miRNA to PCA component 1 and 2. 186
3.12 Pathway analysis using significantly up-regulated miRNAs in cancer-infiltrated LVs. 190
3.13 Pathway analysis using miRNA up-regulated >1·8 fold in cancer-infiltrated LVs. 190
3.14 Pathway analysis using miRNA down-regulated >1·8-fold in cancer-infiltrated LVs. 190
3.15 Summary of dysregulated miRNA roles. 195

B.1 The non-expressed miRNA in the LVs. 242
B.2 Pathway analysis results using the miRNAs identified when comparing inflamed LVs to non-inflamed LVs. 243
B.3 Pathway analysis of miRNA up-regulated >1. 244
B.4 Pathway analysis of all miRNA down-regulated >1. 244
B.5 Differentially expressed LV miRNA in relapse patients. 245
B.6 Pathway analysis results of miRNA that showed a up-regulation >1·8 fold-change in LV samples of patients who relapsed. 246
B.7 Pathway analysis results of miRNA that showed a down-regulation >1·8 fold-change in LV samples of patients who relapsed. 246

Chapter 1

Introduction to the lymphatics

The lymphatic system has multiple functions; it is a drainage system that allows maintenance of fluid balance throughout the body, a crucial component of the immune system, and a provides a major route for cancer cell metastasis. However, many of its key mechanisms are still to be fully elucidated. Indeed, the rate of increase in knowledge regarding the lymphatic system lags far behind that of the cardiovascular system, making it an exciting area of research today. Even in the past 5 years, major anatomical discoveries in the lymphatic field have been made, such as the characterisation of functional lymphatics in the brain in 2015 [1].

1.1 A brief history of the lymphatics

Descriptions of lymphatic system organs date back to approximately 300BC when the Greek physician Hippocrates described lymph nodes (LNs), containing a fluid he termed '*inos*,' located in the armpit, ears, mesentery area and kidney, [2, 3]. Around 100 AD, the Roman physician Rufus of Ephesus first described the thymus, a primary lymphoid organ in the chest, that we now know shrinks with age [4]. As macroscopic organs, LNs were easy to identify, and further described by Greek physician and surgeon Galen several generations later [5]. Galen also identified a milky fluid secreted during gut dissection as mistakenly draining into veins. We now know this milky fluid as Chyle, a mix of fats and lymph formed following absorbance of dietary lipids by lymphatic villi of the small intestine. In 600 AD the Byzantine physician, Paul of Aegina, first illustrated the tonsils and described infected LNs of the lower cervical region around the neck [6].

Lymphatic vessels (LVs) connect the lymphatic organs but due to the delicate nature and near translucency of LVs, they proved much harder to identify. In 300BC ancient Greek philosopher and scientist Aristotle first mentioned what is likely to have been LVs as an intermediate between veins and nerves that carried a colourless fluid. However, further research into this system subsequently stagnated for centuries [2, 3, 6]. In the 16th century, the largest lymphatic vessel in the body, the thoracic duct, was identified but it was in the 17th century that simultaneous discoveries in lymphology led to large gains in knowledge [3, 4]. The term lymphatics was coined by a Danish anatomist Bartholin but Swedish scientist Olof Rudbeck was likely the first anatomist to correctly describe the lymphatic system as a network throughout the body [7] In fact as a medical student Rudbeck charged the Danish professor with antedating his findings and plagiarism [4]. It is thought that the first painting of the lymphatic system was provided in by Italian surgeon Giovanni Gugliemo Riva(1627-1677), depicting blood, chyle and lymphatic vessels but it was anatomist Paolo Mascagni who provided the first full body illustration of the lymphatic network in 1787 (Figure 1.1) [8, 9].

Figure 1.1: A historical painting of the lymphatic network. Paolo Mascagni, Tab XXIV, 1787. Vasorum Lymphaticorum Corporis Humani Historia et Ichnograhia.

1.2 Current understanding of the lymphatic system

Today, the lymphoid system is known to contain specialised primary and secondary lymphoid organs, including lymph nodes (LNs) that act as lymphatic filtration organs and have a key role in adaptive immune responses. The primary lymphoid tissue consists of the bone marrow, foetal liver and the thymus, where development and maturation of lymphocytes occurs. There are two major subsets of lymphocytes, B and T cells, that are derived from common lymphoid progenitor cells. These progenitor cells, themselves derived from long term haematopoietic stem cells, undergo initial development in foetal liver (pre-birth) or bone marrow (post birth) where they mature. Contrastingly, common lymphoid progenitors that will become TCs undergo a maturation and selection processes in the thymus.

T cells are a critical component of the adaptive immune response, with subsets equipped to kill and transform cells via cytokine expression, directly destroy cells through perforin, granzyme and FAS mediated mechanisms, and to drive high affinity humoural based responses. To be able to destroy pathogen, T cells must firstly recognise small fragments of protein antigen, presented within Major Histocompatibility complex (MHC) proteins on antigen-presenting cells, such as mature dendritic cells, by expressing the complementary receptor (see Box 1). A higher-affinity interaction between T cell receptor and the peptide-MHC complex can trigger T cell activation via a complex cascade of cellular signalling events. With sufficient antigenic stimulation, activated TCs can proliferate multiple times and subsequently differentiate into cells equipped to destroy the type of pathogen that provided the initial antigen fragment.

However, as well as expressing foreign antigenic peptides, MHC proteins also express self-peptides that can be recognised by mature T cells. To avoid development of spontaneous auto-immune disease, TCs must undergo central tolerance, where self-reactive T lymphocytes are removed through a process of negative selection in the thymus. Adaptive immunity takes place in the highly organised secondary lymphoid tissues, including the LNs, the spleen, Peyer's patches, isolated lymphoid follicles, and in humans, the tonsils. The secondary lymphoid tissues facilitate interaction between antigen-presenting Dendritic

Cells to highly motile TCs, by providing a specialised compartment, optimizing the likelihood of interaction and subsequent immune response. Similarly, B lymphocytes are localised in the B cell zone of the lymph node, where they are presented with unprocessed antigen-complement complexes by follicular dendritic cells. This results in the initiation of high affinity humoural responses. The secondary lymphoid tissue can also provide an area for lymphocytes to undergo peripheral tolerance through several mechanisms (see 1.5).

Unlike the closed circulatory system, the lymphatic system is an open-ended system. Interstitial fluid enters blind-ended small initial lymphatics, consist of a layer of lymphatic endothelial cells that drain most tissues of the body (Figure 1.2.A). Exceptions to this include the epidermis, mucous membranes and bone marrow. Once inside the initial lymphatics, the fluid, now termed lymph, enters the lymphatic capillaries (microlymphatics), which are composed of a layer of lymphatic endothelial cells and a basement membrane [10]. Lymph is transported in the microlympahtics to join larger collecting lymphatic vessels (LVs), that additionally have a layer of smooth muscle cells and endothelial valves to prevent backflow (Figure 1.2.A) [11]. [12]

The lymphatic capillaries are specialised to absorb interstitial content, which enters mainly non-selectively, through inter-endothelial junctions, including adherens junctions, as well as large inter-endothelial pores and trans-endothelial vesicles [13–17]. Consequently, it is thought that the lymph protein content of initial lymphatics is about the same as the protein concentration of the interstitium [10]. The fluid, small proteins and waste products then flow into the collecting lymphatics (rev.[18]). Unlike lymphatic capillaries, the collecting lymphatics have continuous adherens junctions, to help retain contents of the lymph [19]. Experiments using varying sizes of dextran molecules have shown that molecules 70kDa or larger are retained in the collecting lymphatics and thus similarly only molecules <70kDa can passively perfuse in [20]. Despite acting to absorb fluid, it is also possible for solute to move from vessel lumen to the interstitium, which supports the hypothesis that the lymph can become more concentrated as it passes through the collecting LVs [21]. The layer of smooth muscle cells can contract spontaneously to pump lymphatic fluid along an increasing pressure gradient, with the valves helping to prevent backflow

[22–24] (Figure 1.2.B). Collecting LVs eventually converge into two lymphatic trunks at the base of the neck that are connected to veins. The right lymphatic trunk drains the right upper part of the body and deposits lymph into the right subclavian vein. The left lymphatic trunk is called the thoracic duct and drains the rest of the body, depositing lymph into the left subclavian vein. As a result, the contents of the lymph eventually access the blood and the fluid is recycled into the bloodstream.

1.3 Contribution to maintenance of fluid homoeostasis in the body

Throughout the body, net leakage of fluid out of veins, arterioles and capillaries into the interstitial spaces occurs, due to hydrostatic and oncotic pressure differences. Much of the interstitial fluid is reabsorbed into lymphatic capilliaries and eventually returned to the blood stream via the right lymphatic trunk or thoracic duct. Disruption of the lymphatic drainage system can lead to swelling of the affected limbs or tissues, termed lymphoedema (Figure 1.2 (Figure 1.2.C). Primary lymphoedema is a result of a genetic defect at birth that is currently un-curable, and can worsen over time due to subcutaneous fibro-adipose deposition. In the early stages of Lymphoedema, the swelling of tissues occurs, that become soft to touch and often accompanied by tissue fibrosis, defined as 'excessive deposition' of extracellular products, in the surrounding tissue, and eventually fibrosis in the lymphatic vessels themselves [25]. Fibrosis causes the tissues to harden which obstructs lymphatic drainage further, resulting in increased lymphoedema and increased scar tissue, further exacerbating the problem in addition to inhibiting lymphatic regeneration [26].

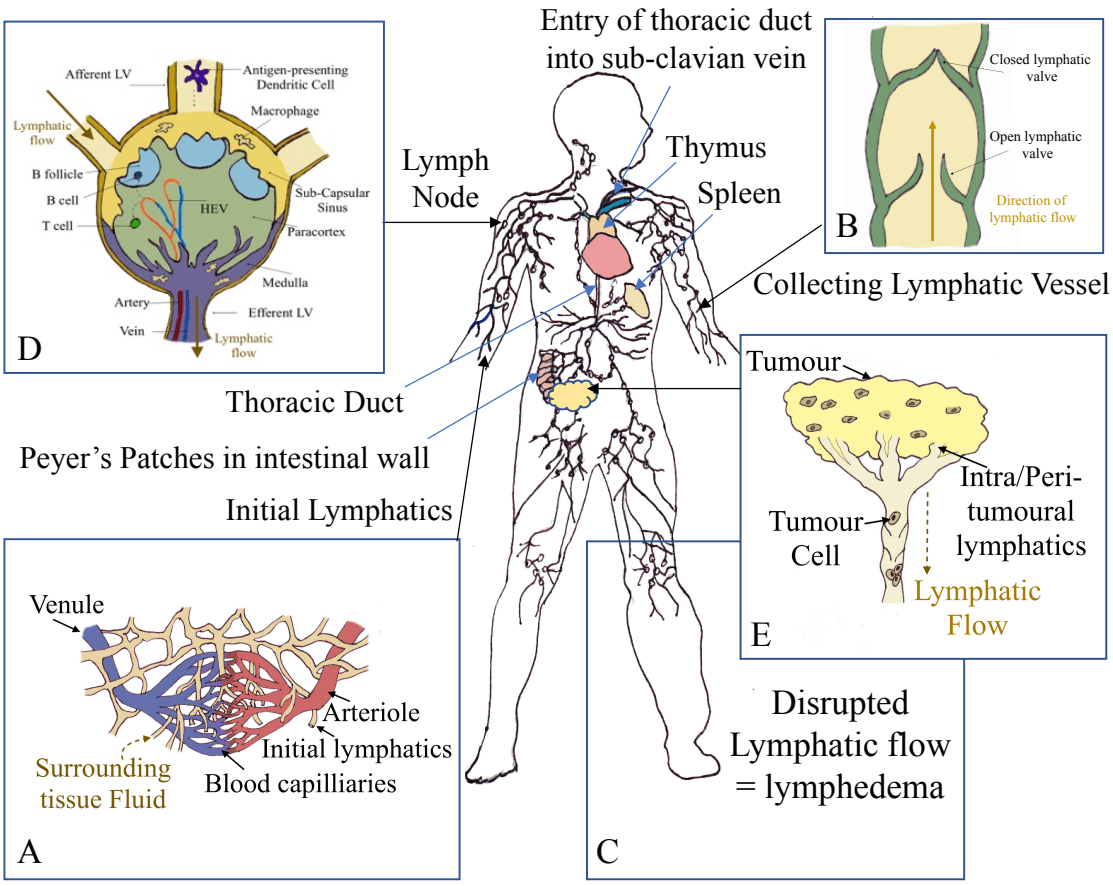

FIGURE 1.2: A summary of the roles of the lymphatic system. The lymphatic system is an open-ended system beginning with initial lymphatics that perfuse and drain waste products and fluid from tissue into microlymphatics (A). Microlymphatics lead to collecting lymphatics which have one-way valves (B) and systolic pumping to transport lymphatic fluid against and unfavourable pressure gradient to the right or left lymphatic (thoracic) duct.From here the lymph is deposited into the right or left sub-clavian vein and enters the blood supply. Disruption of lymphatic flow can result in the collection of waste fluid and tissue swellling (C). Lymph nodes (LNs) are stationed along the lymphatic network, sample the draining lymph and allow initiation of the adaptive immune response if antigen is detected (D). Lymphatic vessels grow in and around tumours and provide a major route of metastasis from the tumour (E).The spleen and thymus are primary organs of the lymphatic system whilst the appendix, LNs and Peyer's patches are secondary organs.

Secondary lymphedema can be triggered by multiple causes. During breast cancer surgery, the draining axillary LNs in the armpit area are often removed to help prevent cancer cell metastasis. As a result, the normal pathways for fluid transport in lymphatic vessels from the arm to the thoracic duct, or right lymphatic trunk, are severely disrupted. Consequently, approximately 20% of women who undergo this procedure develop lymphedema of the arm of their operated side due to insufficient ability to transport reabsorbed interstitial fluid (Figure 1.3a) [27]. Secondary lymphoedema can also result from filariasis. This tropical disease, also known as Elephantiasis, is caused by the transfer of infective larvae from mosquito's proboscis to humans skin at the site of the mosquito bite, allowing penetration of the skin. The larvae can then migrate to the lymphatic system, and mature into worms that clog the lymphatics. Lymphatic filariasis can lead to debilitating lymphedema due to blockage of the lymphatic system and thickening of the lymphatic walls that prevents normal fluid transport (Figure 1.3b)(rev [28]) . The lymphedema is accompanied by acute episodes of LN, LV and skin inflammation whilst other less obvious symptoms of lymphatic filiarisis include internal damage to renal and lymphatic systems [29]. As of 2018, 856 million people in 52 countries worldwide remain threatened by lymphatic filariasis (WHO 2018) [30].

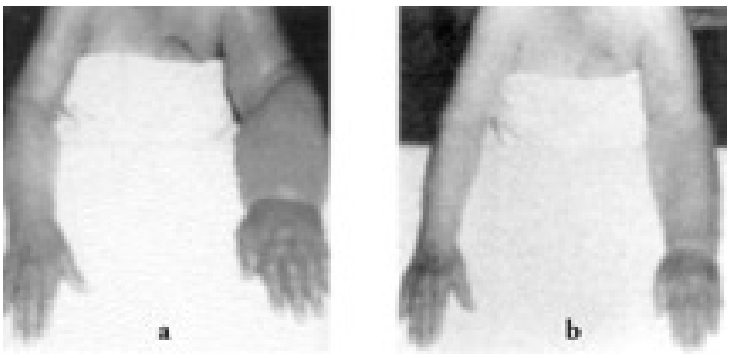

(A) Lymphoedema post mastectomy [31]

(B) Lymphatic filariasis [30]

FIGURE 1.3: Two causes of secondary lymphoedema

1.4 Lymphatics and immune response

The lymphatic network has a crucial role in the efficient function of the immune system, by transporting immune cells (including dendritic cells), antigen, cytokines, chemotactic factors, lipids and metabolic products from the peripheral tissues, in the lymphatic vessels to the LNs. In the LN the adaptive immune responses are initiated, often accompanied by LN swelling (Figure 1.2). Once transported to the LN, careful coordinated trafficking of the immune cells is achieved via multiple mechanisms. For example, molecules in the lymph are filtered both passively and actively into different areas based on size or receptor expression, while LN structural cells secrete chemo-attractant molecules to localise specific types of immune cells to distinct areas.

The process of antigen detection begins with the entry of antigenic components from tissue into the initial lymphatics with minimal molecular requirements. The major type of antigen-presenting-cell for the adaptive (specific) immune response, antigen-presenting Dendritic Cells (agDCs), can also enter initial lymphatics during inflammation[32–34]. DCs enter in an integrin-aided manner facilitated by chemotactic gradients, formed by small molecules called chemokines that are immobilised on the endothelium with agDCs expressing the complementary receptors (rev.[18]) [35]. DCs and free antigen are then transported in lymphatic flow to the draining LNs.

In the lymph node, lymph is initially deposited into the sub-capsular sinus where macrophages engulf and digest antigen in a non-specific manner. The lymph and agDCs may perfuse into separate compartments where B cells and T cells, which enter from specialised high endothelial venules (HEV) that form part of the LN vascular network, interact with free antigens and agDCs. Successful interaction initiates two branches of the adaptive immune response (rev.[36]). The cell-mediated response produces effector T cells equipped to destroy specific pathogens (see Box 1 for details). The humoural response is carried out by B cells that produce antibodies that will bind to invading pathogen, flagging it for removal by other immune cells. Resulting effector T cells and antibodies exit in efferent lymph to be eventually transferred back into the blood at the thoracic duct and then circulate to the site of infection. During the adaptive

response LNs often swell several-fold in volume, a macroscopic change with unknown effects on immune cell behaviour. As such, the contribution of chronic enlargement in diseases, such as Rheumatoid Arthritis, remains unclear, as does the role in a normal response. As the antigenic signal decreases, activated and effector TCs that remain in the LN undergo apoptosis and the LN returns to pre-stimuli volumes, with an increased number of effector memory TCs.

Box1: T cell immune response

The antigenic stimulation of T cells (TCs) is achieved through recognising peptide fragments expressed within surface proteins called Major Histocompatibility Complex (MHC) molecules [37–40]. Type I is expressed by all cells and present to cytotoxic TCs. Generally, MHCI peptides originate from endogenous sources, where the fragment expressed originates from the cell itself, for example, aberrant proteins resulting from viral infection or on pathogenic cells. Cross presentation can also occur when exogenous molecules are passed to MHCI molecules. Type MHCII is primarily expressed highly by professional antigen presenting cells (APCs). The peptide fragment expressed on MHCII molecules originates from extracellular sources, where antigens are phagocytosed, digested and re-expressed by the APC. TCs all express a cluster of differentiation (CD) molecules named $CD3^+$ and are divided into two major subsets expressing glycoprotein $CD8^+$ or $CD4^+$ (rev [41]). $CD8^+$TCs are cytotoxic TCs that when activated by antigenic stimuli can differentiate into effector TCs that are equipped to kill target cells. $CD4^+$ TCs are helper TCs that are further divided into subgroups that express different cytokine profiles and aid other immune cells. $CD8^+$ TCs are stimulated through interaction with MHCI molecules and $CD4^+$ TCs through interaction with MHCII molecules.

1.4.1 Modelling TC behaviour in the LN

Many different types of computational models have been used as tools to investigate aspects of the TC response in the LN that would be extremely costly, difficult or near impossible to carry out *in-vivo*. Signal integration between TCs and DCs and behaviours involving growth and decay are well suited for description using ordinary differential equation (ODE)-based models. For example, by using ODEs to describe $CD8^+$ TC and tumour cell interaction in the blood, the spleen and the tumour site, it was possible to investigate how dendritic cell

dose impacted the optimum injection site, eg. intravenously or directly at the tumour site [42]. However, ODEs-based models don't account for the geometry of the system. Use of partial differential equations (PDEs) can improve the description of spatially dependent aspects, such as chemotaxis and diffusion, but models with many PDEs can become computationally intense and similarly restrictive when considering changes in the environment geometry. TC migration has been modelled using several biophysics-based models, describing migration with different models of motion such as Brownian motion, Lévy walks and variable persistent random walks with noise, with one such model also including signal exchange between interacting TCs and DCs [43–45].

Computationally expensive Cellular Potts Models and Agent Based Models are able to account for complex geometries, by dividing the environment into grid compartments, each with individual properties. In CPM, a cell can be described using a cluster of points, spread over multiple grids, allowing cells to elongate and contract. The movement of the cluster is governed by calculating forces and energy, considering the cell state and the surrounding environment. This allows consideration of complex geometries but also makes CPM relatively very computationally expensive compared to ODE based models. Nevertheless, CPM has been used to describe TC and DC transit and interaction in a 100μm area of the LN under non-antigenic conditions to investigate the most influential parameters on TC transit [46]. The results of simulations using this model suggested that TC velocity fluctuations are a result of environmental alterations rather than pre-programmed motility. Several ABMs have previously been used to model TC interactions in the LN (further discussed in section 2.1.7). In ABMs, each cell is modelled as a discreet point, with behaviour determined by following simple probabilistic rules regarding cell internal state, environment state and the state of any other cells the initial cell is interacting. Agent based modelling is much less computationally demanding than CPU models, can capture emergent properties of systems due to the individual probabilistic behaviour of many agents at once, and can consider changes in complex geometries.

Mechanisms of increase in LN volume during the adaptive response are not well-understood, and despite the aforementioned models, those that incorporate LN swelling are limited. One series of models developed by Bogle and Dunbar,

described the TCs transition and adaptive response of an entire paracortex, with the capability to alter the paracortical volume [47, 48] . However, the relative ratio of TCs to overall paracortical volume remained constant, thus allowing the changes in size, but also perhaps overlooking the effects of TC crowding. A better understanding of the impact of LN swelling is desirable as it could lead to identification of new immune targets to modulate immune response, contribute to improvements in vaccine design and provide clarity into the effects of chronic LN swelling.

1.5 Structural cells of the lymph node and lymphatic vessels

The cells that contribute to maintaining the structure of the LVs and the LN also contribute to regulation of immune function in multiple ways. In the LN specialised fibroblastic cells, called Fibroblastic Reticular Cells (FRCs), can wrap around reticular fibres to form conduits from the SCS to the paracortex and also form a meshwork throughout the paracortex. This supports the LN structurally but FRCs can additionally secrete CCL20 and CCL19 chemokines to guide DCs, TCs and B cells (that express the complementary CCR7 receptor) to the paracortex to facilitate interactions (rev[49]). During an immune response, the FRCs may also suppress TC response by producing Nitric oxide that suppresses TC proliferation [50–52].

Marginal reticular cells are a recently discovered subset of stromal cells that form a monolayer around the B-follicles. The MRCs can secreting CXCL13, similarly contributing to B cell localisation via chemotactic guidance of B cell that express the complementary CXCR5 receptor [53]. Inside the B-follicles, follicular dendritic cells (FDCs), are a non-hematopoietic mesenchymal stromal cell type that express CXCL13 and regulate B cell migration and survival (rev [54]).

The LECs constitutively express CCL21, and line the upper and lower ceiling of the SCS and the medullary sinuses [55]. The upper LECs can express atypical chemokine receptor CCRL1 that binds CCL19 and CCl21, a property thought to

help guide DCs into the lymphatic vessels by creating a concentration gradient for DCs that express the corresponding CCR7 receptor[56]. LECs may play a role in memory T cell generation by capturing soluble antigen and presenting it several weeks after the initial DC response during the $CD8^+$ T cell contraction phase. This allows LECs to cross-present antigenic peptides to DCs that re-stimulate $CD8^+$ to aid induction of a memory response [57].

The FRCs expression of surface protein podoplanin (PDPN), is also important during LN swelling. In the initial 1-2 days post infection, the engagement of PDPN by surface protein CLEC-2 expressed on DCs allow FRCs of the LN to relax [58]. The reduced tension means that the FRCs stretch to support the enlargement and maintain LN architecture. In the following days, the FRCs then undergo proliferation and can also secrete vascular endothelial growth factors that can promote LEC proliferation, aiding structural cell maintenance of the larger LN structure [58–60]. The engagement of PDPN with CLEC-2 with on the agDCs also promotes agDC motility and membrane protrusion, while the PDPN interaction is also involved in modulating HEV permeability, and thus lymphocyte entry rate (rev. [49]) [61, 62].

FRCs and LECs also play roles in peripheral tolerance which is a secondary process to central tolerance. Peripheral tolerance prevents T cells that have missed deletion in the thymus from triggering an autoimmune response through repeated exposure to a weak stimulus in several mechanisms. T cells can become non-responsive to antigen if engaged with an MHC molecule without co-stimulation, TC effector function can be suppressed by regulatory T cells (Tregs), and T cells can be deleted or converted into Tregs following interaction with immature or semi-mature antigen presenting Dendritic cells (rev.[63]. The FRCs and LECs of the LN can also express tissue-specific self-antigens scavenged from peripheral tissue to $CD8^+$ T cells at homoeostasis whilst specific receptor expression (PD-L1) on LECs can drive deletion of a type of $CD8^+$ T cell (rev.[64]) (see section 3.1.2).

The lymphatic vessels can also contribute to immune response. LECs outside the LN can up-regulate MHCII expression in response to an inflammatory cytokines [65, 66]. LECs of the LVs may then interact with passing $CD4^+$ T cells

potentially tolerising $CD4^+$ cells directly or indirectly via interaction with DCs [67–69]. They can also be affected by inflammation, secreting cytokines and growth factors in response that can affect downstream nodes and impact LV permeability and contraction, potentially affecting flow of immune cells to the LN [70–72].

1.6 Lymphatics and metastasis

Globally cancer is the second leading cause of death, which caused an estimated 9.6 million deaths in 2018 (WHO 2018) [30]. The lymphatic vessels are specialised for the uptake and transport of macro-molecules but this can become a harmful property during cancer. Research regarding intra-tumoural lymphatics and lymphangiogenensis in the draining LN points to lymphatic involvement in both immune regulation and metastasis, but an understanding of the contribution of draining lymphatic vessels to immune response during cancer remains elusive. Additionally, chronic inflammation in the collecting LVs induce changes including LV dilation and inhibition of contractile ability but physical characterisation of changes in the draining LVs during cancer is lacking [71, 72].

At the tumour site both blood vessels and LVs grow in and around the tumour, providing a major route for metastasis (Figure 1.2.E), (rev.[73]). Tumour cells are transported to draining LNs, where anti-tumour responses should be initiated. However, cancer cells often escape immune detection or the immune response is impaired. The cancer cells then colonise the LN and proliferate. LNs that return positive for cancer cell presence during patient staging correlate with a poorer prognosis although the role of systemic LN removal and patient survival is currently under debate (rev.[74][75]). Tumour cells may spread through the lymphatics to other parts of the body but experiments in mice have recently shown that tumour cells can enter the blood vessels in the LN and metastasise in the circulatory system [74, 76–78].

Research regarding LVs presence at the tumour site has shown that, in addition to providing routes for metastases, the LECs can secrete VEGF, the presence

of which is associated with poor prognosis with accompanying increased lymphangiogenesis and vascular growth throughout the tumour [79]. The LECs of the LVs can also modulate anti-tumour responses and cancer-induced immunosuppression, for example by expressing the transmembrane PD-L1, the ligand for TC inhibitory receptor PD-1 [80, 81].

To infiltrate the lymphatic system, tumour cells are thought to enter the LVs passively or in a chemokine-aided manner, with the LECs of primary tumour sites secrete corresponding chemokines to chemokine receptors expressed on the tumour cells lymph (rev.[74]). Tumour cells may on occasion arrest in the LVs themselves, and some studies suggest inflammation induced changes in the connecting LV integrity may allow cancer cell metastasis directly out of LVs [82, 83]. There is limited research regarding alterations in functional LVs adjacent to, but not directly at the tumour-micro-environment but LVs are not simply passive transport channels. Upregulation of MHCII expression on LECs has been observed in response to inflammatory cytokine IFNγ, and LEC presentation of antigen on MHCII molecules to passing CD4$^+$ TCs may contribute to tolerance [65, 66] [67, 68]. Lymphatic vessels also respond to pro-inflammatory cytokines that promote lymphangiogenic pathways and further secretion of cytokines impact the downstream LN [70]. Extensive studies have identified gene expression and miRNA alterations in tumours that are clinically correlated (see Section 3.1.3). Studies regarding gene expression alterations of the connecting LVs are sparse, but have shown that lymphatic vessel gene expression in response to tissue inflammation occurs in a stimuli dependent manner and that LVs draining a tumour upregulate the gene for chemokine CXCL1 [84, 85]. Alteration in miRNA of the draining LVs are lacking, but human LEC culture models of gastric cancer, presenting tumoural or draining LVs showed differential miRNA expression, (see Section 3.1.5) [86].

When tumour cells reach the draining LN, chemokine involvement has again been shown to aid melanoma cell entry. CCL1 is expressed by LECs in the first compartment that lymph is deposited into, the sub-capsular sinus, and its receptor CCR8 is expressed on melanoma cells [87]. From the SCS, lymphatic fluid percolates through the LN or siphons the LN in a thin layer of SCS. but the route that cancer cells may take is unclear.

Once within the LN, the survival of cancer cells in what should be an inhospitable environment is not fully elucidated, but is thought to be partly due to the formation of a pre-metastatic niche (rev.[74, 88]). This is where signalling molecules produced by tumour cells drain to LNs and induce changes in the local microenvironment in both stromal and immune cell behaviour, favourable to cancer cell survival. In pre-metastatic LNs, growth of the lymphatic vasculature and lymphatic sinuses of the LN, lymphangiogenesis, may potentiate change through increased lymphatic drainage[89–91]. LECs can contribute to peripheral tolerance through interaction with $CD8^+$ T cells and this has been shown to include tolerance to tumour cell antigens [74, 92, 93]. As in the tumour-associated lymphatics, LECs may also inhibit T cell responses through expression of TC inhibitory receptor PD-L1 [80, 81]. At the gene expression level, during colonization of LNs by cancer cells, the normal immune response to antigen is inhibited, and research has revealed diagnostic signatures of metastatic LNs [94]. Research regarding miRNA expression alteration in the LN is limited, but the miRNA-141 showed decreased expression in patients with metastatic LNs, leading to increased expression of target gene MAPK4, which was associated with increased proliferation and metastasis of tumours [95].

1.7 Problem Definition

Overall the goal of the PhD project was to improve the knowledge base of immune function, using a combination of computational modelling and wet-laboratory-based research to explore two specific functional aspects of the lymphatic system; the effect of LN swelling on immune response, and whether changes occur in functional lymphatic vessels in patients with ovarian cancer that may affect patient relapse (see Figure 1.4).

The aim of gaining insight into the effects of macro-scale alterations of the LN swelling on the efficiency of effector TC production is discussed in chapter two of this thesis. Specifically, the objectives were to build a reliable and accurate computational model of TC trafficking and response to antigenic stimuli, with the capability to include paracortical swelling and factors important in transit and swelling that have not been simultaneously incorporated in previous modelling efforts. These include: increased recruitment due to both accompanying HEV growth and antigen detection, the effect of regulation of key T cell transmembrane protein Sphingosine-1-Phosphate 1 receptor (S1P−1r) and the changes in paracortical volume and accompanying change in TC exit rate.

Previous computational modelling work has successfully utilised agent based modelling to describe T cell migration, DC to T cell signalling, T cell activation and proliferation, with moderate computational demand, and accurate description of TC behaviour but with a focus of TC interactions and signalling either without swelling or with limited description of swelling [47, 48, 96–99]. Accordingly, an ABM was selected as the framework for the model, describing the LN paracortex with TC and DC agents and meeting the criteria listed above.
The reliability of the computational model was determined by :

1. Applying antigenic stimuli and reproducing realistic T cell responses
2. Performing a global sensitivity analysis to identify influential parameters to inform modelling decisions to better minimise uncertainty.
3. Reproducing experiments performed *in-vivo* to validate the model.

The hypothesis that LN swelling pattern does not alter the efficiency of TC response to stimuli, and the accompanying transit, trafficking and interaction

with DCs was then tested. The model parameters regarding the rate, the extent and the manner of LN swelling were varied and resulting changes in effector TC response analysed. To investigate whether the way that entry and exit areas alter with swelling affects the response, the rules regarding entry and exit area alteration were also varied. To investigate the effect of prolonging the influence of $S1P_1r$ regulation on TCs, parameters regarding $S1P_1r$ expression on newly differentiated effector TCs were also varied, whilst modulating maximal swelling. This was to elucidate whether the influence of $S1P_1r$ expression and swelling may show dependencies. The resulting effects of expansion and influential parameters are discussed along with suggestions for future work towards modulating efficiency of TC response.

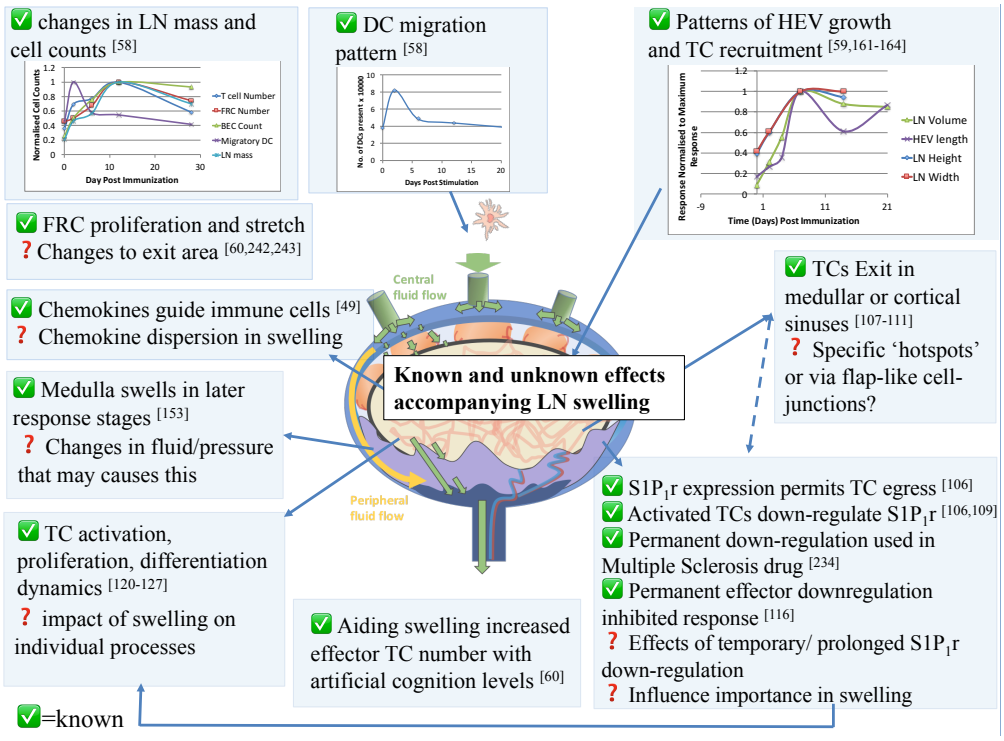

FIGURE 1.4: Summary of current research regarding LN swelling and cell-mediated response. Many observations have been made regarding immune cell motility and proliferative dynamics in addition stromal cell counts, LN mass and immune cell counts. The role of $S1P_1r$ in regulation of TC exit has previously been identified, but temporary modulation of $S1P1_1r$ expression has not been investigated. Little is known regarding the effects of swelling on TC response, TC exit and chemokine gradients that aid TC retention.

The third chapter of this thesis discusses work carried out with the aim of

advancing knowledge regarding the role of draining lymphatic vessels during ovarian cancer (see Figure 1.5). Many gains in recent years have been made in the field of immunotherapy, which focuses on reactivating the body's natural immune defence system, including T cell response, to attack and destroy cancer cells. LEC presentation of scavenged tumour antigen has been shown to contribute to anti-tumour response through inducing tolerance of TCs at both the LN and the tumour-associated LVs. Influence of the connecting lymphatic vessels has remained unclear, despite identification of RNA and miRNA however, LVs are not passive vessels. The LVs show altered gene expression in response to tissue inflammation, secrete cytokines and growth factors and cell culture models representing draining lymphatics report differential miRNA expression [70, 84–86]. Therefore, an important step towards future research in this area is to characterise underlying changes that may identify areas to target to prevent tumour cell transport or facilitate immunotherapy.

Towards this goal, research was performed to identify any alterations in the connecting LVs at the gene transcription level during ovarian cancer by quantification of the inflammatory state of the LVs and analysis of miRNA, the transcription factors that form a higher regulatory network through inhibition of gene transcription. This was achieved through isolation of macroscopically normal tumour-draining lymphatic vessels from ovarian cancer patients and subsequent processing for miRNA extraction and immuno-histochemical staining, using markers for lymphatic vessels, inflammation and cancer. Analysis of the resulting images and miRNA expression results allowed identification of key miRNA changes associated with inflammation and/or cancer cell presence. The associated pathways, significance and correlation with clinical outcomes are then discussed.

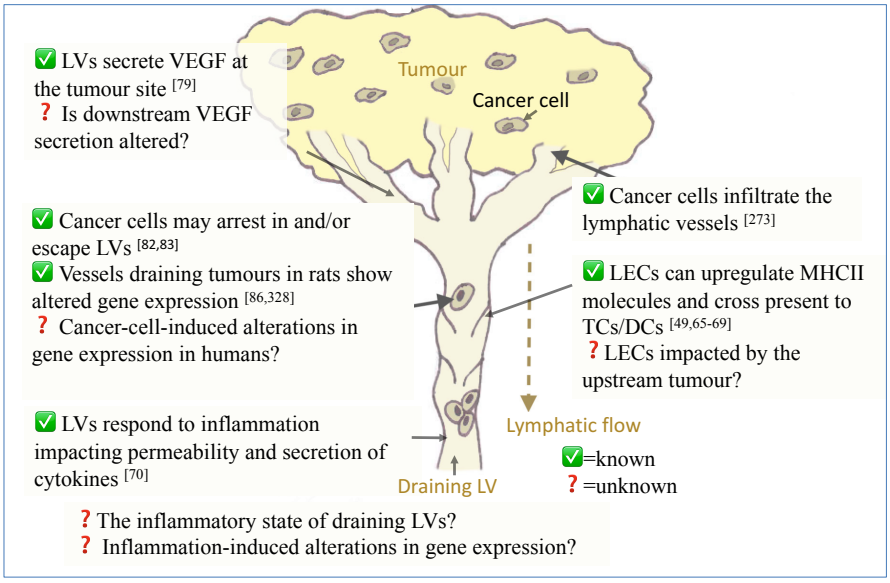

FIGURE 1.5: Summary of current research regarding tumour draining lymphatic vessels, away from the tumour micro-environment. While research using rat LVs has shown that tumour draining LVs undergo gene expression alterations (both mRNA and miRNA), confirmation of changes in Humans is lacking.

Chapter 2

The impact of lymph node swelling on T cell response

2.1 Introduction

The lymphatic system is a converging network of organs and lymphatic vessels that maintains fluid balance in the body by functioning as a fluid transport system while also playing a vital immunological role through antigen and immune cell trafficking. Adaptive immunity initiates in Lymph Nodes (LNs) when antigenic signal transported in lymphatic fluid from peripheral sites interacts with lymphocytes migrating from specialised blood vessels. T cells (TCs) provide the cell mediated response by differentiating into effector cells equipped to destroy pathogens at peripheral sites. Ensuring optimum antigen detection and response helps to prevent hypersensitivity or immunodeficiency. This regulation is partly achieved through careful coordination of lymphocyte entry, migration and trafficking using both LN architecture and signalling molecules [100]. During an immune response LNs often temporarily swell, a feature termed reactive hyperplasia. In certain disease states, such as Lupus and HIV infection, chronic lymphadenopathy is both a symptom and a potential contributing pathogenic factor. The mechanisms driving hypertrophy during the adaptive response and the overall consequences of LN swelling on T cell trafficking and behaviour are largely unknown.

2.1.1 Lymph node structure and cell transit

Dendritic cells (DCs) are the most potent type of antigen-presenting cells in the LN and are critical to induce a complete TC response [32, 33]. Migrating DCs capture antigens at the periphery, enter lymphatic vessels and travel in the

lymph to draining LNs. During transport, the DCs undergo changes including expression of costimulatory molecules and incorporation of fragments of the internalised antigen into surface proteins called Major-Histocompatability Complexes (MHC) [32]. Multiple afferent lymphatic vessels feed into a single LN and deposit lymph that contains antigen-presenting DCs (ag-DCs), free antigen, and interstitial waste into the sub-capsular-sinus (SCS) (Figure 2.1A) [34, 101, 102]. Fluid can either siphon through the LN periphery in a thin layer of SCS to merge with a medullary region at the LN base (Figure 1 A: purple area), or drain centrally into the cortex. DCs cross the SCS floor in a chemokine and integrin-aided fashion to migrate into the paracortex [34]. A dense network of blood vessels exists throughout the LN and lymphocytes mainly enter the LN by transmigrating from specialised High Endothelial blood vessels (HEVs) in the paracortex [101, 103, 104].

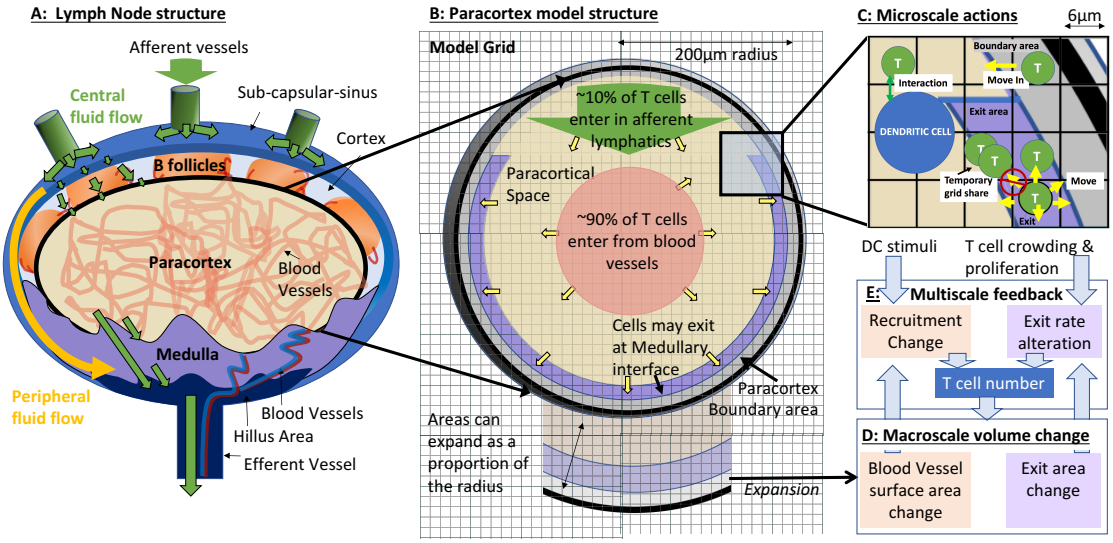

FIGURE 2.1: The structure of the LN and the ABM geometry. A: Popliteal LN structure displaying the pathway of arriving lymphatic fluid. B: The model describes a spherical paracortex, TCs enter in the center and exit near the interface with the medulla and SCS. The paracortex radius expands as a function of TCs present. C. The environment is divided into compartments of $6\mu m^3$. Each compartment can represent different paracortex areas. TCs move to adjacent compartments, interact with neighbouring agents and are influenced by the compartment type. Micro-scale signals can influence recruitment, exit and DCs interaction. D. Macro-scale changes in paracortex size influence TC recruitment and exit rate. E. Micro-scale and macro-scale changes influence each other and affect the number of TCs present

The Sphingosine-1-Phosphate type 1 receptor ($S1P_1r$) expressed on TCs has been shown to play a crucial role (in the entry and exit of TCs) in several mechanisms, summarised in Figure 2.2. During transmigration, TCs express $S1P_1r$ at very low levels due to its reciprocal regulation by high ligand S1P concentrations in the blood [105, 106]. However, in the low S1P LN environment, within 45 minutes TCs begin re-expressing $S1P_1r$ [106]. TCs exit the paracortex in an $S1P_1r$-dependent manner by probing cortical sinuses in the paracortex and the interface with the medulla (Figure 2.1A: purple area), which both contain higher S1P concentrations [107–111]. Additionally, TC $S1P_1r$ expression is thought to be reciprocally regulated by CD69, an early TC activation marker that can be up-regulated in TCs by the presence of inflammatory mediators (rev[112]). The detection of inflammatory signals and subsequent non-selective inhibition of TC egress results in blockage around the egress points. This is thought to contribute to the phenomenon of 'LN shutdown', a rapid and temporary reduction in TC egress at early stages in immune response [113, 114].In any egress scenario, it remains unclear whether TC exit can occur at any endothelial cell junction or only at specific portals [111]. In the medulla, fluid and TCs enter medullary sinuses that feed into a hillus at the LN base, where the fluid directed around the LN periphery also drains [101, 110, 115]. TCs that enter cortical sinuses are also lead to medullary sinuses or directly to the hillus where lymph is siphoned away in an efferent vessel [100, 110].

2.1.2 Cell mediated response

In the paracortex, the long dendrites of the DCs can probe and contact many TCs. Typically, 1 in 10,000 TCs will be 'cognate', meaning they express a complementary TC receptor (TCR) to an antigen fragment presented by ag-DCs within the MHC molecule [37–40]. Cytotoxic $CD8^+$ TCs interact with DC non-self MHC type I molecules and $CD4^+$helper TCs interact with DC type II MHC molecules[32]. Cognition is required for sustained interaction stabilized by co-receptors including $CD3^+$ and $CD4^+/CD8^+$ [117].

The duration of interactions between TCs and DCs alters during the course of the immune response. Naïve cognate TCs make short contacts of minutes in the first 8 hours of encounters, progress to longer interactions of hours for the

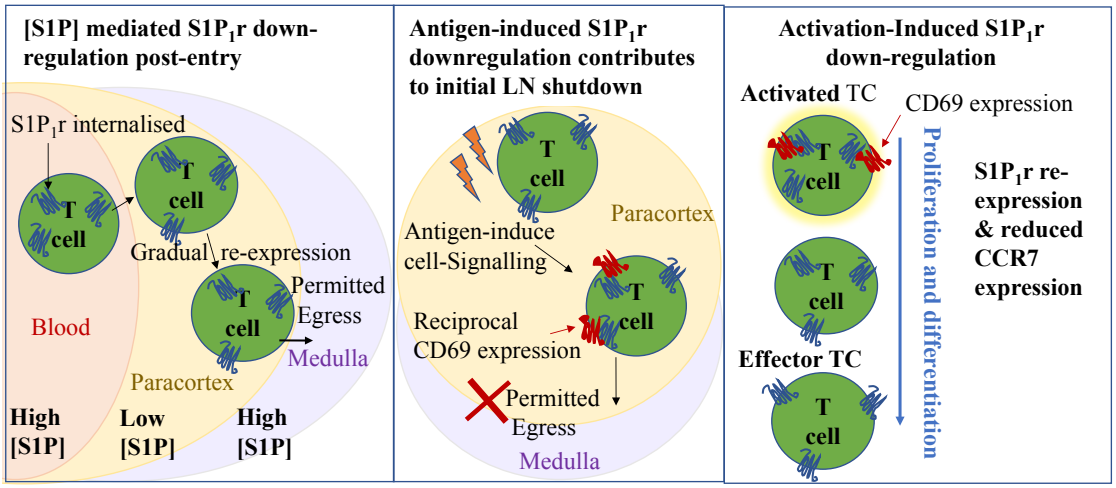

FIGURE 2.2: $S1P_1r$ signalling contributes to three aspects of TC egress. (a) Initial TC retention post-entry into the paracortex by S1P concentration-mediated $S1P_1r$ regulation,(b) initial non-selective retention of TCs that contributes to LN shutdown, by reciprocal regulation of CD69 (c) retention of activated TCs that express CD69, down-regulate $S1P_1r$ and lose expression of CCR7 and associated retention by CCL21 [106, 113, 114, 116].

next 12 hours, then return to short interactions as cells activate and divide. [118–124]. TC activation can occur when it's TCR, co-stimulation and time thresholds have been met [122, 125–127]. Activation induces down-regulation of $S1P_1r$ expression, partly through reciprocal regulation by trans-membrane protein CD69, an early TC activation marker, promoting retention in the LN, and inflammatory and activation-facilitating cytokines are secreted [105, 106, 109, 113, 114]. TCs begin to proliferate and by 4 divisions up-regulate $S1P_1r$ to pre-activation levels, and reduce expression of CCR7, but are still partly influenced by chemokine-mediated retention [106, 109]. TCs can differentiate into effector TCs and/or continue to divide 12-24 times, with a small but increasing proportion of TCs differentiating into memory cells over time to divide 12-24 times, with a small but increasing proportion of TCs differentiating into memory cells over time [104, 117, 119, 128, 129]. Current understanding is that the $CD8^+$ response can continue independent of further stimuli, possibly with an impaired memory cell response [130, 131]. $CD4^+$ TCs require a degree of sustained inflammatory stimulation for continued differentiation [130, 132–135]. After further proliferation, re-expression of $S1P_1r$ plus diminished chemokine-mediated TC retention allows effector TCs to exit the LN [106, 116,

136]. Mature migrating DCs undergo controlled cell death within the LN after a few days. As infectious signals resolve, remaining effector TCs also undergo apoptosis while long-lived memory cells recirculate [115, 123, 137–139]. Stimulation of $CD4^+$ TCs also results in migration to the B follicle boundary where they can interact with B cells [117].

2.1.3 Stromal cells contribution to immune response

Several types of cells support the complex LN structure that allows localization and compartmentalization of TCs to the paracortex and B cells to the B follicles [140, 141]. The ceiling of the SCS is lined with LECs, which constitutively express CCL20. The LECs on the ceiling of the SCS express the atypical chemokine receptor CCRL1 which can bind CCL21 and CCL19, helping to form a chemokine gradient across the SCS to aid the migration of corresponding receptor expressing mature DCs [56]. LECs also line the medullary sinuses and contribute to lymphocyte egress by expressing Sphingosine-1-Phosphate (S1P), to produce higher concentrations of S1P in the medullar than the paracortex, that is sensed by $S1P_1r$ expressing TCs [109–111].

The fibroblastic-reticular-cells (FRCs) are specialised myofibroblasts of mesenchymal origin, that secrete collagen and other ECM components, with several subsets found in the LN. FRCs wrap around reticular fibres, creating conduits from the SCS to the paracortex and a dense three-dimensional mesh throughout the paracortex [142, 143]. The FRCs in the paracortex (T-zone FRCs), secrete chemokines CCL19 and CCl21 help to attract and retain CCR7+ve naive TCs and DCs in the paracortex [66, 142, 144]. A subset of stromal cells called Marginal reticular cells form a monolayer around the B follicles and can secrete the chemokine CXCL13 [53]. This helps to localize B cells which express the complementary CXCR5 receptor. Inside the B-follicles, follicular dendritic cells (FDCs), a non-hematopoietic mesenchymal stromal cell type also express CXCL13, contributing to regulation of B cell migration and survival (rev [54]).

Stromal cell secretion of signalling molecules contributes to the LN alterations during swelling. FRCs also secrete VEGF-A, and thus contribute to endothelial cell proliferation, both during LN expansion and during remodeling of lymphoid

organs after resolution of infection [145]. FRCs express the surface protein Podoplanin, (PDPN) which interacts with the CLEC-2 receptor which is upregulated by agDCs. The PDPN-CLEC-2 interaction regulates DC motility [146] and induces relaxation of FRCs, thought to allow the LN to 'stretch' in the early stages of expansion. Pericytic FRCs also contribute to regulation of HEV permeability, by reinforcing cell-cell junctions at the HEV barrier in a PDPN dependent manner [147]. The HEVs are part of the vascular vessels formed by blood endothelial cells [148].

Stromal cells also contribute to T cell survival and regulation. The FRCs and LECs transcribe IL-7, a signalling molecule that aids in TC survival and whose expression by LECs and fibroblastic reticular cells is critical for lymph node remodelling [149]. Chronic inflammation can damage FRCs, and in chronic HIV-1, the T regulatory response results in increased secretion of collagen, causing fibrotic LNs due to accumulation of collagen around the FRCs. As a result, naïve TCs lose contact with the secreted IL-7, which is thought to contribute to the high levels of $CD4^{+}$ apoptosis [150–153]. Stromal cells regulate lymphocyte responses as FRCs can secrete Nitric Oxide, suppressing TC response, and the LECs can express TC inhibitory ligand PD-L1 at high levels, also suppressing TC response and driving deletion of a type of CD^{8+} T cell [65]rev([64]). In response to inflammation, the FRCs, LECs, BECs can all upregulate interferon and/or TLR-4-inducible genes, triggering pathways releasing inflammatory cytokines, and can up-regulate regulatory genes, chemokines (CCL5 and CXCL9) and components of the MHCII antigen presentation pathway [66].

Stromal cells can also cross-present antigen to TCs or DCs. The FRCs, LECS and BECs can increase MHCII expression following infectious signals, and FRCS and LECs can scavenge antigen and present on MHCII molecules, potentially further inducing $CD4^{+}$ tolerance by presenting a weak stimuli directly or via cross-presentation to DCs [65–69]. The LECs may also play an important role in memory T cell generation by capturing soluble antigen and presenting it several weeks after the initial DC response during the CD^{8+} T cell contraction phase. This allows LECs to cross-present antigenic peptides to DCs that re-stimulate CD^{8+} to aid induction of a memory response [57].

2.1.4 Types and Causes of Lymphandeopathy

Lymphadenopathy refers to the diseases of LNs, and can refer to abnormal size, number or structure. Lymphandeopathy is observed in lymphoma and more commonly reactive lymphoid hyperplasia. This is a reversible and benign enlargement in response to many different antigens and diseases pathways. Histologically it is possible to loosely divide different types of LN hypertrophy into 4 groups. Reactive paracortical hyperplasia refers to expansion of the paracortical areas of the LN associated with a response to inflammatory and immune reactions that trigger a TC response. It is caused by many types of infectious agents, vaccine administration, therapeutic drugs and immune-dysregularatory disease. Viral responses are often accompanied by this hyperplasia including herpes simplex, Epstein-Barr and cytomegalovirus. Reactive follicular hyperplasia describes LNs with predominantly enlarged follicles, associated with a B cell response pattern and disease such as rheumatoid arthritis (RA). LNs exhibiting Sinus Hyperplasia are often filled with macrophages or histiocytes and associated with Rosai-Dorfman disease. However many cases present a 'Mixed' pattern in most reactive hyperplasias the morphological pattern is not indicative of specific agents.

In addition, diseases or stimuli that may produce aforementioned LN characteristic responses at one stage in the immune response can display different patterns of LN expansion at another stage. For example, following a virally induced paracortical hyperplasia response, in the later stages of the immune response, the cortical and medullary sinuses have been observed to expand [154]. This allowed more TCs to egress and could be a key factor in the process of returning the LN to a quiescent state.

Another example is RA, an auto-immune disease where lymphadenopathy is present both systemically and at the draining LNs near to affected joints. The swelling is a results of both increased lymphatic drainage from affected joints and pathological disease aspects such as control of cell efflux and local immune response. Typically RA is associated with reactive follicular hyperplasia but RA mice models show both hypertrophic cortices and enlarged sinuses and ultrasound of superficial LNs in human RA patients show enlarged follicular and para-cortical areas prior to clinical detection, suggesting relevance of early

cortical and paracortical LN expansion is also of interest in RA [155, 156].

2.1.5 Mechanisms of paracortical enlargement

Reactive paracortical hyperplasia is a common response to many antigens and many experimental studies investigating immune response use adjuvants and antigens that produce this pattern of expansion. Driving factors and signalling pathways that underly resulting paracortical expansion vary. In Ovalbumin (OVA)/CFA model allergen induced response, DCs are critical mediators of initial vascular endothelial cell proliferation, which is followed by a T and B cell-dependent expansion phase [157]. Other studies using OVA and pre-stimulated DCs have observed that in both cases expansion can be triggered by TC trapping alone [158]. However, in virally induced LN expansion using lymphocytic choriomeningitis virus (LCMV), the LN expansion and remodelling requires an influx of B cells and B cell expression of the cytokine LTα1β2 [159]. Images of LN vascular growth while comparing LCMV and OVA response suggest they follow different signalling pathways, because of the difference in sequence of events. Braching of HEVs precedes elongation in length of HEVs in LCMV whereas elongation precedes branching in OVA induced hypertrophy [59, 159]. By day 8 in LCMV treated mice, the vasculature appears similar to day 4-7 in OVA treated mice.

2.1.6 Observed changes during paracortical enlargement

Regardless of the root causes, changes in LN mass, volume and cell counts occur in two phases [58, 59, 158, 160, 161]. In the initial few days of the response, blood flow to the LN increases 2-4 fold in rats, mice and sheep [162–167]. Inflammatory signalling results in a higher TC transmigration rate, producing a 3-5 fold increase in TC recruitment [163–168]. A phenomenon termed LN shutdown, whereby TC exit rate drops in the initial 6-18 hours, also contributes to an increase in TC number [163–168]. This is partly thought to be mediated by inflammatory signalling that results in CD69 expression and reciprocal downregulation of TC S1P$_1$r expression that results in a temporary 'logjam' at the

egress points [112–114]. LN mass also begins to increase, reaching a 2-5x increase at a similar time to peak cellularity [58, 167, 169]. During the first 48-96 hours, the structural cells fibrobastic reticular cells (FRCs) respond to DC mediated signalling with elongation, facilitating accommodation of fluid and cells whilst maintaining LN structural integrity [60]. LEC proliferation is also observed during this time [58–60].

The second phase, after 2-3 days, is characterised by proliferation of FRC and LEC to maintain LN architecture whilst undergoing further expansion [49, 60]. This is accompanied by a steady growth in blood vessel volume throughout the cortex that is proportional to LN size for 5 days, increasing BV surface area and thus TC recruitment [59, 159, 160, 165]. At day 4, 95% of the increase in TCs present is due to increased recruitment of non-dividing lymphocytes [165]. Between 2 and 5 days post-immunisation, the number of antigen-presenting DCs in the LN peaks, and with sufficient stimuli, TC activation and proliferation is well underway [58, 158, 160, 161]. The rate of TC egress, having dropped in the first phase of response, then increases 3-6 fold [166].

At the quiescent stage HEV and FRC proliferation subsides and trafficking efficiency declines [59]. Recent studies also show that toward the end of the response medullary and SCS areas expand, enabling increased TC egress rate [154]. A combination of increased egress, decreased recruitment and apoptosis allows lymphocyte levels to fall and the LN returns to its original size. Recent work has shown that following a primary response the structural FRCs,LECs and BECS, appear to remain elevated for at least a month following infection, with a denser lymph node structure and eventually returning to a slightly higher baseline level[170]. Expansion following subsequent immuno-challenge produces similar kinetics and maximal expansion as the primary response, and eventually reverts to the same post primary challenge baseline rather than a further increased baseline.

2.1.7 Previous work

Computational models allow for individual control of parameters but can maintain inclusion of complex components to provide insight into biological behaviour that would be difficult to gain using *in-vivo* or *in-vitro* techniques. Investigations of TC trafficking *in-vivo* are very complex, do not allow for isolation of individual variables and parameters, and are usually limited to animal studies. Models *in-vitro* allow for better control of variables but lack the *in-vivo* complexity. Several different approaches have previously been used to model TC behaviour in the LN, including those using frameworks based on variants of differential equations, biophysics based mathematical models, cellular potts models (CPM) and agent based models (ABM). These models describe TC behaviours at varying temporal and spatial scales using different levels of detail and often represent a different number of environments(compartments), with choices determined by the focus of the project.

Ordinary differential equations, with only one independent variable, have been used to model many different aspects of T cell behaviour, often in a specific compartment, and easily describe rates of decay, expansion, trafficking and cell signalling. For example, the change in human naïve TC numbers circulating in the body, based on availability of interleukin-7 (IL-7), from childhood to adulthood was modelled using just three ODES, describing changes in IL-7 availability and describing TC cell cycles. The model could then be used to identify the parameter range that resulted in a decline in the stable production of naïve TCs, which could impair immune response [171].

Delayed Differential equations have also been incorporated into models using ODEs to account for lags in transport across space or signalling. One example of use of ODEs is describing interaction between DCs, cytotoxic T lymphocytes and tumour cells in three different compartments[42]. In the blood compartment, DC and T cell flow was described, with a trapping term to describe retention of activated TCs when DCs were present and an ODE to represent injection of DCs into the blood. In the tumour compartment, ODEs described effector TCs deactivation rates by tumour presence, effector TC death rates and tumour cell growth as well as destruction rates by effectors present. In the spleen compartment, a delayed differential equation was used to represent the contact time

between TC and DC before proliferation could begin. From these equations, it was possible to see that hypothetical intravenous DC injections were more effective at suppressing tumour growth than low doses at the tumour site while the opposite was observed with a high dose. The behaviour of TCs has also been described using Stochastic Differential Equations (SDEs), derived from ODEs but introducing a probabilistic component to the reaction rates between components of the system. Choo and Murali-Krishna, measured parameters of TC behaviour *in-vivo* post LCMV infection, then determined that resulting memory CD8+ TCs *in-vivo* division kinetics could be described using simple SDEs [172]. These simple models showed that the proliferation of the stably maintained $CD8^+$ TC population was stochastic and homeogenous. However, a major disadvantage of relying on ODE based models is that the geometry of the system is not accounted for.

Partial Differential Equations (PDEs), solving an unknown function with respect to more than one variable, are more complex than the ODEs but can be used to introduce spatial dependencies. Models based on PDEs have been used to describe the immune response including DCs, TCs, antigen chemokines and cytokines with a focus on spatial motility's of immune agents in processes such as chemotaxis and diffusion, rather than adding in time-delays [173]. However, solving many PDEs can be very computationally demanding. PDEs are often incorporated into other models, such as ABM or ODEs, to model a spatially dependent aspect of immune response while relying on simpler equations to describe other processes. For example, when investigating how TNF-α mediated activation of the transcription factor NF-κB. The feedback between transcription factors was described with ODEs while the diffusion of TNFα molecules [174].

Other biophysic-based models have been used to investigate T-cell movement by identifying which pre-determine motions best match *in-vivo* observations. Studies implementing these models have demonstrated that chemokines can boost TC function by encouraging TCs to move with a Lévy walk, allowing them to find targets with a magnitude more efficiency than if they moved with Brownian random motion [43]. A separate study found that in non-inflammatory scenarios, $CD8^+$ TCs motility could be accurately described by allowing two subsets of TCs, with one subset moving with Brownian motion and the other

subset moving with a variable persistent random walk with noise [44]. Other results have shown that TC motion was best described as a correlated random walk with a heavy tailed distribution of step lengths [175]. A bio-physics-bases model was also developed by the de Boer group, that successfully incorporated signal integration of multiple random encounters of T cells and antigen-presenting-cells parameters, while modelling movement through a blood and a LN compartment, represented using a cylinder and a sphere respectively. The time that TCs took to transit through compartments using Brownian motion was then calculated while considering the geometric parameters. This study showed that TCs could be retained for longer in the LN if the TCs could transit stochastically through the geometries [45].

Both agent based model and cellular potts models (CPM) also use 2D or 3D lattices, with rules regarding cell state transition including a dependency on each cells environment. Unlike in ABMs, where agents are a discrete defined point on the grid, in CPMs agents may consist of shaped clusters of grid points, with the movement of the cluster governed by calculating forces and energy. Agents are thus able to alter but CPMs are also very computationally intense because they require the calculation of forces to be converted to energy. A CPM model was developed within the de Boer laboratory group, describing an area of 100μm of the LN, with the aim of accurately modelling TC transit and interaction with DCs and to investigate the effects of scanning rate and movement through the LN [46]. Cells could span several grids (grid mesh of 1μm), could elongate and contract to form a leading edge and were designated a preferred direction of movement based on previous movement. These rules resulted in TCs displaying a persistent motion in the short term, random motion in the long term and periodic pauses. As with ABMs, CPM models allow more consideration of the physical environment and the simulations were carried out with and without the presence of a reticular network. This was represented with a series of static thin, long rods with a random position and orientation that TCs could adhere to preferentially or not. Similar results were obtained with both options. Overall the modelling results implied that TC velocity fluctuations are a result of environmental alterations rather than intrinsically determined. Spatial random network models have also been used to simulate migration of TCs and DCs on FRC networks, showing that constraining cell movement on TRC

network, did not increase T-DC encounters compared to Brownian motion in free 3D space [176].

Agent based models describe cells as a discreet entity, using simple but stochastic rules to govern TC behaviour whilst maintaining the influences of the environment and neighbouring cells. Consequently, each cell is likely to behave slightly differently, and by modelling the interaction of thousands of agents, ABM can reveal emergent behaviour. However, the inherent randomness of the system also means that specific techniques to analyse and apply sensitivity analysis must be selected with care. A cellular automata model is a specific case of ABM where agent decisions must be based neighbourhoods. One such model was used to investigate the effect of chemokine-secreting FRCs in a network. The model consisted of an initial lattice with cells that swapped place with a neighbouring cell or moved into a free space, and a parallel lattice partially occupied by a FRC network. Every edge of the initial lattice was weighted according to distance to a FRC, with the weighting determining the attraction of a cell to an edge, representing relative chemokine influence. The results suggested that the FRC network minimally affected cell contact probability, but that if a FRC network was present and disrupted, this reduced cell-cell contacts [177].

Several other groups have utilised ABMs to approach the modelling of both whole LNs and segments of the LN, with TC agents storing internal variables, interacting with and impacting neighbouring cells as well as being influenced by their environment. Work by Riggs *et al* within the Kirchner group, first developed a 2D on-lattice ABM, modelling a 100x100 lattice with 5μm diameter grids of the TC paracortex. The $CD8^+$ and $CD4^+$ TCs occupied one grid and motility was described in two ways. Firstly, as random motion but with a weighted probability of motion in the same direction as the previous step, and secondly as a chemotactic motion when near a DC, by weighting the probability of direction towards the DC. The subsequent comparison of random versus chemotaxis-driven TC to dendritic cells contacts showed that the first random search strategy increased the likelihood of a rare cognate T cell finding its DC

match [178]. The model was developed further by Linderman *et al*, by incorporating $CD4^+$ TC-DC interactions, signal integration and subsequent proliferation, to characterise $CD4^+$ TC priming dynamics. The model remained a 2 dimensional using 25x200 micro-compartments, representing a diameter of 20μmicron each, and TCs motility was modelled with a persistent random walk. The simulations showed that during infection number of primed $CD4^+$ TCs was linearly related frequency of initial cognate TCs, but non-linearly related to the number of AgDCs present. Further development by Gong *et al* 2014, produced ABMs describing 3D fixed-size conical segment of the LN (0.5% of the LN volume), with grids of 5μm diameter and TCs following a random walk with persistence. Subsequent analysis showed that a 3D representation of physical space was important in reproducing TC-DC interaction dynamics [96]. Further development of the model focused on factors influencing output efficiency, in terms of TC proliferation, priming and memory cell generation. The input stimuli, both DC number and initial MHC presentation, were then varied to investigate the effects on memory cell and effector cell generation, with insights relevant to future vaccine design [97]. The model was then hybridised with an ODE-based model of the blood compartment, linking TC entry and exit from the ABM to TC concentrations in the blood [98]. In this way, TC proliferation could affect blood concentrations that could feedback on recruitment rate, known to increase during the adaptive response. LN enlargement was not included. The hybrid model was used to investigate specific LN cellular interactions such as the effect of stability of specific receptor interactions on TC activation

An ABM of the entire paracortex has been also developed by Bogle and Dunbar, firstly aiming to accurately model TC movement, before incorporating TC proliferation in response to stimuli and chemotactic influence [47, 48, 179]. The paracortex was represented as an initial 378μm (60 grid) diameter sphere within a 100x100x100 lattice grid, each grid of 6.3μm diameter. One TC occupied each grid, totalling 10^6 TCs. TC movement was on lattice as a persistent random motion, with rules to account for differences in diagonal and horizontal step length. The model varied in volume, but a constant TC occupancy of 60% of the LN volume (thereby dictating the total volume) was assumed, which potentially neglected the effects of crowding or sparseness on cell migration. The simulation results reproduced TC response and migration and also highlighted

the need to better identify mechanisms by which paracortical vascularisation is modified [48, 179].

A separate ABM was built by Brown *et al* 2018, describing $CD8^+$ TCs in a model which represented a LN with a fixed 500μm radius [180]. TC migration was modelled using rules allowed TCs to select random velocities and free path lengths drawn from Gaussian and gamma distributions. The model was used to investigate the effect of antigenic peptide separation from MHC molecules and $CD8^+$ TC activation to provide insights relevant for vaccine design. A different spherical ABM of 400μm radius was developed by Celli *et al* 2012 and described $CD4^+$ TC migration as following Brownian motion. This model was then used to investigate aspects of TC-DC interaction that influence TC response, such as the minimum numbers of DCs and cognate TCs required for CTL activation [181].

Baldazzi *et al*, within the Castiglione group, also developed a hybrid model of the paracortex, B cell follicles and medullary sinuses using an ABM to describe TC, B cell and DC interactions and a continuous model to describe chemokine diffusion [99]. The resulting system produced realistic TC response dynamics considering the spatial effects of different compartments but did not include LN swelling. The model simulations predicted that $S1P_1r$ regulation affects magnitude of response but not the temporal effects. The model also showed the possibility of both early antigen removal and regulation of TC exit to affect the balanced system dynamics, and in the example cases, impair the response. Finally, fluid dynamics modelling of the LN has not included the motion of immune cells, but modelling lymphatic flow without LN volume alteration suggested that altered oncotic and medulla pressure would dramatically alter cell, cytokine and chemokine distribution [182]. Therefore, supporting the hypothesis that macroscale alteration is likely to significantly affect the microscale activity.

2.1.8 Summary of aims

As the adaptive immune response involves careful trafficking and coordination of immune cells in the LN it was hypothesised that macro-scale reactive paracortical hyperplasia can significantly influence the resulting immune cell response at the micro-scale. To investigate this hypothesis, a computational agent-based model was developed to investigate changes in TCs and DCs interaction and subsequent stimulation, proliferation and differentiation within the paracortex under different LN swelling conditions in response to antigen. Data outputs including TC entry and egress rates, TC activation and efficiency of effector TC production allowed analysis of the underlying changes that occurred doth directly and indirectly. Manipulation of parameters describing sphingosine-1-phosphate receptors and the agDC stimuli allowed replication of previously performed experiments *in-vivo*. Simulation of new *in-silico* experiments provides a better knowledge of the key factors that can impact immune response in swollen LNs.

2.2 Methods

2.2.1 Geometry of a novel ABM model

Agent based modelling

An agent based computational model of a murine paracortex incorporating the capability for geometric change during a response to antigenic stimuli has been developed. The impact of the macroscale volume change on T cell recruitment and egress is considered through cell recruitment due to HEV angiogenesis accompanying paracortical expansion, and variation in exit rate due to a larger medullary interface. T cell $S1P_1r$ regulation is also included due to the important involvement in T cell retention. T cell $S1P_1r$ regulation also provides comparable *in-vitro* experiments including over-expression and inhibition of T cell $S1P_1r$ expression. Each time step of the model represents 20 seconds, selected to allow realistic T cell motility (see Section2.2.2). Output data is recorded for two weeks of simulated time to capture the response to antigen presenting dendritic cells (DCs) entering the paracortex and subsequent return to a homeostatic state.

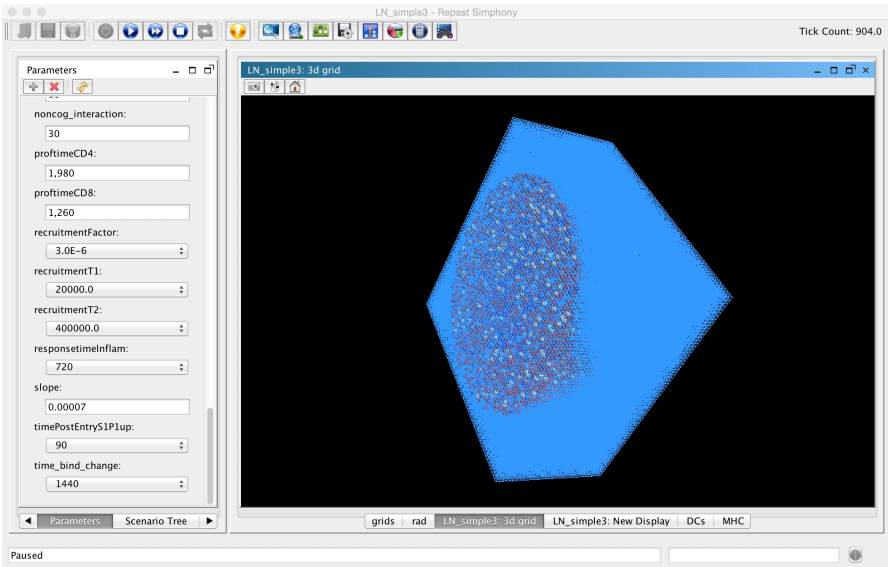

FIGURE 2.3: Visual interface of the ABM. The TCs are represented as red or blue spheres and the DCs larger white spheres. The panel to the left allows parameter adjustment.

The agent based model is considered a class based model built by instantiating thousands of T cell and DC agents that store their own individual variables and probabilistic methods. The agents move around the modelling domain that represents the LN paracortex and is defined by the 'context'class (see Figure 2.4). The domain is divided into grid compartments (cubes) with an edge length of 6μm, represented by a grid class (Figure 2.4A). Additional variables regarding each compartment are stored in a separate ValueLayer class (Figure 2.4). These micro-environment field variables can impact T cell behaviour and vary depending on the region of the paracortex being represented. For example, if cells move into a paracortex border compartment, the rules dictate that cells rebound back inward on their next step, and cells that enter an exit compartment may leave the paracortex. LN swelling and contraction is modelled by changing the type of region that each grid compartment represents so that as the LN expands, grids that were once outside the LN now represent the border or an area inside of the LN.

The behaviours and methods of the cells are described in the subsequent section, and are incorporated into the methods displayed in Figure 2.4. The sequence of events is depicted as a UML diagram in Figure 2.5, with the main processes depicted in Figure 2.6 with submethods depicted in 2.2.5. The full code is available at `https://github.com/johnsara04/paracortex_model_johnson19`.

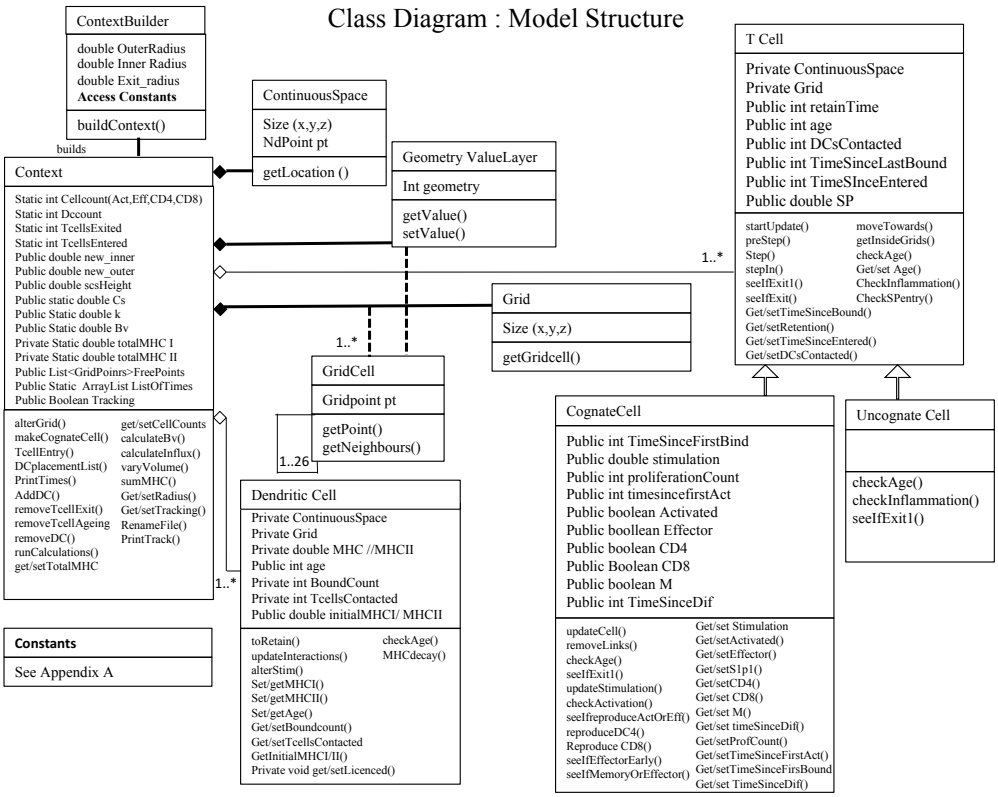

FIGURE 2.4: A class diagram displaying the underlying ABM structure. The model is constructed using instructions in the 'context builder' class. The entire modelling domain is described by the context class, and each compartment of the domain is described by the GridCell class. In a 3D simulation, each grid cell can be queried to identify the 26 neighbouring grids and how many agents they contain. The TC class is a template for the T cell object produced and is instantiated thousands of times to create T cells with the same variables but slightly different values. A subclass of cognate T cells extends the template to contains more methods and variables relating to interaction and proliferative response.

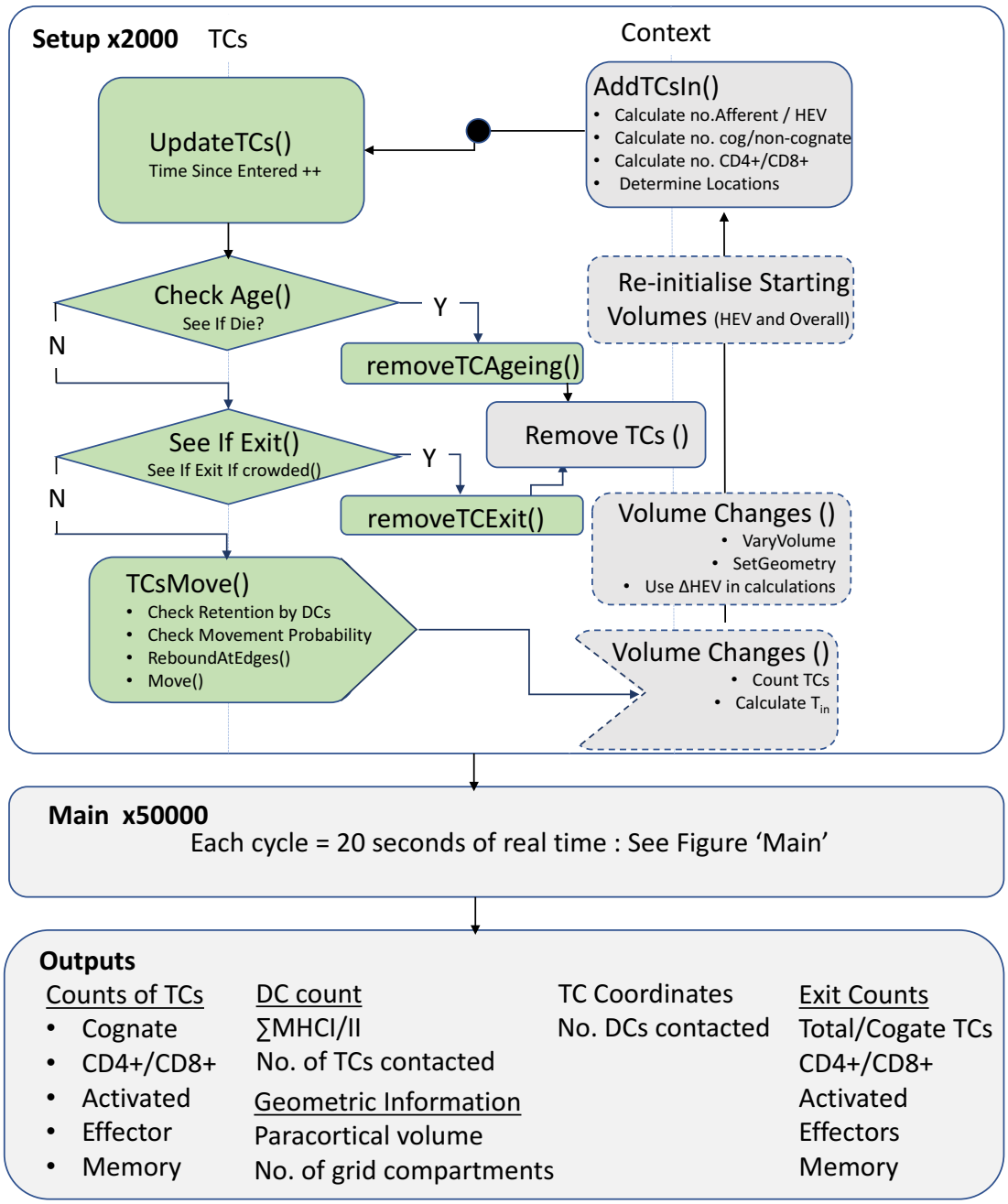

FIGURE 2.5: A flow diagram of the setup processes in the model. Individual agents, (TCs and DCs) store variables relating to their history and present state and 'projections' between agents allow information transfer. The model is equilibrated then volume change is introduced and initial volumes re-initialised. There is discernment between TCs that enter and TCs present from time 0. Each time step represents 20s of simulated time and model outputs are recorded every, 1, 15 or 180 timesteps dependent on user specification. Different methods determining volume change can be used (see 2.2.3)

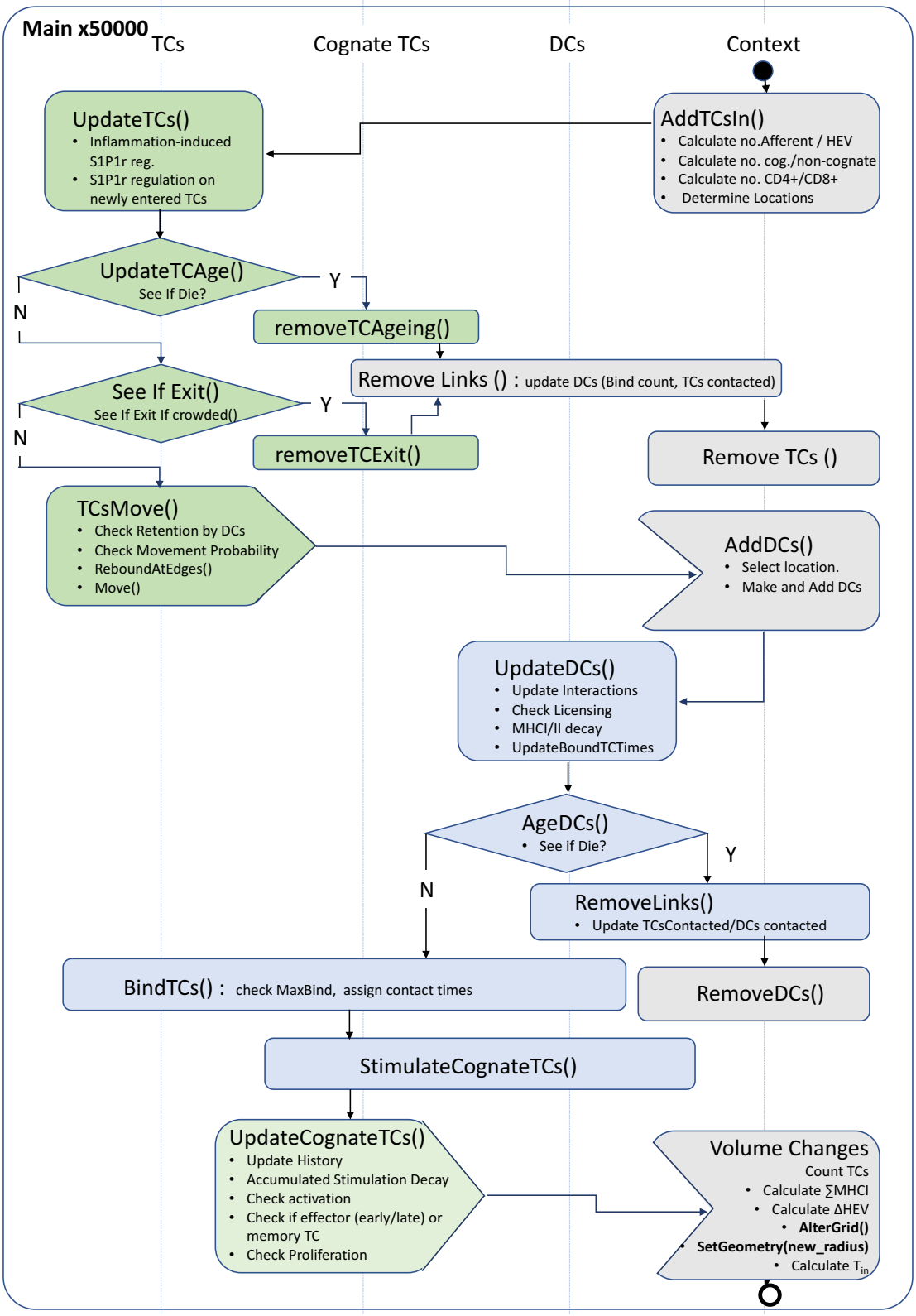

FIGURE 2.6: A flow diagram of the 'main' processes in the model. This sequence is repeated for a user specified amount of time. Sub-methods are depicted in 2.2.5.

The agent-based-model was built with RepastSimphony (http://repast.sourceforge.net), within the Eclipse platform (eclipse.org) using Java as the programming language.This platform was selected as a more advanced option to preliminary models built in Netlogo, allowing faster computation whilst providing a user-friendly graphical interface, access to many predefined functions and libraries and ample online API references. Batch functionality is also provided which exportation of the model with desired parameter combinations for use with High Performance Computing (HPC), which was available through Imperial College Research Computing Service (Figure 2.7). The resulting output files were analysed using Matlab. A more advanced version of Repast (RepastHPC) is also available, which may be useful for future work, which is designed to improve computational efficiency but requires code to be written in C++ and does not include visualisation.

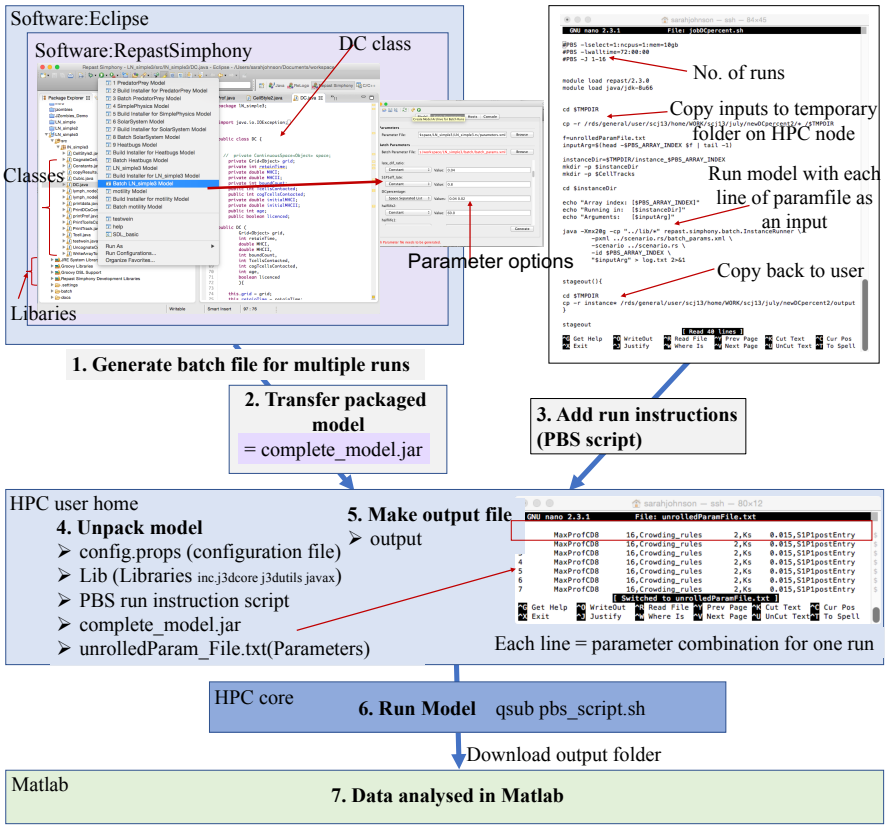

FIGURE 2.7: The process of generating the model for batch simulations. The simulation was carried out using a HPC system, with RepastSimphony and Java-development-kit installed. The key inputs were a jar-file containing the model classes, required libraries and parameters, a configuration file and a PBS jobscript file which contained run commands and the location to return the output file to. Subsequent data analysis was performed in Matlab.

Geometry

The paracortex geometry was derived from confocal images showing a rounded paracortex, with a diameter of 400-700μm. This corresponded to a popliteal LN of 600-800μm diameter and volume 0.113-0.268 mm^3[140, 183]. The LN paracortex was modelled as a hemi-sphere of initial radius R_0= 400μm with periodic boundary conditions applied to the hemisphere face (Fig. 2.1B).

The external surface of the paracortex was divided into two regions. The top half of the external surface represented the interface with the sub-capsular sinus (SCS) where afferent lymph and immune cells enter by draining through the SCS. The bottom half of the external paracortex surface represented the interface with the medulla, where lymph and immune cells could pass through to exit via efferent lymphatics. The geometric center of the hemisphere was fixed as the origin of the modelling domain, and remained so during LN swelling.

To represent 90% of TC entry into the LN from HEVs, grids within 50% of the total hemisphere radius in the center of the LN were designated as 'entry' grids. This was in accordance with images depicting the location of HEVs in the centre of the paracortex [36]. When TCs entered the paracortex at rate T_{in}, they appeared initially in any one of these entry grids. The volume of this central area was also used to represent initial blood vessel volume (V_B), (approximately 12.5% of the LN volume), in agreement with image-based estimates, and was assumed to increase proportionally with the LN radius [159, 182]. Alteration of V_B was incorporated into the calculation of T_{in}, along with changes triggered by stimuli incorporated into a recruitment factor I_F (see Eq.2.3). The remaining 10% of TCs recruited during each time step, were assumed to enter in the afferent lymph, and thus appeared at grid compartments adjacent to the SCS interface [184, 185]. T cell egress via the medullary or cortical sinuses was modelled by designating grid compartments in the lower outer hemisphere as 'exit areas'. This meant that if TCs entered grids with this property there was a probability that they would leave the paracortex. Probability of egress was assumed to depend on location and S1P$_1r$ expression (see 2.2.2)

2.2.2 Model development and governing equations

Agents

The model describes two agent types using a TC and a DC class. TCs were modelled as spheres of radius 3.2μm. A subclass of cognate TCs contain all the variables and methods of the TC class with additional cognate-specific variables and methods (Figure 2.4). Estimations of all following parameters were based on murine *in-vivo* observations with parameter ranges and sources listed in Table 2.4 and key assumptions in Table 2.1. 70% of cognate TCs were designated as Helper TCs (CD4$^+$) and 30% cytotoxic TCs (CD8$^+$) [186, 187]. Non-cognate TCs did not hold CD4/8$^+$ variables as their behaviour rules remained constant regardless of CD4/8$^+$ expression. By limiting the number of variables and methods in the non-cognate TC classes, computational demand was reduced.

The migration of TCs has previously been described using varied modelling methods, such as Brownian motion, random-walk with persistence, step and pause, 'run and tumble' and Lévy walks amongst others (see 2.1.7). This is partly due to the mixed *in-vivo* reports, with limitations contributing to the variation, such as time windows, artefacts and biasing during imaging, imprecise Z calibration and bias of slower cells remaining in view for longer periods. In this model, it was assumed that TCs move with a random walk, but may also take pauses. TC agents could move from grid to grid each 20 second time step, allowing a maximum velocity of 18μ/min. The possibility of pauses, and thus variation in velocity was applied by using the parameter β to determine the probability of TC migration each time-step. Under non-antigenic conditions, the model aimed to replicate average TC velocity of 10-12 μ/min and range of 0-18 μ/min comparable to *in-vivo* observations [36, 188–191].

Migrating TCs moved to a random available neighbouring grid compartment whose availability to accept a new TC was governed by crowding parameter γ=2. Allowing a maximum of 2 TCs per grid reflected the flexing of TCs around each other and that the volume of the cuboid compartment was not entirely occupied by a single spherical TC. These migratory rules produced TC random walk behaviour similar *in-vivo* observations (see 2.3.2) [36, 121, 188–193].

DCs provided the antigenic signal, based on total migrating DC counts post LPS immunisation in mice [58]. DCs were assumed to enter at a constant rate for 2.5 days at any non-exit grid in the paracortex. All DCs carried an initial $MHCII$ and $MHCI$ value, sampled from a Gaussian distribution with the same mean and standard deviation and MHCI and MHCII on all DCs were assumed to decay at the same estimated rate of γ_{MHCI} and γ_{MHCII} respectively [194–197]. DCs were modelled as spheres of 6μm diameter that remain stationary in the current model under the assumption that their movement once within the paracortex is small (2-3μmin) compared to TCs [192]. The DCs were permitted to interact with TCs within a two grid radius, representing the increased sphere of influence due to long probing dendrites that radiate on average 19μm [192, 198, 199]. It was assumed that there was a maximal number of TCs that a DC can interact with at one time, thus interactions between a TC and DC occured only if the Maximum-TCs-Bound parameter (Max_{NT}) was not exceeded, and up to Max_{step} new TCs were bound per time-step. These parameters were selected based on the low-end of *in-vivo* observations and sensitivity later assessed. The cognate frequency parameter (F_{cog}) defined the proportion of TCs recruited each time step that expressed the complementary TCR to the antigen presented, and was assumed to remain constant throughout the simulation time [37–40].

Based on the in-vivo observations that post-antigenic stimulation TCs undergo short then long interactions, it was assumed that a cognate TCs history of interactions with DCs determined the length of subsequent interactions. The duration of cognate and non-cognate TC-DC interactions were drawn from estimated probability density functions as shown in Figure 2.9 [120–124]. Variable parameters define the lower limit (for uniform distributions) or mean (for Gaussian distributions) of the interaction time, dependent on variation in reported durations. Non-cognate TCs interacted for time (T_{NC}), as shown in Figure 2.9A [123, 124]. Following a cognate TC's first DC encounter, TCs could interact with a DC for a short duration (T_{short}) before undergoing longer interactions (T_{long}) of 70-90 minutes (Figure 2.9C) after an estimated 8 hours (T_{change}) [119–122]. Activated and Effector TCs of subsequent proliferations were assumed to return to short interactions with designated times drawn from (T_{short}, Figure 2.9B).

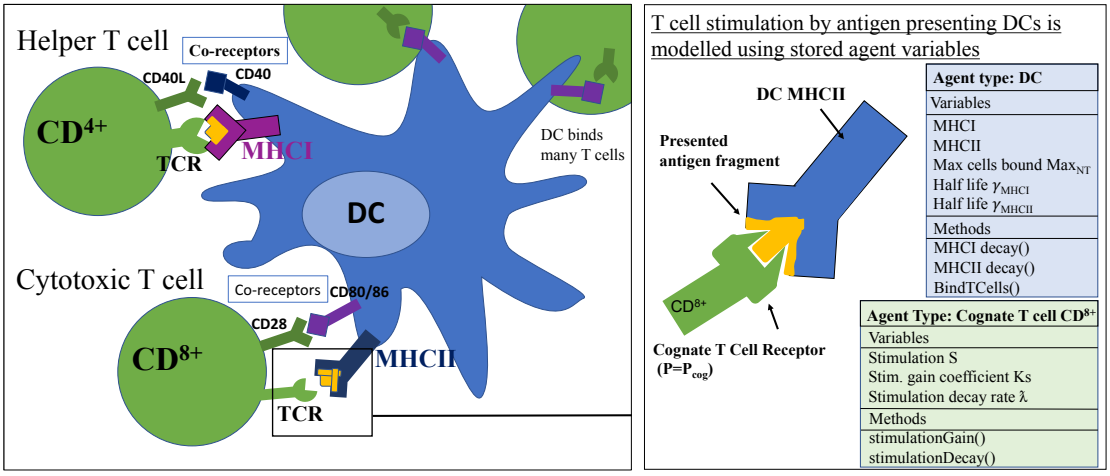

FIGURE 2.8: Modelling the stimulation of TCs by DCs. A: Mature DCs present fragments of antigen within MHCI and MHCII molecules on their cell surface. Physiologically, over time MHC molecules are internalised so antigenic stimulation strength decreases. DCs interact with TCs through a TC receptor (TCR) and co-receptors and can bind many TCs at once. DCs stimulate TCs with a complementary TCR to antigen presented. B.Modelling DCs stimulation of Tcs. TCs may express a complementary TC receptor to antigen fragment presented (probability = P_{cog}). Strength of stimuli is assumed to affects stimulation. The model designates MHCI and MHCII variables to DCs that decay with time at half rate (γ_{MHCI} and γ_{MHCII}), and designates a stimulation S variable to TCs. The value of S is assumed to increases during interaction with DCs at a rate dependent on the MHC variable and rate constant K_s. At all times, accumulated S is assumed to decay at rate λ. See equation 2.1

Interactions

During TC-DC interaction, the TCs were assumed to remain stationary as they are physically attached to the stationary DCs. During cognate $CD8^+$ or $CD4^+$ TCs interaction with a DC it was assumed that they were stimulated and gained 'stimulation' (S) at a rate proportional to the MHCI or MHCII variable presented by the DC , at a rate constant of K_s. Accumulated stimulation was also assumed to decay at a constant rate such that the total change in TC stimulation was given according to the first order rate equation:

$$\frac{dS}{dt} = K_s\, MHCII(t) - \gamma_S\, S(t) \tag{2.1}$$

Where K_s is a rate constant, γ_s is a decay factor and the accumulated simulation will decay to a minimal value of 1. This allowed differentiation between cognate TCs that gained and lost simulation (S=1) and those that never gained simulation (S=0). MHCI (for $CD8^+$ TCs) or MHCII (for $CD4^+$ TCs) was the signal presented by the DC with estimated half-lives $MHCIt_{1/2}$ and $MHCIIt_{1/2}$.

Following an interaction with a DC, the probability of Helper TC (CD_{4^+}) activation P_{a4^+}, at any time point was assumed to depend on the accumulated stimulation S held by each cognate TC. This means that the more stimulation a TC gained, whether through frequent interactions or long interactions, the greater the chance of activation . As agDCs are highly efficient antigen-presenting cells it was assumed that co-stimulatory requirements were met. This signal integration method allowed integration of temporal aspects such as duration of signal and duration of interaction, signal magnitude and frequency of signal. The description of TC activation via signal integration and the subsequent progressive patterns of proliferation and differentiation is supported by *in-vivo* observations and modelling descriptions [122, 125–127]. The probability of activation was then determined using the sigmoidal function with accumulated simulations as an input, based on the observation that the TC response compared to antigen dose presented by DC is sigmoidal in nature [200]. The function was given by:

$$P_{a4^+} = \frac{1}{1 + e^{\frac{-S-\mu_{4+}}{l_{4+}}}} \tag{2.2}$$

Where parameter Actμ_{4+} determined the value of S required for 50% probability of activation and Actl_{4+} determined the steepness of the sigmoid inflection. Parameters were estimated such that TC activation became apparent around 8-15 hours after DC entrance [120–122]. The probability of activation for Cytotoxic TCs (P_{a8^+}) was determined with a sigmoid curve using a lower inflection point, (Actμ_{8+}), which allowed for the assumption that Helper CD4$^+$ TC initially activate at lower simulation thresholds than CD8$^+$ TCs. DCs were assumed to be 'licensed' following interaction with a cognate activated CD4$^+$ TC. During interactions with a licensed DC, CD8$^+$ TCs activated with the same probability as CD4$^+$ TCs, reflecting facilitated CD8$^+$ activation as a result of the presence of activated CD4$^+$-induced production of cytokines [201].

Following activation, proliferation was possible every 11 (CD4$^+$) or 9 (CD8$^+$) $\pm$1hr with the time between proliferations assumed to remain relatively constant [39, 202–204] . Based on *in-vivo* reports, and estimations in previous models, differentiation into effector or memory cells was possible only after 4 or more proliferations [191, 205]. As not all activated TCs differentiate, a second set of functions determined probability of differentiation, P_d of Helper and Cytotoxic TCs. The differentiation probability was also assumed to be influenced by accumulated simulation (S), and used as an input to sigmoidal probability curves with midpoint Difμ_{4+} and Difμ_{8+} respectively. The observed Helper TCs greater dependence on continued stimulation for successful differentiation was implemented by setting a higher minimum threshold of accumulated stimulation for proliferation than cytotoxic TCs [130, 132–135]. As the response continued, the fraction of effector TCs that differentiated into memory TCs increased[206]. Therefore it was assumed that effectors TCs that underwent < 8 proliferations were less likely to differentiate into memory cells than those that underwent more than 8 differentiations. This was implemented by assigning differentiation ratios of dif_{early} and dif_{late} to the two different subsets.

T cell exit and Sphingosine-1-Phosphate regulation

As TC egress was assumed to depend on S1P1r expression and location, all TC agents stored a variable (SP) that represented a S1P$_1$ receptor value that directly influenced probability of TC exit. If TCs moved into exit compartments (Figure 2.1C) they could exit the paracortex with probability $P = P_e * SP$. The fixed value

for P_e was determined by varying P_e and selecting a value that resulted in exit rate equal to recruitment rate. The default value of SP is 1 but is varied between 0.01 (inhibition of exit) and 1.4 (facilitated egress) in three ways (Figure 2.2). When a TC first enters the paracortex, $S1p_1r$ is down-regulated for 45 min-2 hours, reducing likelihood of TC exit during this time [106]. Modelling values of SP were set at SP_{in}= 0.1-0.2 for 1 hour, as *in-vivo* experiments completely inhibiting $S1P_1r$ expression still resulted in 10% of normal TC exit [109].

In the initial 24 hours of a response to antigen *in-vivo*, TC egress decreases, with a 3-30 fold temporary drop in lymphocyte in the efferent lymph [114]. Initially attributed to $S1P_1r$ down-regulation via IFNβ, this non-specific TC retention has also been linked chemokine receptor mediated retention of both naive and activated TCs. In both cases, TC retention is essentially a response to inflammatory signals in the LN. Therefore it was assumed that when >100 agDCs entered,(based on estimates of 85 agDCs required to elicit a response), the SP value of all TCs that had been in the LN for several hours, (based on reported time required for $S1P_1r$ internalisation (T_{inflam}), was down-regulated to the value of SP_{if}[181].

Finally, during activation and subsequent proliferation and differentiation into effector TCs, based on literature reports, TCs down-regulate S1P1r when activated and gradually re-express S1P1r as they differentiate. Although literature reports suggest that re-expression may occur with every proliferation, we assume that relative TCs expression can be divided into three groups based on proliferative status, to reduce computational expense. TCs were assigned SP values (SP_{act}, SP_{early},SP_{late}) where 'early' denotes TCs that have undergone 6 or less than 6 proliferations and 'late' denotes TCs that have undergone more than 6 proliferations. The SP values were based on experimental data regarding $S1P_1r$ receptor expression change [105, 109, 207]. Reports showed that migration of activated TCs was reduced 100 fold at day 1, and 30 fold at day 3, whilst receptor studies have also shown a relative reduction from 1 to 0.46 in $S1P_1r$ expression following the first proliferation, 1 to 0.8 at proliferation 3, and a return to naive TC $S1P_1r$ expression levels by proliferation 4 [105, 109]. Further studies support initial TC retention and return to normal egress probability by day 3 following multiple proliferations [207].

T cell recruitment

To model TC recruitment it was assumed that under non-inflammatory conditions TC entry and exit rate were equal, and that the density of TCs in the paracortex was maintained. The average lymphocyte recruitment for a popliteal LN of 1.15g is reported as 4x10^7 lymphocytes/hour [166]. Our model represents a LN of 0.113-0.268 mm^3. Collaborative measurements of murine popliteal LN mass versus volume imply that this corresponds to a model LN mass 0.18-0.44mg. Therefore, the expected lymphocyte recruitment rate was calculated as 6500-15000 lymphocytes/hour. As up to 40% of lymphocytes in the LN are B cells, and our model represents half a paracortex, the expected TC recruitment rate was 1950-9000 TCs/hour under non-antigenic conditions [208, 209]. The experimentally observed transit time (T_{res}) for naive TCs is 6-24 hours [210, 211].

Considering the above assumptions, and assuming that TCs transit through the LN with mean time T_{res}, TC recruitment under non-antigenic stimulation, was modelled such that TC influx, (T_{in}) was given by T_{res} divided by the initial number of TCs present N_T (see Eq.2.3). In the model it is assumed that blood vessel area increases proportionally to the overall LN volume and the rate of change in blood vessel volume contributes directly to TC recruitment rate, calculated as $\bar{V_B}$. Additionally, it is assumed that recruitment changes due to inflammation-induced signalling cascades at the HEVS can be represented using a Inflammatory factor I_f that is triggered only above a certain level of antigenic presence. Thus , overall T cell influx (T_in) at time t is calculated as :

$$T_{in}(t) = \frac{N_T}{T_{Res}} \quad I_F(t)\bar{V_B}(t) \tag{2.3}$$

Where T_{res} is the the TC residence time and N_T is the initial number of TCs present and $\bar{V_B}$ is the volume of TC entry area at each time-step divided by initial V_B at time 0. This is based on reports that the overall change in TC recruitment rate as the LN swells between day 2 and day 5 is proportional to the accompanying growth in blood vessels[59, 165]. Inflammatory factor (I_f) describes an acute increase in T_{in} following detection of inflammatory stimuli

where I_F at time t is calculated as:

$$I_f(t) = \begin{cases} 1 & \sum_{n=1}^{N_{DC}} MHC(t) \leq T1 \\ 1 + R_F \sum_{n=1}^{N_{DC}} MHC(t) & T1 \leq \sum_{n=1}^{N_{DC}} MHC(t) \leq T2 \\ 1 + R_F T2 & \sum_{n=1}^{N_{DC}} MHC(t) \geq T2 \end{cases} \tag{2.4}$$

It is assumed that the measure of inflammatory stimuli that triggers changes in TC recruitment can be represented by the sum of MHC presented across all DCs in the paracortex. Threshold 1 (T1) is the level of inflammatory stimuli required for I_f to increase recruitment. The value of I_f and thus TC recruitment rate continues to increase up to a second threshold (T2), determining a maximum contribution of I_f to recruitment. Thresholds were estimated based on observations of recruitment fold change and the time lag between stimuli application and recruitment response.

Stromal cells

Explicit modelling of the stromal cells of the LN was not included in the model, despite stromal cell contribute to TC migration via secretion of chemokines and formation of a structural framework, as well as contribution to peripheral tolerance. Firstly, the model represents the paracortex only, thus guidance to the paracortex, is not the focus of the model. It would also be possible to incorporate chemotactic influence in future models without explicitly modelling the stromal cells by designation grid locations as sources and/or receiving data from coupled fluid-dynamic models better suited to describe diffusion. Several simulations have suggested that TC mobility remains similar with and without the inclusion of FRCs, but that disrupted or non-continuous frameworks can inhibit TC migration [46, 177]. Therefore inclusion of erroneous stromal cell structure may impact TCs more than exclusion. Regardless of whether the FRCs cause the random walk or not, the random walk pattern remains observed *in-vivo*. Stromal cell contribution to swelling is discussed in 2.2.3 while

contribution to tolerance requires development of the model in several other signalling processes for stromal cell inclusion to become significant.

Baseline motility and response simulations

Prior to investigating the effect of significant changes in paracortex volume, simulations were performed to ensure that the model accurately described TC motility and response. The first set of simulations focused on TC behaviour under non-antigenic conditions to ensure TCs moved around the paracortex after entering instead of immediately exiting, with a random walk at physiological velocities. The model could output TC coordinate points of newly entered TCs every 20 seconds which allowed calculation of comparable TC motility parameters such as velocity and displacement. Plotting TC displacement versus the square root of time and finding a linear relationship can be concurrent with random walk behaviour as discussed in Beltman 2007 [46]. This relationship can also be directly compared to directly to measures based on in-vivo murine experiments [121, 124, 192].The motility co-efficient, C_M, is a comparative measurement of displacement used in studies observing the T cell movement *in-vivo* and in previously modelling work, calculated as:

$$C_M = \frac{\sum_{i=1}^{n} \frac{x^2}{6} t}{n} \tag{2.5}$$

where n= number of T cells tracked, x = displacement and t = time.

The seconds set of baseline simulations focused on the timing of the response to stimuli. It was important that TCs became active after 8 to 15 hours following DC-antigen entry to ensure that the signal integration parameters and TC thresholds were suitably selected. Similarly the timing of the appearance of effector and memory cells and Helper CD4+ and CD8$^+$ TCs within these subsets, was important to ensure that the correct sequence of events occurred.

2.2.3 Incorporating para-cortical enlargement

Estimating and applying volume change

The driving mechanisms of LN expansion are yet to be fully elucidated but observations in mice show a two phase change in both volume, TCs in the LN, and stromal cell behaviour (Section 2.1.6). Sets of published murine experimental data regarding LN volume, LN mass, TC, stromal and migrating cell counts were compared along with unpublished data regarding murine LN volume and accompanying TC counts (Jafarnahad *et al.*). Consideration of stromal cell behaviour was not explicitly modelled during LN swelling, but features such as initial stretch followed by proliferation allowing a two phase expansion. On the basis of these observations, the relationship between TCs and LN volume was then estimated as best described by a sigmoidal curve due to the two-phase response, the maintenance of a baseline volume and a tailing-off of maximal volumes.

Paracortex volume change was applied by altering the radius every 3 minutes. In mice, snapshot images of the paracortex show that the structural network tends to stretch initially, rather than grow [58]. It is also known that after an initial increase in TC recruitment, the number of HEVs expands at a similar rate to the total cellular growth of the LN [165]. Therefore, in initial simulations, as the paracortex radius alters, the volume of areas within the paracortex were also assumed to alter and thus were defined as a constant percent of the outer radius (Section 2.2.1). The stretch and subsequent proliferation of stromal cells is known to contribute to maintaining the structure of the compartments of the LN, therefore it was assumed that stromal cells changes help to minimize the impact of the swelling on migration through the network rather than applying constrictions beyond that applied by the initial reticular network.

Modulating T cell S1P1r expression and paracortical swelling

The parameters that determined the sigmoid curve shape were the maximal fold change paracortex volume, V_{Max}, the number of TCs required to reach 50% of maximal expansion, T_{mid}, and the slope of the curve l. After a global sensitivity analysis was applied, simulations were run varying the influential parameters T_{mid} and V_{Max}. V_{Max} was varied between 1 (fixed volume) and 2.8 and T_{mid} was

varied between 8e4 and 13e4. Based on the results of these simulations, the model was altered so that the areas altered proportionally to paracortical volume rather than the radius. To investigate what would happen if TC crowding could impact egress rate, a further set of simulations was performed, incorporating a new rule that increased probability of exit if two TCs occupied the same exit area grid. The effect of modulating $S1P_1r$ on activated TCs and newly differentiated TCs was then combined with different expansion scenarios.

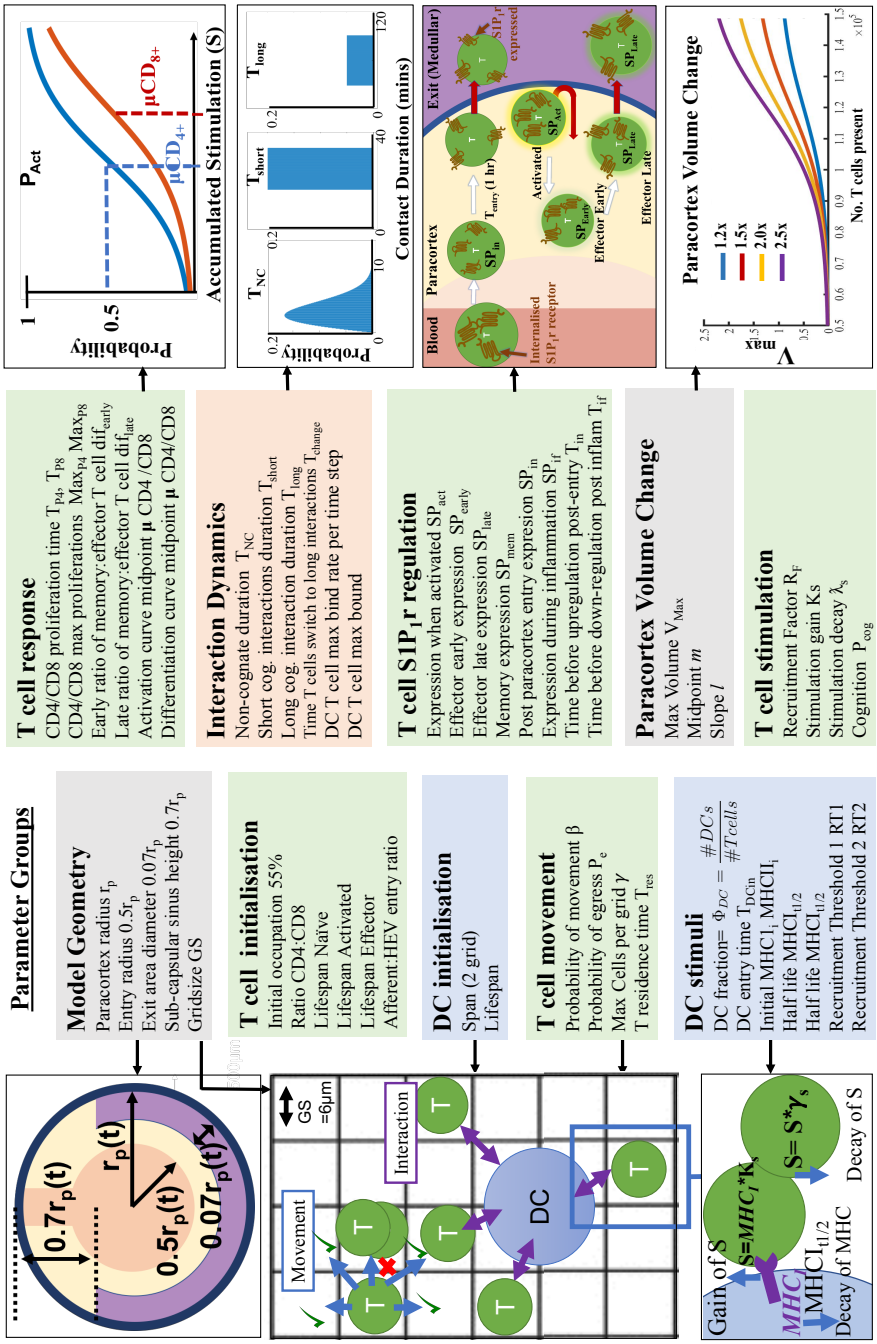

FIGURE 2.9: Grouping the parameters of the model. Model geometry, T cell initialisation, DC initialisation and T cell movement are not varied in the sensitivity analysis. T cell movement parameters were varied in preliminary trials before being fixed.

Summary of Key Assumptions

TABLE 2.1: Table of assumptions. The key assumptions underlying the model of TC trafficking and response to agDCs in the paracortex

Assumption	Reasoning	Ref.
HEV entry area is defined as a central sphere with radius 50% of the paracortex radius	Based on images of HEV location, and HEV volume estimations.	[36, 159, 182]
At homeostasis, TC entry and exit rate are equal	Naïve TC lifespan is long (365days) compared to typical LN transit time (12-24hr), thus few naïve TC die in the model. To maintain TC population, rates must be equal.	[210–212]
Inflammation induced signalling pathways that contribute to rapid increase in TC recruitment rate can be represented by one factor	Antigen detection triggers multiple un-modelled signalling cascades that increase blood flow & TC transmigration rate, but overall result in increased TC entry (the outcome applied to the model).	[163–168]
The sum of MHCI or MHCII in the LN can reflect inflammatory status	Free antigen is not included and MHC expression is considered a proxy for signal strength, therefore summating MHC allows consideration of many weak signals or few strong signals	
TC probability of egress depends on location and $S1P_1r$ expression	Evidence shows TC re-expression of $S1P_1r$ allows egress and TCs exit at the medullary interface or via cortical sinuses.	[107–111]
History of cognate TC interactions determines subsequent interact length	Altered TC behaviour is reported with time since antigen enter the paracortex. Change in TC behaviour was linked here to DC interaction as other signals eg. cytokine secretion, were omitted.	[118–124]
Signal is accumulated via integration of antigenic signal presented by DCs	In-vivo TC behaviour post-DC interaction has been explained by signal integration models.	[122, 125–127]
TC activation & differentiation are influenced by accumulated stimulation and progression can be described with probabilistic sigmoidal curves of accumulated simulation.	Based on *in-vivo* observations and modelling descriptions supporting activation post- signal integration and progressive proliferation & differentiation. Observed sigmoidal relationship between dose to TC response.	[125–127, 213]
LN resident DCs do not contribute to the modelled response	The antigenic stimulus was based on observations of migratory DCs post application of pre-pulsed DCs/vaccinations therefore free antigen scavenged by LN resident DCs is minimal	
Co-stimulatory requirements are met with each TC-DC interaction	DCs are highly efficient antigen-presenting cells, therefore co-stimulation was not considered a limiting factor	

TABLE 2.2: Assumption Table Part 2. A summary of the key assumptions underlying the model of TC trafficking and response to agDCs in the paracortex

Assumption	Reasoning	Ref.
TC migration can be described with a random walk with pauses, without stromal influence, and preferential movement to empty spaces	Based on in-vivo,observations of random-walk behaviour regardless of stromal cell contribution.	[188, 191–193]
TCs can migrate into a compartment of equal diameter that contains another TC if surrounding neighbouring grids are occupied.	T cells can deform into non-spherical shapes and can fill the unoccupied corners of the cuboid compartment	
DCs are assumed to arrive at a constant rate for the duration of defined entry time	Total number of entering DCs is based on observations of DCs in the LN post--vaccination at daily intervals combined with estimated lifespan.	[58]
DCs present MHCI/II values as proxy values for simulation strength, which is assumed to decay at a constant rate	The initial MHC value is a non-physiological parameter, but half-life is estimated from reported MHCI and MHCII expression.	[194–197]
Blood vessel volume alter proportionally with LN radius and the change contributes proportionally to TC recruitment rate	Optimal tomography images show blood vessel network expanding with LN volume. HEV surface area and recruit--ment rate increased similarly at day 3-5.	[159, 165]
LN swelling can be described without explicit stromal cell description	Stromal cells stretch and proliferate to maintain FRC network structure rather than to apply further constrictions. Stromal cell stretch and growth is considered in the sigmoidal description of LN volume increase	[58–60]
Activated TCs express 3 varying levels of $S1P_1r$	With subsequent proliferations (1-7) activated TC $S1P_1r$ is gradually re-expressed but 3 groups were chosen for computational efficiency	[109, 207]
The paracortex expansion can be described as a function of TCs present.	Although many factors contribute to LN swelling, TC number reflects the result of several components, such as initial recruitment & proliferation. Use of a sigmoidal function means sufficient response must be induced prior to significant LN swelling and accompanying alterations that further impact TC number	[58, 158, 160] [59, 161]
LN shutdown is caused by S1P1r medi--ated retention when antigenic-stimuli presence meets a certain threshold	A small (%10) $S1P_1r$ down-regulation was incorporated based on literature reports regarding LN shutdown with scope for future refinement.	[163–168]

2.2.4 Global sensitivity analysis

Considering parameter uncertainty

The model contains many parameters that may interfere with each other (Figure 2.9), therefore it was important to ensure model robustness and output reliability despite uncertain parameters. Epistemic uncertainty regarding parameter inputs exists in the model due to incomplete knowledge and varying or conflicting measurements from different experimental sources. An additional aleatory uncertainty, where the same input doesn't produce the same output, is due to the probabilistic nature of ABMs and is also a characteristic of biological systems. As such, a combination of uncertainty and sensitivity analysis was used to help identify critical parameters requiring refining and those that may be uncertain but have a negligible effect on the system.

A parameter sensitivity analysis was performed using the method detailed by Marino *et al* 2008 [214]. A complete list of all model parameters and their values are listed in Table 2.4. This involved using Latin Hypercube Sampling to sample over the parameter range in a manner that was guaranteed to captured the extreme values (see 2.10 below). Simulations were then carried out using the resulting parameter combinations. Each experiment (of 100 parameter combinations) was replicated three times and the mean resulting values use in further analysis to reduce aleatory uncertainty from inherent stochastic variations. It was assumed that the parameters had monotonic relationships with the outputs of interest at any one time-point but the influence of the parameter can alter at different time points. A partial rank correlation coefficient (PRCC) was then calculated between parameter of interest and outputs of interest at multiple time points. The purpose of this analysis was to identify the influence of the parameter on the output, whilst accounting for the linear effects of the other (ranked) parameters, and has been used to analyse several LN ABMs [96–98].

Alternative analyses could have been used, that are better suited to analyse the effects of parameters with non-linear and non-monotonic relationships, eg, prey and predator cycles. The extended Fourier Amplitude Sensitivity Test (eFast) technique is a reliable variance-based technique, using the decomposition of

variance to produce both a total sensitivity and a sensitivity indices for each parameter [214, 215]. The sensitivity indices indicates the degree of interaction that a parameter has with other parameters, providing a means to identify when a large total sensitivity may be representative of a parameters individual influence that is heavily influenced by other parameters. Analysis using a Random forest model has also previously been used to carry out sensitivity analysis of ABMs, producing importance factors for each parameter, with no prior assumption of monotonic relationships [180].

Latin hypercube sampling

To analyse parameter space, Monte Carlo analysis methods can be used where simulations using the entire range of possible parameter values are carried out. However, this can be computationally expensive. Reducing the number of sampling points from each variable may help but due to randomness, the edges of distributions can easily be under-sampled. Therefore a sampling technique called Latin hypercube sampling (LHS) (Mckay*et al* 1979) was used to spread sample points more evenly by partitioning each input distribution into N intervals of equal probability and selecting one sample from each interval (see Fig.2.10). This allowed the number of required simulations to be reduced whilst ensuring that the extremes of parameter space were sampled.

Where possible, input parameter distribution, minimum, mean and maximum values were sourced from murine experimental data. 'Non-biological' parameters were assumed to have a uniform distribution, unless there was reason to suggest otherwise. Table 2.4 shows the parameter distribution and range. Parameters involved with the initial setup and Tc motility were omitted from the parameter sensitivity analysis as their effects were established and fixed to accurately describe TC movement (Table2.3). The sensitivity analysis was performed with and without permitting LN swelling. The range of parameters known to magnify the TC response, such as the number of DCs that enter, were intentionally kept within less extreme ranges. This ensured that large values combined with more extreme values of other parameters did not cause TC proliferation and number to extend into non-physiological levels which could cause the model to fail. This would produce uneven parameter space coverage.

Model outputs

A large amount of data was extracted from the model(Figure 2.5). This included the TC activation state, $S1P_1r$ expression level, contact history with antigen-presenting DCs, differentiation state and time taken to transit through the paracortex. Information regarding all activated, effector and memory TCs (and $CD4^+/CD8^+$ status) present in the paracortex, and those which exited the paracortex was also recorded. Information regarding TC motility was calculated by recording TC coordinates and overall TC numbers and rate of TC entry and egress were also stored. Outputs data was stored at 5minute or 1hour intervals of simulated time. Simulations were repeated and the mean reported. Standard error of the mean (SEM) was calculated to provide a measure of dispersion from the mean.

To perform the global sensitivity analysis, the parameters in Table 2.4 were sampled and 300 combinations selected per analysis, which was repeated 3 times. The effects of each parameter on one output was then isolated and analysed by calculating partial rank correlation (see below 2.2.4). The global analysis was performed with and without paracortical expansion, and sensitivity of each parameter assessed for each of five key outputs:

1. Activated TCs in the paracortex from day one to day eight.
2. Effector TCs in the paracortex from day three to thirteen.
3. Effector TCs that have exited the paracortex from day five to thirteen.
4. Memory TCs in the paracortex from day five to day thirteen.
5. Memory TCs that have exited the paracortex day six to thirteen.

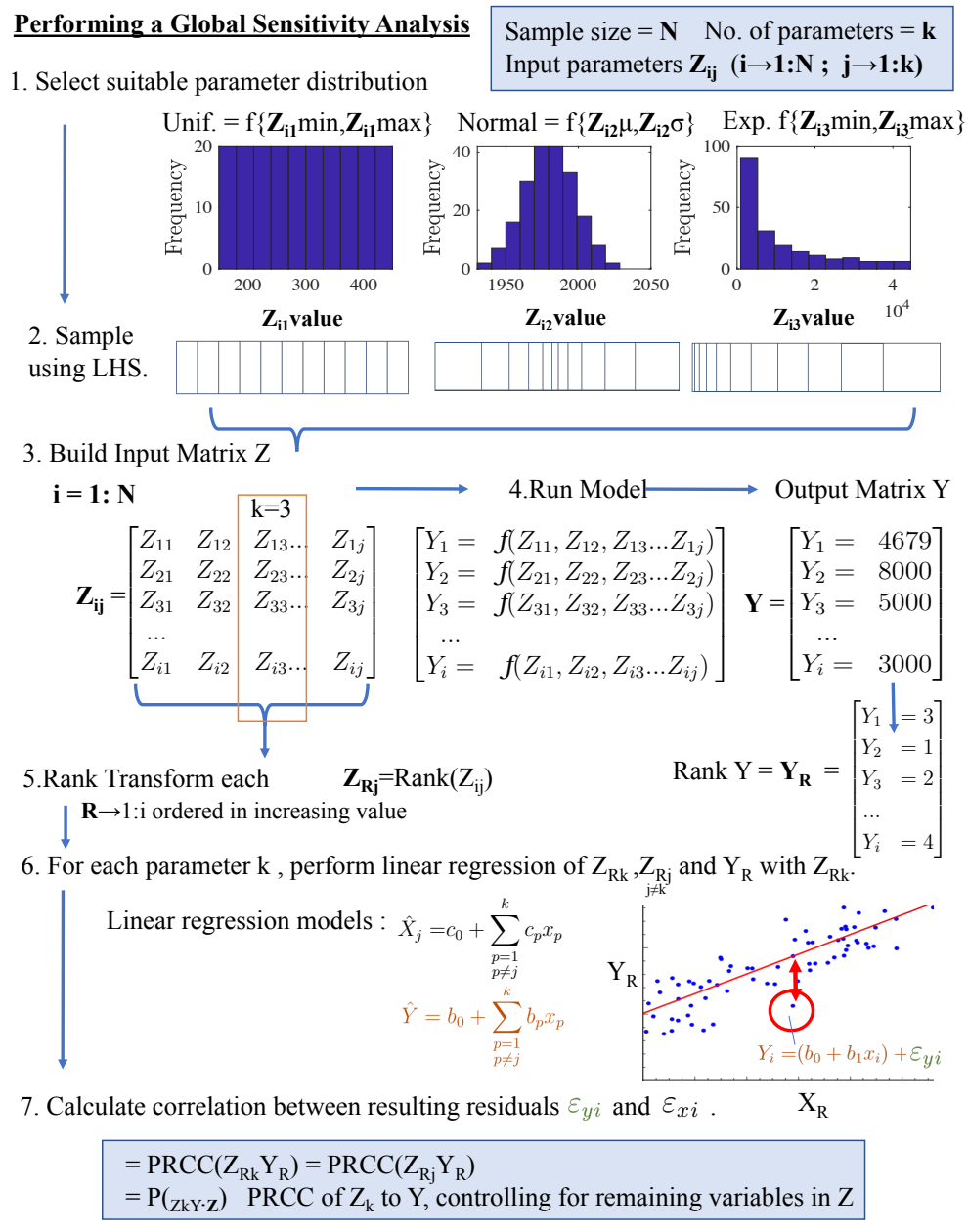

FIGURE 2.10: Applying a global sensitivity analysis. Suitable probability distributions are selected for parameters $Z_1 \ldots Z_k$. The parameter range is divided into N equal probability intervals. Each interval is randomly sampled and the sample set shuffled then used to build a (Nxk) input matrix Z. The simulation is run Ntimes, producing output Y, using parameter combination in a new row of matrix Z each time. Partial correlation is performed for each parameter, (each column of Z) using ranked input Z_R and ranked result Y_R

Analysing correlation

To assess the sensitivity of each parameter on an output correlation was assessed. The most commonly used correlation method, Pearson's correlation measures the strength of the linear relationship between a variable x_i and output y using individual variance of xi and y , (the square root of the standard deviation), and the co-variance of X_i, Y. This method is dependent on the distribution of the data around their respective means $(x_i - \overline{x})$ and $y - \overline{y}$. Pearson's correlation is calculated as :

$$\text{Pearson correlation } r_{x_j \cdot y} = \frac{Cov(x_j, y)}{\sqrt{Var(x_j)Var(y)}} = \frac{\sum_{i=1}^{N}(x_{i_j} - \overline{x})(y_i - \overline{y})}{\sqrt{\sum_{i=1}^{N}(x_{i_j} - \overline{x})^2 \sum_{i=1}^{N}(y_i - \overline{y})^2}}$$
$$j = 1, 2, ...k \tag{2.6}$$

Where x_j is the parameter of interest from 1 to k parameters (Eq.2.6 and Figure 2.11). By rank transforming the data, the correlation between X_i and Y with non-linear monotonic relationships can be quantified. Spearman's rank correlation performs the same analysis as Pearson's correlation, but with rank transformed data (Figure 2.11).

Partial correlation measures the strength between two variables while controlling for the effects of the others by removing linear affects of all but one variable. Pearson partial correlation (PCC) begins by fitting regression models to input variable (Xi,y) and (Xi,Z) where Z is the other parameters in the model. This is using a measure of how far away from the line of best fit each data point is rather then the variance of the data. The (pearsons) correlation is then calculated between the two sets of residuals that are obtained from the two regression models. Partial Rank Correlation Coefficient is the same process as partial correlation, but XR, ZR and YR are rank-transformed prior to fitting linear regression models (see Eq.2.7). The PPRC produces is the correlation between the two sets of residuals. Significance tests can be then used to assess

if a PRCC is significantly different from zero and inferences made.

$$\hat{X}_j = c_0 + \sum_{\substack{p=1 \\ p \neq j}}^{k} c_p x_p \qquad \hat{Y} = b_0 + \sum_{\substack{p=1 \\ p \neq j}}^{k} b_p x_p \tag{2.7}$$

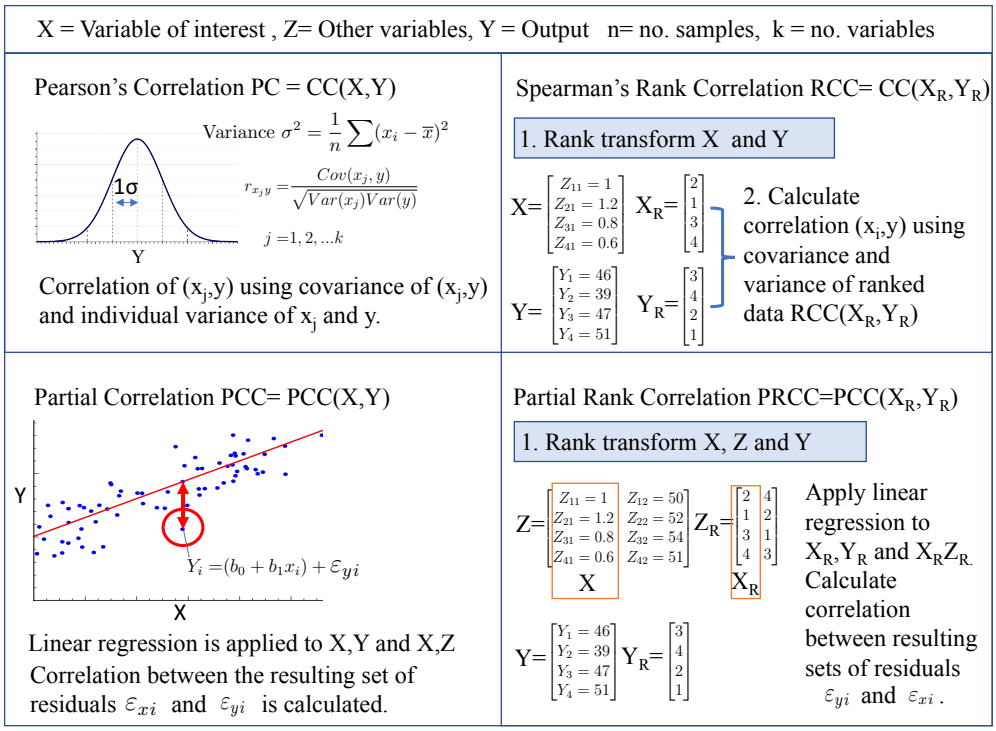

FIGURE 2.11: An explanation of the correlation methods used in the study. Pearsons correlation uses the variance of the data to identify correlation. Partial correlation uses regression to fit the data then quantifies the deviation from this fit to determine the correlation. By ranking the data first, Spearman's ranked correlation and Partial Ranked Correlation can identify monotonic relationships instead of only linear relationships.

2.2.5 Model validation

After developing a 'baseline' model of TC response to agDC it was important that the model was able to reproduce non-baseline behaviour that had been carried out *in-vivo*. Four different experiments were replicated.

1. The initial proportion of cognate TCs in the naive TC population (P_{cog} was varied *in-silico* between 1.0x10^{-5} and 1.4x10^{-4}. Firstly the results were analysed in order to see if the number of the effector cells produces was diminished relative to the value of P_{cog}, as reported in several *in-vitro* experiments [40]. Secondly whether the the number of effector TCs produced could eventually reach similar peak magnitudes was assessed. In some cases lower cognate frequencies have been shown to result in a delayed TC response that can reach similar peak number of effector TCs [216]. Thirdly, simulations were carried out replicating *in-vivo* experiments by varying P_{cog} to match the proportion of cognate TCs to different antigen in the naive TC population *in-vivo* [206, 216].

2. The stimuli was varied by altering the number of TCs that enter the paracortex as a fraction of total TCs (ϕ_{DC}). The results were compared experiments altering the dose of bacterial antigen or number of DCs injected into mice, and application of antigen-pulsed DCs to TC cell culture [134, 217].

3. A baseline influx rate of DCs was applied, that would normally continued for 60hrs, but at 12hours all the DCs that had entered were removed in the subsequent 2hour period. The effector TC response was compared to a corresponding *in-vivo* experiment carried out in rats by Prlic *et al* 2006. This study was selected because agDCs were eliminated within the LN at specific time-points post-stimuli, rather than the TCs transferred to an antigen free environment at a specific time-point [118]. This maintained the presence of previously induced inflammatory factors, and better matched the *in-silico* method.

4. The down-regulation of $S1P_1r$ on activated TCs was abolished *in-silico* and the results compared to similar experiments carried out by Graler *et al* 1997 [218] and Lo *et al* 2005 [106]. Down-regulation of $S1P_1r$ on activated TCs and re-expression on effector TCs is a key feature of the model, due to the impact on TC trafficking, therefore it was important to ensure that the model accurately captured the behaviours observed *in-vivo*.

Parameter tables

TABLE 2.3: Parameters that were not varied in the global sensitivity analysis

Parameter	Symbol	Value	Reference
Model Geometry			
Initial paracortex radius	r_p	200μM	[140, 183]
Entry radius	-	0.5 r_p	[140, 183]
Exit radius	-	0.07r_p	[140, 183]
Sub Capsular Sinus height	-	0.7r_p	[140, 183]
Grid Size	GS	6μm	-
TC initialisation			
Initial occupation	-	55%	[219]
Ratio CD4:CD8	-	0.7:0.3	[140, 183]
Lifespan naive	-	0.5 r_p	[220]
Lifespan naive	-	0.5 r_p	[212]
Afferent:HEV ratio	-	0.1:0.9	[184, 185]
DC initialisation			
DC span	-	2 grids	[198, 199]
DC Lifespan	-	2.5days	[58, 123, 221]
T cell movement			
Probability of movement	β	0.6	[36, 188–191]
Probability of egress	P_e	0.0106	-
Max cells per grid	γ	2	-
TC residence time	T_{res}	24hrs	[210, 211]

TABLE 2.4: Parameters varied in the global sensitivity analysis. Continued overleaf.

Symbol	Parameter Description	Default	Min	Max	Mean	SD	Distrib.	Ref
	TC response parameters							
$Act\mu_4$	$CD4^+$ activation curve mean	120	70	230	-	-	Unif	[222–227]
$Act\mu_8$	$CD8^+$ activation curve mean	140	90	250	-	-	Unif	[222–227]
$Dif\mu_4$	$CD4^+$ differentiation curve mean	60	30	90	-	-	Unif	[222–227]
$Dif\mu_8$	$CD8^+$ differentiation curve mean	40	20	60	-	-	Unif	[222–227]
T_{P4}	Min time between $CD4^+$ proliferations (hrs)	11	-	-	11	1.16	Norm	[39, 202–204]
T_{P8}	Min time between $CD8^+$ proliferations (hrs)	7	-	-	7	0.88	Norm	[202, 203]
Max_{P8}	Max proliferations $CD8^+$	16	-	-	16	1.2	Norm	[130, 228–230]
Max_{P4}	Max proliferations $CD4^+$	10	-	-	10	1.2	Norm	[39, 203, 204]
Dif_early	Early Memory:Effector cell differentiation	0.01	0.001	0.02	0.01	-	Exp	[231]
Dif_{late}	Late Memory:Effector cell differentiation	0.04	0.01	0.08	-	-	Unif	[231]
	TC interaction dynamics							
T_{NC}	Mean non-cognate T-DC interaction (min)	3.5	-	-	3.5	1	Norm	[123, 124]
T_{short}	Short cognate TC-DC interaction (min)	10-15	-	-	10	3	Norm	[121, 123, 124]
T_{long}	Long cognate TC-DC interaction (min)	50-70	-	-	50	12	Norm	[119–122]
T_{change}	Time TCs switch to long interactions (hr)	8	-	-	8	1	Norm	[119–122]
Max_{step}	Max TCs a DC can bind per-step	3	1	5	-	-	Unif	-
Max_{NT}	Max TCs a DC can bind	15	4	20	-	-	Unif	[193]
	TC Stimulation							
K_s	Stim. gain coefficient	0.015	0.005	0.02	-	-	Unif	-
λ	TC stim. decay factor	0.99	0.99545	0.9999	-	-	Norm	-
MHC_i	Initial MHCI/II	250	150	350	-	-	Norm	[194–197]
γ_{MHCI}	MHCI half life (hrs)	19.7	-	-	19.7	6	Norm	[194, 195]
γ_{MHCII}	MHCII half life (hrs)	60	-	-	60	6	Norm	[196, 197]
P_{cog}	Frequency of cognate TCs that enter	1e-4	5e-5	1.5e-4	-	-	Unif	[37–40]
Φ_{DC}	Total DCs entering as % of initial TCs	0.04	0.02	0.06	-	-	Norm	[58]
T_{DCin}	DC entry duration (days)	2.5	0.5	4.5	-	-	Unif	[58]

Symbol	Parameter Description	Default	Min	Max	Mean	SD	Distrib.	Ref
	Sphingosine-1-phosphate receptor regulation							
SP_{entry}	$S1P_1r$ expression post entry	0.1	0.01	1	-	-	Unif	[105, 106, 109]
SP_{act}	$S1P_1r$ expression when activated	0.01	0.001	0.02	-	-	Unif	[105, 106, 109, 207]
SP_{late}	Effector $S1P_1r$ (Proliferation>6)	0.8	0.3	1.3	-	-	Unif	[109, 207]
$S1_{early}$	Effector $S1P_1r$ (Proliferation<=6)	0.4	0.01	1	-	-	Unif	[109, 207]
SP_{mem}	Memory $S1P_1rr$	1	-	-	1	0.1	Norm	[109, 207]
SP_{IF}	$S1P_1r$ on all TCs during inflam.	0.4	0.2	0.8	-	-	Unif	-
T_{Entry}	Time $S1P_1rr$ is low post-entry (min)	60	13	120	-	-	Unif	-
T_{inflam}	Time to alter $S1P_1r$ during inflam.(hr)	4	1	7.5	-	-	Unif	-
	T cell recruitment							
RT1	recruitment increase stim. threshold	2e4	2e4	1e5	-	-	Unif	[160, 164, 167, 232]
RT2	Stim. threshold for max. recruitment	4e5	2e5	2e6	-	-	Unif	[160, 164, 167, 232]
R_F	Recruitment Factor	3e-6	1e-6	4e-6	-	-	Unif	[160, 164, 167, 232]
	Paracortex expansion							
V_{Max}	Max fold-volume increase	1	2	2.5	-	-	Unif	-
l	Rate of volume change around m	7e-05	3e-05	1e-04	-	-	Unif	-
m	No. of TCs for 50% max-volume	120000	90000	150000	-	-	Unif	-

UML diagrams

The following section presents the logic underlying the sub-methods that are called during the simulation. The order that each method is called is summarised in the previously shown 'Main' diagram 2.6).

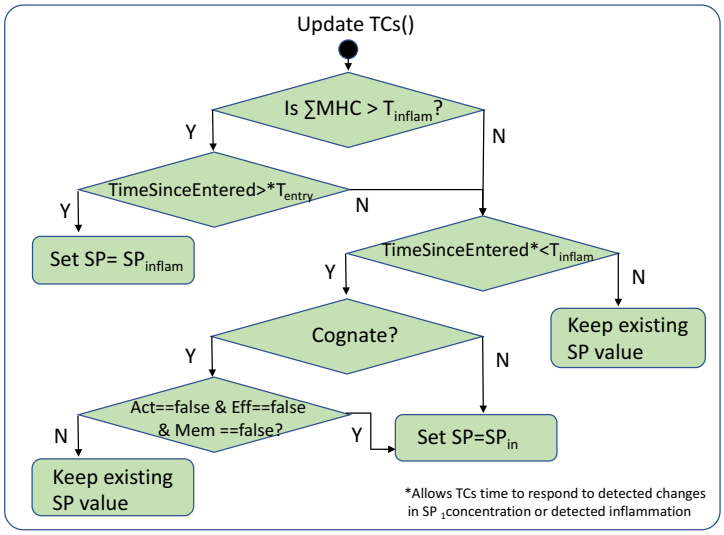

FIGURE 2.12: UML diagram for 'UpdateTCs'. By checking the time since the TC entered, a 'lag time' representing time for detection of signals and receptor internalisation to occur.

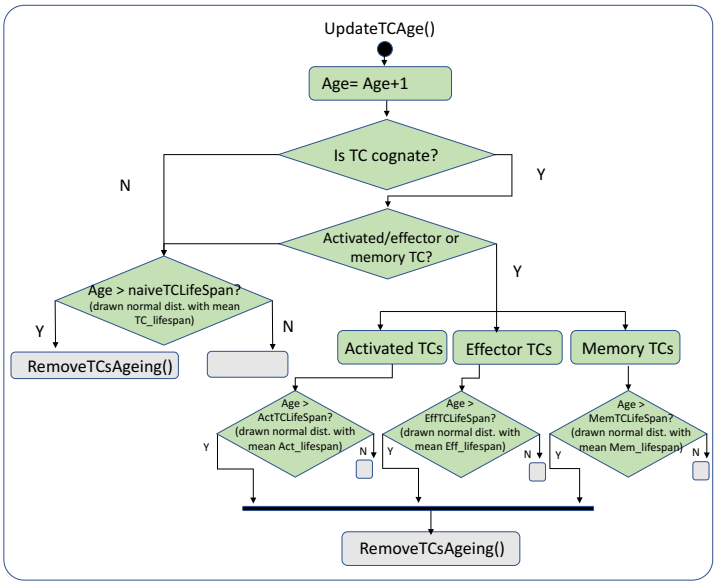

FIGURE 2.13: UML diagram for 'UpdateTCsAgeing'.

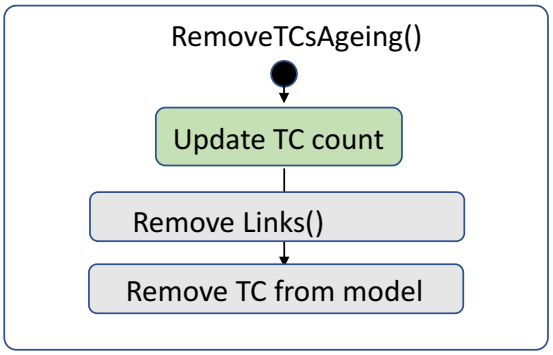

FIGURE 2.14: UML diagram for 'RemoveTCsAgeing'. The different types of TCs draw ages from gaussian distributions with a different mean value.

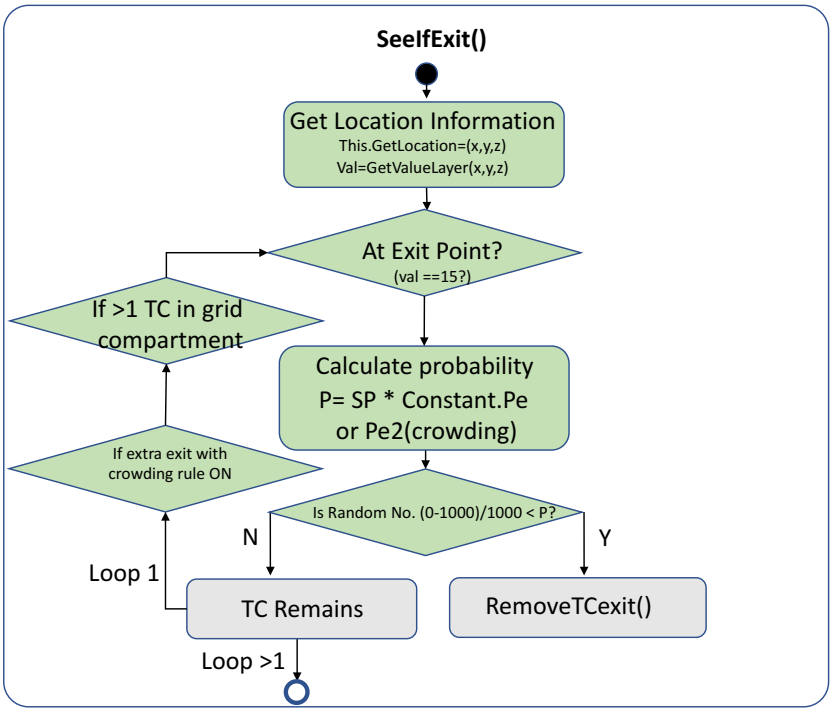

FIGURE 2.15: UML diagram for 'SeeIfExit'. The original simulations did not incorporate the second check of TC crowding (crowding rule).

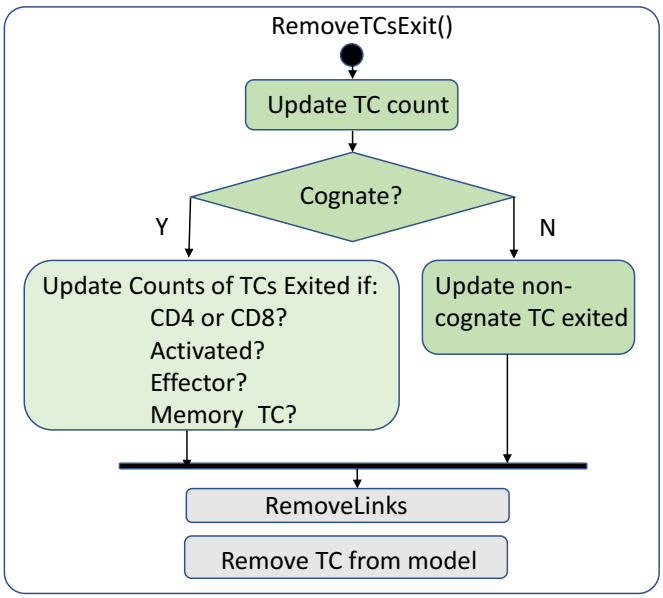

FIGURE 2.16: UML diagram for 'RemoveTCExit'. Ageing and TC exit are treated differently due to different counters being updated

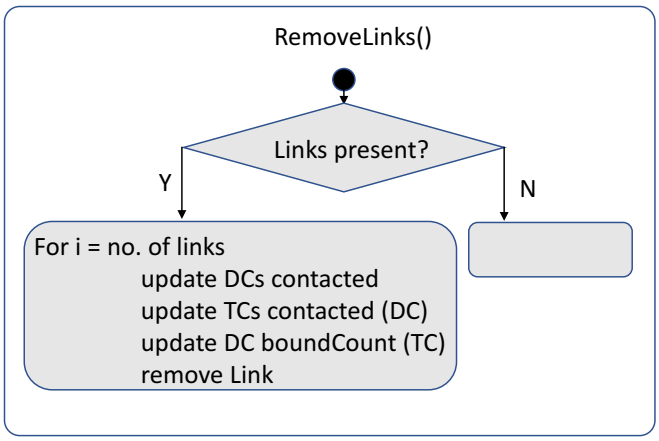

FIGURE 2.17: UML diagram for 'RemoveLinks'. Links between TCs and DCs are formed using a projection network, a feature of RepastSimphony, and must be removed when the connection is over.

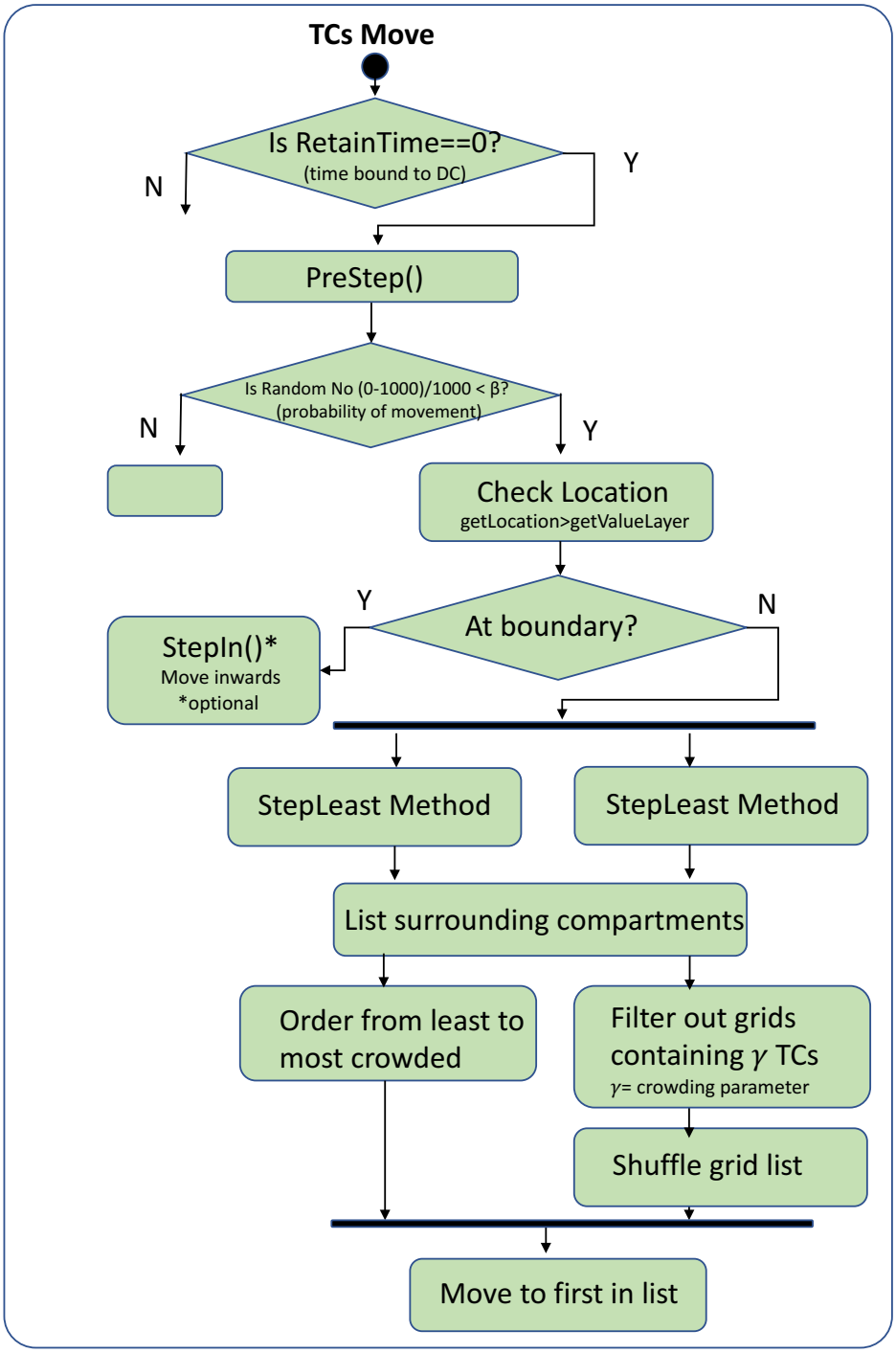

FIGURE 2.18: UML diagram for 'TCsMove'. The model has the capacity for different movement options, and maximum TCs per grid is set with crowding parameter γ

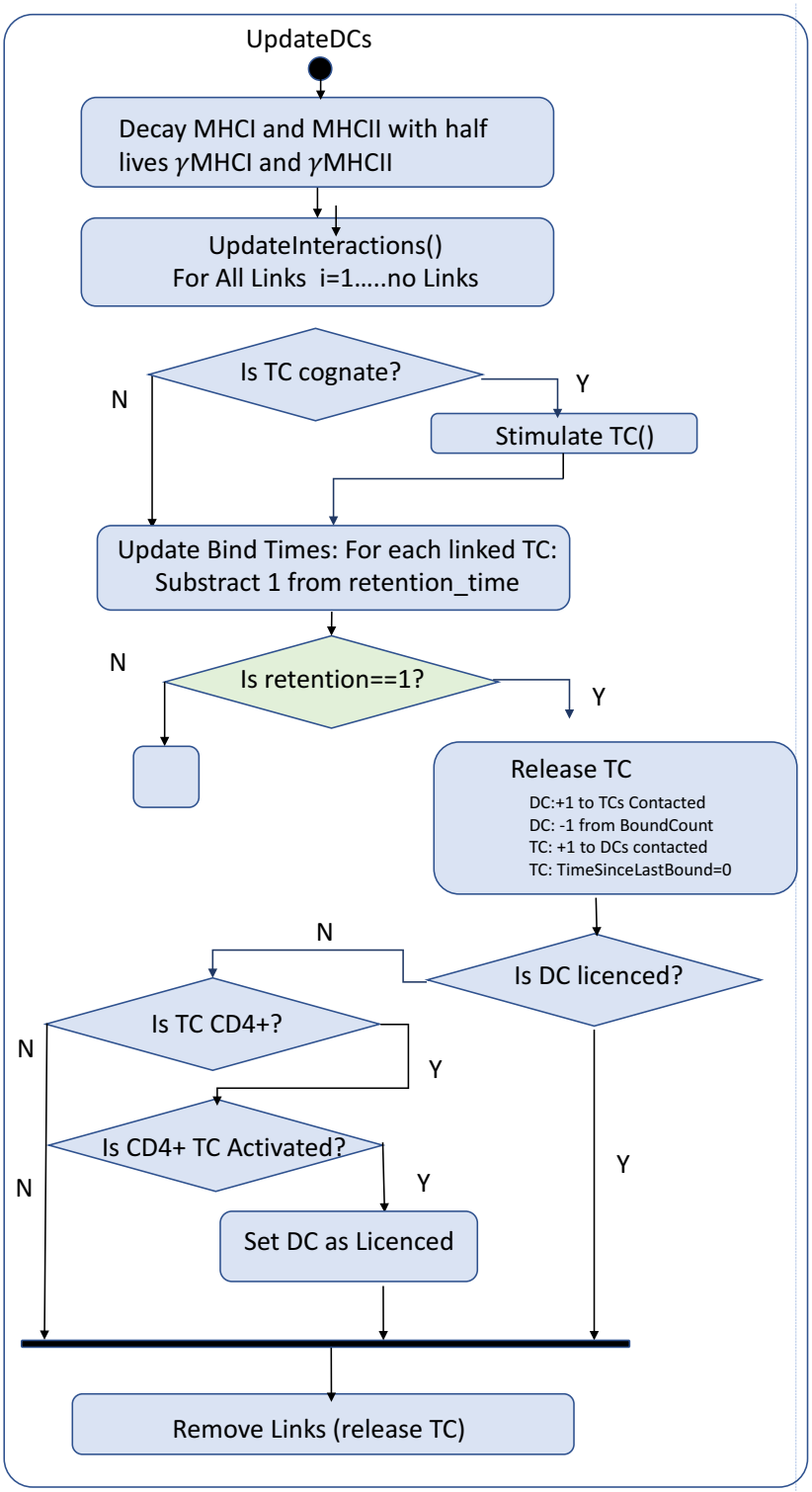

FIGURE 2.19: UML diagram for 'UpdateDCs'. DCs enter as mature migrating DCs but may become licenced through interaction with activated CD4+ TCs

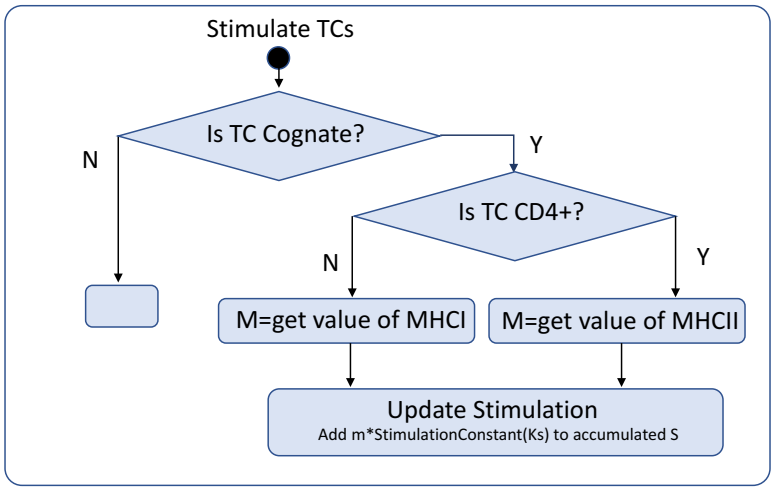

FIGURE 2.20: UML diagram for 'StimulateTCs'. DCs can access the variables of the agent attatched via a projection link and thus alter their state based on the DCs MHCI/II presentation and the Stimulation constant, Ks.

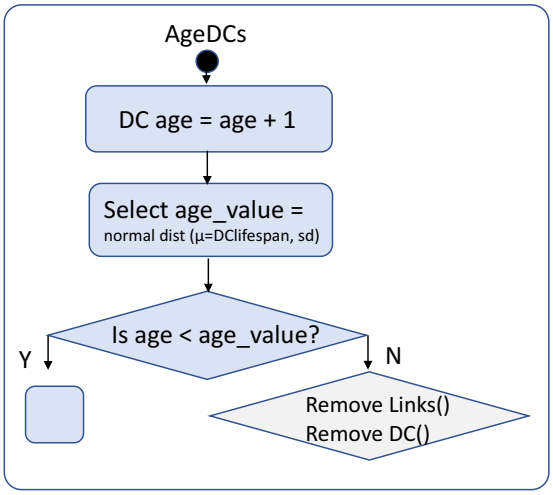

FIGURE 2.21: UML diagram for 'AgeDCs'. Mature DCs have a lifespan of around 2.5 days.

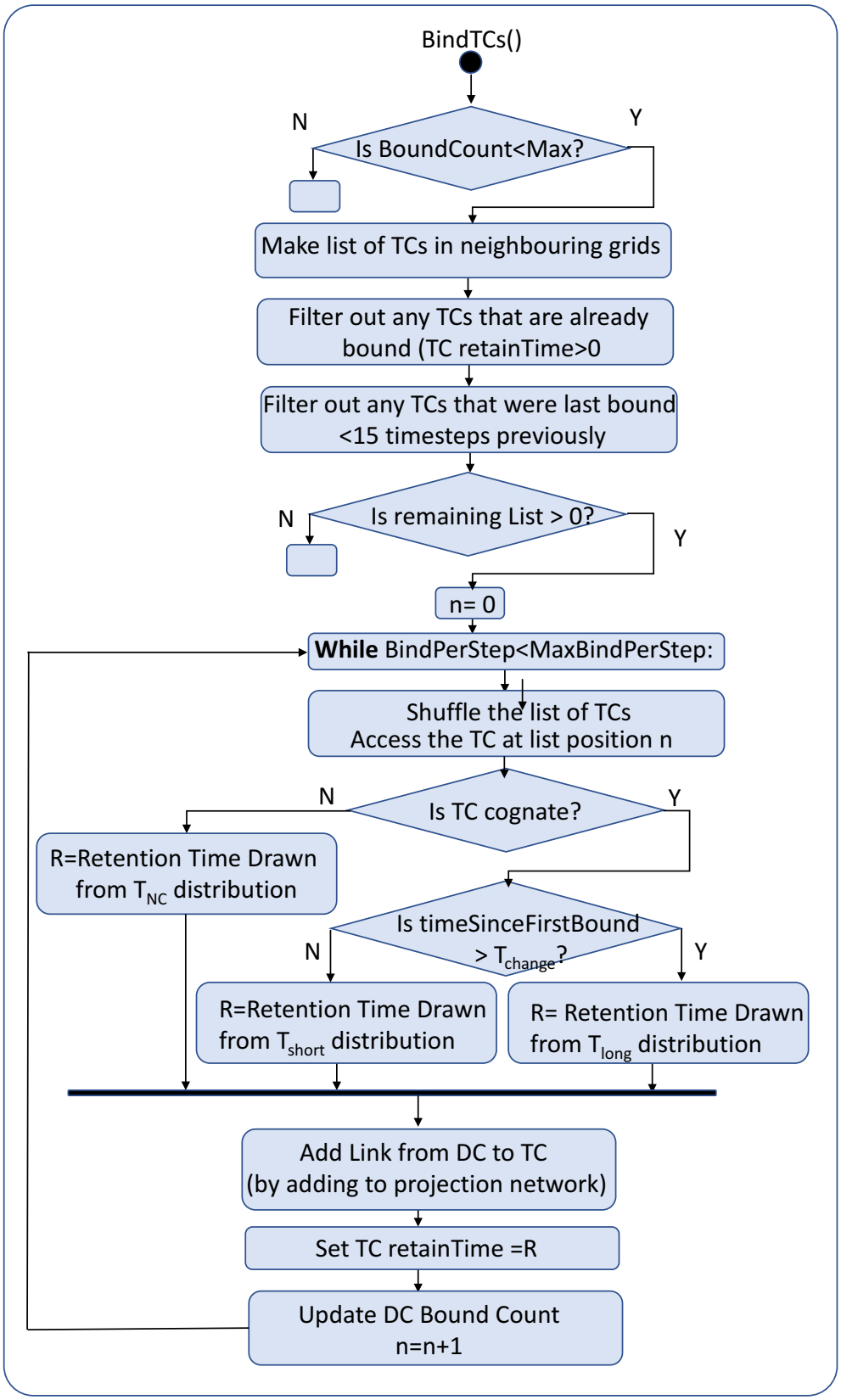

FIGURE 2.22: UML diagram for 'BindTCs'. TCs receive a 'interaction time' drawn from a relevant probability density function, based on their type and history.

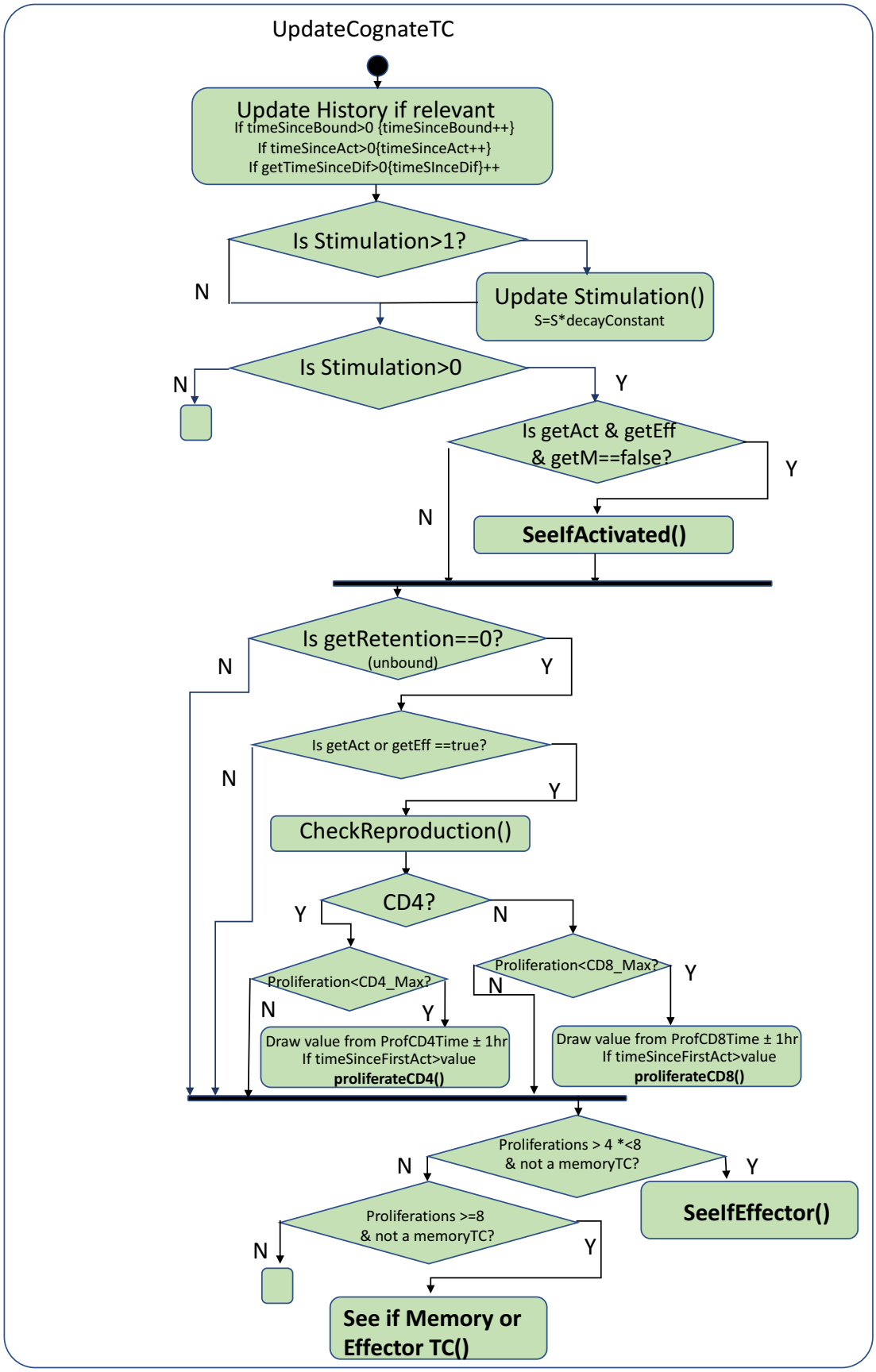

FIGURE 2.23: UML diagram for 'UpdateCognateTCs'.

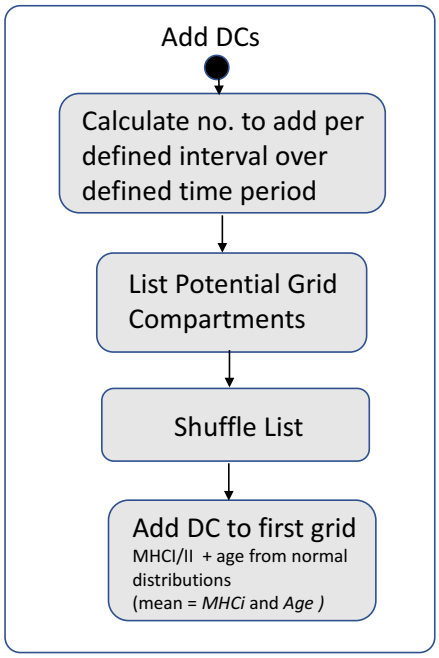

FIGURE 2.24: UML diagram for 'AddDCs'.

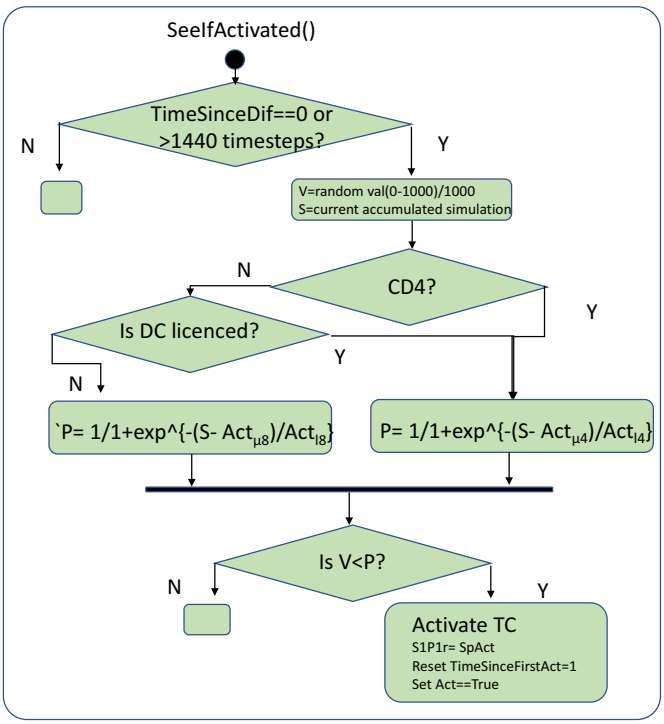

FIGURE 2.25: UML diagram for 'SeeIfActivated'

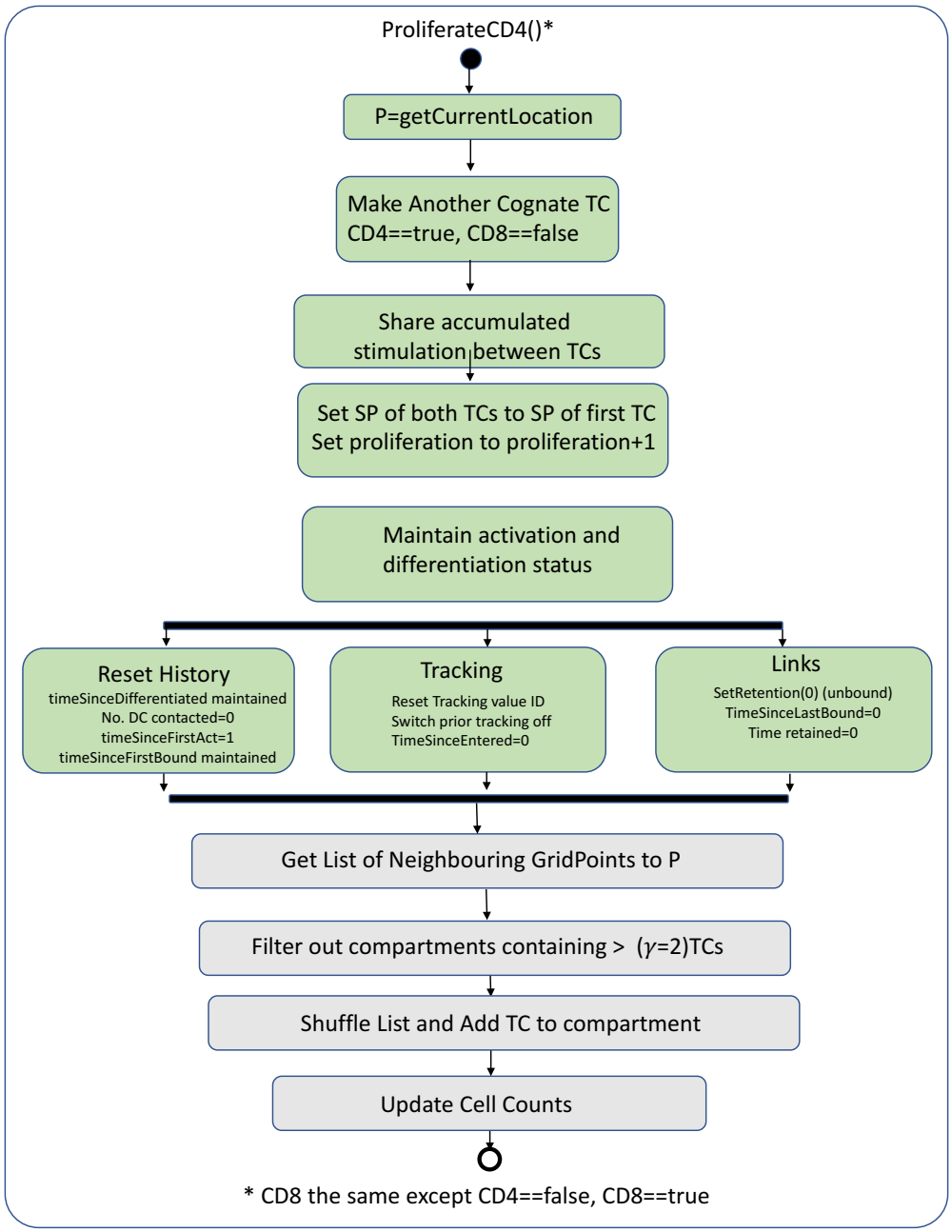

FIGURE 2.26: UML diagram for 'Proliferation'.

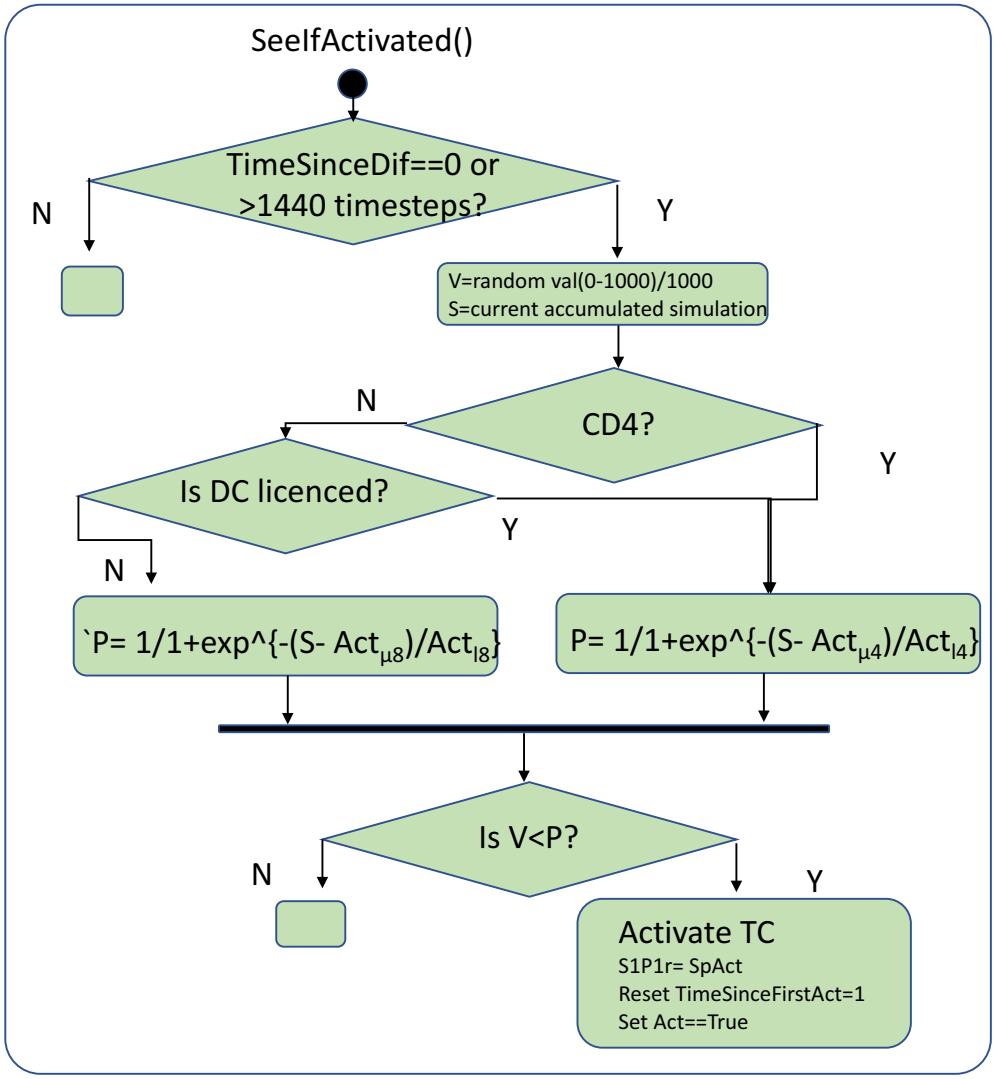

FIGURE 2.27: UML diagram for 'SeeIfEffector' or 'SeeIfEffectorMemory. The two behaviours are similar but for seeIfEffectorMemory, the time since differentation cannot be zero, as the TC must have previously differentiated, and more memory TCs are made.

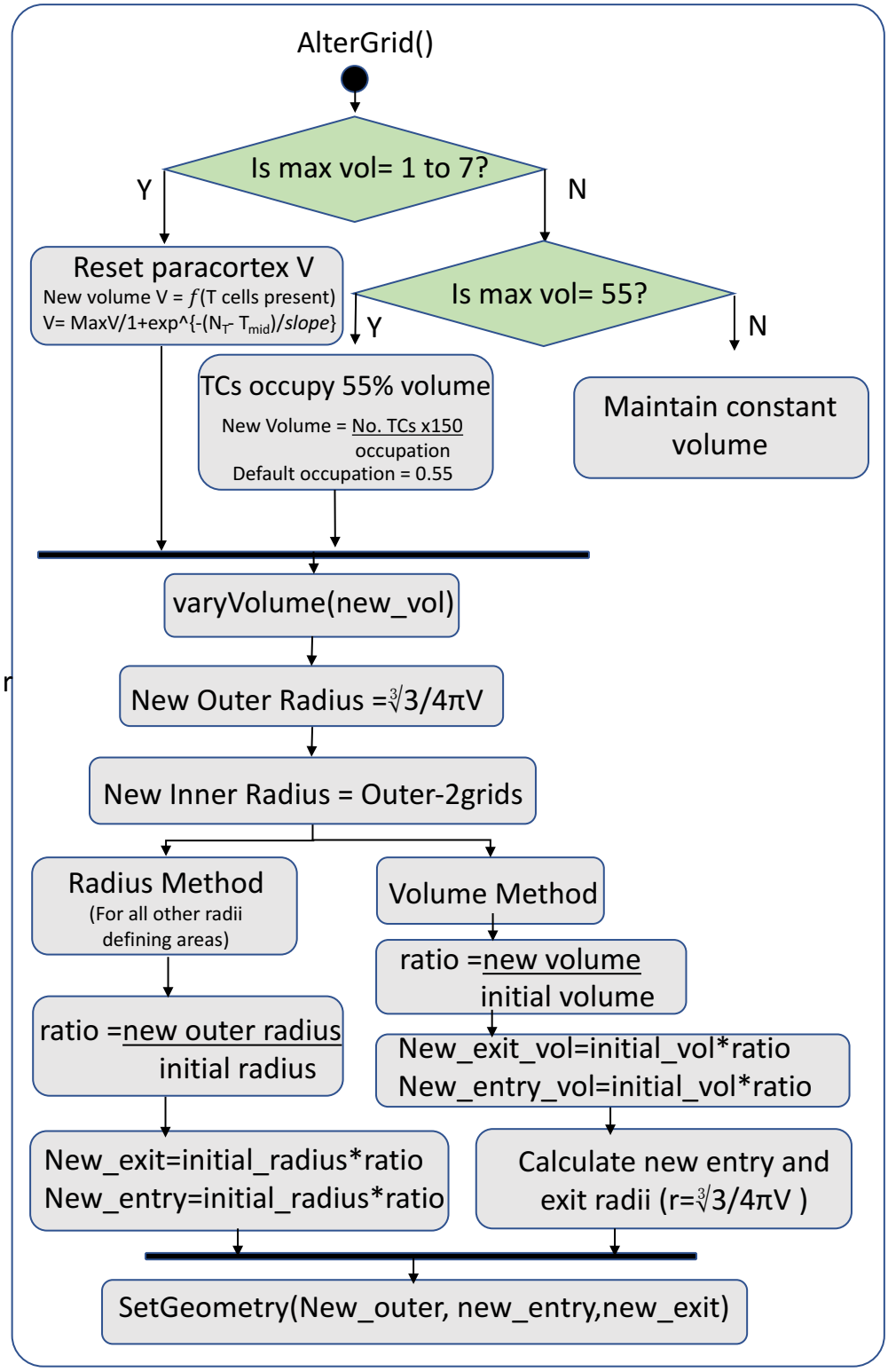

FIGURE 2.28: UML diagram for 'AlterGrid'. This methods carries out the calculation of the new paracortex volume then passes the calculated radii to 'Set Geometry'.

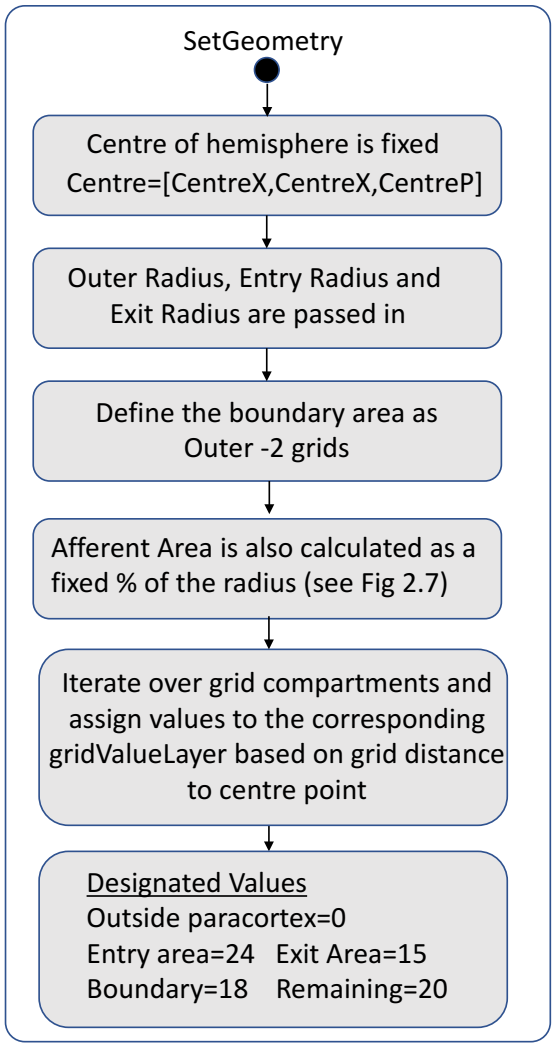

FIGURE 2.29: UML diagram for 'SetGeometry'. Only the radii are required as inputs to determine the geometry of the LN (See Figure 2.9)

2.3 Results

2.3.1 Overview

An original model was developed that described realistic TC motility and TC response to antigen in a LN paracortex capable of expanding in volume, while incorporating volume-dependent changes in HEV surface area, TC recruitment rate and exit areas. The effects of LN swelling on the TC trafficking and response to antigen are largely unknown, aside from the results of *in-vivo* experiments involving pre-injection into the LN of responsive TCs, rather than physiological numbers of cognate TCs [60].

The model simulations produced results that showed that LN swelling aided the activation of TCs, regardless of the later outcome regarding effector TC production. The increased TC activation did not correlate with the number of DC and TC interactions. The simulation results also showed that promoting LN swelling can impair the production of effector TCs if the timing of the swelling results in volume expansion prior to sufficient proliferation of $CD8^+$ TCs. The amount of proliferation considered sufficient varies with the swelling manner and maximum.

The model additionally incorporated the effects of $S1P_1r$ regulation and showed that the number of resulting effectors TCs was affected more by varying expression of $S1P_1r$ on newly differentiated effector cells than by varying LN swelling. This novel finding implies that temporary $S1P_1r$ down-regulation may present as a mechanism to counteract suppressed effector production or aid in scenarios where a response to a low antigen dose is desirable, such as in vaccine design. This finding also emphasises the influence that retentive features, including factors such as chemokines, may have on effector TC response.

Increased egress rates accompanied LN swelling, and the results of the model simulations also highlighted the need to understand how egress areas alter with swelling, as this is likely to contribute to the poor effector TC responses. Maintenance of increased TC crowding was also observed in more efficient TC responses when the LN swelled, while in non-expanding LN, increased crowding rose to almost non-physiological levels. This could contribute to decreased

access to exit and highlights the need to better account for changes in pressure in the LN that may impact lymphocyte egress.

The reliability of the model was confirmed by replicating non-baseline scenarios that have been carried out *in-vivo* and ensuring that comparative TC behaviour and response was produced *in-silico* (Section 2.3.6). A global sensitivity analysis was also performed to ensure awareness of influential parameters (Section 2.3.5). The results of the global sensitivity results also highlighted the ability of parameters to be beneficial early in the response but detrimental at later time-points, as well as some inter-related effects of $S1P_1r$ regulation and LN swelling.

2.3.2 The model produced realistic baseline T cell motility

TC motility under non-antigenic conditions reproduced measurements observed *in-vivo* in murine LNs. Average TC velocity was 13.1μm/min and reached 24 μm/min (Figure 2.30D) [36, 188–191]. The coordinates of 200 TCs were recorded to analyse TCs movement (2.30A,B). The TC displacement versus the square root of time (Figure 2.30E,F) was concurrent with random walk behaviour (R2=0.9986), as discussed in Beltman 2007 and motility co-efficient (CM) was calculated as 63.2μm/min[46]. This is within the 50-100μm/min observed in mice *in-vivo*[46]. The mean TC paracortex transit time was 13.1 hours (n = 16000) and ranged from 20 minutes to >60 hours (Figure 2.30C).

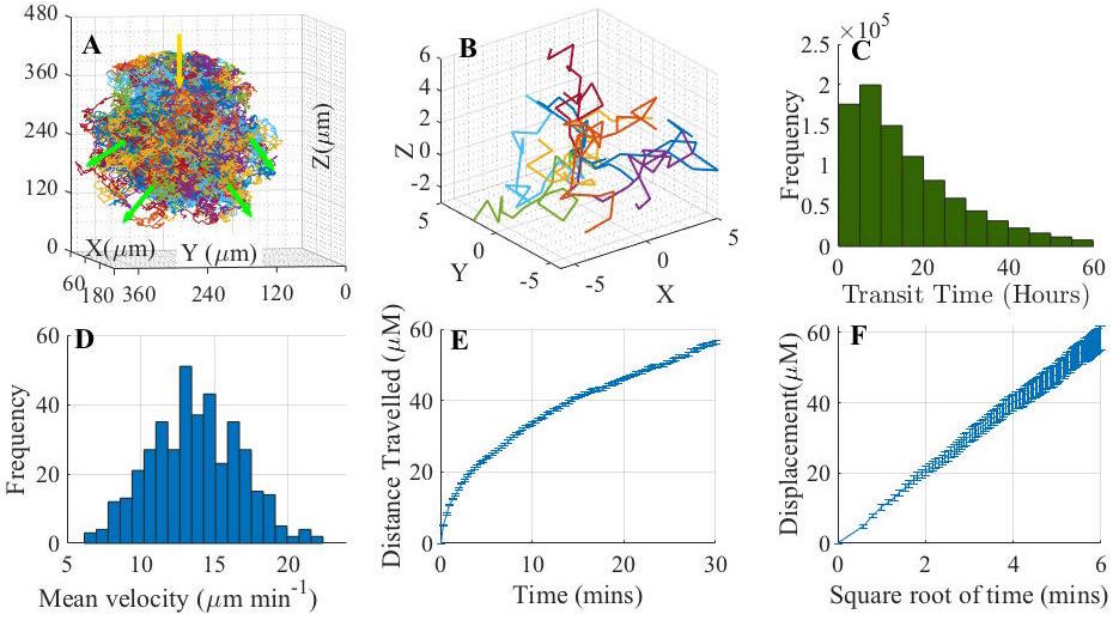

FIGURE 2.30: Baseline TC motility. A. TC tracking through the paracortex with individual tracks displayed. TCs entered centrally, representing entry from HEVs, and at the top of the paracortex, representing entry in afferent lymph (yellow arrow). TCs exited at the periphery (green arrows). B. Tracks of TCs (each colour represents one TC path) transposed to the same origin point display the random walk behaviour outwards from the origin.C. Most TCs completed transit in <24hrs. D.Mean velocity of TCs. E. Mean and SEM (n=100) of TC displacement from entry point. F. Mean (+-SEM) of TC displacement showed a linear relationship to the square root of time.

2.3.3 The model produced a realistic T cell response to agDCs

With baseline parameters, application of an antigenic stimulus produced TC responses that corresponded well to experimental data from mice, sheep and rats, both temporally and in terms of the magnitude of fold-increase in TC number. Sensitivity analysis and replication of *in-vivo* experiments were also carried out to ensure reliability of the model (see 2.3.62.2.4). During baseline simulations of TC response to antigen the maximum fraction of volume increase, (V_{max}), was limited to 1.2. This was to limit the potential effects of volume increase that would be later investigated in more detail, whilst ensuring that model was capable of volume changes and accompanying alterations in geometry. The stimuli was provided by antigen-presenting DCs that entered gradually from 10hrs into the simulation for 60hours (Figure 2.31B) as described in Methods 2.2.2. The DCs underwent apoptosis at a mean of 60hours post-entry, so that by day 5, no agDCs remained in the paracortex.

The number of TCs in the paracortex began to increase several hours after the initiation of agDCs entry and returned to within 10% of initial numbers within 10 days (Figure 2.31A). The activation phase of TC response began at 16 to 24 hours after the agDCs began to enter and activated TCs remained in the LN up to day 7 (Figure 2.31B). Activated TCs could increase in number through the activation of naïve cognate TCs and proliferation of previously activated TCs, and peaked at day 2.8 of the simulation. The differentiation phase began from day 3.5, when the first effector TCs appeared in the paracortex as a result of the differentiation of activated TCs 2.31A). The peak number of effector TCs within the paracortex was observed at 6 to 7 days, which was the accumulation of activated TCs differentiating into effectors and effector TCs continuing to proliferate. Memory TCs appeared from 5 days onwards and reached numbers two orders of magnitude less than effector TCs (Figure 2.31B). The contraction phase, whereby the number of TCs begins to return to pre-stimuli levels, began at day 7 and continued through to day 11, where TC numbers remained slightly higher than pre-stimuli.

The proliferation of cognate (activated, effector and memory) $CD4^+$ helper TCs, representative of effector TC emergence due to the difference in magnitude of number of effector TCs and activated TCs, began at 2.5 days, 1-1.5 days before

CD8$^+$ cytotoxic TCs underwent proliferation (Figure 2.31C). The peak number of cognate CD4$^+$ cells in the paracortex occurred between 6 to 8 days post stimuli. Cognate CD8$^+$ TCs underwent significant proliferation from day 3.5 to day 4 post stimulus, but reached peak numbers, representative of CD8$^+$ effector TCs, ten times higher than peak number of CD4$^+$ TCs (Figure 2.31C) at 6-7 days post stimulus.

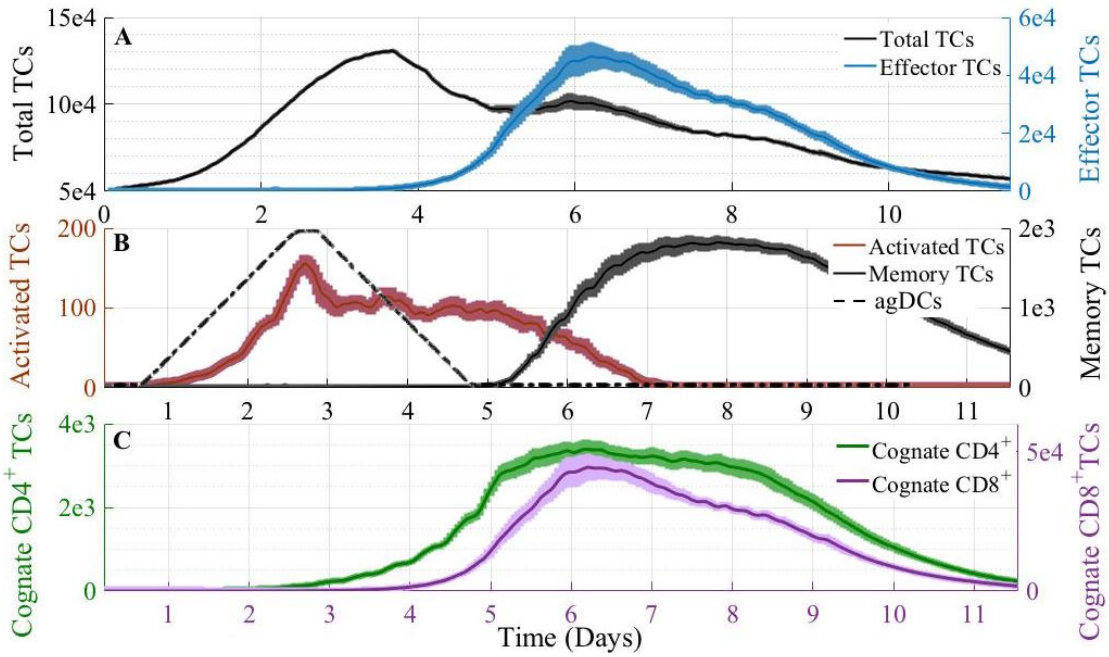

FIGURE 2.31: Types of TCs in the paracortex following entry of agDCs. (DCs, dot-dashed line in B). Average with SEM of 12 simulations. The total number of TCs (black line in A) peaked in the paracortex at 3.5 days, and was comprised mainly of non-cognate naïve TCs, as the number of effector TCs (blue line A) peaked at day 6. This can be seen as a second peak in the total TC number. Th number of activated TCs (red line in B) began 12 hours after the first agDCs entered. Memory TCs (black line in B) began to appear at 5 days and 25% of the peak number of memory TCs remained at the end of the simulation. Cognate CD4$^+$ TCs (Green line in C) began to proliferate extensively at day 2.2, compared to cognate CD8$^+$ TCs (purple line C) that began to proliferate at day 4 and reached numbers 10x more than cognate CD4$^+$TCs.

The component of increased recruitment due to volume increase contributed very little to overall TC recruitment as V_{max} was limited to 1.2. Figure 2.32 shows TC entry rate increased 2.2x which was mainly due to increased recruitment following detection of antigenic stimuli. TC entry rate began to increase 6 hours after antigen-presenting DCs (agDCs) appeared in the paracortex.

The TC egress rate decreased slightly (5%) in the first two days of the simulation, corresponding well to literature reports of initial 'LN shutdown', meaning TC retention in the first 24hours[232]. TC egress then increased to 2.8x initial TC egress rate in the next 2 to 4 days which was slightly less than the 3 to 5x increase that is observed in sheep, mice and rabbit lymph LNs [160, 164, 167, 232]. From day 4 to 6 TC egress rate fluctuated but from day 6 to 10 TC egress rate gradually decreased to reach near pre-stimuli levels at day 10 (Figure 2.32B). Figure 2.33 summarises the phases of TC behaviours captured by the model in the baseline simulation.

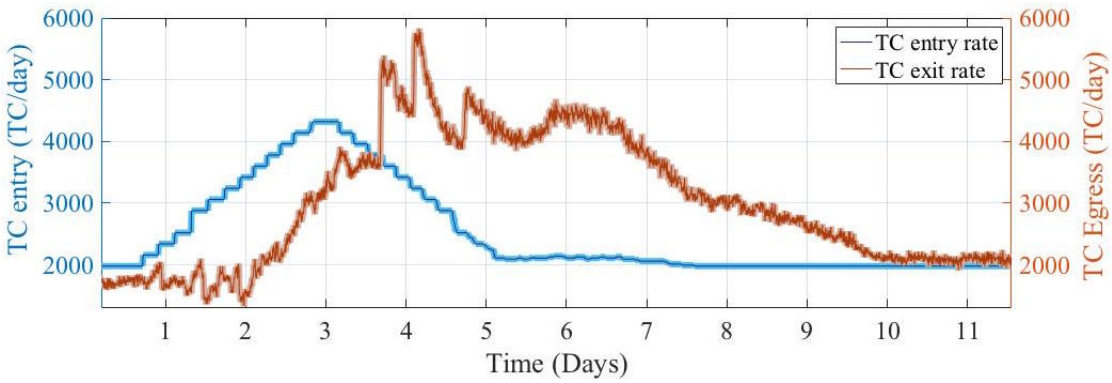

FIGURE 2.32: TC trafficking rates. TC entry rate increased 2x due to detection of antigenic stimulus whilst TC egress rate declined between day 1 and 2, then increased 3x by day 4.

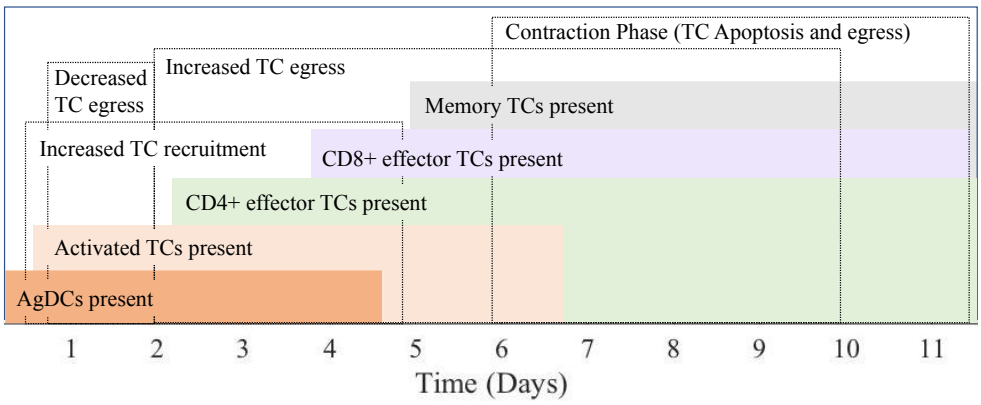

FIGURE 2.33: Captured phases of TC trafficking and response to AgDC stimuli. Changes in proliferation and differentiation continued after the initial stimulus was no longer present. TC recruitment and TC egress changes also accompanied the response.

2.3.4 Paracortical expansion and T cell response

The effect of varying maximal paracortical swelling (V_{Max})

When the value of V_{Max} was varied in 0.2 increments from 1 to 2.8, the number of activated TCs positively and significantly correlated with V_{max} (p=1.07e-6) and increased 2 fold (Figure 2.34B,2.35A). The number of total effector TCs negatively correlated with V_{max} (p=1.23e-04) and decreased by 15% as V_{Max} was increased from 1 to2.8 (Figure 2.35B). The number of effector TCs exited showed no significant variation (Appendix A.2A,B). In the initial 2-5 days post-stimuli, the larger the value of V_{Max}, the more total TCs were present (Figure2.34A).

The highest peak number of TCs present in the paracortex increased with (V_{max}, aside from when the paracortex did not swell (Figure 2.34A). Simulations with a fixed volume parcortex (lilac line Figure 2.34A) reached a intermediate peak number of TCs but due to the longer maintanance of increased TC number, during the course of the simulation more TCs were present (Appendix A.2E). Similarly, as the maximum swelling was increased from V_{max} =1 to 1.8, despite the greater peak number of TCs,the total number of TC number present over the course of the simulation decreased. This is likely due to increased egress in the second week of the simulation(Appendix A.2F,G).

Total number of $CD4^+$ helper TCs and total number of $CD8^+$ cytotoxic TCs varied differently in response to an altered maximum paracortical swelling. Varying V_{max} did not significantly affect the total number of $CD4^+$ TCs in the paracortex (Figure Appendix A.2C) but the number of cognate $CD4^+$ TCs that exited the paracortex by day 10 positively correlated with V_{Max} (p=0.001) and increased 1.3x between V_{max}=1-2.8 (Figure 2.35C). Observation of a higher $CD4^+$ exit rate, but no accompanying change in the total number of $CD4^+$ TCs present in the paracortex at one time, implied that overall $CD4^+$ effector TC production rate was higher when V_{max} was larger, and $CD4^+$ TCs left the paracortex more quickly.

Cognate $CD8^+$TC presence showed the opposite pattern. The total number of cognate $CD8^+$ TCs present decreased 0.25x between V_{max}=1 and 2.8, showing a negative correlation with V_{max} (p=1.28e-4) (Figure2.35D). However, the number of cognate $CD8^+$ TCs that exited did not significantly vary (AppendixA.2D). This showed that despite the decrease in total number present, the $CD8^+$ output remained the same, implying that mechanisms must be involved that prevent the increased number of effector TCs present translating to increased effector TCs exit at larger values of V_{max}.

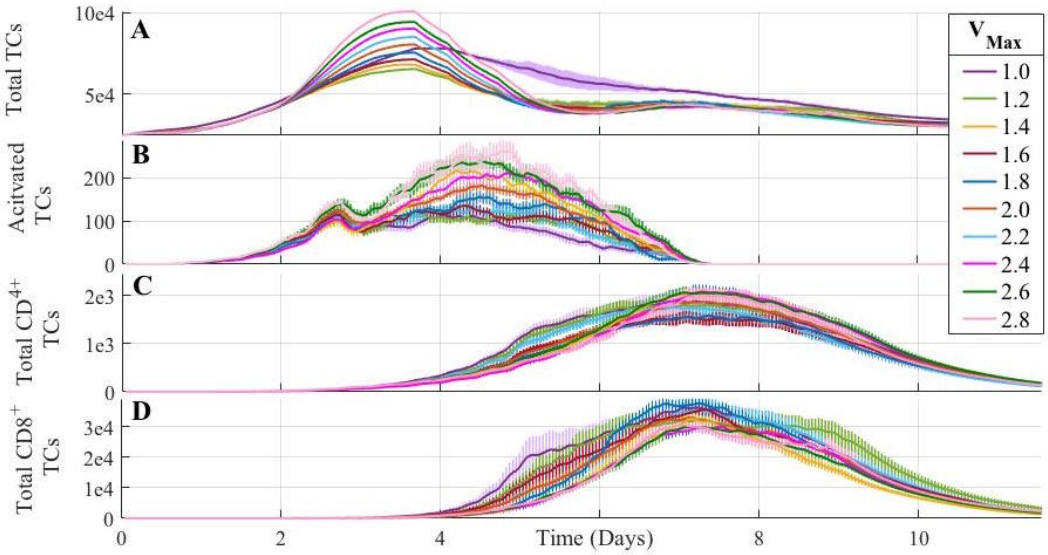

FIGURE 2.34: TC response over 11 days when V_{Max} was varied from 1 to 2·8. A.The total TCs in the paracortex between day 2 and 5 incrementally increased with (V_{Max}, except when the paracortex volume was fixed (V_{Max}=1). B. The number of activated TCs in the paracortex doubled when V_{Max} was increased from 1 to 2.8. C. The no. of cognate $CD4^+$ TCs in the paracortex showed no significant difference between groups (ANOVA p=0.44) (Appendix A.2C). D. The no. of cognate $CD8^+$. At V_{Max}=1.0 (purple), cognate $CD8^+$ TCs began proliferating earlier and at V_{Max}>2, less effector TCs were produced.

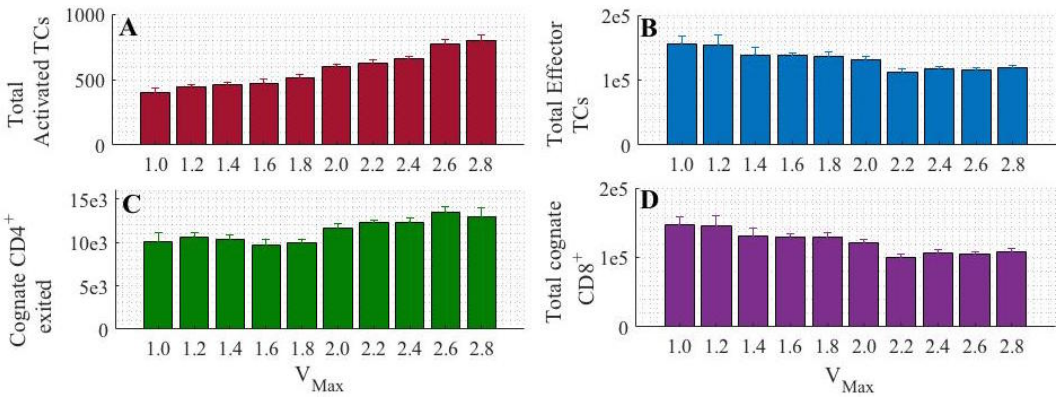

FIGURE 2.35: The variation in TC subsets as V_{Max} was varied from 1 to 2·8. A. The total activated no. of TCs in the paracortex incrementally increased with V_{max}, and doubled in number between V_{Max}=1 and 2.8 B. The total no. of effector TCs decreased 0.3x with increasing V_{Max}. C. The total no. of cognate $CD4^+$ TCs that exited positively correlated with V_{Max} (ρ=0.87,p=0.001) and increased 1.3x. D. The total cognate $CD8^+$ TCs negatively correlated with V_{Max} (ρ=-0.92,p=1.28e-4). All results are the mean of n>=7 simulations with SEM displayed.

As activation was shown to positively correlate with V_{max}, the next step was to investigate the hypothesis that greater paracortical swelling resulted in more TC activation due to more contact between DCs and cognate TCs. The mean number of non-cognate and cognate TCs that agDCs contacted was recorded for all agDCs that entered between 30-60hours after the first agDC entered. The total non-cognate TCs a DC contacted slightly increased as V_{Max} was increased from 1 to 2.82.36B. Analysis of variance between groups showed a significant difference between the groups (p=0.0104) and further analysis confirmed a significant positive correlation between V_{max} and number of non-cognate TCs contacted (p=2e-04). 2.36B. Contrastingly, a negative correlation was observed for the number of cognate TCs contacted and V_{Max} (p= 2.02e-04). 2.36C.

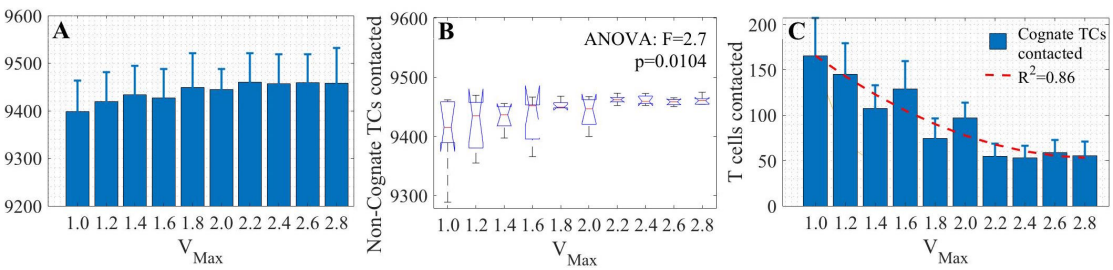

FIGURE 2.36: Paracortex swelling and cognate TCs contact with DCs. V_{max} was varied between 1 and 2.8 and DC-TC contacts at 30-60 hours after the first DC entered were recorded (n>=7+SEM). A. DCs contacted more non-cognate TCs as V_{max} increased, showing a positive correlation (ρ=0.91, p=2.7e-04). B. Analysis of the significant variance between groups (p=0.0104) showed that at lower values of V_{max} there was greater variance in the number of TCs contacted. C. The number of cognate TCs contacted by DCs negatively correlated with V_{max} ρ=-0.92, p= 2.02e-04). A polynomial fit with 2 degrees (R^2=0.86) describes the pattern.

A comparison of the mean number of contacted TCs and the mean number of total activated TCs in simulations varying V_{max} showed that as V_{max} increased, less cognate TCs were contacted but more activated TCs were present. A a negative correlation was confirmed between cognate TCs contacted and activated TCs (p= 0.002), contradicting the initial hypothesis (Figure 2.37A). However, at lower values of V_{Max} (<1.8), the number of effector TCs produced increased as the mean number of TCs contacted by DCs increased (Figure 2.37A). The number of effector TCs that exited the paracortex did not show any relationship to the number of cognate TCs contacted (AppendixA.2I).

There is a distinct difference in the way that $CD4^+$ and $CD8^+$ TCs respond to changes in V_{Max} and contact with DCs also differs. The number of cognate $CD4^+$ TCs in the paracortex did not show any correlation to the number of cognate TCs contacted (p=0.7) (AppendixA.2G). However the number of cognate $CD4^+$ TCs that exited showed a significant correlation with higher values of V_{Max} (p= 0.013) that could be described with a linear fit (p=0.0126), despite the decrease in DC contact with cognate $CD4^+$TCs (Figure 2.37C).

$CD8^+$ TCs showed the opposite pattern. The total number of $CD8^+$ TCs produced significantly positively correlated with the number of cognate TCs contacted by DCs (p= 7.6e-05), but this occurred at decreasing values of V_{Max} (Figure 2.37D). No correlation was observed between total $CD8^+$ TCs and cognate TCs contacted by DCs (AppendixA.2I). It is also important to consider that, although the contacts were recorded from 30-60hours post stimuli if the cognate TC response is larger there are more cognate TCs to contact, which may mask the early behaviour of increased contact driving response.

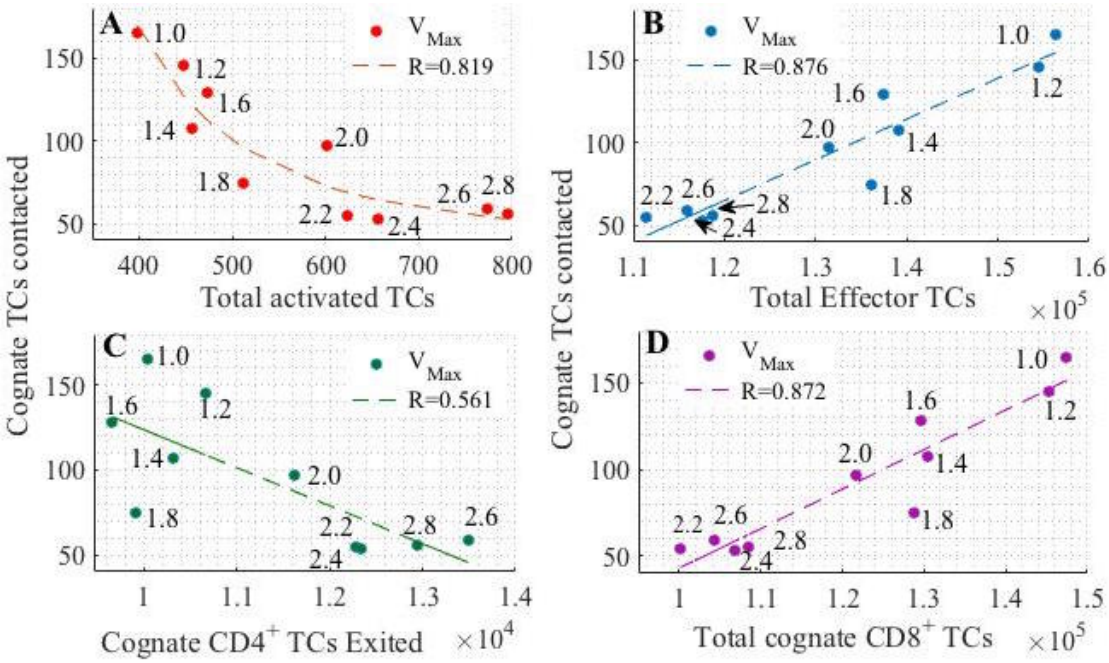

FIGURE 2.37: The relationship between the maximal swelling, TC-DC contact and TC response. A. The mean no·of total activated TCs negatively correlated with TCs contacted, which occurred as V_{Max} became larger (2 degree exponential fit, ρ=-0.85, p=0.002). B. The mean no. of total effector TCs, positively correlated with TCs contacted, ρ=0.93 p= 7.6e-05 (linear fit p=4.21e-05). C The mean no. of total $CD4^+$ TCs that exited the paracortex negatively correlated with mean TCs contacted by DCs ρ=0.75, p=0.013, (linear fit p=0.013), D. The mean no. of total $CD8^+$ TCs in the paracortex positively correlated with TCs contacted, ρ=0.93, p=7.63e-05, which increased as V_{Max} became smaller (linear fit p=7.63e-05). Each data point represents the mean of 10 simulations.

To investigate whether increased DC contacts with cognate TCs affected effector TC production without the impact of altered V_{max}, the results of simulations carried out with a constant V_{max} were analysed. A loose correlation was observed between but statistical analysis failed to give a significant correlation. At V_{max} =2.0, fitting a linear model produced an R squared value of 0.57 showing a stronger correlation (Figure 2.38A) and the correlation was significant (p=1.85e-04). Applying a t-test between results and estimated model confirmed the linear relationship (p= 0.007). The results suggested that contact becomes more important when the LN is expanding or alternatively production impacts contact, which could feedback.

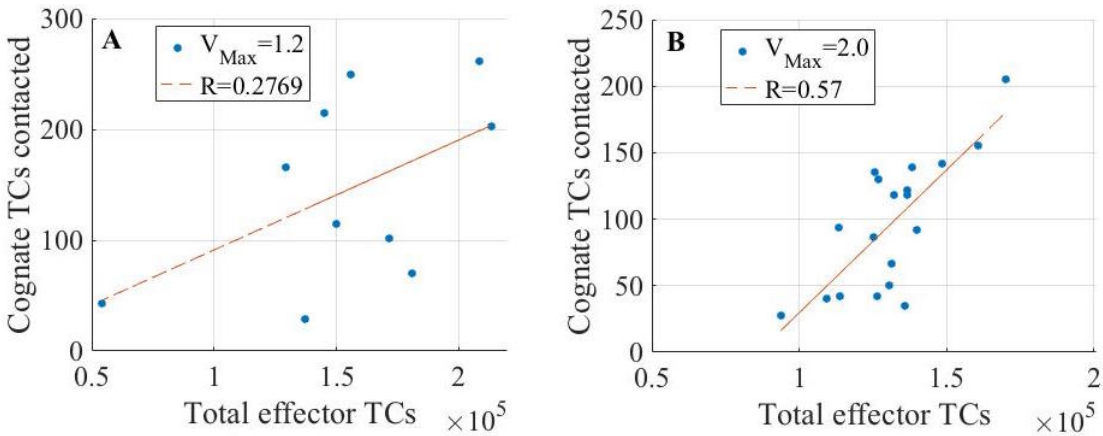

FIGURE 2.38: TC-DC contact is more important at larger swelling values. A. At V_{Max} =1.2, a slight linear correlation can be seen between total effector TCs produced and cognate TCs contacted but this was not significant (ρ=, 0.52, p= 0.12) and the linear fit was also not within a 95% confidence interval (t-test between data and fit p=0.12). At V_{Max} =2.0 there was a significant positive linear correlation between cognate TCs contacted by DCs and effector TCs produced that could be described with a linear fit (goodness of fit (t-test) p=0.0066).

Varying T_{Mid} can counteract the effects of V_{Max}.

The effect of increased V_{Max} leading to a reduced number of effector TCs produced could be counterbalanced by increasing the parameter T_{Mid}, that alters the number of TCs required to reach half the maximal paracortical volume. Simulations using V_{Max}=1.2 or V_{Max}=2.5 were repeated with a lower (8e4) and higher (12e4) value of T_{Mid} than the baseline value of 10e4. Instead of a doubling of TCs in the paracortex required to reach 50% of maximum volume, a 1.6x or 2.4x increase was required. Figure 2.39A shows the resulting change in the way that paracortical volume varied when V_{Max} and T_{Mid}. The paracortex began to expand a day later with T_{Mid}=12e4 compared to T_{Mid}=8e4. At V_{Max} =1.2 there was no significant difference between simulations with different T_{Mid} values (t-test, p=0.12), but at V_{max}=2,5, significantly more TCs were produced at a lower T_{Mid} (t-test, p=0.002). As previously, activated TCs doubled at the larger value of V_{Max} =2.5 regardless of T_{Mid} (Figure 2.39A). By varying T_{Mid}, similar numbers of effector TCs were produced at V_{Max} =1.2 and V_{Max} =2.5 (Figure 2.39C). After inspecting the change in cognate $CD4^+$ and $CD8^+$ TCs, it could be concluded that the change was due to cognate $CD8^+$ TCs, as there was no significant difference between cognate $CD4^+$ TCs with different T_{mid} values at either V_{max}=1.2 (p=0.17) or V_{max} =2.5 (Figure 2.39D,E,F,G).

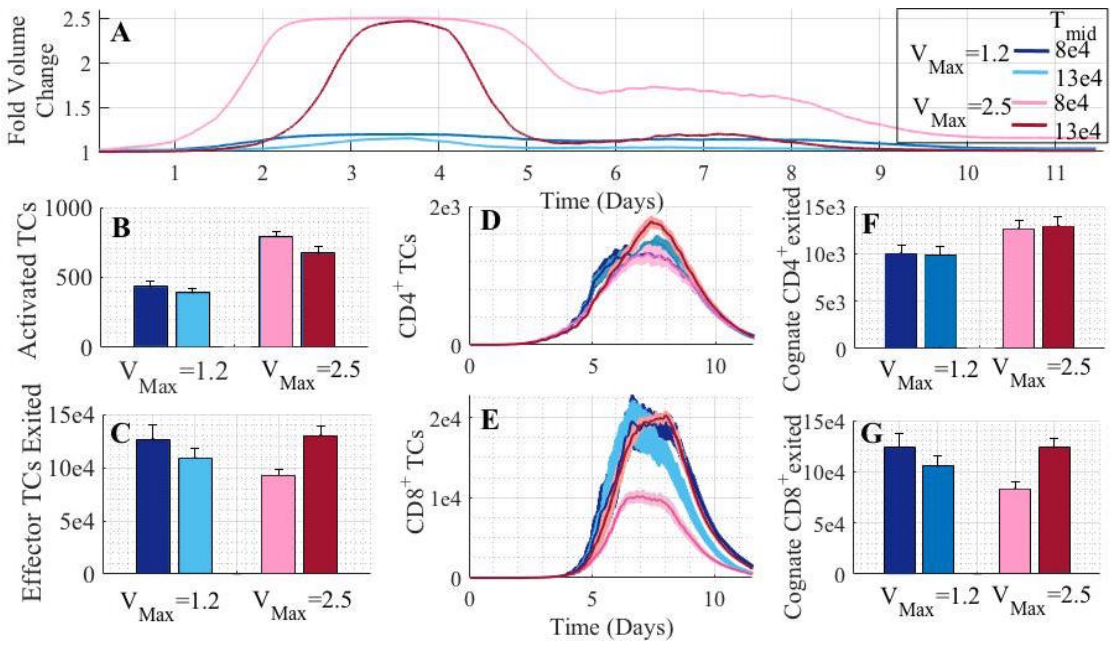

FIGURE 2.39: Increasing T_{Mid} counteracts the loss in effector TCs with V_{Max} A. The fold-volume change of the paracortex using different parameter combinations of V_{Max} and T_{Mid}. B. Activated TCs increased at larger values of V_{Max}. At V_{Max} = 1.2 there was no significant difference when T_{Mid}=8e5 or 10e5 (t-test p=0.12) but there was a significant difference at V_{Max} = 2.5 (p=0.002). C. Increasing T_{Mid} at V_{Max}=2.5 meant effector TC numbers became the same or more than at V_{Max}=1.2. D. $CD4^+$ TCs over time remained similar in all parameter combinations but more exited at a larger V_{Max}. F. Total $CD4^+$ TCs increased with V_{Max} only, and showed no significant difference with T_{Mid}=8e4 or 12e4 at V_{Max}=1.2 (p=0.17) or V_{Max}=2.5 (p=0.57). E. $CD8^+$ TCs over time showed that a high V_{Max} and low T_{Mid} resulted in the least total $CD8^+$ TCs. G. Total $CD8^+$ TCs exited reflected the pattern of overall effector TCs.

The conditional effects of varying Tmid

After identifying the sensitivity of T_{Mid} and V_{Max}, T_{mid} was varied across a greater range of V_{Max} values which revealed that the larger the value of V_{Max}, the more influential T_{mid} became on the number of effector TCs produced. The number of activated TCs increased with expansion, but correlated negatively with T_{mid} regardless of the maximal paracortical swelling (Figure 2.40A). A higher value of T_{mid} delayed volume expansion which suggested that early paracortical volume increase, that is facilitated by a low T_{mid} value and high V_{Max} value, aided activation.

No significant variation in the total number of effector TCs was observed in the simulations that used the two lower values of V_{Max}, (1.2 and 1.5) when T_{mid} was

varied. However at larger values V_{Max} =2.0 and 2.5, increasing T_{mid} from 10e4 to 13e4, led to a significant variation in effector TCs with 1.2x to 1.4x more effector TCs produced (Figure 2.40B,C,D). This suggested that delayed expansion at larger V_{Max} values may have aided effector TC production. Correlation was only significant at V_{Max}=2.5 (p=3.3e-04).

The corresponding changes in helper TCs and cytotoxic TCs that make up the effector TCs were then analysed, showing different dependencies on Tmid. It was concluded that the observed change in effector TC number at different T_{Mid} values was mainly due to the cognate $CD8^+$ TC response as they showed the same pattern of change (Figure 2.40C,G). At V_{Max} =2.5 the value of T_{Mid} correlated positively with the number of cognate $CD8^+$ TCs that exited paracortex (p=0.0129).

Overall, the number of cognate CD4+ TCs increased when V_{max} was increased from 1.2 to 2.5 regardless of the value of T_{mid}. However, at V_{Max} and V_{Max} =1 or 1.5, the larger the value of T_{Mid}, the less $CD4^+$ TCs exited the paracortex, although the negative correlation was not quite significant (V_{max}=1,(p=0.08, V_{max}=1.5,(p=0.051) (Figure 2.40J).

In summary, when there was little overall paracortical expansion (V_{Max} =1.2/1.5), increased earlier expansion aided $CD4^+$ production, but did not at V_{Max} =2 or 2.5 ,where expansion may not be a limiting factor. The opposite behaviour of $CD4^+$ to $CD8^+$ TCs, could be related to the earlier response of $CD4^+$TCs.

The effect of T_{Mid} on TC and DC interactions was then investigated. There was no clear relationship between TCs contacted by DCs and the value of T_{Mid} at values of V_{Max} =1.2 or 1.5 or 2.0 (Figure 2.40F,G). At V_{Max} = 2,5, the larger the value of T_{mid}, the more cognate TCs DCs contacted (Figure 2.40H), At Vmax = 2, the relationship between cognate TCs contacted and overall cognate TCs contacted was unclear but T showed a linear positive correlation effector TCs produced, $CD8^+$ TCs produced (p=0.03) and $CD8^+$ exited (p=0.027) (Appendix Figure A.4A). At lower values of V_{Max}, no correlation was found between cognate TC contact and effector TC production. This is consistent with the earlier results (Figure 2.38) that at larger paracortical expansions, the number of TCs contacted became more important.

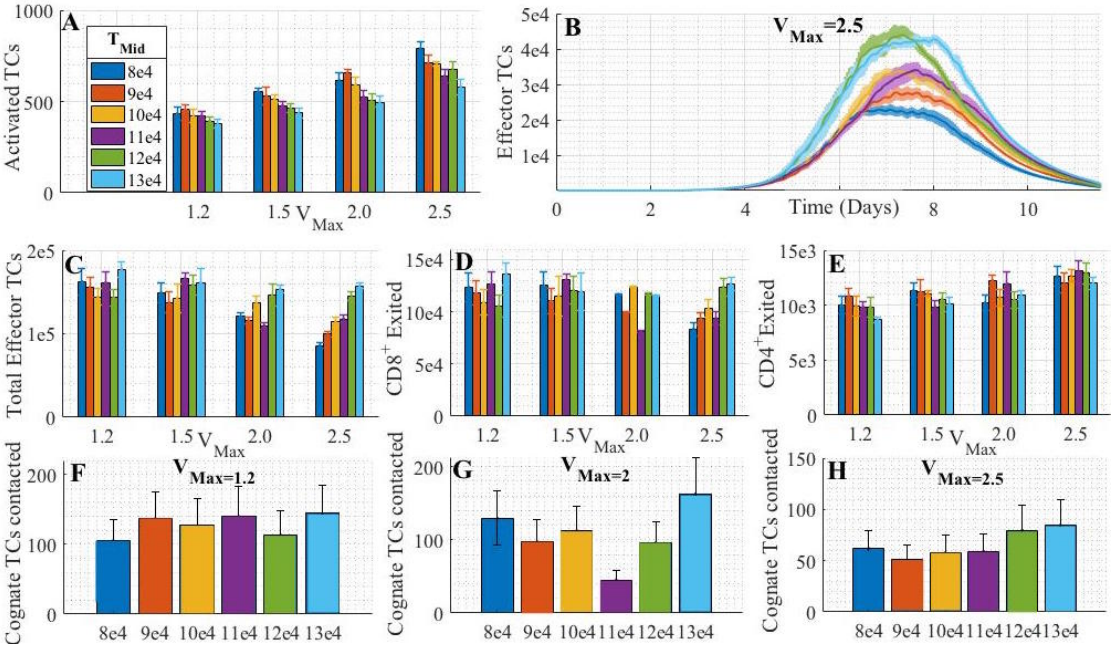

FIGURE 2.40: Further simulations showed that T_{mid} became more influential at higher values of V_{Max}. (n=8). A. The number of activated TCs increased with increasing V_{Max} but negatively correlated with T_{mid} at every value of V_{Max} (pearson's correlation, V_{Max}=1.2, p=0.018, 1.5 p=1.5e-05, 2.0 p=0.01, 2.5 p=0.01). B. At V_{Max}=2.5, the higher T_{mid}, the more effector TCs were produced.C. At V_{Max}=2.5, the value of T_{mid} correlated with number of effector TCs (r=0.99, p=3.3e- 04) but there was no significant variance at V_{Max}=1.5 or 1.2. C. The total number of effector TCs decreased with increasing V_{Max} only when T_{mid} was <12e5. D. The no. of $CD8^+$ TCs that exited the paracortex showed significant variation at V_{Max} = 2 and 2.5 (p=0.02,p=1.9e-04) but not at V_{Max}=1.2 and 1.5. At V_{Max}=2.5 only, T_{mid} significantly positively correlated with the no.of $CD8^+$ TCs exited (r=0.9, p=0.01). The no. of $CD4^+$ TCs that exited the paracortex increased as V_{Max} increased. In addition, $CD4^+$ TCs negatively correlated with T_{mid} at V_{Max}=1.2 (ρ=-0.76 p=0.08) and 1.5 (ρ=-0.8, p=0.05). F,G,H. At V_{Max} =2.5, the higher the value of T_{mid}, the more cognate TCs were contacted. However,overall, at V_{Max}=2.5, less TCs were contacted than at V_{Max}= 1.2 or 2.

Factors that contribute to optimal paracortical expansion

After identifying that increased T_{mid} at higher values of V_{max} could aid the number of effector TCs that exited, the next goal was to investigate what features altered in the model that contributed to this effect. Simulations were carried out (n=8) with a higher T_{mid} value compared to baseline over a wider range of V_{Max}. Using the higher value of T_{mid}=12e4 the optimal maximal paracortical expansion for effector TC production was V_{Max}=1.8 (Figure 2.41A), which contrasted to the value of V_{Max} =1 at T_{mid}=10e4. At V_{Max}=1.8, activation was increased by 40% which was much less than the 120% increase at V_{Max}=2.6. Simulations using V_{Max}=1.8 resulted in the highest total number of cognate $CD8^+$ TCs but unlike when T_{mid}=10e4 (Figure 2.35), increasing V_{Max} did not decrease the number of cognate $CD8^+$TCs and the number of $CD4^+$ TCs positively correlated with V_{max} (p=0.002).

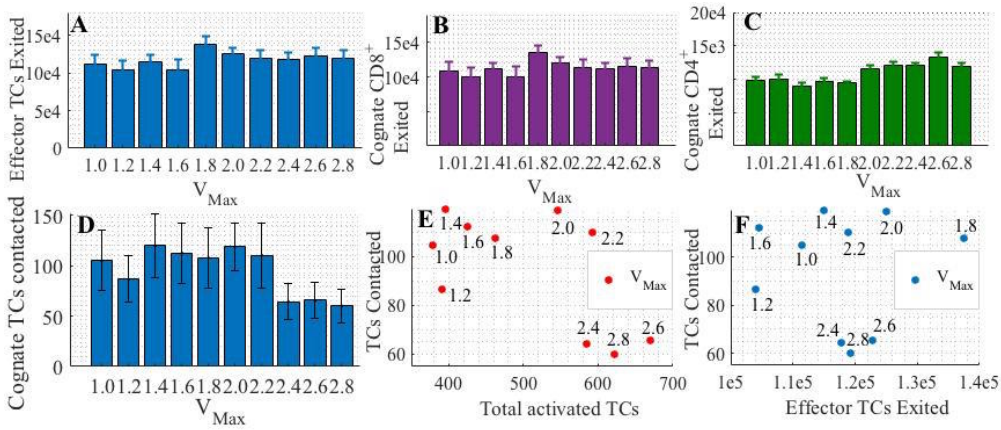

FIGURE 2.41: Increasing T_{mid} to 12e4 changes optimal swelling from 1 to 1·8-fold. A. The number of total effector TCs did not decrease with V_{Max}, as it did when T_{mid}=10e4. B.The number of Cognate $CD8^+$ TCs that exited the paracortex peaked at V_{Max}=1.8. B. The no. of cognate $CD4^+$ TCs that exited the paracortex positively correlated with V_{max} (pearson's ρ =0.84 p= 0.002). D. The mean number of cognate TCs contacted by agDCs decreased only from V_{Max}>=2.2. E. Activated TCs compared to TCs contacted showed no clear relationship between TCs contacted and activation. F. The Effector TCs exited also showed no clear relationship with TCs contacted.

The number of TCs contacted and number of activated TCs produced at different values of V_{max} did not show any correlation (p=0.06) (Figure 2.41E), unlike at lower value of T_{mid}=10e4. The number of cognate TCs contacted and the number of effector TCs exited at different values of V_{Max} also showed no correlation (Figure 2.41D,F) but the most effector TCs exited at a value of V_{Max}=1.8. When the mean number of TCs contacted by DCs was compared in simulations using

a range of V_{Max} values, the number contacted at V_{Max}=1.8 was in the upper half of the range of values.

Taken together, this information implied firstly that the optimal V_{Max} resulted in a balance between increased activation, increased numbers of $CD4^+$ TCs and the negative impact on numbers of $CD8^+$ as the value of V_{max} increased. The reason for this remained unclear, as although increasing the midpoint of the sigmoidal volume expansion curve helped to increase the TCs contacted at values of V_{Max} >1, there was not a linear relationship between TCs contacted and effector TCs produced, suggesting other factors were important.

Parcortical swelling and T cell egress

Other factors that were considered as potential contributors to variation in TC response as the paracortex swelled included those related to accompanying changes in TC entry and exit rate, and TC crowding. As it is unclear how areas in the paracortex change with expansion, the defined areas (such as entry and exit areas) initially varied by altering their radius as a fixed percentage of the outer radius (expansion method 1, see 2.2.3). To investigate whether the way the areas altered may impact response, a second paracortical expansion method (EM2) was applied where change in HEV area and remaining non-exit areas was set proportional to overall change in paracortex volume. Consequently, the most effector TCs were produced at V_{Max} =1.4 instead of V_{Max} =1. For all values of V_{Max} >1.2, effector TCs production increased slightly but only significantly at V_{Max} =1.4 and 2.2 (2.42A). TC entry and egress remained similar, but TC egress patterns occurred 3 hours later using EM2. (2.42B,C).

A second modelling feature to consider was the way in which TC density in the paracortex altered, measured as a ratio of TCs to total grid compartments present in the paracortex. The limit of the ratio is defined by the crowding parameter γ=2 at baseline, but TCs move preferentially to empty grid compartments. When the paracortical volume was fixed, the TC to grid ratio rose to 2 instead of fluctuating between 0.6 and 1.3, which occurred when the paracortex volume varied. This represented non-physiological crowding as the grid-compartment is a cube of $6\mu m^3$ and the TC is modelled as a sphere of radius of $3\mu m$, occupying 57% of a compartment. A compartment should, on average, hold a maximum of 1.75 TCs per grid. Simulations were then run with the addition of rules that increased TC egress likelihood if more than one TC occupied a compartment (Expansion Method 3). This did not significantly alter the results, with a similar high ratio of TC to grid compartments observed

when the paracortex volume remained fixed(2.42E,D). This was potentially because the probability increase for exit grid compartments containing two TCs was insufficient.

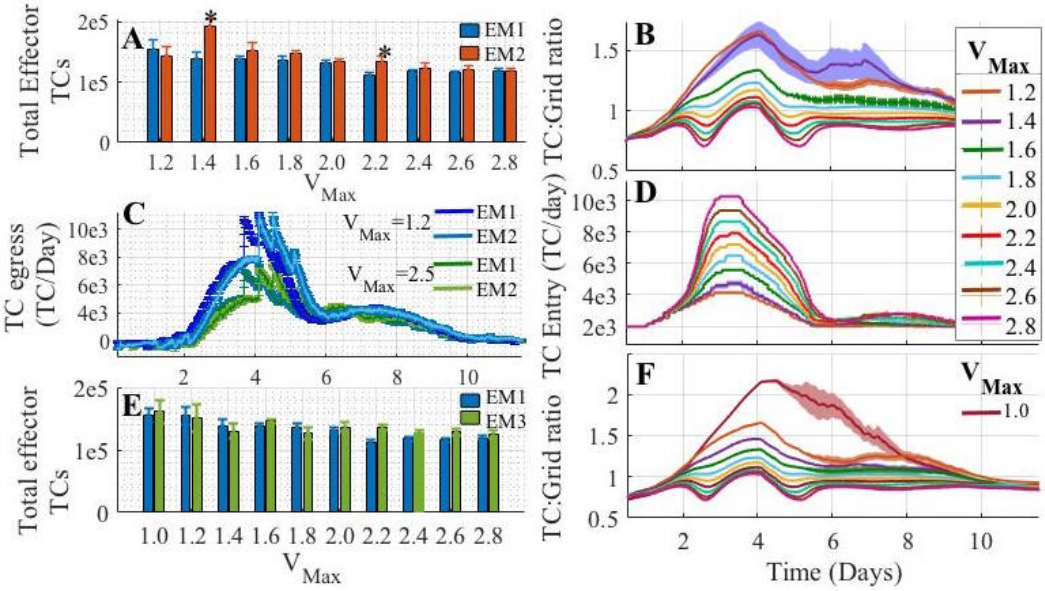

FIGURE 2.42: variation of underlying model rules regarding egress and expansion. The effects of an alternative expansion method (EM2) where areas expanded relative to overall para-cortical volume instead of to para-cortical radius (Expansion Method 1 (EM1)).A. Comparison of effector TCs produced with,(EM1)) and (EM2) showed that slightly more effector TCs were produced with EM2 at values of V_{max} >1.2 but this was only significant in two cases. B. Resulting TC to grid compartment ratio with EM2 showed that the highest TC:grid ratio occurred at V_{max}=1.4, the same value at which most effector TCs were produced. C.Comparison of TC egress rates using EM1 and EM2 showed a 3 hour delay with EM2 but an overall similar pattern. D. Changes in TC entry rate with EM2 which were similar to with EM1 (Appendix A.1). E. Comparison of effector TC response when increased egress with crowding was applied (Expansion Method 3(EM3)), showing no significant difference. F. TC to grid ratio with EM3 showed increased TC crowding at V_{Max} =1.

Modulating effector T cell S1P1 receptor expression

A further factor that could influence the way paracortical swelling affects TC response is the degree to which responding cognate TCs are selectively retained in the paracortex via chemotactic attraction or prevention of egress through down-regulation of the sphingosine-1-phosphate receptor ($S1P_1r$). Due to its important role in allowing TCs to exit the LN, $S1P_1r$ has already been identified as a therapeutic target to modulate the immune response and several murine experiments show the results of non-selective $S1P_1r$ modulation on TC responses. One set of such experiments were replicated as part of the model validations (see 2.3.6).

TC populations that have been activated and undergone several rounds of proliferation, express slightly different markers to activated TCs that have not yet differentiated, providing a means to separate the activated and effector TC populations (2.1.2). $S1P_1r$ expression has been linked to the number of proliferations a TC has undertaken and the value of SP_{Early} represents the relative expression of $S1P_1r$ on newly differentiated effector TCs that have undergone 4-6 proliferations, set at a value of 0.8 ($S1P_1r$ on naive TCs was designated as 1.0) (Methods 2.2.2). During the following simulations, the value of SP_{Early} was varied between 0.05 and 1.2, representing selective $S1P_1r$ down-regulation and over-expression on this sub-population of effector TCs. This was repeated using different values of V_{max}.

Specific down-regulation of $S1P_1r$ on early effector TCs helped to increase the number of effector TCs in situations where $V_{Max} > 1$ resulted in less effector TC production. At all values of V_{max}, SP_{Early} <0.8 allowed a sustained increase in total TCs in the paracortex, despite acting on only the small subset of TCs that were early effector TCs (Figure 2.43A). The value of SP_{Early} did not significantly impact the activation response at any value of V_{max} (ANOVA, V_{max}=1.2, p=0.95, 1.5 p=0.68, 2.0 p=0.85) but increased V_{max} did aid activation (Figure 2.43F). Down-regulation of $S1P_1r$ to 40% of that of naive TCs, doubled the number of effectors TCs produced, whilst SP_{early} =<0.1 increased the number of effector TCs 3 fold (Figure 2.43G). At the larger paracortical swellings of V_{max}=2 or 2.5, the most effector TCs were produced when SP_{early} was <0.05 but at a smaller swelling of V_{max} =1.2, no further benefit was observed with SP_{early} =<0.1.Overall, the most effector TCs were produced at the largest values of V_{max} values with the most $S1P_1r$-mediated retention (SP_{early}=0.05).

The number of both Helper $CD4^+$ TCs and cytotoxic $CD8^+$effector TCs that exited the paracortex by day 10 increased 3-4 fold with SP_{early} =< 0.1. When

the paracortex only underwent a small swelling (V_{max} <1.2), no further increase in $CD8^+$ TCs exited was observed when SP_{early} was decreased from 0.1 to 0.05 (Figure 2.43H,I).

The mean number of TCs contacted by DCs increased up to 3x more when SP_{early} was decreased from 0.8 to 0.1 at all values of V_{max} (Figure 2.43J). Decreasing SP_{early} further to SP_{early}=0.05 only increased the mean number of TCs contacted at V_{max}=2. However, overall, when SP_{early} was >=0.1, the same or more effector TCs were still produced at larger values of V_{max},2.0 and 2.5 even though less cognate TCs were contacted by DCs. Therefore, although reduced values SP_{early} resulted in more effector TC production, this was not due to increased DC contact alone.

Accompanying changes that occurred when SP_{early} was reduced, and therefore may have contributed to increase early-effector TC retention, included an overall increased TC egress rate that was sustained for 2 days longer than simulations at the baseline SP_{early} value. This was regardless of the maximal paracortical swelling (Figure 2.43B,D). TC egress rate at day 6 to 8 was similar at all values of V_{max} <, despite the 2x larger initial egress at V_{max} >1.2.

The TC to grid ratio increased as SP_{early} was decreased without reaching ratios representative of non-physiological crowding (Figure 2.43C,E). This again suggested that the retention of effector TCs could impact the overall TC transition, or that overall TC crowding impacted effector TC exit. Finally, TC to grid ratio was higher at lower values of V_{Max} and SP_{early} <0.1, but the combination did not produce the most effector TCs. This suggested that maintaining a high TC density alone did not produce the most effector TCs (Figure 2.43C).

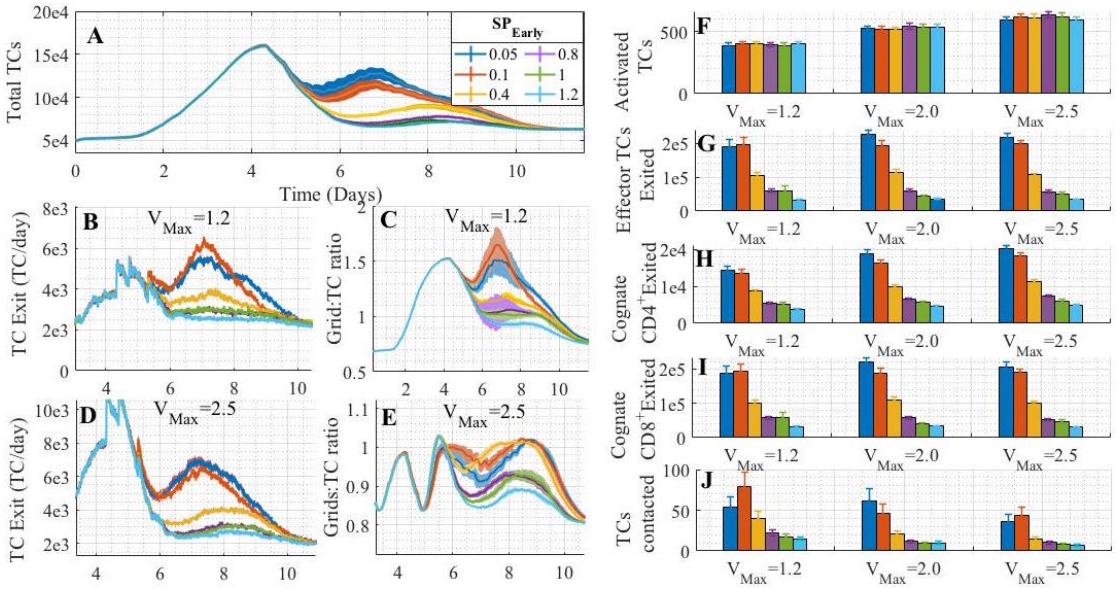

FIGURE 2.43: Varying SP_{early} and thus retention of newly differentiated TCs. A. Reducing SP_{early} resulted in a higher total number of TCs in the paracortex. B,D. At V_{max} =1.2, reducing SP_{early} to <0.1, despite retaining TCs, increased the peak TC egress rate beyond the peak rate at baseline SP_{early}. At V_{max} =2.5, reducing SP_{early} did not result in TC egress exceeding the peak rate at baseline SP_{early}. C. At V_{max} =1.2 and 2.5, the TC to grid ratio was increased in the second half of the simulation when SP_{early} was reduced. E. At the larger V_{max} =2.5, SP_{early} <0.4 maintained the peak TC to grid ratio for 4 days. The no of activated TCs increased as V_{max} was increased but did not vary with the value of SP_{early}. G. The number of Effector TCs that exited the paracortex was influenced more by SP_{early} than by V_{max}. The most effector TCs exited when SP_{early} was <=0.1 and when V_{max}=2. H. The largest number of $CD4^+$ TCs exited when SP_{early} was at the smallest value and V_{max} at the largest value. I The most $CD8^+$ TCs exited when SP_{early} was at the smallest value of 0.05 and an intermediate value of V_{max}=2.0. J. The mean no. of cognate TCs contacted decreased with more paracortical swelling (>V_{max}) but increased with smaller values of SP_{early}.

2.3.5 Global sensitivity analysis results

The ABM contained many parameters that were obtained directly from the literature, inferred from the literature or were estimated free parameters representative of unknown signalling pathways or mechanisms. It was important to check the sensitivity of the parameters to ensure that small variations in uncertain parameters that were not the focus of the study, did not affect the model output in such a way that would mask or prevent output changes due to other parameter alterations.

To reduce the number of samples required, parameter space was sampled using Latin Hypercube Sampling and monotonic relationships between parameter input and output of interest were quantified using partial rank correlation to consider linear effects of other parameters (Section 2.2.4, Figure2.10). The partial rank correlation coefficient (PRCC) value ranges between 1, a strong positive correlation, and -1, a strong negative correlation and a p-value of <0.05 was used to determine whether a parameter significantly affected the output of interest. A sensitivity analysis with 300 simulations was carried out with a fixed volume paracortex (V_{max}=1) and with a varying paracortex volume. The analysis was repeated 3 times in each case and the mean PRCC calculated between the output of interest and each parameter input at 1 day intervals (Methods 2.2.4).

Calculation of PRCC allowed a clearer assessment of the relationship between each parameter and the output, by accounting for variation due to other parameters, than when using Pearson's correlation or Spearman's ranked correlation. For example, correlation between Probability of Cognition (P_{cog}) and Fraction of DCs that enter (ΦDC), and output of interest, the number of activated TCs at 24hrs became clearer with each assessment (Figure 2.2.4). Each dot represents the results of one simulation. P_{cog} shows a clear positive correlation with activated TCs at day 1 in the pearson's correlation. The data was then ranked and Spearman's co-efficient displayed any correlation within ranked data (Figure 2.44 B). Correlation with ΦDC is less clear when visualising the raw and ranked data (Figure 2.44 D,E). PRCC applies a Pearson's correlation to the residuals of the linear regressions performed on the ranked input parameter versus other parameters, and the residuals of applying linear regression

to the ranked output versus ranked input parameter (Methods 2.2.4). Visualisation of the PRCC-transformed data shows that the correlation between P_{cog} and activated TCs at day is stronger (Figure 2.44 C),and the positive correlation between ϕ_{DC} and the activated TCs is much clearer (Figure 2.44 F). The results of the global sensitivity analysis are shown in Tables 2.5-2.10.

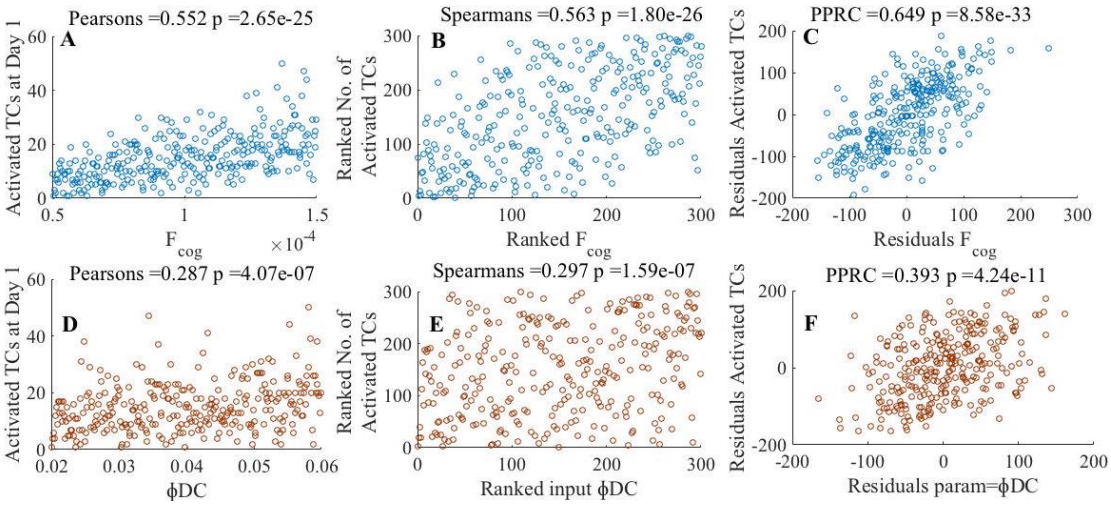

FIGURE 2.44: Sample sensitive parameter identification. For the no. of activated TCs at day 1 and Frequency of TC cognition parameter (F_{cog}): A. Raw data and resulting Pearson's correlation coefficient. B. Rank transformed data and resulting Spearman's coefficient C. Residuals of linear regression of ranked F_{cog} input versus other parameters and residuals of linear regression of ranked F_{cog} input values versus ranked output and resulting PPRC value. D,E,F as above with parameter ϕDC (fraction of DCs)

During the simulation, many significant parameters were influential at different time-points and some reversed how they impacted the output. The duration of DC influx, DC_{in}, negatively correlated with activated TCs produced in the first 3 days of the simulation but positively correlated with effector and memory TCs produced from day 4. The pattern was consistent in both non-expanding and expanding paracortexes. This behaviour is likely because a short influx, therefore a higher entry rate of DCs is likely to activate TCs quickly. For more effector TC production later in the response, a lower entry rate that is sustained for a longer period allows DCs to be present and able to continue to stimulate TCs later on in the response.

Several parameters were significant only in non-expanding paracortexs and related particularly to factors involved in TC proliferation and interaction. For example, the maximum TCs a DC could stimulate at once, Max_{Nt}, positively correlated with effector TCs produced at day 5. Other parameters showed positive correlation throughout the simulation in the fixed volume model, but in expanding models the positive correlation was lost by week 2. For example, P_{cog} positively correlated with effector TCs present only to day 8 and Φ DC correlated positively with the effector TCs to day 6 but negatively to effector TCs that exited from day 7.

Many significant parameters in the expanding paracortex showed the same pattern, such as initial MHCI/II expressed by DCs and the TC recruitment factor R_F. The parameter V_{max}, that determined maximal paracortical swelling, positively correlated to activated and effector TCs in the paracortex up to day 4 and 6 and to memory TCs at day 5. The reverse relationship occurred from day 6 for activated and effector TCs present and effector TCs exited and from day 7 for memory TCs present and exited.

An additional analysis was performed increasing the range of SP_{act} from a upper threshold of 0.4 to 0.8, meaning a greater proportion of simulations were run with less $S1P_1r$ down-regulation. This resulted in the removal of positive correlation of V_{max} and effector TCs, and emergence of negative correlation increasing T_{mid}, suggesting that V_{max}, can mask the effects of SP_{act} or vice versa. The relationship between V_{max}, and SP_{act} was investigated in more detail in later (Section 2.2.3).

A key point to take from the sensitivity analysis is that several factors that showed positive correlation in fixed volume models only display positive correlation in expanding models in the first week of the simulation. Parameters exhibiting this behaviour tended to be parameters that would logically drive TC proliferations. The reversal in the positive effect of several parameters on effector TC production throughout the simulation time-frame highlights the need for differential regulation and control at different time points within the TC response. The most influential parameters were those related to $S1P_1$ regulation of activated, early effector TCs and memory TCs (SP_{act}, SP_{early}, SP_{mem}), parameters relating to signal shape (Φ_{DC}, T_{DCin}), TC cognition (P_{cog}), TC recrutintemnt (R_f, RT2) and parameters maximal volume and midpoint of the expansion curve.

TABLE 2.5: Parameters that significantly affected number of activated TCs. Present in the paracortex from day 2 to 6 post-stimuli, in a fixed volume and an expanding paracortex.

	With Swelling					Without Swelling				
Parameter	Day 2	Day 3	Day 4	Day 5	Day 6	Day 2	Day 3	Day 4	Day 5	Day 6
Max_{NT}						+				
P_{cog}	+++	+++	+++	+++	++	+++	+++	+++	+++	++
ϕ_{DC}	+++	++	+++			+++	+++		++	++
T_{DCin}	−−−	−−−	++	+++	+++	−−−	−−	+	+++	+++
R_F		+++	+++		−		++	++		
V_{Max}	+	+++	+++		−	N/A	N/A	N/A	N/A	N/A

TABLE 2.6: Parameters that significantly affected the number of activated TCs after increasing SP_{act}. Simulated in an expanding paracortex from day 2 to 6 post-stimuli. V_{Max} no longer appeared significant and instead the smaller the value of SP_{act} became significant. The parameters involved in TC recruitment, R_F and RT2, while still important, were less significant.

	With Swelling				
Parameter	Day 2	Day 3	Day 4	Day 5	Day 6
Max_{NT}					
P_{cog}	+++	+++	+++	+++	++
ϕ_{DC}	+++		++	++	
T_{DCin}	−−−	−−	+	+++	+++
$S1P_1r_{act}$	−−				
$S1P_1r_{mem}$				−	
$RT2$		+	+		
R_F		++	+	+	
T_{mid}				−	

TABLE 2.7: Parameters that significantly affected the number of effector TCs. Effector TCs in the paracortex from day 3 to 12 post stimuli. There is a greater correlation between maximum CD8$^+$ TCs proliferation and effector TCs produced in the expanding paracortex than the fixed volume paracortex. In an expanding paracortex there is also negative correlation with TC recruitment, and maximum paracortical swelling in the second week of the simulation.

Parameter	Day 3	Day 4	Day 5	Day 6	Day 7	Day 8	Day 9	Day 10	Day 11	Day 12
					Without Swelling					
Max_{P4+}							+		+	+
T_{short}					+					
Max_{NT}			+							
MHC_i					+					
P_{cog}	+++	+++	+++	+++	+++	++	++			
ϕ_{DC}	+++	+++	+++	+++	++					
T_{DCin}	−−−	−−−	−−							
$S1P_1r_{early}$		−								
					With Swelling					
Max_{P8+}					+	++	++	+++	++	+
Max_{P4+}				+						
T_{NC}									+	+
T_{short}	+									
MHC_i										−
P_{cog}	+++	+++	+++	+++						
ϕ_{DC}	+++	+++	+						−	−
T_{DCin}	−−−	−−−	−−−	−−						
$S1P_1r_{early}$		−								
R_F						−	−−	−−	−−	−−
V_{Max}		++		+	−−−	−−−	−−−	−−−		

0.05> p >0.001 = +/- 0.001> p >10^{-6}= ++/- - 10e^{-6} > p >0 = +++/- - -

TABLE 2.8: Parameters that significantly affected the number of effector TCs that exited the paracortex. Fom day 3 to 12 post stimuli. In week 2 post stimuli many of the parameters in the expanding model negatively correlated with the number of effector TCs that exited the LN, despite some of these showing either consistent positive affects, or unidentified in the fixed model.

Parameter	Day 3	Day 4	Day 5	Day 6	Day 7	Day 8	Day 9	Day 10	Day 11	Day 12
					Without Swelling					
TP_{4+}						+	+			
Max_{P8+}					+	+				
γ				−	−−	−−	−	−	−	−
P_{cog}	+++	+++	+++	+++	+++	+++	++	++	++	++
ϕ_{DC}		+								
T_{DCin}		−−−	−−−	−−						
$S1P_1r_{early}$	+++	+++			+	−	−−	−−	−−	−
V_{Max}	N/A	N/A	N/A	N/A	N/A	N/A	N/A	N/A	N/A	N/A
T_{Mid}	N/A	N/A	N/A	N/A	N/A	N/A	N/A	N/A	N/A	N/A
					With Swelling					
TP_{4+}										
Max_{P8+}						−−	−−	−−	−	
γ			−	−	−					
HMC_i							−−	−−	−	−
P_{cog}	+++	+++	+++	+++	+					
ϕ_{DC}	+				−−	−−	−−	−−	−−	−−
T_{DCin}	−−−	−−−	−−	−						
$S1P_1r_{early}$	+++									
$S1P_1r_{mem}$					−					
R_F					−−	−−	−−	−−	−−	−−
V_{Max}	−−			−−	−−−	−−−	−−−	−−−		
T_{Mid}	−−									

$0.05 > p > 0.001$ = +/- $0.001 > p > 10^{-6}$= ++/- - $10e^{-6} > p > 0$ = +++/- - -

TABLE 2.9: Parameters that significantly affected memory TCs number in the paracortex. Data is only shown from day 5 to 12 post-stimuli, as they are not produced in the first few days. At day 5, V_{Max} still shows some positive correlation with memory TCs present but 7 shows a negative correlation.

	Without Swelling				With Swelling			
Parameter	Day 5	Day 7	Day 9	Day 12	Day 5	Day 7	Day 9	Day 12
Max_{P8+}						++	+++	+
$diff_{late}$	+++	+++	++	++	+++	++		+
γ			−		−			
P_{cog}	+++	+++	+		+++			−
ϕ_{DC}	++	++						−
T_{DCin}	−−−	−−			−−−	−−		
R_F						−−	−−	−−
V_{Max}	N/A	N/A	N/A	N/A	+	−	−−−	−−−
T_{mid}		N/A	N/A	N/A	−			

0.05> p >0.001 = +/- 0.001> p >10^{-6}= ++/- - $10e^{-6}$ > p >0 = +++/- - -

TABLE 2.10: Parameters that significantly affected the number of memory TCs exited in the paracortex. From day 5 to day 12 post stimuli.

	Without Swelling				With Swelling			
Parameter	Day 5	Day 7	Day 9	Day 12	Day 5	Day 7	Day 9	Day 12
TP_{4+}			+			+	+	
Max_{P8+}						−	−−−	−−
dif_{early}	++				++			
dif_{late}	+++	+++	+++	+++	+++	+	++	+
T_{NC}								+
K_S	+							
γ	−−−	−−	−		−−	−−		
MHC_i							−	−
P_{cog}	+++	+++	++	++	+++			
ϕ_{DC}						−−	−−	−−
T_{DCin}	−−−	−−			−−−			
$S1P_1r_{early}$	−−				−−−	−		
R_F						−	−−	−−
V_{Max}	N/A	N/A	N/A	$(N/A$		−−−	−−−	−−−

0.05> p >0.001 = +/- 0.001> p >10^{-6}= ++/- - $10e^{-6}$ > p >0 = +++/- - -

2.3.6 Validation

To validate the model, a series of simulations were carried out that replicated a range of experiments performed *in-vivo* that were not used as input-parameter sources. The results of the *in-silico* and *in-vivo* experiments were then compared and the model could accurately recapitulate scenarios that deviated from the designated baseline immune response.

Varying the initial proportion of cognate T cells

The first comparison involved varying the proportion of cognate TCs to the stimuli in the naive TC population (P_{cog}). This has been achieved *in-vivo* by adding a specific amount of cognate TCs carrying specific receptors to a particular stimuli into a naive TC population. The stimuli that the cognate TCs recognised was then applied and the TC proliferative response recorded [206, 216]. The results in several experiments in mice showed that the number of effector TCs produced directly relates to the starting proportion of cognate TCs within a population, with both $CD4^+$ and $CD8^+$ TCs [40].
Figure 2.45A shows the results experiments by Moon *et al* 2007 where the number of cognate TCs in a naive TC population, harvested from LNs and spleen, was known to vary [216]. The starting proportion of cognate $CD4^+$ TCs for each antigen was estimated, the 3 different antigen applied and the resulting number of $CD4^+$ TCs recorded. Figure 2.45C shows the results of a study by Obar *et al* 2008, quantified the initial proportion of cognate $CD8^+$ TCs for different types of antigen stimuli in a naive TC murine LN sample. Mice were injected with the 3 types of antigen and the $CD8^+$ response was shown to correlate to the initial cognate TC frequency [206].

Simulations were carried out using the same starting proportion of cognate TCs (estimated from the published data). When replicating the experiments by Moon *et al* 2007, the overall number of $CD4^+$ TCs overall increased when P_{cog} was increased from 1.4e-6 to 1.18e-5, but reduced in number in the intermediate value (Figure 2.45B). Further simulations were carried out which confirmed that the number of cognate $CD4^+$ TCs increased with P_{cog} in a linear manner (Figure 2.45F). This is also consistent with previous *in-silico* simulations [205]. The procedure was repeated to replicate the study by Obar *et al*

2008. This showed that the proportional increase in $CD8^+$ TCs produced when P_{cog} was increased from 7e-5 to 13e-5 was similar in both *in-vivo* and *in-silico* experiments (56% vs 62%). Simulations over a wider range of P_{cog} values confirmed that the number of cognate TCs produced increased with P_{cog}, which is consistent with the literature reports [40].

The simulation results are in line with the results *in-vivo* with the starting proportion of cognate TCs determining the overall number of cognate TCs produced (Figure2.45D,E). The size of the cognate $CD8^+$ and $CD4^+$ response ,the summation of activated, effector and memory $CD4^+/CD8^+$ TCs produced, showed the same trend of decreasing as the starting cognate frequency became smaller.

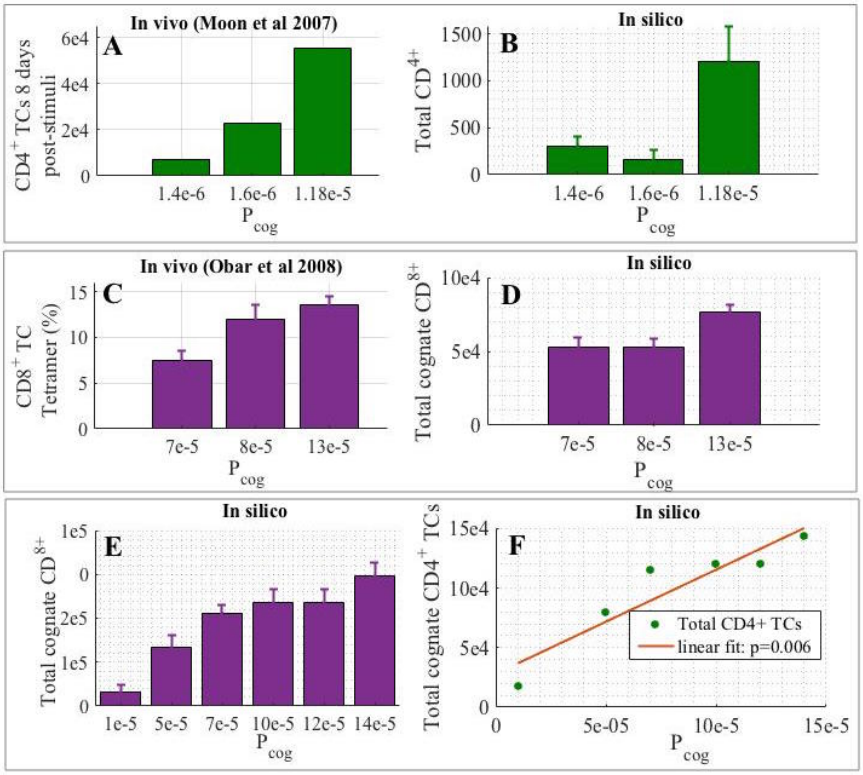

FIGURE 2.45: TC responses *in-silico* and *in-vivo* when proportion of cognate TCs was varied.A. $CD4^+$ magnitude of response in dLNs of mice to injected antigen correlated to starting estimated frequency of cognate TCs in a sample of $1x10^7$ TCs). Adapted from Moon et al 2007 [216].B. The corresponding results *in-silico* showed an overall increase in response with increasing P_{cog} (n=8). Simulations using a wider range of P_{cog} values (E,F) confirmed that number of total cognate $CD4^+$ TCs and $CD8^+$ TCs increased linearly with P_{cog} (A.8). C. Mice were infected with VSV-M45 or VSV-ova with starting precursor CD8+ frequencies of 7e-5,8e-5 and 13e-5 respectively. The peak number of resulting TCs as a percent of overall $CD8^+$TCs present is shown. Adapted from Obar *et al* 2008 [206]. D. Simulations using the same value of P_{cog} *in-silico* showed a similar increasing trend at a similar rate of increase.

Varying the stimuli strength

To further validate the model, comparisons were made to the results of experiments carried out in mice where the strength of stimuli was varied by altering the antigen dose (Figure 2.46A-D). In the model, the number of agDCs that enter the paracortex, and therefore the strength of stimuli (Φ_{DC}), was determined as a fraction of the overall initial number of TCs present . Simulations (n=8) were carried out decreasing the value of ΦDC incrementally from 0.04 to 0.0015. The resulting number of agDCs to enter over 60hours ranged from 2200 to 77.

As the number of DCs that entered was reduced, the number of total effector $CD4^+$ TCs present and the number of total effector TCs also decreased. 2.46E-H). Injection of decreasing doses of antigenic agent to mice resulted in the same decrease in $CD8^+$ proliferation *in-vivo*, as did the application of a number of DCs to $CD8^+$ TCs in cell culture 2.46B). Furthermore, an exponential increase in $CD8^+$ TC response to the number of DCs applied was observed both *in-vivo* and *in-silico* (Figure 2.46D,G). This effect has also previously been noted during a computational study [205]. Another *in-vivo* study by Martin-Fontecha *et al* 2003, showed that size of the proliferative response and the total number of cells in the LN also correlated to the strength of the in initial stimuli [217]. The number of DCs injected showed variation in the efficiency of recruitment to the LN therefore ϕ_{DC} was not calculated. The overall trend, however, was also an exponential increase with stimuli.

Additionally, $CD8^+$ TCs that were sufficiently stimulated continued to divide extensively, showing a propensity towards and all or nothing response[134]. Comparison of the individual simulations at ϕ = 0.0015 showed that in all simulations the $CD4^+$ TCs undergo a similar reduced response compared to at ϕ = 0.02 (Appendix A.7), whereas the $CD8^+$ TCs showed a significant response in some simulations, or little response in others 2.46E. This is in line with the capabilities of $CD8^+$ for sustained proliferation without sustained stimuli if a threshold level of stimuli is met [206]. At the smallest value of Φ (equivalent to 152 DCs in a whole paracortex), some response remained. This is inline with a model developed by Celli *et al* 2012, that predicted a threshold of 85 agDCs for eliciting a TC response in mice and human LNs [181].

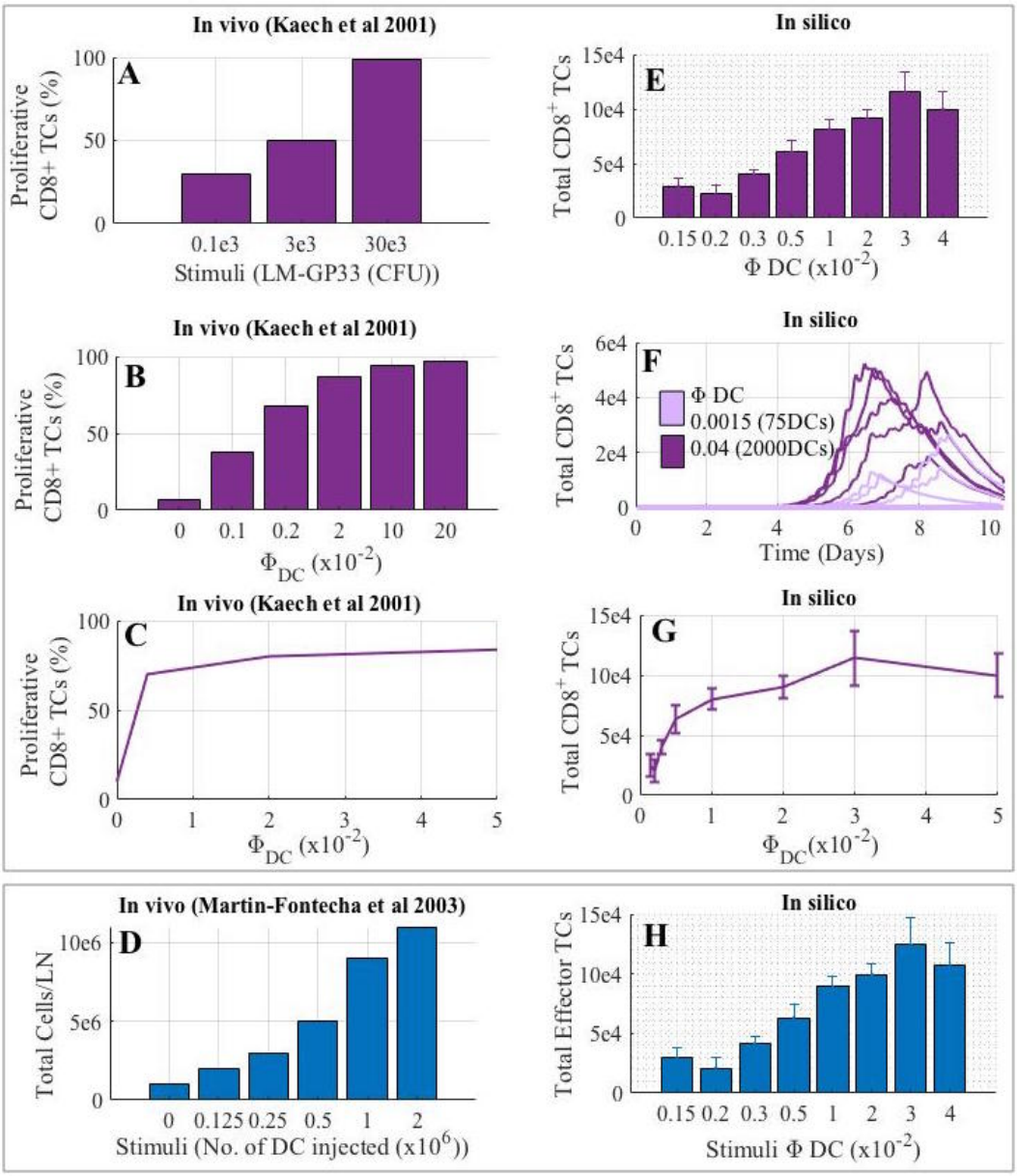

FIGURE 2.46: TC responses *in-silico* and *in-vivo* when the DC stimuli is varied. The no. of DCs that enter is calculated as a fraction of initial TCs present Φ_{DC}. A. The estimated % of TCs that had proliferated by day 7 in the LNs of chimeric mice and injected with doses of antigen LM-GP33. C.E, DCs were applied to cell culture (50000 $CD8^+$ TCs) and proliferative response recorded. A,C,E were adapted from Kaech *et al* 2001 [134].C. Increasing numbers of mature DCs were injected into mice hind-pads and total cell counts of the draining LN were recorded. Adapted from Martín-Fontecha *et al* 2003 [217]. B The mean no. of total $CD8^+$ TCs present in the paracortex increased with (Φ DC). D. The individual $CD8^+$ response at ϕ =0.04 and ϕ =0.0015 showed that with less DCs, some $CD8^+$ TCs respond and proliferate profusely, whereas others show no response. F. The total no. of $CD8^+$ TCs showed an exponential increase with ϕ_{DC} as did the no. of effector TCs (H).

Curtailing the stimuli duration

Studies investigating the duration of exposure to stimuli and optimal CD8$^+$ TC response have differed in their conclusion of how long CD8 TCs must be exposed to a stimuli for in order to reach a peak response (see Methods2.2.5). Overall, CD8$^+$ TCs are thought be able to sustain proliferation once a minimum threshold is reached whilst CD4$^+$ TCs show a greater dependence on sustained stimulation, with a few studies citing an initial stimuli requirement only [233, 234].

A study by Prlic *et al* 2006 was selected as a relevant comparison. This was because DCs that expressed a GFP-diphtheria toxin receptor transgene (DTRtg) were eliminated whilst in the LN by injected DT, that removed virtually all DTR-tg DCs within 12hours. This meant that only DCs that entered as migrating agDCs were affected. This also maintained the presence of previously induced inflammatory factors, in contrast to experiments where TCs are moved to new non-inflammatory environements [118]. This is better suited to replication in the ABM model as only one parameter alteration, agDCs present, is directly altered. Injection of DT at 1 hour resulted in a 93% reduction in CD8+ TC magnitude and at 12 hours led to a 85% reduction.

In the model the agDC stimulus was applied but DCs that had entered were removed at 12-14 hours instead of continuing to enter over 60 hours (Figure2.47D).The overall magnitude of the CD8$^+$ response in the control simulation, as a percent of the total TCs present, was similar to the *in-vivo* results (2.4% versus 2.1% respectively. The overall the cognate CD8$^+$ TC response was diminished by 91%, with individual simulations showing that in some simulations, CD8$^+$ TCs did not proliferate at all. and in some, a delayed proliferative response was observed Figure2.47B,C). The results of the model initially seemed to show a higher reduction in CD8$^+$ TCs (91%) by removing DCs at 12 hours than in vivo (85%) in the experiment by Prlic *et al* 2006. In addition, the 1 hour *in-vivo* inhibition may match the model results more closely because after application of DT, although most DCs were removed within 6 hours, 12 hours were required to eliminate virtually all the DC. Therefore a small number of DCs remained for the TCs to maintain interact with.

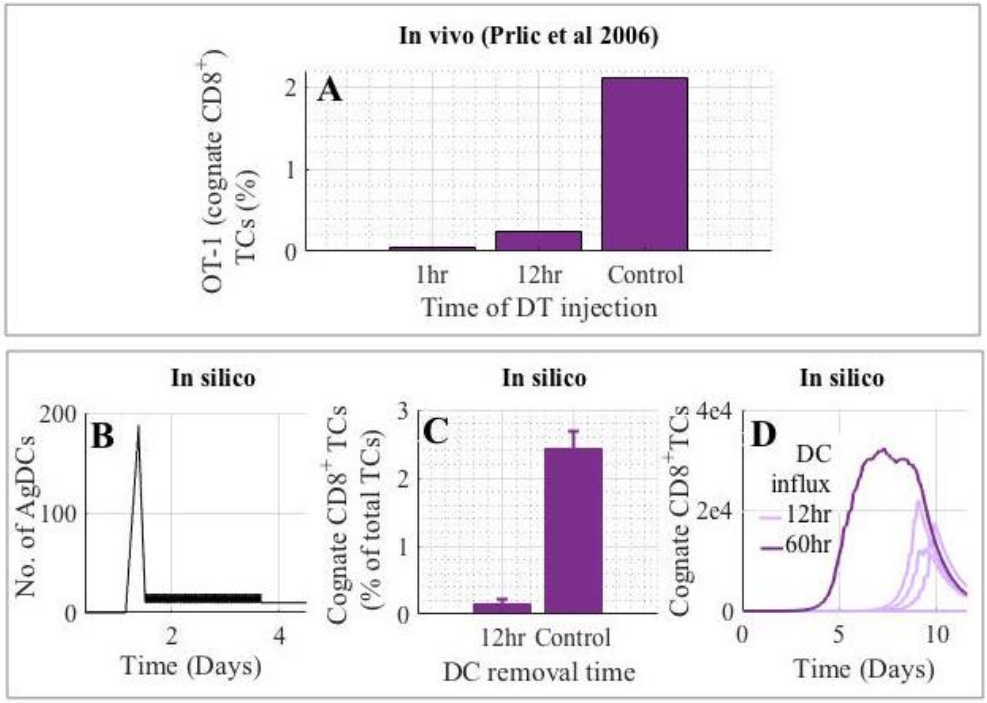

FIGURE 2.47: TC responses *in-silico* and *in-vivo* when a stimuli is abruptly abolished. A. Transgenic Rats were used that would eliminate specific injected agDCs when the rat was injected with DT within 12 hours. The rats were injected with OT-1 CD8+ TCs specific for agDCs that were subsequently injected. DT was then injected 1h, 12 and 48hr(not-shown) later, curtailing the time that the agDCs would normally spend in the LN. Adapted from Prlic *et al* 2006 [118]. B. The disrupted stimuli achieved by curtailing the 60hr DC influx at 12+-2hr. C-D. The results of simulations (n=8). Mean (+-SEM) $CD8^+$ TCs were reduced 91% when the stimuli was curtailed at 12hrs compared to sustained entry for 60hrs. D.individual $CD8^+$ TC responses varied by a magnitude of 10 in an all or nothing response manner.

Removing S1P1r down-regulation on activated T cells

The modulation of $S1P_1r$ on both naïve and activated TCs has an important role in regulation in naïve TC trafficking, retention of activated TCs and subsequent impact on immune function (see Methods 2.2.5). $S1P_1r$ modulation is included in the baseline model, therefore the final validation simulation compared the modulation of S1P1 *in-silico* and *in-vivo*.

Several experiments have been performed *in-vivo* in mice to investigate changes in TC response when down-regulation of $S1P_1r$ is prevented. A study carried out by Lo *et al* 2005 investigated over-expression of $S1P_1r$ on transferred pre-activated TCs by using retroviral gene expression to prevent $S1P_1r$ down-regulation. After 15 hours, the number of transferred activated TCs that remained in the peripheral LNs (brachial and inguinal) was 90% less than the control mice undergoing normal $S1P_1r$ regulation, whose numbers increased due to activated TC proliferation (Figure 2.48B). This showed that without SP expression, activated TCs were not retained in the paracortex, therefore despite proliferative capability, numbers decreased [106].

A second study carried out by Graler et al 1997, used transgenic mice with constitutive expression of $S1P_1r$ showed a reduced number of initial TCs in the LN, but after accounting for this, following primary immunisation, there were 40% less activated TCs than in immunised control mice [218]. The proliferative $CD4^+$ and $CD8^+$ TC response was also decreased to 34% and 10% of that of the wildtype mice (diminished 66-90%) respectively (Figure 2.48D,E).

A scenario was modelled where $S1P_1r$ down-regulation as a result of antigenic stimuli was abrogated. The value of V_{max} was varied between 1.2,1.5 and 2 to see if the effects differed with paracortical expansion. The mean total number of activated TCs in the paracortex was reduced to 40%, 28, and 19% of the original response at V_{max} = 1.2,1.5 and 2 (Figure 2.48B).

Compared to the results of Lo *et al* 2004, the modelled disruption diminished the number of activated TCs to a similar degree, and more than the 40% reported by Graler *et al* 1997. However the 40% figure was calculated after accounting for a reduction in number of TCs that had homed to the LN *in-vivo*,

therefore absolute changes in number of TCs would have been larger. The total number of CD4$^+$ TCs were dimished 90-92% at the different values of V_{max} in the model compared to 66% recorded by Graler *in-vivo* (Figure 2.48D) and the number of CD8$^+$ TCs 75-83% versus 90%) (Figure 2.48D). As an additional observation, the cognate CD4$^+$ and CD8$^+$ TC response was affected more by removal of S1P$_1$r down-regulation than when V_{max} was varied (Figure 2.48D,E), as did the total TCs in the paracortex (Appendix Figure A.10).

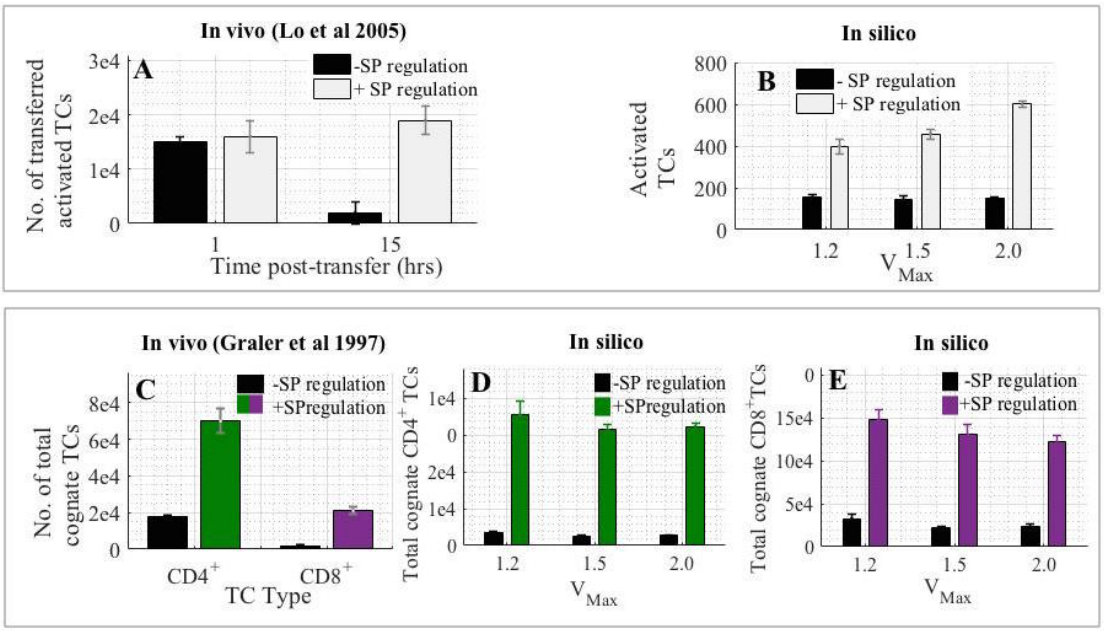

FIGURE 2.48: TC responses *in-silico* and *in-vivo* when S1P$_1$r down-regulation is inhibited. A. Pre-activated wildtype TCs (S1P$_1$r) and pre-activated TCs over-expressing S1P$_1$r (S1P1r++) were transferred into mice and further entry of TCs was blocked. 15hrs later there was a 90% reduction in retention of S1P1r++ activated TCs. Adapted from Lo et al 2005 [106]. B. Simulation results (n=10) where S1P$_1$r down-regulation was abbogarated (-SP regulation), compared to baseline simulations (+SP regulation). Mean (+-SEM) total number of activated TCs present was reduced 60%, 72% and 81% at V_{max} = 1.2,1.5 and 2. C. the proliferative CD4$^+$ and CD8$^+$ TC response of transgenic mice with constitutive S1P$_1$r expression produced was decreased to 10-34% of that of the wild-type mice. Adapted from Graler *et al* 1997 [218]. D. When TC S1P$_1$r down-regulation was abbogarated the mean (+-SEM) number of CD8$^+$ TCs, was diminished 75,85 and 82% at V_{Max}=1.2,1.5 and 2.0. E. CD4$^+$ TCs were affected similarly (diminished 90%-92%) at all values of V_{max}.

2.4 Discussion

The aim of the project was to build an ABM describing the TC response in the paracortex and carry out simulations varying aspects of LN swelling and effector response to gain a better insight into how LN swelling may impact effector TC response. The maximal paracortical swelling was varied, as well the point at which the swelling occurred relative to the number of TCs present, and features such as $S1P_1r$ expression were manipulated. The insight gained from these simulation results suggest that, although LN swelling may aid TC activation, avoidance of excessive LN swelling may be desirable to boost effector TC response in situations where the initial response is currently insufficient or small. For example, in patients with suppressed immune systems or when optimizing vaccine design to use low levels of antigen but maintain a sufficient effector response.

It was shown that changes in egress, and probable changes in access to egress areas that accompany LN expansion, could contibute to the detrimental effects of swelling. The requirement for more information regarding TC egress with swelling was highlighted as well as the impact that TC crowding could have on response. The effect of swelling on the efficiency of TC response was dependent on at what time point the swelling occurred, with differences in $CD4^+$ and $CD8^+$ TC response. The paracortical swelling that occurred earlier in the response, when less TCs were present could inhibit the number of $CD8^+$ effector TCs present and exited. However, if swelling occurred only when more TCs were present, at a later time-point when more proliferation had occurred, this aided efficiency of response. Simulations with more effective TC response were defined as those where more TCs exit the paracortex by day 10 but total effectors produced over the 10 days was also recorded and considered.

Retention of newly differentiated TCs via the modulation of the TC receptor sphingosine-1-phosphate-1-receptor ($S1P_1r$) was also investigated. Re-expression of $S1P_1r$ was permitted following two further proliferations. This showed that selective modulation on the small subset of effector TCs could strongly impact the efficiency of the TCs response and overcome loss in efficiency of TC response due to early enlargement. The drug fingolimod (FTY720), that causes blockade

of effect TC egress from the LN by maintaining $S1P_1r$ down-regulation of TCs, is currently used as a Multiple Sclerosis treatment, to prevent effector TCs crossing the blood brain barrier (rev. [235]). However temporary retention of effector TCs to boost subsequent effector TC production is a novel insight. In addition to highlighting the potential for temporary $S1P_1$ down-regulation as a mechanism to counteract suppressed effector production, this finding also emphasizes the influence that retentive features, including factors such as chemokines, may have on effector TC response. The insight provided by the model also highlights the benefit of *in-silico* experimentation as selective retention would be difficult to carry out *in-vivo*.

2.4.1 Retention of newly differentiated effector T cells, impacts the response more varying maximal swelling.

The maximal fold-change in paracortical volume was varied by varying the parameter V_{max}. Several other parameters were varied whilst also modulating maximal swelling to determine whether the effects on TCs observed were also co-dependent on paracortical swelling. The modulation of sphingosine-1-phosphate-1 receptor on TCs is known to play and important role in the TC trafficking, with expression required for TC exit (see 2.2.2). In-vivo, S1P1r is down-regulated on activated TCs and re-expressed after 4 proliferations, coincident with differentiation into effector TCs. In the model, newly differentiated effector cells are activated TCs that have undergone 4-6 proliferations, which are termed 'early effector' TCs. These express slightly less $S1P_1r$ than late effector TCs and are less likely to differentiate into memory TCs. The parameter SP_{early}, determines the relative expression of $S1P_1r$ on early effector TCs. To investigate the effect of extending the $S1P_1r$ downregulation, the $S1P_1r$ early expression was reduced from a 1.25-fold down-regulation to a 2.5-fold down-regulation. As a comparison, activated TCs down-regulate $S1P_1r$ 100-fold whilst $S1P_1r$ is fully expressed on TCs that have proliferated more than 6 times. This was repeated at different maximal-fold swellings (1.2x, 1.4x, 2.0x).

As a result of down-regulating SP_{early}, the number of TCs doubled or more than doubled at all values of maximal swelling (2.43). The increase in total effector TCs due to SP_{early} modulation was larger than any increase due to maximal

swelling, regardless of the value of SP_{early}. Decreasing SP_{early} 10-fold resulted in 4 times as many effector TCs. As effector TCs can proliferate up to 10 to 16 times ($CD4^+/CD8^+$), modulation of S1Pearly acted on a small subset of TCs (less than 1% of TCs present), midway through the response. Since a small change in retention had a strong impact on TC response, this suggested that the temporary retention of effector TCs should be further investigated.

Functionally, the SP_{early} value effectively represents all retentive influences induced by inflammation on the early effector TC. Values less than one reduce the likelihood that TCs will exit the LN. Although studies show re-expression of TC S1P1r after 4 proliferations, $S1P_1r$ was down-regulated 1.25-fold on early effector TCs. This was because other factors, such as chemokine expression, may still act to retain the TCs. In-vivo, TCs express CCR7 trans-membrane receptors. This helps to localise TCs under non-inflammatory conditions to the paracortex by allowing them to respond to gradients of chemokines, CCL19 and CCL20, that are secreted by stromal cells. Expression of CCR7 also promotes TC motility in the paracortex [236–238]. Inhibition of the TC expression of CCR7 under non-inflammatory conditions in-vivo resulted in faster TCs exit, while CCR7 over-expression slowed down TC egress [109]. In the first 24 hours after LN antigen entry, the baseline expression of CCl19 and CCL20 is upregulated, therefore contributing to TC retention [239]. The diffusion and duration of this increased expression, in addition to the increased concentration of the chemokines, is currently unknown. TC sensitivity to CCL21 and CCR7 expression also varies during the response and decreases after TCs have undergone four divisions [109]. However, only $S1P_1r$ regulation was selected for inclusion in-silico initially. This was because inhibition of both CCR7 and $S1P_1r$ expression in-vivo resulted in the movement of TCs to the edge of the paracortex, having lost the CCR7 retention. The TCs then remained in the paracortex as $S1P_1r$ expression was required to exit. Therefore, $S1P_1r$ expression appeared most important to include [116].

Now that the strong impact of selective retention on a small subset of effector TCs on the response has been identified, future work should focus on improving the modelling of factors that affect TC retention. This should include the previously overlooked chemotactic influence, in addition to refining the S1P1r

modulation.

2.4.2 Paracortical swelling results in more initial TC activation.

The sole effects of incrementally increasing maximal swelling on TC response were analysed using several outputs. This included the number of activated TCs produced and efficiency of TC response, but also information regarding TC and DC interactions, TC crowding in the LN as well as changes in recruitment and egress. The maximal fold swelling was incrementally increased from no-swelling to a 2.8x fold increase in volume. Over the initial 5 days of the simulation, the larger the maximal volume, the more TCs were activated (Figure 2.35A). However, the number of effector TCs that exited the paracortex by day 10 decreased (Figure 2.35A).

The difference in activation with larger paracortical maximal swelling could be partly due to accompanying increased TC recruitment. The recruitment rate increased as the paracortex volume increased (Figure 2.42D). This occurred because a component of the recruitment rate considers the increase in blood vessel surface area in the paracortex as the LN swells [165]. Therefore, the accompanying increased recruitment rate increased the absolute numbers of cognate TCs present. This effect was amplified when the cognate TCs were activated and proliferated. With larger swelling, the TC to grid compartment ratio decreased, allowing more space for TCs to move and access DCs (Figure 2.42D). However, the mean number of TC contacts that a DC made decreased with paracortical swelling 2.36. It is possible that although DCs made less contacts with TCs, they contacted a greater range of TCs, with less repeated contacts, due to greater freedom of movement. Regardless, the TC activation was un-constrained by DC and TC interaction during these simulations. Analysis of simulations using 95% less DCs did show some correlation between TC-DC contact and the number of activated cells (Figure A.6, suggesting DC contact becomes a limiting factor when there are significantly fewer TCs.

The TC egress rate also increased with swelling, and therefore the overall TC trafficking rate was increased. Activated TCs were retained due to S1P1r down-regulation, making the LN a more efficient filter for activated TCs. The extra

space could also allow easier activated TCs movement away from exit compartments. In addition, when S1P1r expression on activated TCs was removed, as in-vivo, the number of activated TCs was reduced by 60%, highlighting the strong dependence on specific retention Figure (A.10).

The number of effector TCs produced did not increase with swelling, despite the increase in activated TCs. As the paracortex swelled, the number of exit compartments also increased. The lack of $S1P_1r$ mediated retention of effector TCs likely means that they are more affected more by the increased opportunity to exit. Allowing effector TC egress is important to allow effector TCs to travel to the site of infections. However, the earlier that effector TCs exit, the less exponential proliferation occurs, and this could explain why there were less total effector TCs as the paracortex swelled.

2.4.3 Paracortical swelling dynamics impact effector TC response.

The parameter T_{mid} is a measure of the ease of paracortical swelling as a function of TCs present. A higher T_{mid} requires more TCs to be present to reach maximal expansion. Physiologically, T_{mid} could relate several different factors that may facilitate LN swelling, stromal cell elastic properties and proliferation rate, the sensitivity of immune response to antigen signalling, or the sensitivity to accumulated fluid and TCs present. The value of T_{mid} was varied whilst also varying the maximal swelling. This allowed investigation of whether the size of paracortical swelling had different effects depending on whether increases in volume occurred with more or less TCs present. Due to the proliferative pattern of TCs, this meant that the swelling occurred temporally earlier or later, and remained high for a shorter or longer duration (Figure 2.39A).

Increasing the value of T_{mid} aided the number of effector TCs that exited the paracortex, with a larger paracortical swelling (>1.5-fold) only 2.412.40. However, a low T_{mid} and large swelling produced the least amount of effector TCs at day 10. This implied that the effect of paracortical swelling is partially dependent on at what point in the progression of the TC proliferative response that it occurs. Studies *in-vivo* have suggested that facilitated swelling may aid the TC proliferative response [60]. However, the experiment involved transferring

a large number of cognate TCs (1x10^6) into the LN. This would be the equivalent of increasing the starting number of cognate TCs modelled here at least 1000x over. As the results of section 2.3.6 show, the size of the proliferative response is proportional to the starting frequency of cognate TCs [40, 206, 216]. Therefore, with an artificially high number of initial cognate TCs, the threshold at which LN swelling becomes helpful is likely to occur much earlier. The swelling-facilitated response would therefore be consistent with the suggestions made from the modelling results.

To better understand why this effect was observed, some of the accompanying changes whilst varying V_{max} and T_{mid} were analysed. This included the alterations in TC crowding, determined as the ratio of TCs to grid compartments. With a large V_{max} and a high T_{mid}, the ratio of TCs to grid compartments was higher in the first 4 days of the simulation than with a low T_{mid}, although still less than when swelling was minimal 2.42BA.5. This showed that a lower T_{mid} allowed for TC recruitment and retention to be a stronger influence than TC egress in the initial few days. The timing of the maximal swelling occurred slightly later with higher T_{mid} values and was also shorter in duration. The swelling was accompanied by a drop in the ratio of TCs to grid compartments at day 5. It is likely that the increased space and relatively higher ratio of exit compartments allowed TCs to access exit points more easily. When large swelling was delayed using a higher T_{mid}, the efficiency of effector TC response was greater than or equal to when a small maximal swelling was applied 2.39C2.40D. This implied that at later time points, TC recruitment and retention became less important whilst more space and access to exit points became preferable. In contrast, simulations using a large maximal swelling and low values of T_{mid}, resulted in less effector TC production than simulations with limited swelling and either high or low T_{mid}.

Together the results of modulating T_{Mid} and maximal swelling implied that LN swelling too early can negatively impact TC response. It also implies that manipulation of the way the LN swells, for example facilitating an early swelling, could present as handle on immune response, to promote or inhibit effector TC production.

2.4.4 Paracortical swelling impacted CD4+ and CD8+ TCs response distinctively

The TCs in the model represent both $CD4^+$ helper TCs and $CD8^+$ cytotoxic TCs. While modelling the paracortical swelling, the $CD4^+$ or $CD8^+$ status of the cognate TCs (non-activated, activated, effector and memory) was also recorded. This allowed a comparison of the response of the two subsets. As with overall effector TCs, the number of cognate $CD4^+$ or $CD8^+$ TCs that exited by day 10 and the total number present during the simulation was recorded. As maximal swelling increased, total number of $CD4^+$ effector TCs that exited also increased but the total number of $CD8^+$ TCs decreased. Overall, less TCs exited when the paracortex volume more than doubled 2.35C,D. When paracortical swelling was delayed by increasing the value of T_{mid}, the number of $CD4^+$ TCs that exited remained unchanged (Figure 2.41B,C). However, the number of $CD8^+$ TCs that exited was highest at a median fold change in paracortical volume of 1.8 and less TCs exited at fold change <1.8. The changes that accompany LN swelling, such as increased space, TC recruitment and TC exit, appear to be less detrimental to $CD4^+$ TCs than $CD8^+$ TCs (Figure 2.49).

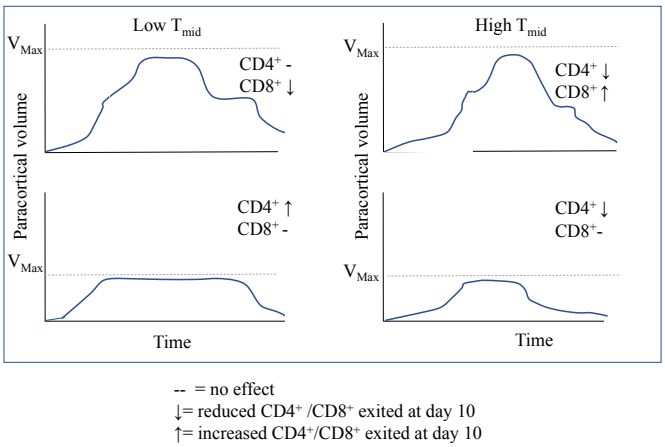

FIGURE 2.49: A summary of the effect of modulating T_{mid} on the number of effector TCs exited at different maximal swelling.

The difference in the timing of swelling relative to the progression of the $CD4^+$ proliferative response and $CD8^+$ TCs may be why $CD4^+$ and $CD8^+$ TCs respond differently. At a higher maximal swelling, the paracortex will be larger even before maximal swelling is reached. For example, a 1.5-fold swelling is reached sooner if the maximal swelling is 2.8 than if maximal swelling is 1.6. In baseline

simulations with minimal swelling, the cognate CD4+ TCs underwent proliferation earlier than cognate CD8+ TCs. Therefore, the difference in response to swelling may partly be because LN swelling may occur at a time-point where sufficient cognate $CD4^+$ TC activation and proliferation has occurred to produce TC numbers high enough to counteract any losses by increased egress rate through further proliferation, but CD8+ TCs may not have. Analysis of DC and cognate TC contact suggested that increased contact became more influential at larger LN swelling values (Figure 2.38) but was not a limiting factor in the initial conditions simulated. This is in line with the requirement of $CD8^+$ TCs for stimuli later on in the response. With more space to move around, and less overall contacts, each individual interaction with a DC becomes important.

The maximum number of proliferations is also less for $CD4^+$ TCs. This means that in the later stages of the response, $CD4^+$ TCs may be less affected by egress, because they have reached nearer to their maximum number of proliferations than $CD8^+$ TCs. To fight infection, effector TCs must exit the LN before they undergo apoptosis. Therefore, for optimal effector response, a quick TC egress when there is minimal proliferative capability left, but prior to initiation of TCs apoptosis, is desirable.

A delay in proliferation may mean $CD8^+$ TCs are affected more by apoptosis signals than $CD4^+$. At the later stages in the response when TC apoptosis signals initiate, there are more $CD8^+$ TCs than $CD4^+$ remaining in the LN. During the later stages in response, it is $CD8^+$ TCs that maintain LN expansion. This is shown by the lack of agDC presence, the later proliferative response and the ability to reach numbers 10x higher than $CD4^+$ TCs 2.31. Factors that delay the progression of $CD8^+$ proliferation may mean that $CD8^+$ TCs experience apoptosis signals prior to optimal expansion.

Finally, it is important to note that the timing of $CD4^+$ response may occur later with different stimuli, the effects of which could be investigated in future simulations. The early response of $CD4^+$ TCs is likely partly due to the assignment of initially lower $CD4^+$ stimulation requirement to activate, when interacting with mature DCs, and thus to trigger the process leading to proliferation. The lower threshold was designated, due to the observation that activated $CD4^+$ Helper TCs aid the $CD8^+$ response but do not require assistance themselves

[120]. However, mature DCs could become licenced DCs after interacting with activated $CD4^+$ TCs, based on in-vivo reports that cognate recognition of antigen by $CD4^+$ TCs is required [120]. $CD8^+$ TCs that interacted with licenced DCs subsequently were permitted to activate at the same thresholds as $CD4^+$ TCs.

The simulation results are in-line with previous simulations by Gong *et al* 2013, where , $CD4^+$ TCs also began to proliferate a day earlier than $CD8^+$ TCs, and at day 10 were 7x less in number than $CD8^+$ TCs. In the study by Gong *et al*, when the cognate frequency of $CD8^+$ TCs was varied, the effectiveness of $CD8^+$ response was affected more by the variation when the separate cognate frequency of $CD4^+$ TCs was low, reflecting a dependency on $CD4^+$ response [96].

However, some *in-vivo* observations have been reported that state that $CD4^+$ TCs respond much more slowly than $CD8^+$ TCs , with few $CD4^+$ TC reaching 7 proliferations by day 8 while simarlarly simulated $CD8^+$ TCs reached > 7 proliferations [203]. $CD4^+$ TCs have been reported to activate in 20-24 hours, as observed here, but some studies have shown that CD8+ TCs are capable of faster activation in a few hours [130, 240, 241]. However, the former studies involved application of CD4+ TCs to cell culture wells containing bound antigen whilst the latter involved antigen-specific CD8+ hybridomas suggesting that the mechanism of activation could affect response.

Other *in-vivo* observations have been reported that state that CD4+ TCs respond much more slowly than $CD8^+$ TCs , with few $CD4^+$ TC reaching 7 proliferations by day 8 while similarly simulated $CD8^+$ TCs reached > 7 proliferations [203]. Indeed, the slower proliferation was considered in the model, as the designated mean proliferation time of $CD4^+$ TCs was 11 hours whilst $CD8^+$ TCs was 7 hours, but it is important to note that $CD8^+$ proliferation time has been reported as 5 hours, 13 hours and ranging between 6-30hours depending on the day post-stimulation [130, 228, 229].

The model could be used to investigate the scenarios in more depth, by applying different thresholds and proliferation lengths to better simulate situations where $CD4^+$ TCs respond more slowly. Indeed, the global sensitivity analysis

showed that maximum $CD4^+$ proliferation affected the number of effector TCs present in the non-expanding LN, and max $CD8^+$ proliferation affected effector TCs present in expanding LN, further supporting the observation that the two subsets respond differently to the swelling mechanisms, and that this may be due to their response dynamics.

In summary, increasing the maximal swelling too soon may hinder the initial proliferative response, so that by the time the $CD8^+$ TCs are thriving, the initial antigenic signal has been cleared and a higher proportion of $CD8^+$ TCs undergo apoptosis than $CD4^+$ TCs. Although $CD8^+$ TC response is aided by $CD4^+$ responses, the differential response of $CD4^+$ and $CD8^+$ TCs suggests that modulation of LN swelling could also be used to favour the promotion of $CD4^+$ TCs production over $CD8^+$ TCs or vice-versa to influence specific aspects of immune response related to the downstream actions of each type of TC.

2.4.5 Increase in TC egress rates limit the TC response.

Little is known regarding how the paracortical exit points of TCs into the adjacent SCS, cortical sinuses or medullary sinuses change when the LN swells. *In-silico*, as the volume of the paracortex increased, the surface area correspondingly increased. Therefore, the number of points that TCs may exit at also increased. Although TC recruitment was amplified as the LN expanded, so did the ratio of TC exit to entry (Figure 2.42D, Appendix A.1). In-silico, when the LN swells over 2.5-fold, the TC egress rate increased over 7-fold 2.42C. This is higher than the 3-5 fold reported in the literature [160, 164, 167, 232]. However, the corresponding LN swelling values were not reported.

The increased TC egress at larger values of V_{max} may accurately reflect changes in LN structure that contribute to increased TC egress and LN contraction. Indeed, Tan *et al* 2012 showed that during the first few days of the LN response to antigen areas around the sub-capsular sinus area expanded relatively more as the LN swelled. However, in the later stages of the response, there was preferential VEGF-A dependent expansion of cortical and medullary sinuses [154]. These changes may occur to allow increased TC egress rate by increasing the surface area of the sinuses where egress can take place. During LN expansion, conduits that form direct channels from the sub-capsular sinus

into the paracortex for fluid and small antigen become leaky during LN expansion (pre-print)[242]. Whether the walls of the paracortex and cortical sinuses also behave the same way is yet to be determined.

In-silico, the ratio of TCs to grid compartments was higher when the LN expanded less. To see if TC crowding would increase TC egress, the probability that a TC would egress when more than one TC occupied an exit compartment was increased. This did not show a significant effect (Figure 2.42A). This could be due to the application of too small an increase in egress probability. It could also be due to a lack of access to exit points during crowding.

During the immune response, lymphatic flow to the LN is increased. As the number of cells in the LN increases, and correspondingly the LN mass, pressure alteration may also occur. Increased lymphatic flow could also contribute to the changes in the medullary and cortical sinuses. Work carried out using computational modelling suggested that LN pressure alterations could reverse the direction of fluid transport to HEVs. However, little is known about the contribution of LN lymphatic flow and pressure to TC trafficking. Increased pressure from accumulated fluid could make decreased LN swelling less favourable; for example, through increased TC egress that reduced effector TC production. Fluid flow changes may also impact the distribution of chemokines. Thus incorporation of lymphatic flow into the model could improve the modelling of TC egress and retention.

2.4.6 Validation and Limitations

Baseline stimulations

Slight deviation in expected results in the baseline simulations can be attributed to the size of the paracortex and the limited swelling. For example, the motility coefficient (CM), a measure of displacement, is slightly smaller than that reported *in-vivo*. However, this is likely due to confinement as a small popliteal LN was modelled. In addition, a hemisphere was used so that TCs that reach flat face and reflect, due to the boundary conditions, may appear to move less from an original starting point. Overall TC velocity, however, matched in-vivo reports. Transit of TCs (13.1 hrs) is within the range cited in the literature (12-24 hr), but on the lower end (Figure 2.30).

Secondly, the egress rate reached a 2-fold increase instead of the 3 to 5-fold increase observed in sheep rats and mice (Figure 2.32). However, in the baseline simulations, a maximal fold swelling of 1.4-fold is used. This meant that there was little change in paracortical volume and therefore a lack of increased egress that accompanies volume change. Once volume change was included, TC egress reached up to 7-fold.

Thirdly, the number of TCs in the paracortex does not return to pre-stimuli levels within the 12-day time-period. However, studies show that although a return to homeostasis can occur with a month post-stimuli, the expanded node can remain above baseline for more than 3 months [170].

Replicating *in-vivo* experiments

The purpose of the validation experiments was to verify that the model could replicate the known outcomes of *in-vivo* experimental work that focused on several different themes. In each simulation, a different parameter was modulated, and the outputs compared well to *in-vivo* results (see 2.3.6). This showed that the model could stimulate a range of experiments, and that the rules were not specific to the conditions that were focused on during investigation of LN swelling. In addition to confirming the expected behaviour, additional observations regarding the difference between $CD4^+$ and $CD8^+$ TCs were observed. Studies *in-vivo* have shown that $CD8^+$ TCs tend to respond to stimuli in an all or nothing manner, whereas $CD4^+$ TCs did not. This difference could be seen in some of the simulations when the strength of the stimuli was less (Figure 2.46). The response of $CD4^+$ TCs *in-vivo* is often reported as more dependent on sustained simulation, but *in-silico* the $CD4^+$ TCs maintained a complete but reduced response at low numbers [233], This may be because the signal required was still above threshold. Indeed, some reports *in-vivo* suggest that $CD4^+$ TCs do not required a maintained simulation, which again may be due to the strength of the initial simulation [234]. The results also correspond well with the results of previous in-silico models, replicating the reported linear relationship between responsive $CD4^+$ TCs and cognate frequency and non-linear relationship between effector TCs and the number of agDCs.

Sensitivity analysis

The sensitivity analysis was designed to identify unexpectedly influential parameters. Most sensitive parameters were those involved in TC recruitment, the strength and duration of the stimuli, the maximal LN swelling, and S1P1r regulation. TC recruitment parameters were fixed in all simulations and could present as an area for future study. Other key factors were analysed in more detail in further simulations. A significant finding was that, when LN swelling was applied, several parameters positively correlated with effector TC production in the first 4 days of the response. They then reversed their correlation in the remaining days of the response. The same parameters in fixed-volume LN simulations only showed positive correlation in the first week of the response. Many of these parameters would drive an increase in TC number and therefore increases LN expansion, such as TC recruitment rate, proportion of cognate TCs in the paracortex, and number of agDs. The reversal of influence emphasised the importance of time-dependent regulation of immune response.

Improving confidence in the model

Further testing could be carried out on the model to ensure model robustness and reliability. To improve confidence in the model, standard tests such as unit testing and edge-case testing should be carried out. Unit testing involves individually testing each of the user-defined functions to ensure that each function (usually a single agent method/behaviour) does exactly what it is meant to, using a series of known inputs and comparing calculation of expected outputs. Unit testing is used during model development, because as the list of functions grows, the likelihood of a function containing an error increases. Secondly, edge-case testing is used to find out the limits of parameters/scenarios that 'break' the model in terms of producing non-physiological results. This kind of testing can be quite challenging in biological investigative scenarios as it is often difficult to determine the difference between an impossible and unlikely scenario with limited prior knowledge.

Experimental limitations

LN expansion is due to many more factors than just TCs. This includes factors such as stromal cell proliferation rate, fluid accumulation, and cytokine signalling, which are regulated by both innate and adaptive signalling pathways. However, the model captures the effects of many aspects of these pathways without explicitly specifying ligand-receptor signaling chains. For example, the innate signaling that occurs in vivo during initial TC recruitment is included by linking TC recruitment changes to the detection of antigen-presented on DCs. In-vivo, stromal cell growth is initially inhibited by increased secretion of IFN type 1 that inhibits LEC proliferation (Rev.[64, 243]). By day 2, innate signalling switches to favour LEC expansion. The DCs can also trigger changes in LEC elasticity that facilitates early LN swelling, and VEGF-secretion by stromal cells is induced by DCs and macrophages, promoting stromal cell growth. [58, 60, 146] [154, 157, 160, 243, 244]. *In-silico*, the use of the sigmoidal function to determine volume as a function of TC number allowed TC number to increase without triggering significant swelling at day 1, while omitting the stromal cell signalling and proliferation rate that limits expansion. Increased LN volume was then caused by agDCs that interacted with, thus retained, naive and cognate TCs and also triggered 'LN shutdown'. The switch from innate to adapt signalling from day four to seven is coincident with paracortical volume dependency switching to effector TC proliferation instead of DC-mediated retention. At this time-point, increased recruitment is due to increased HEV surface area that accompanied swelling instead of the initial fast antigenic stimuli detection.

Maximal swelling of LNs was less than observed *in-vivo*. Due to the computational demand, the maximal fold swelling described was a 2.8-fold volume change. Yet *in-vivo*, LN swelling is reported to reach a 5 to 7-fold increase in volume. Firstly, this expansion reflects expansion in the paracortex driven by TCs only, without the information regarding fluid, the B cell follicles and other immune cells. Secondly, the simulation results using this range showed that even moderate alterations in LN volume were enough to alter activation and effector TC production. Several correlations were identified between measured outputs and the maximum swelling, suggesting the trends would continue with

further swelling. To identify whether larger maximal swelling effects could deviate from the observed patterns, the model could be halved to represent a quarter of a LN. Simulations could then be carried out with larger fold volume changes, but TCs could show signs of confinement. Alternatively, the model could be re-written to allow simulation using the RepastHPC version of the current RepastSimphony platform. This would allow larger fold-changes to be simulated by dividing the computational workload up over several parallel processes. However, this would also result in a loss in the ability to visualise the simulation.

The parameters may be non-proportional with one another as they are sourced from multiple murine experiments. However, it also means that the model is a very generic model, focusing on the processes and behaviour with minimal sensitivity on exact parameter values. There are several non-physiological parameters that often represent signalling thresholds or a series of signalling processes. A strength of ABM is the ability to simplify these processes and focus on the overall emergent behaviour. However, physiological parameters also add additional uncertainty into the model. To minimise the effect of uncertainty, a global sensitivity analysis was used to identify/ensure that there were no unexpectedly influential parameters. If the model is used to focus on different outputs in future studies, the ABM structure means that it is easy to refine and/or replace relevant pathways.

The infiltration of free-antigen and the inclusion of LN-resident agDCs was not included in the model. The model focused on the response to antigen captured at the periphery and presented by migrating DCs in the paracortex, but unbound antigen can enter in the LN in the afferent lymph and filter through the SCS, B-folliclles and paracortex. At the B-follicles free-antigen can be captured and presented by B cells, to trigger further actions culminating in antibody-production by B-cells. In the paracortex, free-antigen can be capture and presented to TCs by LN resident DCs. Unbound antigen, such as viral particles that evade DC capture were not included in the model, as the dendritic cells are the most potent antigen-presenting cells, therefore migrating DCs reach the LN following many types of infection (rev.[245]). Mature DCs also present co-stimulatory molecules, induce accompanying inflammatory pathways, and

have recently been shown to retain the ability to capture antigen [246]. Additionally, many new vaccinations towards cancer and autoimmunity focus on DC based-vaccinations that can efficiently trigger the T cell-mediated response to produce cytotoxic TCs rather than traditional vaccines that induce antibody production from B cells (rev. [247]). Nevertheless, the inclusion of LN resident TCs could easily be added to the model, allowing modelling of response to free antigen and viruses in the paracortex. However, modelling such a scenario would also increase the need to add a description of the immune response in the B-follicles into the model.

The LN stroma, which secrete chemokines and cytokines during the immune response, were not included in the model. The model was constructed in such a way that the dynamics of volume change still reflected the known changes in the stromal cells. However, it remained difficult to describe the influence of secreted signalling molecules that may remain after the end of the initial agDC stimuli. In future simulations, the inclusion of cytokines and chemokines could help to better describe secondary antigenic signalling processes that lag behind the agDC presence.

The definition of a successful immune response could fail to encompass all successful responses. It is assumed that a combination of the overall effector TCs produced and the number of effector TCs that exit the LN to the site of infection by day 10 correlate positively with a successful immune response. However, in some cases it may be possible that the speed of the effector TC production and exit from the LN is most important.

2.4.7 Summary

The simulation results disprove the study hypothesis and suggest that LN swelling does impacts the effector TC response, and that the manipulation of factors that influence LN swelling could present as new handles on immune response. In particular, temporary retention of effector TCs early in the response, on a relative minor scale, can have immense impact on the immune response. As such, it is crucial to develop the model to include the retentive role of chemokines and refine the S1P1r mediated TC retention.

The study showed that *in-silico* LN swelling aids the activation of TCs. Swelling can also limit the effector TC response, particularly if swelling occurs too soon. However, delayed swelling combined with large fold changes in volume can enhance effector TC production. This insight suggests that in chronically enlarged LNs, the immune response is likely to be impaired by the change in physical volume alone. Physiological factors that may present as targets to alter timing or size of LN swelling include early-phase stromal-cell stretching, inhibition of stromal cell proliferation, TC egress rate, and TC retention. This may be useful in conditions that present with LN swelling where immune response intervention is desirable. This includes during the pre-arthritic LN expanding phase in rheumatoid arthritis, Or in pre-metastatic LNs where lymphangiogenesis is induced and anti-tumour responses may become ineffective [91, 248, 249]

The study also highlighted that during swelling increased access to egress points prior to completion of the TC proliferative response presents as one mechanism that may reduce effector TC production. TC egress increased up to 7-fold as the LN maximal swelling was increased 2.8-fold. Increased TC egress contributed to LN contraction and likely to the reduced $CD8^+$ effector TC production. The crowding of TCs also varied throughout the response. This highlighted the need to incorporate accompanying changes in pressure and fluid flow that could impact the TC egress rate, particularly when there are altered numbers of TCs in the LN. Finally, the response of $CD4^+$ and $CD8^+$ TCs to the timing of LN swelling also varied. This suggests that modulation of LN swelling could also bias towards the $CD4^+$ or $CD8^+$ response.

Chapter 3

Lymphatic vessel miRNA expression during ovarian cancer

3.1 Introduction

The goal of the study was to investigate whether changes in miRNA expression occur in lymphatic vessels (LVs) draining ovarian cancer tumours, and whether they correlate to patient prognosis and/or changes in LV state. This section introduces the role of the LVs in ovarian cancer followed by the role of miRNAs in regulating LV behaviour. Previously identified miRNA expression changes in tumours associated with LV growth are then summarised, as are miRNA and mRNA expression changes in cancerous lymph nodes. The role of miRNA therapy in future cancer treatment and the study objectives are then discussed,

3.1.1 The lymphatic involvement in ovarian cancer

Ovarian cancer (OC) is the 6th most common cancer amongst females in the UK, with 20 new cases diagnosed every day (2013-2015) [250]. During advanced Epithelial Ovarian Cancer (EOC), lymphogenic spread accounts for one of the main metastatic pathways, with 55% to 75% of patients presenting with lymph node (LN) metastasis and 35.9% of patients presenting with both para-aortical and pelvic LN involvement [251–255]. Greatest overall survival is associated with minor LN involvement, and an increasing ratio of positive LNs leads to significant decreased overall survival [75]. Contrastingly, a better prognosis for patients with stage IIC EOC occurs when LN metastasis is present but involvement of the peritoneum is absent [256]. However when peritoneal involvement is apparent, patients without LN metastasis present with a more favourable

prognosis than with LN metastasis, complicit with the observation that LN involvement overall contributes to poor survival.

Box1: Ovarian Cancer Stages [257]

Stage I: Cancer cells are limited to the ovary/ovaries or fallopian tubes

Stage II: The cancer is in one or both ovaries or fallopian tubes and has spread into the pelvic area (uterus/womb/bladder).

Stage III: Metastases outside of the pelvis into the abdomen retroperitoneal LNs at the back of the abdomen.

Stage IV: Metastases to distant organs outside of the abdomen/pelvis.

Optimal cytoreduction, meaning successful near-complete tumour removal, is one of the most important prognostic factors for survival post-surgery in ovarian cancer [75, 258–262]. The removal of all lymph nodes in the draining axilla is also commonly performed, but the significance on prognosis remains unclear due to a lack of randomised control studies [75, 263, 264]. Several studies suggest systemic lymphadenectomy accompanying cytoreduction positively impacts prognosis [251, 265]. A study by Panici showed that systemic lymphadenectomy positively impacted progression-free-survival when compared to removal of bulky nodes only [252]. However no significant impact on overall survival was observed. A study involving patients with serous cancer (the most common type of EOC), identified a better post-surgery prognosis when patients presented with positive LNs than with negative LNs, which was possibly due to the systemic lymphadenectomy subsequently performed on patients with positive LNs [75]. This study suggests patients with minor node involvement could also benefit from systemic lymphadenectomy. Overall the evidence suggests that regardless of the disease-facilitating mechanism, curtailing the LV transport route via removal of LN is of clinical beneficial[75].

3.1.2 Lymphatic involvement in metastasis

Transport

LVs are specialised in the uptake and transport of macromolecules from tissue fluid and consequently can facilitate metastases both passively and through active changes in lymphatic endothelial cell (LEC) expression. At the tumour

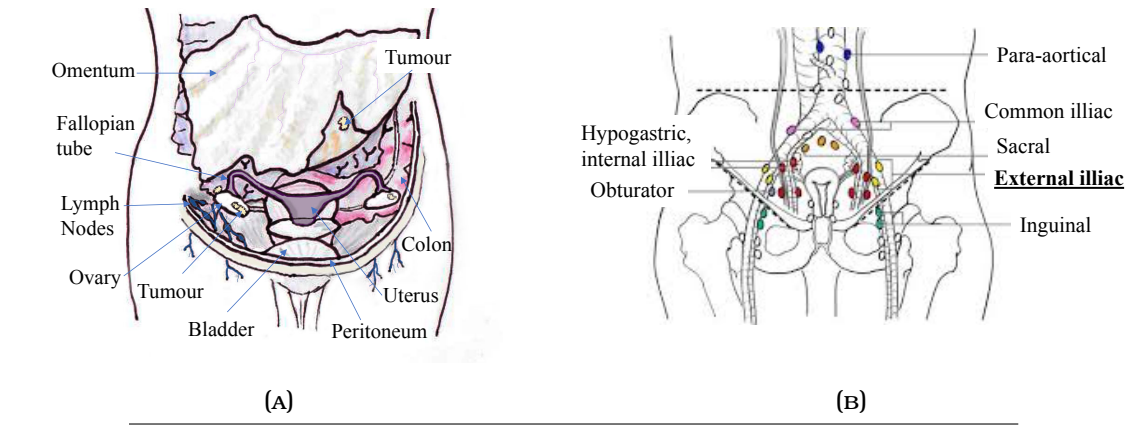

FIGURE 3.1: The location of the EOC tumour and LVs. (a)Stage IIB ovarian cancer depicting tumour growth on the ovaries that has also spread to the omentum.(b) The location of the major draining LNs of the pelvic area. The samples are harvested from the external illiac network.

micro-environment (TME), alongside angiogenesis and chronic inflammation, Vascular Endothelial Growth Factor C (VEGF-C)-induced lymphagiogenesis occurs. This has been shown in many studies to increases the efficiency of cancer cell spread [79] (Figure 3.2). LVs at the TME can be classed as those that infiltrate the tumour (intra-tumoural) and those at the tumour margin (peri-tumuoral). The role of the intra-tumoural LVs is yet to be fully elucidated as they tend to be collapsed and unable to transport cells due to a high interstitial fluid pressure [266]. Peri-tumoural lymphatics provide an open passage that can act as a transport route for tumour cells.

Cancer cells enter LVs either passively or in a chemokine-aided manner due to tumour cell expression of CCR7 and /or CXCR4 and secretion of corresponding chemokines CCL21 and CXCL12 by the LECs of LVs at primary tumour sites [267] rev[74]. CCR7 is up-regulated in many types of cancer cells and in many cases associated with LN metastasis (rev[268]). Tumour cells drain from LVs at the TME with lymphatic flow to the draining LNs but on occasion arrest in the LVs themselves[269, 270]. Visualisation of cancer cell lymphatic drainage pathways suggest changes in LV barrier integrity could also allow cancer cells to escape [82, 83]. Chronic Inflammation induces changes in collecting LV including dilation and inhibition of contractile ability but effects on metastasis are unknown [71, 72]. In addition, ageing of LVs results in a decrease in thickness of endothelial cell glycocalyx (a coating on the lumen LECs with a proteoglycan

and glycoprotein backbone), and loss of gap junction proteins that overall result in hyperpermeability [271, 272].

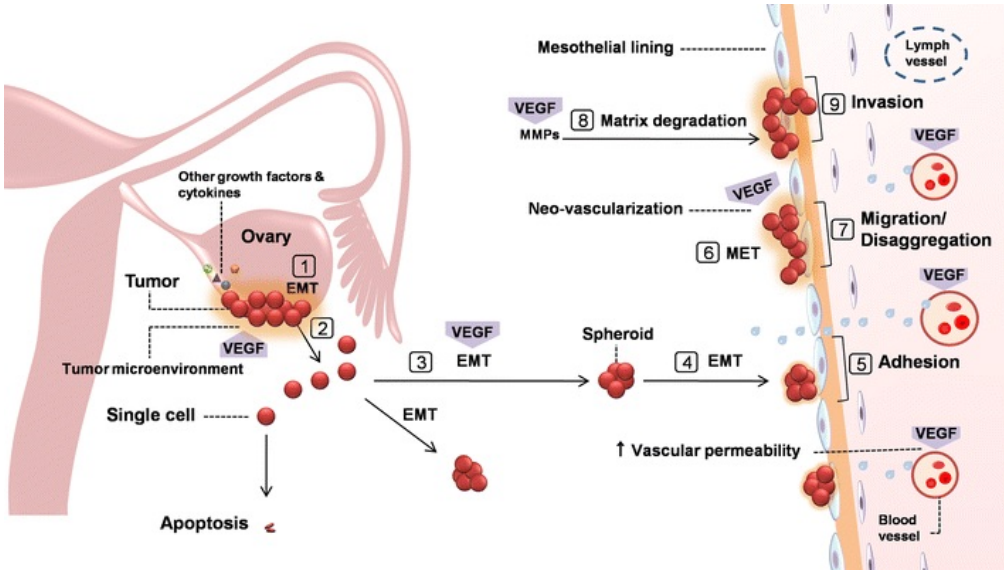

FIGURE 3.2: Schematic describing steps in EOC metastasis to LVs. A proposed model for intra-peritoneal dissemination of OC from the tumour into draining LVs. To metastasise tumour cells must undergo epithelial-mesenchymal-transition to detach from epithelial membranes and migrate. VEGF-C aids metastasis. "A proposed model for intraperitoneal dissemination of ovarian cancer" by Masoumi *et al* 2011 [273] licensed under CC BY 2.0

Tumour cells are transported in LVs to draining LNs with some research suggesting chemotactic facilitation [87]. LNs are usually inhospitable sites for tumour cells due to recognition by lymphocytes and subsequent destruction by immune cells. Indeed, implantation of tumour cells into the naive LNs of mice results in tumour cell rejection. However, when tumour cells were implanted into the dLN of a primary tumour, they thrived[274]. Growing evidence suggests that other signals transported in the lymph, such as cytokines and growth factors from the primary tumours, can pre-condition dLNs prior to metastasis by inducing more favourable conditions for tumour cells [275]. Lymphagiogenesis of LNs is associated with pre-metastatic LNs, and may potentiate pre-conditioning by facilitating increased lymphatic drainage from the tumour [89–91]. However lymphangiogenesis can occur in LNs draining any chronically inflamed site, suggesting inflamed but non-cancerous LNs or non-lymphangiogenic LNs may still contribute to the development of a metastatic

niche. From the LN, tumour cells are thought to metastasise in LVs but recent experiments in mice showed that tumour cells can also enter the LN blood vessels and metastasise via the circulatory system [74, 78].

Immunity

Lymphatic endothelial cells (LECs) can modulate immune cell function at the TME in both anti-tumour immune response and cancer-induced immuno-suppression [276]. LECs within tumour-associated lymphatics, and in the LN and express transmembrane Protein-Death-Ligand 1 (PD-L1), the ligand for T cell (TC) inhibitory receptor, PD-1[80, 81]. A greater LEC presence inside tumours has been correlated with a significant positive tumour response to anti-PD-1 therapy, implying the induction of tolerance by LECs has significant impact on tumour cell survival [277].

During colonization of LNs by cancer cells, the normal immune response to antigen is inhibited and the cancer cells thrive. Under normal conditions the LN stromal cells contribute to peripheral tolerance to prevent immune response to self antigen, but during cancer this may result in tolerance to cancer cells. Under homeostatic conditions, LN fibroblastic reticular cells (FRCs) can express tissue-specific self-antigens from peripheral tissue, and can present these to $CD8^+$ TCs to induce deletional tolerance (rev [49]). FRCs also express a protein called DEAF, that is involved in regulating expression of some peripheral tissue antigens [148, 278]. LECs have endocytotic capabilities and LECs that express PD-L1 can also induce deletional tolerance by endocytosing soluble antigen in their environment then presenting the antigen to $CD8^+$ TCs [279]. LEC expression of a tyrosinase molecule on their cell surface can also dampen $CD8^+$ TC responses by driving deletional tolerance of a type of MHC-I restricted $CD8^+$ TC [65, 280] (Restriction means the TC only responds to the foreign peptide when bound to MHCI). Studies have shown that LEC contribution to peripheral tolerance through interaction with $CD8^+$ TCs can also contribute to tolerance to tumour cell antigens [74, 92, 93].

Outside of the LN, LECs do not express PD-L1 or tyrosinase but upregulation of LEC MHCII expression occurs in response to inflammatory cytokine, Interferon gamma (IFNγ), stimulation[65, 66]. As $CD4^+$ TCs interact with MHCII, it

is possible that LECs can present antigen to $CD4^+$ as they pass through LVs and interact with polypetides on the vessel wall, with one study further suggesting LECs can tolerise $CD4^+$ TCs directly [67, 68]. Other studies suggest presentation of antigens on MHCII to DCs by LECs can induce $CD4^+$ responses indirectly, while inhibited [49, 69]. Inducing or suppressing $CD4^+$ TC responses can then impact priming of $CD8^+$ TCs in the LNs and subsequent response to tumour antigen.

Changes in LVs could impact anti-tumour immune response, as the LVs sample, and respond to, signalling molecules and immune cells in tumour draining lymph. In addition, immune cells such as macrophages and dendritic cells, reside on LV walls [281–283]. Once thought to be passive vessels, LVs have been shown to be sensitive to signalling molecules released during inflammation, such as pro-inflammatory cytokines that promote lymphangiogenesis[70]. Other studies have shown changes in lymphatic vessel gene expression in response to tissue inflammation and in a stimuli dependent manner [84, 85]. Experiments using mice showed that during contact hypersensitivity-induced inflammation, cutaneous LECs express lower mRNA levels of pro- lymphangiogenic VEGF-3 and *PROX-1*, an important gene in lymphangiogenesis and embryogenesis. When inflammation was induced using complete Freund's adjuvant, this change was not observed. This was significant as the change in mRNA expression influenced DC migration to LNs response, and therefore adaptive response [84, 85]. Finally, little is known regarding the changes in lymphatic flow between the TME and the LN, but variation in lymphatic flow can also trigger LEC gene expression. The changes observed can alter the fluid and solute permeability of the LECs, in addition to the uptake and expression of adhesion molecules involved in immune cell migration [284].

3.1.3 Micro RNA and dysregulation in cancer

Micro RNA (miRNA) are short strands of highly conserved non-coding short RNA molecules that regulate gene expression at the post-translational level and are considered major epigenetic factors [285–288]. Micro RNA are transcribed from

DNA in the nucleus and require processing by enzymes Drosha and Dicer before becoming mature miRNA [289]. Mature miRNA can inhibit mRNA translation or promoting miRNA degradation by binding to single stranded mRNA (Figure.3.3). It is predicted using bioinformatic analysis that nearly 1000 miRNAs in the human genome have the capacity to regulate almost 60% of the human transcriptome [290]. Down-regulation of miRNAs results in increased expression of target mRNA and vice-versa. It is important to note that the effects of miRNA regulation are dependent on a pre-existing transcriptional program. A single miRNA can regulate multiple mRNA targets and several miRNAs can act together on the same gene [291].

Dysregulation of miRNA expression in human malignancies is widely reported, but causation and effect have proven difficult to untangle, partly because one miRNA can target expression of multiple genes. In addition, there are many methods of miRNA dysregulation, including abnormal transcriptional control of miRNAs, amplification or deletion of miRNA genes and defects in the miRNA biogenesis machinery, making identification of feedback loops more complex (rev[292]). Mice heterozygous for the Dicer enzyme required for miRNA expression develop an increased incidence of tumours [293, 294]. In ovarian cancer specifically, high levels of DICER and DROSHA mRNA are associated with increased median survival and conversely, decreased DICER expression significantly correlates with reduced patient survival [295–297].

MicroRNA profiling of different kinds of tissue samples, including tumour, serum and LNs, has been used to identify specific cancer and metastatic expression patterns, that can be followed up with functional studies to confirm individual miRNA tumour suppressors or oncogenenic function. [298, 299][298–301]. Regarding specifically OC, a large study by the Cancer Genome Atlas research network analysed miRNA expression in 489 high grade serious ovarian adenocarcinomas and for a significant subset of these samples, identified a miRNA-regulatory network associated with poor survival [302]. Eight key miRNAs were predicted to target 89% of this network (Table 3.1)[303]. 50% of these were regulators of the epithelial-to-mesenchymal transition (EMT) pathway, which means epithelial cells that are normally attached to a basement membrane differentiate into a mesenchymal cell phenotype capable of detachment and migration

[304–306]. Differential expression of miRNAs has been identified in several studies comparing healthy and diseased ovary tissue in addition to comparisons of diseased ovary tissue at different cancer stages and association to patient prognosis (Table 3.1). Investigation of serum levels of miRNA in ovarian cancer patients have indicated miRNAs with diagnostic and prognostic potential (Table 3.1) [307].

Studies have also been performed to identify correlation in tumour miRNA expression and patient response to chemotherapy medications. A 2016 study used tumour biopsies from patients undergoing interval de-bulking surgery to identify miRNA families associated with survival and drug response, miRNA associated with overall and progression-free survival, and miRNA associated with residual tumour volume (Table 3.1) [308]. Overall, differentially expressed miRNAs were found to be clustered within 4 miRNA families, miR-199, let-7, miR-30, miR-181 and miR-29. A study using miRNA profiling of drug-resistant ovarian cell culture lines identifed 6 commonly dysregulated miRNA (Table 3.1). Within this study, down-regulation of miR-130 was linked to translational activation of the M-CSF gene, a known resistance factor for ovarian cancer [309].

Micro-RNA expression profiling of EOC cell lines representing early stage and advanced stage high grade ovarian cancer compared to control cells revealed consistent down-regulation of ten miRNAs (Table 3.1) and significant down-regulation of 44 miRNAs between early and late stage EOC. These included the known tumour supressors mir-15a, mir-34a, and mir-34b. [310]. A study using both EOC cell lines and EOC tumour tissue showed highly elevated mir-221 and mir-21 and down-regulation of several members of the let7 family in both cell lines and tissue [311]. Profiling different types of ovarian cancer cell lines has also shown that miRNA expression profiles vary with different histopathologies[312].Changes in miRNA associated with metastasis have also been identified by comparing miRNA expression in EOC primary tumours to secondary tumours on the omentum (Table3.1 [313]). Further comparisons of benign versus malignant ovarian cancer tumours identified four miRNA, let-7i-5p, miR-122, miR-152-5p and miR-25-3p, as significantly down-regulated in malignant tumours, that all also target signalling pathways associated with chemo-resistance [314].

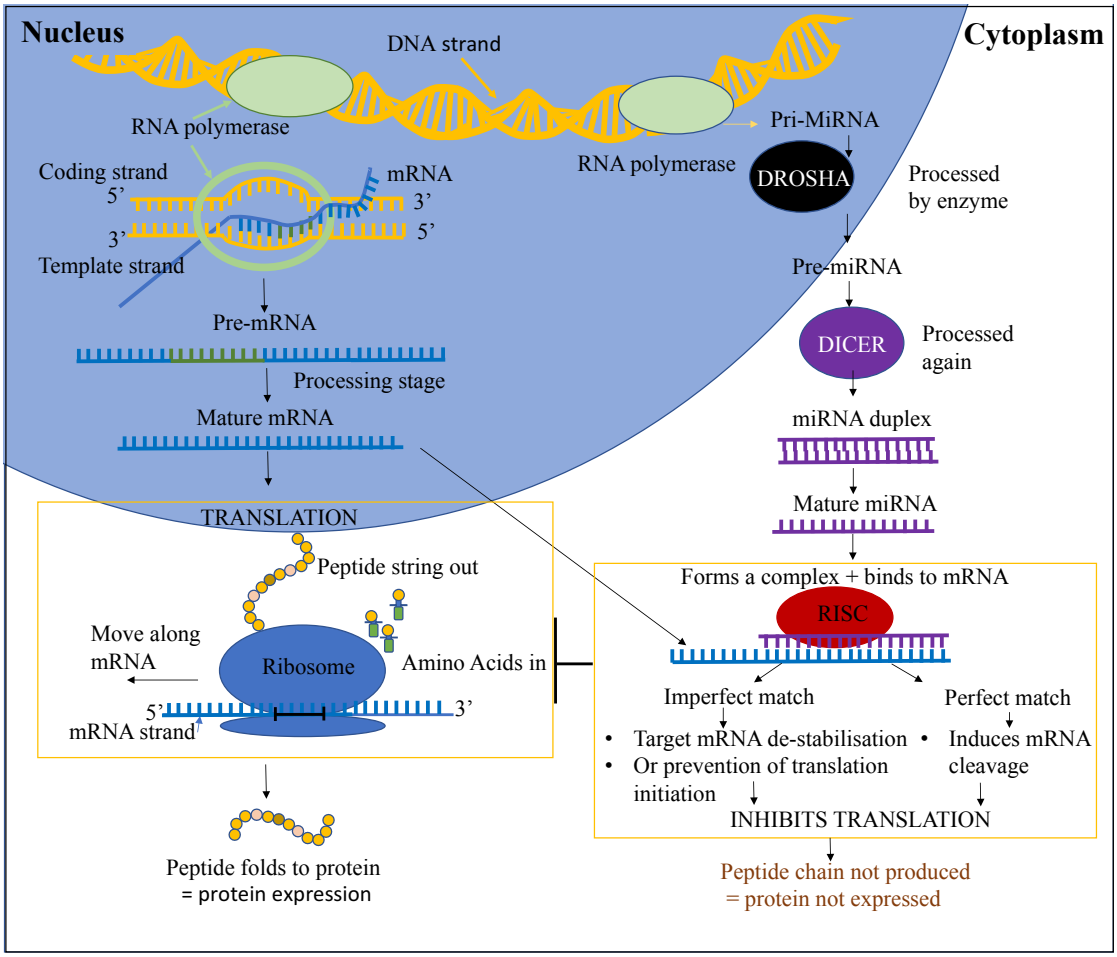

FIGURE 3.3: Regulation of gene expression by miRNA. Inside the nucleus, mRNA is transcribed by the enzyme RNA polymerase from unfolded strands of the DNA helix. Pre-miRNA is processed into mRNA. In the cytoplasm, translation of mRNA produces peptide strands that fold into proteins. MicroRNA is also transcribed from the DNA strands by RNA polymerase and undergo processing both inside the nucleus and cytoplasm. The mature miRNA forms a complex with the RISC protein and mature strands of mRNA . This results in inhibition of mRNA translation by preventing the initiation steps of translation or destabilizing the mRNA.

TABLE 3.1: Summary of up-regulated and down-regulated miRNA in expression profiling studies relevant to ovarian cancer

Experimental Comparison	miRNA expression		Reference
	Up-regulated	Down-regulated	
Key regulators of miRNA network (HGS ovarian)	miR-101, miR-200c miR-141, miR-506	miR-25,miR-29c miR-182 miR-128	[303] [302]
Healthy ovary versus diseased ovary	miR-200a, miR-141 miR-200c, miR-200b	miR-199a, miR-140 miR-145, and miR-125b	[315]
Healthy ovary versus stage III/IV ovary	miR-200a/b, miR-126 miR-200c, miR-141, miR-429 miR-142-3p miR-195 miR-338-3p miR-378	miR-100,miR-127-3p, miR-302 miR-210, and miR-22, miR-222 miR-409-5, miR-485-5, miR-493	[316]
Serous OC tumour versus normal tissue	miR-200a/b,miR-23a miR-27a, miR-141,miR-16 miR-93,miR-23b	miR-214,miR-26a, miR-29a let7b, and miR-100, miR-10b miR-125a, miR-125b miR-143, miR-199a miR-125b,miR-99a	[317]
Changes in Serous OC tumour associated with poor prognosis)	miR-200, miR-141 miR-18, miR-93,miR-429	let-7b, miR-199	[317]
Changes in Serous OC tumour associated with decreased PFS/OS	miR-200a/b/c miR-141, miR-18a miR-429 , miR-93	ambi-mi-R-7039 , let-7b miR-199a	[317]
Serum from EOC and healthy patients	miR-7 miR-429	miR-25, miR-93	[307]
Overexpression in Primary OC	ambi-miR-7510,miR-21 let7a/b/c,miR-103,miR-106a miR-16,miR17-5p,miR-191 miR-200b/c, miR-26a miR-24, miR-23a/b		[318]
Comparison of tumours associated with PFI < 6mnth, residual tumour >1cm and reduced patient survival	miR-181a, miR-199a-5p miR-199a-3p		[308]
Tumours from relapse patients	miR-181-5p		[308]
Chemo-resistant cell cultures (5/6 lines)	miR-125b	miR-30, miR-130a miR-335, let 7e	[309]
Chemo-resistant cell cultures (1/6 lines)	let7e	miR-30, miR-130a, miR-335 miR-125b	[309]
Advanced stage HGS OC versus control		miR-15a, miR-34a, miR-34b	[310]
Clear Cell versus Mucinous histotype	miR-30a, miR-192 miR-194		[312]
EOC cell lines and tumour versus control	miR-22	miR-21, let7 family members	[311]
Omental lesions expression associated with survival	miR-146a, 150		[313]
Benign versus malignant tumours		let7i-5p, miR-122 miR-152-5p, miR-25-3p	[314]

HGS = high grade serous PFS=Progression-Free survival OS=overall survival

3.1.4 Regulation of lymphatics by miRNA

To understand how miRNA dysregulation may impact lymphangiogenesis and cancer progression, it is important to consider previously identified roles for miRNA with the lymphatic vessels. Translational changes by miRNA are known to play crucial roles in regulating lymphangiogenesis during embryonic development and inflammation. The miRNA 31 (miR-31) negatively regulates lymphatic development and miR-181 negatively regulates PROX-1, an important gene in lymphangiogenesis and embryogenesis [319, 320]. The miR-466 acts to inhibit PROX-1 and tube formation, an initial step in lymphangiogenesis [321]. It is also important to note that miRNAs can regulate their own miRNA biogenesis machinery; for example LEC expression of miR-132 regulates a pathway involved in the mechanism of RNA-mediated gene silencing, therefore amplifying the extent of influence by one miRNA [322].

Micro RNAs also regulate multiple pathways in lymphatic tissue during inflammation. A study investigating inflamed lymphatic endothelium in rat tissue and human cell culture showed expression of a distinct set of different miRNAs at 2,24 or 96 hours post TNFα application. This included down-regulation of miR-144 at 2 hours, up-regulation of miR17-5p, miR-203, miR-20a, miR20b-5p, miR-21, miR-325-3p, miR-9, miR-27a, miR-322 at 24 hours and upregulation of miR-34a/down-regulation of miR-205 at 96hours. Subsequent pathway analysis revealed involvement in inflammation, angiogenesis, endothelial mesenchymal transition, cell proliferation and senescence. The miRNA 9 (miR-9), which was induced by TNFα, was also identified to hold an important dual role. Over-expression of miR-9 repressed expression of the pro-inflammatory nuclear factor NFκB expression and suppressed inflammation, but also promoted LEC tube formation. Over-expression of miR-9 also promoted expression of pro-lymphangiogenic molecules, endothelial nitric oxide synthase and VEGFR3[70]. A second study using human LEC culture showed that miR-1236 reduces expression of VEGFR3 and inhibits inflammatory lymphangiogenesis as a result [323]. Finally, the miRNA miR-155 has been shown to regulate inflammation in human dermal lymphatic cell (HDLEC) culture. After treatment of HDLECs with IFNγ and TNFα, miR-155 was the identified as the most highly up-regulated miRNA [324]. During the treatment, the endogenous miR-155 controlled levels of PD-L1, a critical regulator of T cell function. This suggests that miR-155 could contribute to peripheral immune tolerance. Expression of miR-155 is not restricted to LECs and similar results were found using fibroblasts.

3.1.5 Cancer-induced lymphatic miRNA expression change

Despite the cellular heterogenity of tumour-tissue, expression profiling of tumours have led to identification of lymphangiogenesis-inducing miRNAs. In oral cancer, down-regulation of miR-126 induces angiogenesis and lymphangiogenesis by activation of VEGF-A [325] whilst studies using human tissue found that microRNA-128 plays a critical role in human non-small cell lung cancer tumourigenesis, angiogenesis and lymphangiogenesis by directly targeting VEGF-C [326].

Lymphangiogenic LVs at the TME display abnormal gene expression, as do primary LECs isolated from fibrosarcomas implanted in mice, but specific miRNA expression studies of isolated intra-tumoural LVs are lacking [327]. A 2013 study using human LEC culture models of gastric cancer, which could represent tumoural or draining LVs, identified a panel of differential microRNAs expression changes [86]. Key up-regulated miRNA included miR-648, miR-5002-3p, miR-4754, miR-4760-5p, miR-4491, miR-4252, miR-5007-3p, and miR-647 whilst miR-3178, miR-593-5p, miR-4485, miR-135a-3p, miR-17, miR-1469, and miR-124-5p were down-regulated. The expression changes were associated firstly with lymphangiogenesis and secondly with positive lymphatic metastasis of the primary gastric tumour implying that LV/LEC changes could influence metastasis.

Further miRNA expression studies of draining LVs are lacking but a gene expression study in 2012 using isolated LECs from afferent LVs of sentinel LNs draining a metastatic gastric cancer tumour in rat models identified many gene dysregulations including up-regulation of chemokine CXCL1 [328]. Further investigation using a co-culture system showed that gastric cancer cells induced CXCL1 secretion from LECs, which stimulated LEC migration and tube formation. The expression of the corresponding receptor CXCR2 in human gastric cancer samples was positively correlated with LN metastasis and LV density, suggesting the change could promote metastasis.

To investigate changes in the dLN, both RNA and miRNA expression studies have been performed. RNA profiles of cancerous LNs have revealed abnormal phenotypes and elevated expression of genes associated with inflammation, cell growth and cell migration [329]. In cervical cancer, gene expression studies have identified a diagnostic signature of metastatic LNs [94]. A study comparing mRNA expression in metastatic (involved) and non-metastatic (non-involved) LN tissue in auxiliary breast cancers showed changes associated with metastatic colonization. These included heightened immuno-tolerance, reversal of the Epithelial-Mesenchymal-Transition and cellular proliferation that can support successful metastatic growth in a distant micro-environment [330]. Expression profiles of LN miRNA during colorectal cancer show significant decreased expression of miRNA-141, both in the draining LN, the serum and the

tumour tissue, with a further decline observed in patients with LN metastasis [95]. The miRNA-141 suppresses expression of its target gene MAP4K4 and the expression levels of MAP4K4 were found to be increased in the LN and altered the anti-tumour response, leading to increased proliferation and metastasis of tumours.

3.1.6 Therapeutic potential

Following recognition of the crucial role of miRNA in development and disease, miRNAs have become an attractive therapeutic target. Both miRNA mimics and anti-miRNA molecules have shown promise in pre-clinical development. Anti-miR-132 suppressed angiogenesis and decreased tumour burden in a xenograft mouse model of human breast carcinoma [331]. In murine OC models, increasing mature miR-155 activity in tumour-associated DCs by injecting components of precursor miR-155 led to a more immuno-suppressive DC phenotype, alongside reduced progression in established OCs. [332].

Several miRNA pharmacological agents are now under further development, eg, MGN-1374 that targets miR-15 and miR-195 for the treatment of post-myocardial infarction re-modelling (rev[333]). A liposome-encapsulated miR-34a mimic termed MRX34, showed promise in pre-clinical trials as an anti-cancer drug, but the phase I clinical trail ended early after some toxic immunological side affects (NCT01829971)[334, 335]. Although targeting miRNAs that drain to the LN via LVs may reduce off-target side effects, this highlights the need to identify alternate roles in immune response of the miRNA in question [336–338]. Perhaps the most successful story so far has been that of the miR-122 mimic, marketed as Miravisen, which is currently at phase II clinical trials for the treatment of hepatitis C virus infection [339].

3.1.7 Summary of the study goal

During EOC, presentation of metastatic LNs correlates with poor patient prognosis and the normally inhospitable dLNs undergo changes that inhibit the LN anti-tumour immune response. The changes are thought to be partially

driven by the contents of the tumour-draining lymphatic fluid transported in LVs. LVs are not passive passageways but respond to chronic inflammation and have shown potential involvement in immune response through presentation of molecules by LECs to immune cells in transit. Micro RNAs form an overarching control network on gene expression. A limited number of studies have shown that alterations in LEC miRNA expression occurs during cancer and inflammation but the changes in miRNA expression and function of the draining LVs in EOC that may impact inflammatory or metastatic pathways are, so far, unknown. Our aim is to quantify miRNA expression changes in the tumour draining LVs of OC patients to better understand the role(s) of LVs during OC, in both transport and immune response, that could aid future therapeutic development.

3.2 Methods

To investigate miRNA expression changes in the lymphatic vessels of cancer patients,tissue samples were collected directly from surgery and immunohistochemical imaging was used to divide isolated vessels into those containing or lacking cancer cells. The use of inflammatory markers enabled consideration of accompanying inflammation and comparison of miRNA expression in both groups.

3.2.1 Sample collection

Lymphatic vessels (LVs) were collected from patients undergoing primary debulking surgery for advanced EOC at Hammersmith Hospital, Imperial College Healthcare NHS Trust, London, United Kingdom. Informed consent was acquired from each patient. Ethics committee approval was obtained from Hammersmith and Queen Charlotte's and Chelsea Research Ethics Committee (REC reference: 05/Q0406/178), and tissue samples were provided by the Imperial College Healthcare NHS Trust Tissue Bank (ICHTB). The ICHTB is approved by NRES to release human material for research (12/WA/0196), and the samples for this project (R14036) were issued from sub-collection reference number Gyn_HG_13_020. Macroscopically normal looking lymphatic vessels along the external iliac vessels with surrounding fibrofatty tissue were removed during lymph node (LN) harvesting for LN staging. As a result, no additional procedures were required. Vessels were ligated with VIcyl03 or PDS-4-0, avoiding bipolar coagulation and other thermic energy to limit vessel damage. All patients presented with nil residual disease after surgery.

TABLE 3.2: Samples collected from 10 patients undergoing primary debulking or interval debulking for advanced EOC.

Sample	Patient age	Surgery	Stage	Histology Histology	LN Sampled	LN	Relapse* (13mth)
1	54	Primary	IVB	HGS	Right pelvic	negative	Yes
2	57	Primary	IVA	HGS	No	n/a	Yes
3	62	Interval	IIIC	HGS	No	n/a	Yes
4	64	Interval	IV	HGS	No	n/a	Yes
5	57	Primary	IIIB	Clear Cell	No	n/a	No
6	61	Interval	IIIC	HGS	No	n/a	No
7	81	Primary	IIIC	HGS	Pa LN	positive	No
8	41	Interval	IIC	HGS	-	-	N/A^{+}
9	75	Primary	IVB	HGS	-	-	N/A^{+}
10	64	Primary	IIC	HGS	Left Pelvic & Pa	negative	N/A^{+}

* HGS= high-grade serous *Mean time since surgery 13.2 +/months

3.2.2 Vessel isolation

Tissue specimens were immediately placed in ice cold Phosphate Buffered Saline (PBS) (VWR, Leighton Buzzard,UK, E504) and transported directly from theatre to the laboratory. With the help of a Stemi DV4 dissection microscope, LVs were identified and isolated whilst maintaining a small amount of the surrounding tissue. Each vessel was then cut in half into two cylindrical shaped sections (see Figure 3.4).

One half of each vessel was further cleaned of surrounding fatty tissue and immediately placed in RNA stabilising solution, RNA later^{TM} (ThermoFisher scientific, Loughborough,UK AM7020), then frozen on dry ice and stored at -20°.

The other half of each vessel with the surrounding tissue was processed for later immuno-histochemical (IHC) staining. The sample was fixed in 4% paraformaldehyde (PFA) for 45 minutes, followed by submersion in 15% sucrose for 3 hours then 30% sucrose for 6-12 hours. The vessel half was then embedded in OCT compound (Scigen, Cardiff, UK AGR1180) using dry ice and isopropyl alcohol. The OCT blocks were stored at -80°C. Multiple vessels were collected from the tissue samples but only one vessel, usually the largest, was used in subsequent analysis per patient (see Figure 3.8).

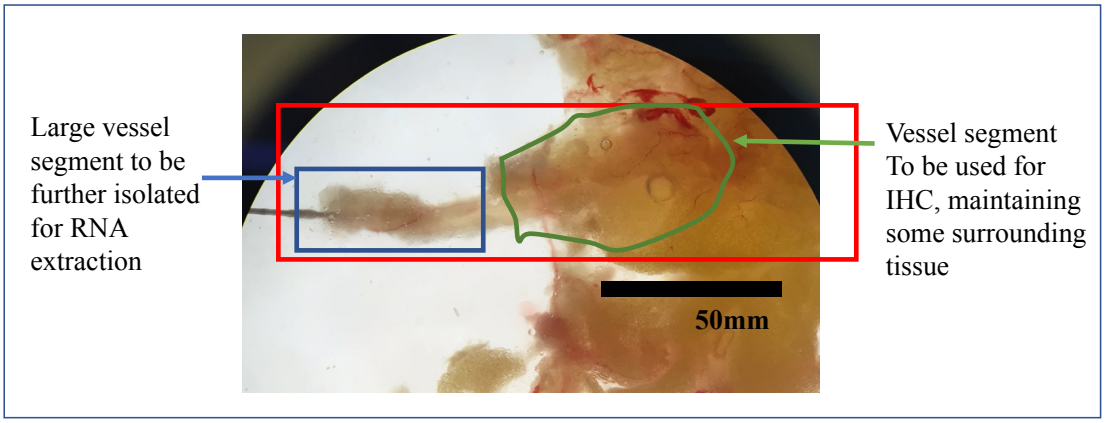

FIGURE 3.4: Lymphatic vessel isolation technique. LVs were identified within each macroscopically normal sample then partially isolated to the state shown above. Each lymphatic vessel was then divided and one half further cleaned of surrounding tissue whilst the other section was fixed in 4% paraformaldehyde with some surrounding tissues.

3.2.3 RNA extraction from the whole vessel

To extract RNA from the vessels, the samples stored in RNAlaterTM were defrosted on ice in RNAlaterTM. Each sample was then dipped briefly in QIASol Lysis Reagent (Qiagen, Manchester, UK) 79306) to remove excess RNAlaterTM and placed into a RNAase-free 1.5μm Eppendorf tube containing 700μL of QIAzol. The samples were homogenised in the Eppendorf using a PT 1300 D homogenisor with a 3mm dispersing aggregate head (E050 ,Kinematica, Luzern, Switzerland).To avoid LV samples clinging to the head resulting in no LV disruption, the homogeniser was brought to 20,000 RPM prior to insertion into the Eppendorf tube.

RNA was extracted from the resulting homegenate using a RNeasy Mini Kit (Qiagen 74104) and following the standard protocol. Post-extraction, RNA quality was checked using a NanoDropTM 2000 to record the absorbance spectum and the A260/280 and A260/230 ratios (Figure 3.5). An aliquot of 100ng of RNA sample was reverse-transcribed to cDNA using a miScript II RT Kit (Qiagen 218160), and a negative control sample using nuclease free water was processed simultaneously.

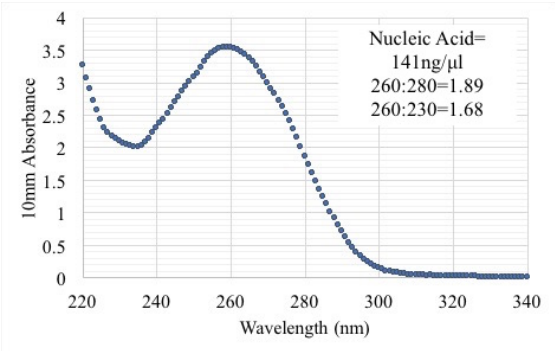

FIGURE 3.5: Assessing RNA quality using absorbance.A nanodrop was used to expose 2μL of each RNA sample to UV light and record the absorbance pattern. Single stranded nuclei acid absorb specific wavelengths. The more light absorbed, the higher the optical density and more nucleic acid present. The ratio of A260nm:A280nm and A230nm:A260nm can help to identify contamination of the sample with ideal ratios for single stranded RNA 2. The absorbance spectrum from Sample 8 is shown here, displaying the desired shape and ratios representative of a successful RNA isolation.

3.2.4 Using QPCR to quantify miRNA expression

To determine miRNA expression patterns, Quantitative PCR (qPCR) combined with a pre-defined microRNA array was chosen as a method. This allowed screening of an intermediate number of miRNA with reliable quantification of known pre-selected miRNA. RNA sequencing (RNA seq.) could also have been used, which would have allowed a deeper investigation of miRNA variation, such as insertions and deletions, but this greater level of detail, the requirement for detailed post-processing analysis, and the associated cost, was beyond the scope of the project. Similarly, single-cell RNA seq, could have been used in combination with cell sorting to ensure that only a LEC cell was sampled. However we were interested in the overall changes in LECs, therefore using single-cell RNA seq. would require multiple expensive single-cell RNA seq. trials per patient.

Digital PCR histopathology presented as an alternative option, which has been shown to produce a lower mean variation coefficient and quantifies miRNA expression linearly rather than the exponential measurement used in qPCR. This allows small fold changes to be detected more accurately [340]. However, in this project, only the large fold-changes were of interest as was relative, rather than absolute miRNA expression. Therefore, the trade-off between additional quantification and increased cost was not great enough to consider using digital PCR.

Finally nanostring in situ technology could also have been used. In this method the RNA is tagged with a capture probe and a reporter probe that is specific to the target of interest, that together create a unique complex. After hybridisation, excess probes are removed and hybrids are immobilised and aligned on the imaging surface. The sample is then scanned by an automated fluorescent microscope and labelled 'barcodes' analysed. The process is quicker, but in this study, finding novel miRNA was not the goal of the project, and using real-time qPCR miRNA arrays with pre-determined miRNA primers in this study was efficient in terms of time and money while still enabling novel findings overall.

Similarly, immuno-histochemical (IHC) imaging was selected for use despite the availability of more advanced techniques such as histo-pathology that provide

better pathological and structural detail. However, the study goal was to focus on the underlying miRNA changes accompanying inflammation and cancer cell filtration. The necessary information, was therefore the presence or lack of cancer cell markers and or inflammatory markers rather than detailed placement or morphology. Histo-pathology may be of use in future studies if LV structural changes were to become the focus.

The cDNA samples were prepared using a real time PCR kit (miScriptSybrGreen Qiagen 218073) and added to a predefined miScript miRNA PCR Array (Qiagen 331221) (see Figure 3.6). The array contained primer pairs for 88 human miRNAs, which have been previously identified or predicted to have target genes involved in the regulation of inflammatory responses and autoimmunity, as well as a panel of 8 housekeeping genes and controls. In addition, well G6 was populated with a negative control sample only. The array was run using a StepOnePlus Real-Time PCR System (Thermo Fisher Scientific), according to the manufacturer's instructions.

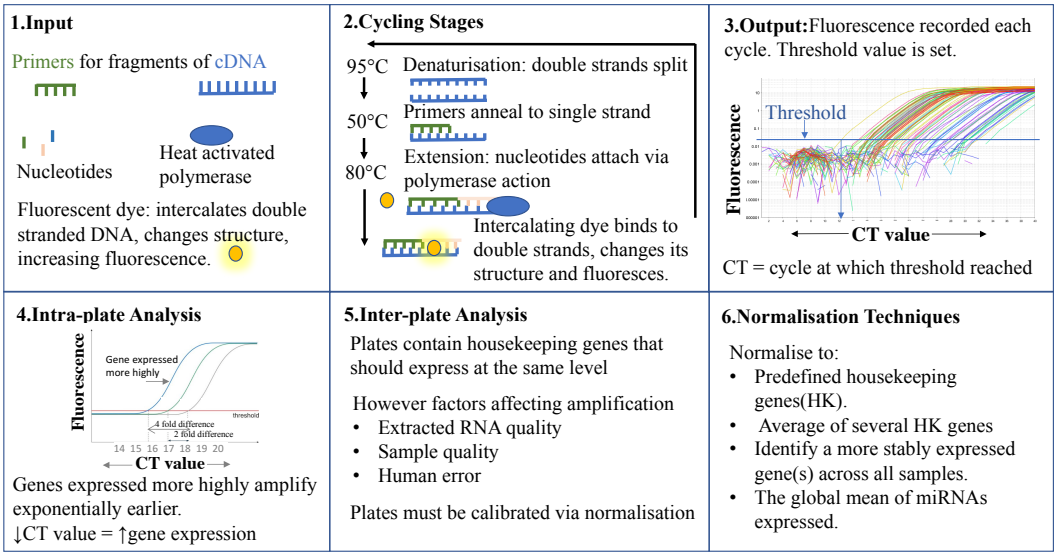

FIGURE 3.6: Underlying principles of real time quantitative PCR. Used to assess relative expression of genes within a cDNA sample using a 96 well array plate.(1) Each array well contains primers for specific miRNAs. Master mix containing the cDNA, nucleotides, heat-activated polymerase and a fluorescent dye is applied to each well. (2) The well is heated to 95°C to activate the polymerase then cycled through different temperatures that allow strand separation, primer attachment, extension and annealing of cDNAs. An intercalating dye fluoresces in its own right, but when it binds to a double stranded structure, its own structure alters, significantly increasing its fluorescence. The more double strands of DNA present, the greater the fluorescent intensity recorded at each cycle. (3) As cDNA amplification progresses, fluorescence increases exponentially. To quantify cDNA present, a fluorescent threshold is selected and the cycle at which each well reaches this threshold is recorded (CT value). (4) Wells that contain more initial specific cDNA to the primers of interest reach the threshold earlier and present lower CT values. Within arrays, CT values can be compared directly. (5) Variation in input sample quality/ human error/cDNA transcription efficiency means CT values comparison between arrays requires calibration. (6) Inter-array comparison is possible by normalising CT values to the expression of known 'Housekeeping genes' that are consistently expressed across samples. In some cases, housekeeping genes on commercial arrays may not be the most stably expressed across the particular tissue of interest. Therefore analysis is performed to identify stable genes to use in normalisation.

3.2.5 Immunohistochemical Staining

Samples were sectioned at a thickness of 10-16μm and stored at -80°. Haematoxylin and eosin (H&E) staining was performed to ensure that sections retained sufficient morphological features for reliable qualification of vessel state through imaging. Slides stored at -80°C were brought to room temperature for 10 minutes. Four percent PFA was applied for 4 minutes followed by ethanol gradients of 100%, 90%, 80%, and 70% for one minute each. Slides were stained for five minutes with haematoxylin solution (Sigma HHS16), then washed twice with distilled water, followed by five drops of acid-alcohol (Sigma 56694). Slides were stained with Eosin Y solution (Sigma HT110216) for five minutes and rinsed with tap water. Slides were air dried briefly then mounted with DPX (Sigma 06522) and further dried at 50°C for 1 hour.

To characterise vessel state, IHC with three different antibodies was used. An antibody for Podoplanin (PDPN), a trans-membrane protein expressed on LECs, was used to confirm that the vessels were lymphatic and not vascular or nerves. The inflammatory marker Myeloperoxidase (MPO) was used to determine inflammatory state of the vessel, and cancer cell presence was detected using ovarian carcinoma markers Wilms Tumour 1 (WT1) and Paired box gene 8 (PAX8).

To prepare slides for IHC, the frozen sections were defrosted at room temperature for 10 minutes then treated with 4% PFA (VWR stores, J61899.AK) for 5 minutes. The slides were then washed three times with Tris Buffered Saline (TBS) (Sigma-Aldrich, Dorset, UK , 94158) and 0.05% Triton X. Non-specific staining was blocked by applying 10% goat serum (Sigma G9023) in TBS for 1 hour.

Slides were then incubated overnight at 4°C with primary antibodies diluted in 5% goat serum and TBS at ratios of 1:200 MPO (Abcam, Cambridge,UK, ab9535), 1:200 WT1 (ab89901) and 1:200 PDPN (ab10288). The slides were washed three times with TBS and 0.01% TritonX (Sigma T9284), then Alexa-488 conjugated secondary antibody, anti-Mouse (ab150113) or anti-Rabbit (ab150-077) was applied at a dilution of 1:250 in 5% goat serum and TBS at room temperature for 1 hour. Samples were washed three times with TBS and stained with 300μmL of dilute DAPI (4',6-diamidino-2-phenylindole) solution (Sigma D9542) (1 μL of 14.3 μM stock for every 5 mL of PBS) for 3 minutes. Slides were washed with PBS and mounted with FluoroshieldTM (Sigma F6182).

3.2.6 Imaging and Image Processing

A Motic AE2000 light microscope was used to visualise H&E stained slides. Confocal images were acquired with a Leica SP8 inverted microscope at 10x, 20x, and 40x magnification using Diode 405nm and Argon 488nm lasers. Z stacks and multichannel images were processed and analysed using FIJI imaging software [341]

The pattern of Podoplanin staining was used to confirm that the vessels were lymphatic. To quantify the inflammatory state of the vessels, we recorded the ratio of staining for the enzyme Myeloperoxidase to the number of cells present, which was determined using the nuclear stain DAPI (see Figure 3.7). The vessels were subsequently classified into a low, medium or a high inflammatory state with thresholds of <3%, 3-10% and >10% MPO to DAPI ratios. The presence of WT1 and Pax 8 determined classification of vessels as cancerous or non-cancerous (may change to $+, ++, +$).

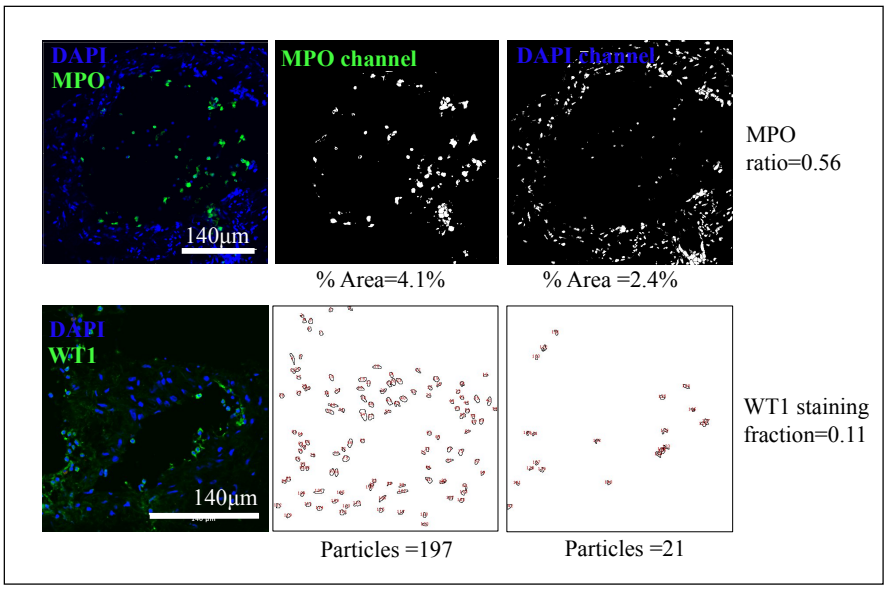

FIGURE 3.7: Quantifying LV state by anti-body staining. A: The ratio of MPO detected and cells present is used to divide samples into high and low inflammatory states (Threshold tbc). B: Particle analysis of the WT1 and Pax 8 stained images was used to quantify cancer cell presence. The ratio of cancer cells to overall cells present was determined.

Summary of Experimental Design

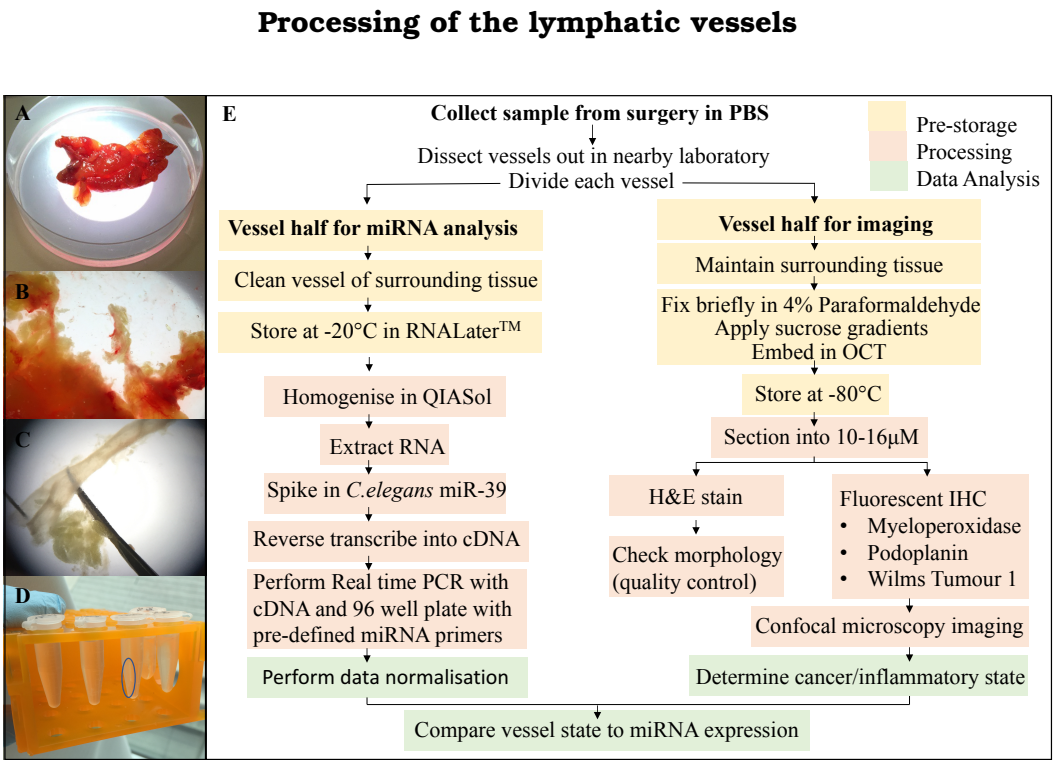

FIGURE 3.8: Experimental design for LV miRNA analysis. A B C Isolation of vessel with surrounding tissue removed. D: Isolated vessel in 1.5ml eppendorfs E: Work flow. Each vessel dissected from one sample is divided into 2 and processed for IHC and miRNA expression analysis.

3.2.7 Analysis techniques

Techniques to identify a stably expressed genes

Real time PCR compares the amount of cDNA from specific genes by amplifying the original cDNA and recording every doubling using increasing signal from fluorescent dye (see Figure.3.6).Gene expression in one sample is analysed through comparison of CT values within one array. Variation in input sample quality, cDNA transcription efficiency, and experimental error means calibration of inter-array results is required to compare CT value between arrays. This is achieved through normalisation of the CT values in each plate to the CT value of a gene that is assumed to be consistently expressed at the same level in all samples. The commercial miRNA array plate used contains primers for six 'housekeeping' (HKG) miRNAs selected to be constitutively expressed in all human samples, but not specifically confirmed for the lymphatic vessel sample used. Therefore two different analysis methods were applied to identify common stable genes and the results of applying several different normalisation techniques reviewed (see Figure 3.9).

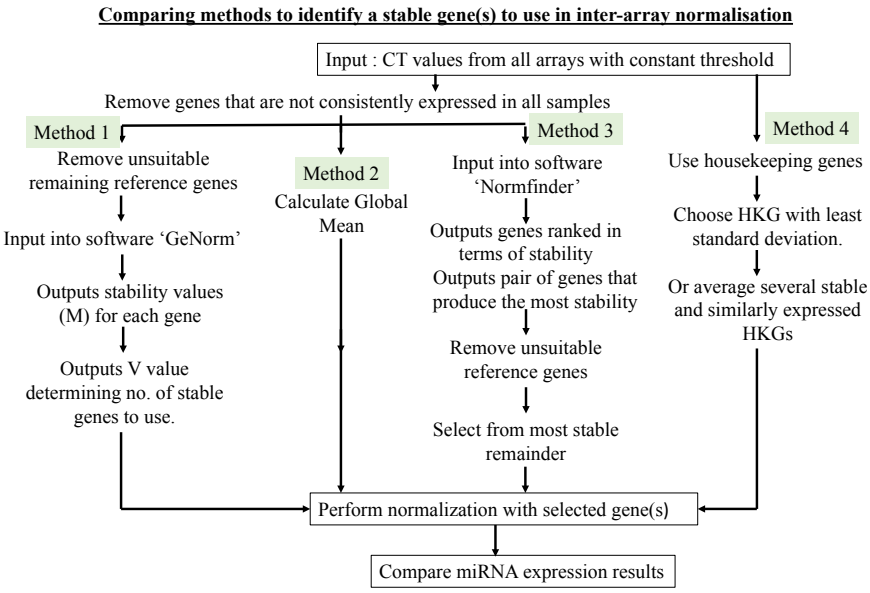

FIGURE 3.9: Normalisation between arrays. A consistently expressed gene must be identified or the results normalised to a global mean (of each array). Different techniques were used to identify stable genes, then the resulting miRNA expression patterns post normalisation were compared to see if any patterns changed.

GeNorm: GeNorm was developed by Vandesompele *et al* in 2002 and uses a global mean normalisation strategy to identify stable genes [342]. For each gene, an stability value M is calculated and the lower the value of M, the more stable the gene (Figure 3.10 panel 1). The second part of the analysis determines the number of reference genes that should be averaged and used to normalise the data. The minimum number of reference genes needed to produce a variance value V threshold of <0.15 is the suggested number of genes to average and use as a normalisation factor (Figure 3.10 panel 4). V is calculated when using the average of n = 1...10 reference genes (see Appendix A.1).

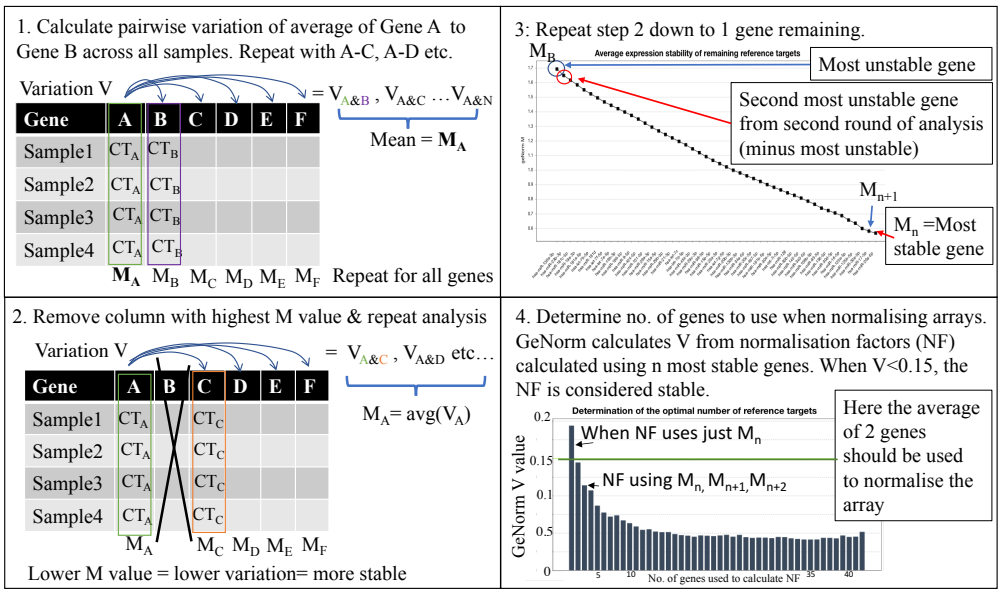

FIGURE 3.10: GeNorm identifies stably expressed genes. 1-3: GeNorm uses an iterative process, removing the least stable gene and repeating its calculation process each time to rank genes in order of stability. GeNorm suggests using the average value of several stable genes as a normalisation factor (NF). To find out how many stable genes to use, a V value is calculated from the pairwise variation of NF using 1...10 genes (see Appendix A.1). The number of genes required to produce V<0.15 is the suggested number of stable genes to average and to use to normalise the array data.

Global Mean Method: Each array is normalised to the average CT value of all miRNAs in that array that were consistently expressed in every sample.

Housekeeping gene method: The miRNA array plate contained 6 primers for pre-identified housekeeping genes; SNORD61, SNORD68, SNORD72, SNORD95 , SNORD96A, RNU6-2. To identify the most stable HKG, we compared the standard deviation of each HKG and other miRNAs across all samples. To identify the most suitable stable pair of HKG, we compared the intra-array standard deviation of the 6 housekeeping genes to each other to identify which pair of housekeeping genes were most similarly expressed and whether this pair also showed a low inter-plate standard deviation.

Normfinder A method to rank candidate reference genes by stability by applying an algorithm developed by Anderson *et al* 2004 [343] and published as 'Normfinder'. A model is defined for k genes and G groups with n_g samples in each group. There are therefore $1...k$ genes and $j..n_g$ number of samples per group g. A value y is calculated, representing gene expression for gene i for sample j of group g using three terms:

α_{ig} : represents general expression level for candidate genes i in group g.

β_{gj} : represents amount of miRNA in sample j.

ϵ_{igj}**:** represents random variation caused by biological and experimental factors. Is assumed to have a mean of zero and variance σ^2 of all genes in the group.

$$y_{igj} = \alpha_{ig} + \beta_{gj} + \epsilon_{igj} \tag{3.1}$$

To identify the most stably expressed gene using the model shown in Equation 3.1, intra-group variation is estimated, followed by estimation of the inter-group variation (see Appendix A.1). The value Z_{ig} is produced, defined as the average of y_{igj} over all samples in group g, and the value θ_g, which is the average amount of miRNA over all samples in group g. The final step is to consider α_i as the mean expression of a specific gene for each group. Then in future experiments Z_{ig}-$\theta_g - \alpha_i$ defines the stability of a gene. Further statistical details can be found in the Appendix B. The free analysis plug-in for excel and R can be found at https://moma.dk/normfinder-software.

The results of the application of several different normalisation strategies commonly identified several stable genes (Table 3.3). This included the miRNAS: mir-30a-5p, miR-125a-5p,SNORD 95. Some miRNAs such as miR20a-5p and miR-17-5p were not considered as suitable normalisation factors despite appearing stable as they play known roles in LEC inflammation [70] .

Table 3.3: Different methods were to identify stably expressed genes. MiRNA-30a-5p, miR-125a-5p, SNORD 95 were selected for further investigation. The miRNA miR20a-5p and were miR-17-5p considered unsuitable for use as normalising genes due to their known involvement in LEC inflammation.

Standard Deviation			NormFinder			Genorm		
B12	2.64	miR-181b-5p	C08	0.010	miR-20a-5p.	C08	-	miR-20a-5p.
B08	2.64	miR-15b-5p	B01	0.011	miR-128	B10	-	miR-17-5p
G12	2.69	miR-98-5p	A10	0.016	miR-106b-5p	D11	-	miR-30a-5p
C12	2.75	miR-98-5p	D12	0.018	miR-30b-5p	A12	-	miR-125b-5p
D01	2.77	miR-98-5p	D11	0.018	miR-30a-5p	A11	-	miR-125a-5p
E01	2.82	miR-30c-5p	E05	0.018	miR-34a-5p	B09	-	miR-16-5p
A11	2.85	miR-125a-5p	B10	0.020	miR-17-5p	E02	-	miR-30d-5p
E03	2.87	miR-30e-5p	C09	0.021	miR-20b-5p	C04	-	miR195-5p
B11	2.9	miR-181a-5p	A11	0.0227	miR-125a-5p	G11	-	miR93-5p
E02	2.94	miR-181a-5p	H06	0.023	SNORD95	H6	-	miR-SNORD95
C04	2.95	miR-195-5p	C04	0.023	miR-195-5p	B06	-	miR-145-5p
A04	2.98	hsa-let-7d-5p	G11	0.023	miR-93-5p	E04	-	miR-340-5p
A07	2.99	hsa-let-7g-5p	E01	0.023	miR-30c-5p	A10	-	miR-106b-5p
C02	3.04	hsa-miR-181d	E02	0.024	miR-30d-5p	A08	-	miR-7i-5p
G11	3.07	hsa-miR-93-5p	H07	0.024	SNORD96A	D12	-	miR-30b-5p
D11	3.10	hsa-miR-30a-5p	B03	0.026	miR-130b-3p	B01	-	miR-128

The standard deviation of the predefined housekeeping genes was also examined(Table 3.5) and the standard deviation of the difference between pairs of HGKs across the 10 samples was calculated(Table 3.4). SNORD95 and SNORD96A showed the least variation and presented with similar CT values.

Table 3.4: Pairwise HKG analysis

Mean Stdev. between pairs						
	SN061	SN68	SN72	SN95	SN96A	RNU6-6P
SN61	x	1.43	1.29	2.11	1.48	**0.87**
SN68		x	2.33	1.16	0.86	1.04
SN72			x	2.97	2.34	2.16
SN95				x	**0.88**	1.79
SN96A					x	1.26
RNU6-6P						x

* SN= SNORD.

Table 3.5: Single HKG analysis

Well	Stdev
SN61	4.108
SN68	3.774
SN72	4.944
SN95	**3.133**
SN96A	**3.206**
RNU6-6P	4.394

* SN= SNORD.

Normalisation of miRNA expression

To ensure identification of a suitable stable reference gene, the raw qPCR data was normalised several times using a selection of the miRNAs identified above. This included SNORD95, the mean of two miRNAs (SNORD95 and SNORD96A), miR-30a-5p and miR-125a-5p. The resulting miRNA δ CT values showed similar result patterns, apart from when the mean of two miRNAs was used. SNORD95 was selected to normalise the data, due to the lack of any known involvement in cancer or inflammation, and as the only pre-defined housekeeping gene that appeared in the top 10 stable genes identified by both Normfinder and GeNorm.

Statistical Analysis of differentially expressed miRNA

Real time qPCR data was analysed using a model of exponential amplification, where N is the concentration of amplified specific cDNA , E is the amplification efficiency and c is the number of cycles. The initial concentration, N_O, is the value that is estimated.

$$N = N_o E^c \tag{3.2}$$

The efficiency is usually set as log2, representing 100% efficiency and doubling of miRNA each cycle. Efficiency of each cycle is assumed to be constant. The CT value that we recorded for each gene is the number of amplification cycles required to reach a signal threshold. To analyse the miRNA array data, CT values produced for each array were normalised to the CT value of the selected stably expressed gene. This is referred to as the Δ CT value. The fold change difference between expression of a gene in two sample groups is calculated as the logarithm (base2) of the mean Δ CT of the gene in group 1 divided by the mean Δ CT of the gene in group 2.

$$\Delta\Delta CT = 2^{-\Delta CT} Fold\,Change = \frac{Mean(\Delta\Delta CTdisease)}{Mean(\Delta\Delta CTControl)} \tag{3.3}$$

The resulting fold-change expression has a value of 1 for exactly no change between groups, a value of 2 for a doubling of expression between groups and a value of 0.5 for a halving of expression between groups. A fold-regulation value is calculated by taking the log2 of all negative values so that values less than

1 are now represented as negative values, eg. 0.5 = -2, to more easily interpret and compare results.

A second statistical analysis is performed using the hypothesis that there is no difference in expression of the miRNA transcripts in one group compared to the other group. A student's T test was applied to the $\Delta\Delta$ CT values to analyse the ratio of the difference between the two groups versus the difference within the groups.

Pathway analysis: The functional pathway analysis programs TARBASE, TARGETSCAN and Micro-CDS were used to analyse the miRNAs that showed a fold-regulation change of $+/-1.8$ and differential regulated miRNA identified using the T-test with a p-value$<$0.05.

Principle component analysis (PCA). PCA was also performed on the normalized miRNA expression data. PCA is a method that linearly transforms multivariate data into a set of uncorrelated variables and orders them in descending order by the variance explained by them. Micro RNA with the largest variation in expression between samples have the most influence on principle components. The expression of each miRNA contributes to the calculation of a single PCA, but the contribution is weighted resulting in an array of loads for each PCA (eigenvector). PCA component captures the most variation in the data set and the second PCA the second most variation in the data. Therefore, miRNA driving PC1 and PC2, (those with the highest absolute weighting), have the greatest relative contribution to the variation between sample groups. Samples with the most similar miRNA expression profile cluster together and clusters may vary over PCA1/PCA2 or both. A PCA scree analysis was also performed to check that the two primary principle components accounted for most of the variation between the groups. The free online software ClustVis was used to analysed the miRNA data [344].

3.3 Results

3.3.1 Overview

Overall, highly inflamed LVs at time of surgery correlated to patient relapse within 13.2 ±3.6 month. This was shown by the significant association detected using Fisher's exact test, and the substantial agreement shown by the Cohen's Kappa value (Table 3.7. This presented the previously unknown finding that macroscopically normal LVs away from the tumour site undergo changes in inflammatory status that accompany or contribute to patient relapse. Highly inflamed LVs samples, quantified using thresholds on positive staining with inflammatory marker MPO, presented with a differential miRNA expression pattern compared to non-inflamed LVs. Combined with the aforementioned novel insight that highly inflamed LVs accompany relapse, the dys-regulated miRNA may present as, firstly, an insight into underlying mechanisms contributing to relapse and secondly as future novel therapeutic targets. Clinical correlation of LVs with cancer-cell infiltration showed a moderate agreement with relapse (Cohen's Kappa 0.61) but the association was not significant (P=0.1) but differential expression of miRNAs was observed between LV samples shown to contain cancer cells and LVs with no cancer cell presence detected.

Alteration in miRNA expression were specific to either cancer containing or inflamed LVs but several common miRNA expression alterations were observed in both inflamed and cancer-containing LV groups, such as the down-regulation of the let-7 family. The let-7 family has previously been identified as tumour suppressors, when expressed in tumours and found down-regulated in tumours in several cancer including ovarian cancer, and chemo-resistant tumouts [308, 309, 311, 314, 317, 345, 346]. Down-regulation of the let-7 family in highly inflamed LVs, presents as a second novel finding. Analysis of the function of let-7 and other dyregulated miRNA, and the implicated pathways showed that inflammation regulation, the EMT pathway and vessel integrity are likely to be affected by the dyregulated miRNA.

3.3.2 Imaging allowed quantification of cancer-infiltration status of macroscopically normal LV samples

Cryo-sections of LV samples that had been stored at -80°C maintained sufficient morphology for the purpose of quantifying inflammation and cancer cell presence. Figure 3.11 shows the H and E stained sections of the LVs, with the nuclei preserved sufficiently to be able to detect the nucleus-locating antibodies for Pax-1 and WT1. The LV lumen can also be seen, and although not always completely intact (3.11c), still presented with sufficient structure and surrounding tissue to be able to detect the presence of enzymes and cancer cells around and within the LV.

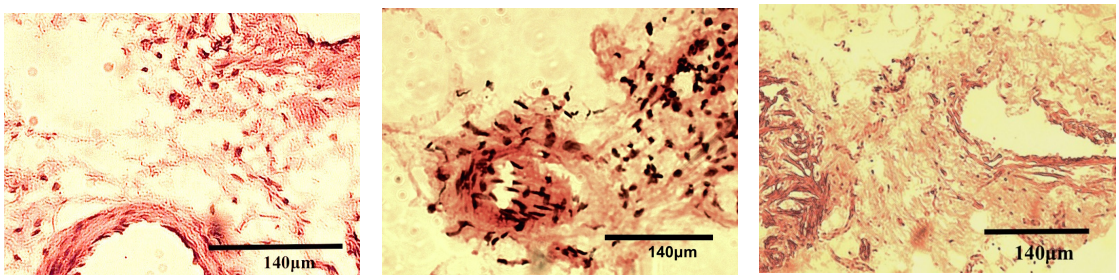

(A) Sample 1 (B) Sample 2 (C) Sample 5

FIGURE 3.11: Sample H & E vessel staining. Hematoxylin (violet) stains the nuclei and Eosin(pink) attaches to basic proteins, staining collagen pink. Together they showed preservation of basic vessel structures and cell nuclei.

The lymphatic status of the vessel samples was confirmed by staining with the lymphatic endothelial cell marker Podoplanin, and recording the positive stain. Figure 3.12 shows examples of the resulting stain around the lumen of the LV samples.

When the presence of inflammatory marker MPO in the LV samples was compared to a section taken from an ovarian cancer tumour (Figure 3.14), all the LVs presented with relatively low inflammation. The LVs were then graded within this subgroup. Low inflammation was classed as a ratio of less than 3% MPO, which in some samples meant no positive staining at all (Figure 3.13a). Medium inflammation was classed as 3-10% (3.13b) and >10% was classed as high inflammation 3.13c. A complete set of images and controls can be found in Appendix B2.

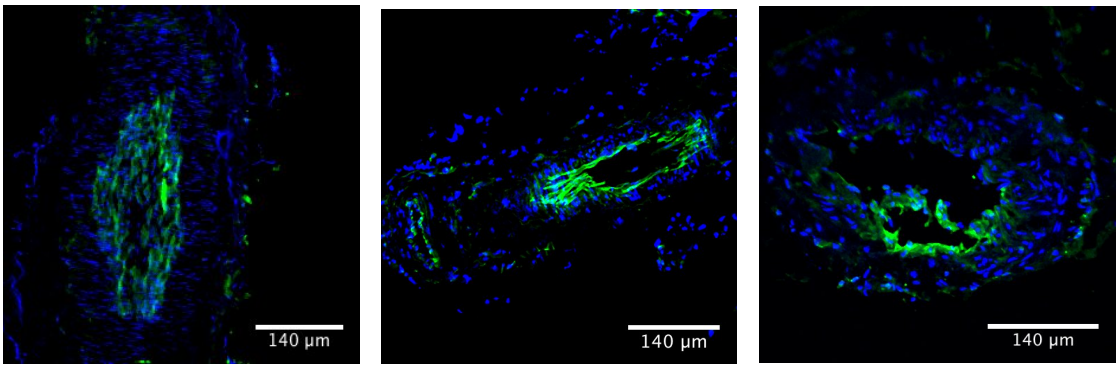

(A) Sample 1 (B) Sample 2 (C) Sample 10

FIGURE 3.12: Staining of the lymphatic endothelium with podoplanin. Podoplanin (green) and cell nuclei (blue). Pane (c) shows a slightly diagonally sectioned vessel.

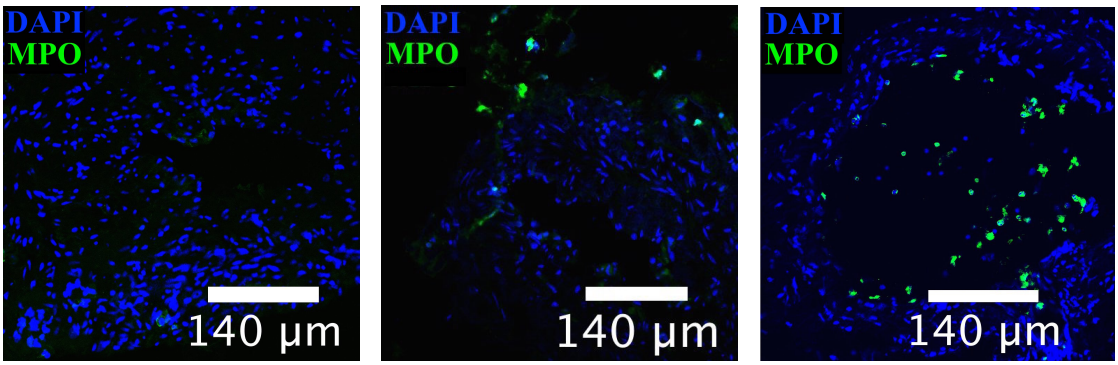

(A) Sample 8: displaying no (low) inflammation (B) Sample 4: displaying medium inflammation: (C) Sample 3: displaying high inflammation

FIGURE 3.13: Sample staining of LV inflammatory marker. Blue = DAPI, green = Myeloperoxidase. Relative levels of inflammation are low across samples but graded within this subgroup. For example, sample 4 (b), displayed relatively low inflammation despite classification into a medium group.

The samples were macroscopically normal and outwardly healthy looking but staining with the ovarian cancer marker WT1 antibody resulted in positive stains for four of the 10 samples collected. Due to the low number of cancer cells present, the positive stains were graded based on number of cancer cells observed in a cross section with 15+ cancer cells, such as in Figure (3.15a), graded as high (+++), 5-10 cells graded as medium (++) and less than 5 cells as no-low (+). A negative sample showed no cancer cells (3.15c)

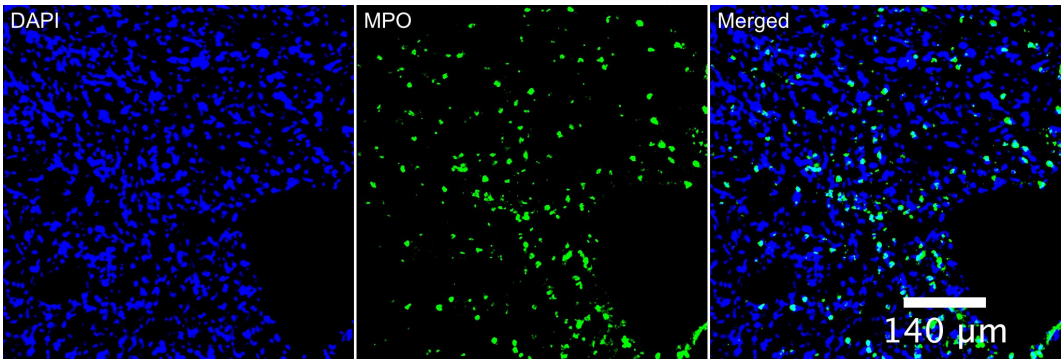

FIGURE 3.14: Sample staining of positive control EOC tumour. Blue = DAPI, green = Myeloperoxidase. Staining of a section of tumour from an endothelial ovarian cancer tumour displayed a high level of inflammation.

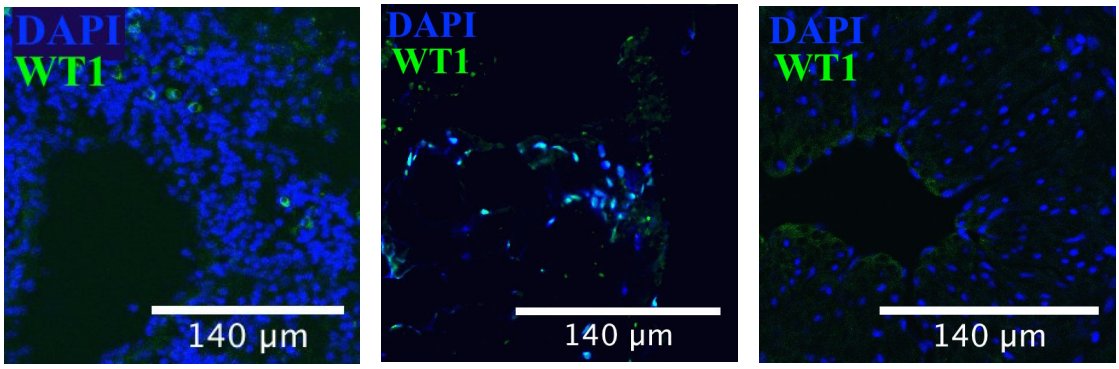

(A) Sample 1: positive +++ (B) Sample 4: positive ++ (C) Sample 8: negative

FIGURE 3.15: Sample LV Wilms-Tumour-1 staining. Blue = DAPI (nuclear staining), green = WT1 staining. Figure (a) shows densely packed cells whilst (b) shows the LV lumen to the right of a cluster of cancer cells. No cancer cells were detected with WT1 antibodies in c.

Staining for a second ovarian cancer marker, the transcription factor paired box gene 8 (Pax 8) resulted in positive stains in three samples. All 3 samples had also stained positively using WT1. A ovarian cancer tumour sample was used as a positive control and stained positively for both WT1 and Pax8 (3.16c). The remaining 6 samples that did not stain positively with WT1 or Pax8 were defined as the non-cancer containing LVs. See Appendix B2.2 for further images.

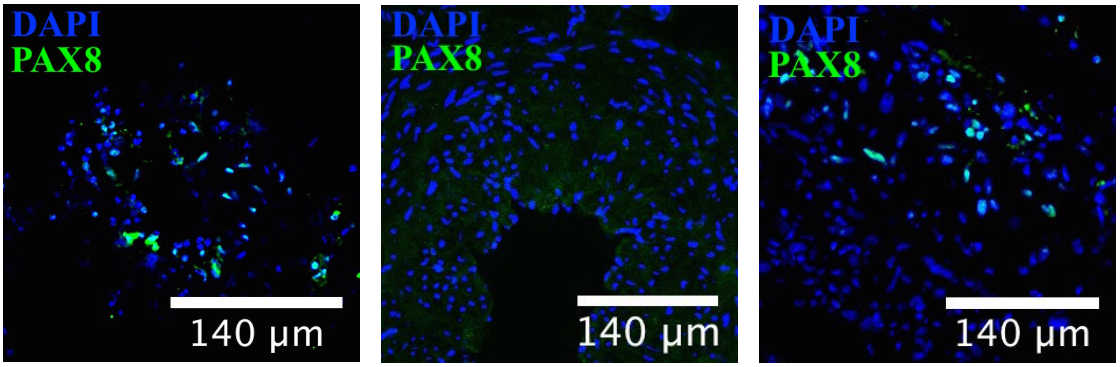

(A) Sample 2: Positive +++ (B) Sample 8: Negative stain (C) Tumour: positive +++

FIGURE 3.16: Sample LV Pax8 staining. Blue = DAPI (nuclear staining), green = PAX8 staining. Figure (c) shows the staining of a tumour sample used as a positive control for the PAX8 antibody

LV state at time of surgery correlated to patient relapse.

Using the results of the image analysis (Table 3.6), the relationship between the state of the LV at time of surgery and patient relapse (within 13.2±3.6 months) and cancer stage was analysed. LVs with high inflammation showed a substantial agreement with relapse when assessed using cohen's kappa coefficient and also showed significant association (p=0.033) (Table 3.7 with relapse. High and medium inflammation showed a moderate association with relapse and association with significant p=0.07. LVs, within which cancer cells were detected, showed a moderate agreement with clinical relapse but this was not significant (p=0.1) (Table 3.7 p<0.05) .

TABLE 3.6: Summary of the LV imaging results and clinical data. Sections of the LVs were stained with antibodies for the inflammatory marker myeloperoxidase (MPO), ovarian cancer markers Wilms-Tumour-1 (WT1) and Paired Box Gene 8 (Pax8), and the lymphatic endothelial marker, Podoplanin (PDPN).

Vessel	Type of marker						
Sample	MPO	WT1	PAX8	Stage	Histology	LN histology	Relapse*
1	+++	+++	++	IVB	HGS	-	y
2	+++	+++	+++	IVA	HGS	n/a	y
3	+++	-	-	IIC	HGS	n/a	y
4	+	++	+	IV	HGS	n/a	y
5	-	-	-	IIIB	Clear Cell	n/a	n
6	-	-	-	IIIC	HGS	n/a	n
7	-	-	-	IIIC	hGS	+	n
8	-	-	-	IIIC	HGS	n/a	n
9	+	-	-	IVB	HGS	n/a	n
10	+	+	++	IIC	HGS	-	n

Key	MPO	WT1/Pax8
	+++ high	+>=15 cells
	+ medium	++ 15> cells >=5
	- low	+ < 5 cells

*Mean time since surgery = 13.2 months ±3.6

TABLE 3.7: Cohen's Kappa Coefficient for inner-agreement between different sample states (1=perfect agreement) and Fisher's exact test for identification of significant non-random association (p<0.05) (n=10). Inflam.= comparison of LVs with high or medium inflammation to low inflammation. High Inflam. = comparison of LVs with high inflammation to low or medium inflammation. Cancer-cell inf.= cancer-cell infiltration.

Cohen's Kappa Co-efficient					
	Relapse	Inflam.	High Inflam.	Cancer-cell infil.	>=StageIV
Relapse	x	**0.615**	**0.783**	0.583	0.583
Inflam.	**0.615**	x	x	**0.615**	**0.615**
High Inflam.	**0.783**	x	x	0.348	0.348
Cancer-cell infil.	0.583	**0.615**	0.348	x	0.583
>=StageIV	0.583	**0.615**	0.348	0.348	x

Fishers Exact Test (p-value)					
	Relapse	Inflam.	High Inflam.	Cancer-cell infil.	>=StageIV
Relapse	x	**0.071**	**0.033**	0.114	0.114
Inflam.	**0.071**	x	x	**0.071**	**0.071**
High Inflam.	**0.033**	x	x	0.300	0.300
Cancer-cell infil.	0.114	**0.071**	0.300	x	**0.071**
>=StageIV	0.114	**0.071**	0.300	0.114	x

Mean time since surgery = 13.2 months ±3.6

The clinical correlations between LVs presenting with high and low inflammation only (no medium)(n=7) were assessed (Table 3.8). Highly inflamed LVs and relapse presented with a near perfect agreement when Cohen's kappa was calculated (1.0) and Fishers Exact test identified significant association (p=0.029). A substantial agreement was found with high inflammation and cancer-infiltration and patients with >=stageIV cancer but Fishers Exact test did not support a significant association (p=0.143). These results support the earlier clinical correlation observed (Table 3.7), with a stronger agreement and smaller p-value, but the smaller sample size (n=7) suggests a larger sample size of LVs with high or low inflammation is needed to generalise this statement.

TABLE 3.8: Assessment of clinical correlation between LVs presenting with high inflammation and those presenting with low inflammation (n=7), using Cohen's Kappa Coefficient for inner-agreement between different sample states (1=perfect agreement) and Fisher's exact test to identify significant non-random association between groups.

Cohen's Kappa Co-efficient			
	Relapse	Cancer	>=Stage IV
Inflam(High vs Low)	1	0.695	0.695
Fishers Exact Test			
Inflam (High vs Low)	0.029	0.143	0.143

LVs showed differential miRNA expression when inflamed or cancer-cell infiltrated

The next step was to analyse the underlying miRNA expression changes in the cancer containing vessels compared to cancer-free vessels, and in highly inflamed vessels versus non-inflamed vessels. The micro array results showed that an entire cluster of miRNAs were consistently not expressed in any of the LV samples. The non-expressed miRNA were therefore not included in any further analysis,but can be found in Appendix A.3 Table B.1. Figure 3.18 shows the remaining relative expression of 74 miRNAs after normalisation to the expression of SNORD95 in each sample. The relative over-expression and under-expression is not a comparison between cancer containing or inflammatory LV groups, but the expression in a particular vessel relative to the expression of SNORD 95.

Inflamed LVs and cancer-containing LVs showed slightly different alterations, as in the cancer-infiltrated LVs, most miRNA expression changes involved up-regulation, whereas the inflamed LVs showed more down-regulation. Table 3.9 depicts miRNA that showed a ± 1.8 fold change expression between groups. The p-value refers to the results of a second analysis using a t-test to identify variation between the mean miRNA expression between groups. Similar changes in the expression of several miRNAs were found in both the inflammatory and cancer-cell containing comparison, as shown in Figure 3.17. The following section summarises the known targets that the identified dysregulated miRNA inhibit (Table 3.10).

The expression of let-7 family members was down-regulated in inflamed LVs and accounted for almost all the down-regulated miRNA in the cancer-containing LVs. The let-7 family are considered tumour suppressors, and the down-regulation is consistent with that observed in ovarian cancer tumours and cell lines 3.1 [308, 309, 311, 314, 345, 346]. Functionally, in endothelial cells, let7 family members have roles in regulation of epithelial-to-mesenchymal transition, apoptosis and inflammation [347–351]. Although predominantly associated with anti-inflammatory roles, pro-inflammatory roles have also been reported (Table 3.10).

TABLE 3.9: Differential expression of miRNA between LV groups. Expression of LV that showed a fold change ± 1.8 and/ or a a significant difference between groups (t-test p>0.05)

Cancerous compared to Non-Cancerous		
miRNA	**Fold Regulation**	**p value**
miR-144-3p	**14.020**	**0.001**
miR-181c-5p	**10.629**	**0.017**
miR-301a-3p	7.300	0.309
miR-19a-3p	6.896	0.197
miR-19b-3p	6.055	0.147
miR-101-3p	5.083	0.074
miR-381-3p	**4.070**	**0.014**
miR-181a-5p	3.875	0.274
miR-130a-3p	3.853	0.115
miR-186-5p	3.214	0.131
let-7a-5p	2.920	0.287
miR-497-5p	**2.902**	**0.026**
miR-590-5p	2.780	0.521
miR-15a-5p	2.767	0.182
miR-511-5p	2.570	0.130
miR-93-5p	**2.252**	**0.001**
miR-29a-3p	2.166	0.525
miR-29b-3p	2.098	0.320
miR-16-5p	**2.077**	**0.031**
let-7i-5p	**-2.080**	**0.021**
let-7b-5p	-2.274	0.070
let-7e-5p	-2.505	0.432
let-7c-5p	-2.556	0.078
let-7d-5p	-2.672	0.122
let-7f-5p	-3.239	0.270
miR-202-3p	-4.800	0.299

up-regulated | down-regulated

Bold= p < 0.05

Inflamed compared to Non-Inflamed		
miRNA	**Fold Regulation**	**p value**
miR-301a-3p	13.657	0.340
miR-186-5p	6.327	0.104
miR-410-3p	5.817	0.167
miR-19a-3p	5.740	0.385
miR-144-3p	4.933	0.193
miR-548d-3p	4.780	0.202
miR-19b-3p	4.423	0.343
miR-101-3p	4.180	0.340
miR-29b-3p	2.528	0.348
miR-590-5p	2.453	0.792
miR-497-5p	2.442	0.289
miR-15a-5p	2.301	0.405
miR-381-3p	2.175	0.240
miR-195-5p	-1.945	0.132
miR-29a-3p	-2.013	0.724
let-7i-5p	-2.132	0.078
miR-301b-3p	-2.605	0.430
miR-23a-3p	**-2.889**	**0.018**
let-7g-5p	-3.122	0.121
miR-875-3p	-3.152	0.328
let-7e-5p	**-3.163**	**0.040**
let-7f-5p	**-3.462**	**0.041**
miR-98-5p	-3.790	0.168
miR-15b-5p	**-4.167**	**0.047**
let-7d-5p	**-4.907**	**0.004**
miR-202-3p	-5.950	0.236
miR-181d-5p	-6.426	0.131
let-7c-5p	**-6.666**	**0.001**
miR-130a-3p	-6.752	0.652
let-7b-5p	**-11.026**	**0.003**
miR-513b-5p	-12.343	0.054
miR-23b-3p	**-13.016**	**0.010**
let-7a-5p	**-222.405**	**0.024**

up-regulated | down-regulated

Bold= p < 0.05

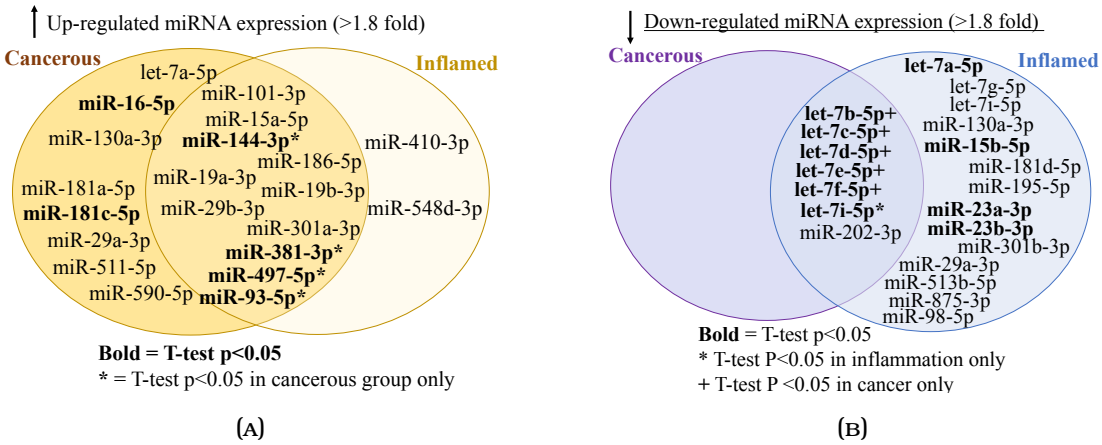

FIGURE 3.17: Overlap was observed between differential expression of miRNA in inflamed LVs and in cancer-infiltrated LVs. In particular, the down-regulation of the let-7 family was identified in both comparisons. (a) There are many more miRNAs that are up-regulated when comparing LVs with or lacking cancer-cell infiltration than when comparing inflamed versus non-inflamed LVs. (b) The majority of miRNA expression changes identified in inflamed LVs involved down-regulation.

Expression of miR-181a-5p, which was up-regulated in cancer-containing LVs The miR-181a-5p, which was up-regulated in cancer-containing LVs, is known to inhibit the gene Prox-1, the expression of which is required to maintain an LEC phenotype . [319, 320, 352]. Expression of miR-181a in EOC tumours also correlated poorly with prognosis and promoted TGF-β-mediated EMT, suggesting expression is likely detrimental to maintenance of a normal LEC phenotypes [308, 353]. In the cancer-containing LVs miR-144 was also up-regulated, which has known roles in differentiation of LVs and blood vessels in mice and zebrafish.

Upregulation of miR181-c expression was identified in the cancer-containing LVs only. Target genes have not been identified in endothelial cells but studies in brain cancer have shown that miR-181-c targets PDK1, a protein integral in the PI3k-AKT pathway [354]. Mutations in the PI3K pathway have been observed in the LECs of patients with lymphatic malformation [355].

The miR-15a-16-1 cluster are known tumour suppressors and inhibitors of vascular endothelial growth factor (VEGF) and were upregulated in the cancer –infiltrated LVs [356–358]. In EOC, miR-15a-5p and miR-16-5p directly target

oncogene Bmi-1 and may inhibit mechanisms that promote EOC progression and chemo-resistance [359, 360]. Both miR-15-5p and miR-16-5p also target anti-apoptotic gene BCL-2 in leukaemia [361].

Expression levels of miR381-3p increased 4-fold in cancer containing LVs and is known to inhibit VEGF-C dependent lymphangiogenesis [362]. In EOC cultures, miR-381 contributed to inhibition of EOC cell proliferation, migration and invasion by targeting YY1 in a miR-381/YY1/p53 and miR-381/YY1/Wnt-signaling axis [363].

MiR-497-5p was up-regulated in cancer-containing LVs and inflamed LVs, consistent with up-regulation observed in inflamed rat LVs, and has been shown to suppress endothelial cell proliferation [70, 364]. Oncogenic function of miR-497 has been reported in some cancers such as colorectal cancer and glioma but in many other cancers, including ovarian cancer, miR-497 has been associated with tumour suppressor-like functions (rev. [365]).

The expression of miR-93-5p was upregulated in cancer containing vessels only. Limited research has been carried out to understand the function of miR93-5p in endothelial cells, but overexpression of miR93-5p in HUVECs was pro-angiogenic and accelerated proliferation, migration and sprouting [366]. Binding sites for miR-93-5p were predicted in both chemokine IL8(CXCL8) and VEGF, which was confirmed in a study using neuroblastoma SKNAS cell lines [367]. In EOC, miR-93-5p up-regulation has been significantly correlated with poor prognosis and directly targets the tumour-suppressor PTEN [317, 368]. However, it has also been found to inhibit oncogene RhoC and reduce cancer-cell proliferation [369].

MiR-29b was upregulated in both cancer-containing and inflamed LVs and miR-29a in cancer-containing LVs only. Both miRNA are known to contribute to regulation of endothelial cell inflammation and nitric oxide production [370]. In endothelial cells miR-29 may also aggravate inflammation by increasing secretion of inflammatory cytokines TNF-α, IL-1$\alpha$and INF-γ [371]. In ovarian cancer, miR-29a/b target AKT2 and AKT3, which are involved in cancer cell metabolism, miR-29b targets an anti-apoptotic bcl-2 family member and miR-29a is known to target SIRT1, suppressing EOC progression[308, 372, 373].

Micro RNA miR-19a and miR-19b were upregulated in the inflamed and cancer-containing LVs. Both miRNA are part of the miR-17-92 cluster, which regulate inflammation, maintain vascular integrity and promote anti-angiogenic effects in endothelial cells [374–376]. MiR-19b has been shown to reduce TNFα induced endothelial cell apoptosis and inhibit TGF-β1/Smad induced apoptosis [377, 378]. In EOC lines, miR-19a negatively regulates the expression of PTEN and promoted the growth of ovarian cancer cells [379].

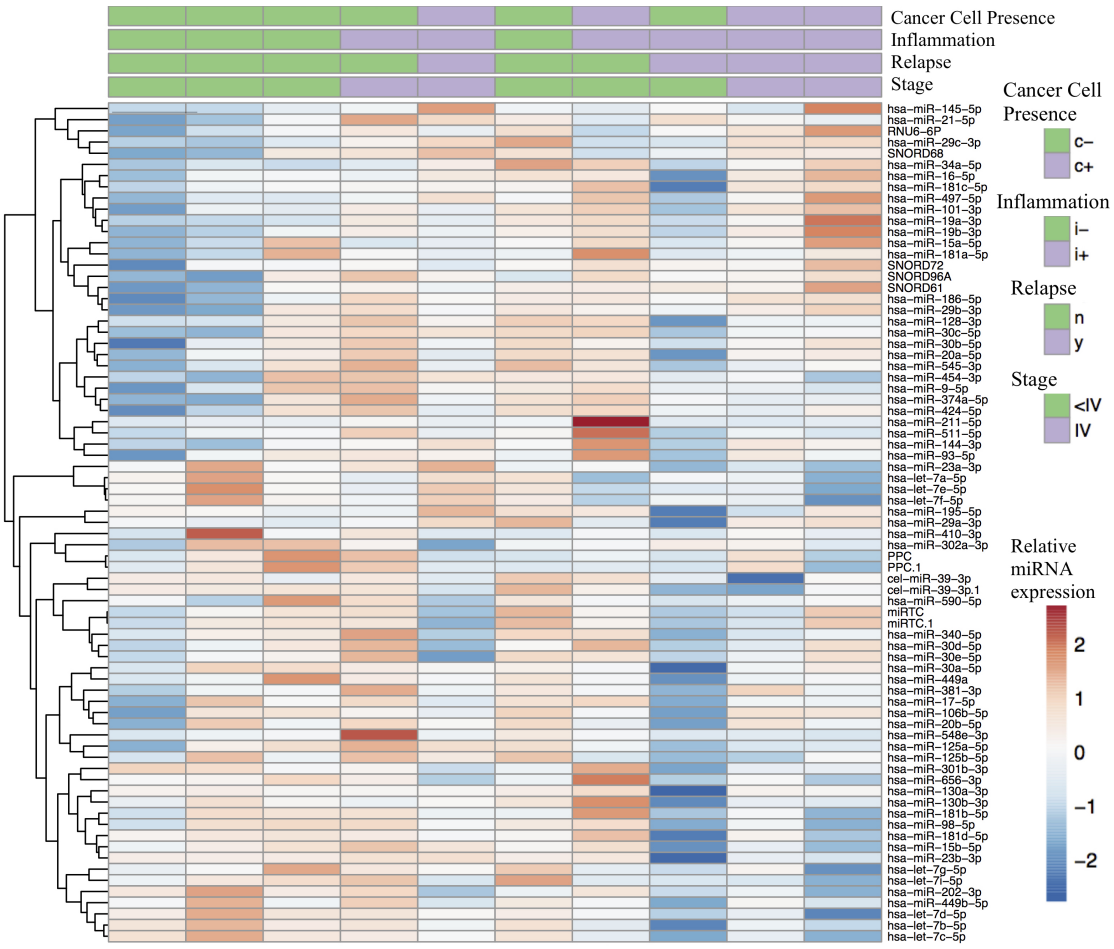

FIGURE 3.18: Normalised expression of miRNAs. To the expression of SNORD95 in each sample. One cluster of miRNAs did not express across all samples and is therefore not shown here (Appendix B.1). The variation in sample expression is partly due to the natural variation between patients and the quality of each sample. However further analysis allowed identification of commonly up-regulated and down-regulated miRNA in the different sample groups from this raw data. Produced with ClustVis [344]

TABLE 3.10: The known function of the dysregulated-miRNA in cancer-infiltrated and/or inflamed LVs. Roles in endothelial cells and epithelial ovarian cancer (EOC) are prioritised with additional relevant targets listed.

miRNA	Target	Cell type	Pathway/Function	Ref.
let7e-5p	IL$\beta\beta$	Endothelial (HUVECs)	pro-Nfkβ pathway	[347]
	TGFβ	Endothelial (HUAEC)	pro-EMT	[348]
let7g-5p	LOX-1	VSCMs	anti-apoptotic	[380]
	IL10	TH1/TH17 T cells	pro-inflammatory	[349, 350]
let7f-5p	IL10	CD4$^+$ T,cells	pro-inflammatory	[381]
	IL3	Lymphocytes	anti-inflammatory	[351]
let7a-5p	IL6	epithelial (Malignant)	pro-cancer-cell survival	[382]
let7 family	RAS	EOC lines	tumour/Ras/MAPK-suppressor	[346]
	HMAG2	EOC lines	anti-apoptotic, tumour-suppressor	[345]
miR 181a-5p	Prox-1	Endothelial (LECs/VECs)	maintain LEC phenotype	[319, 320]
	Smad7	EOC line	promotes,TGF-β-mediated-EMT	[353]
miR 181c-5p	PDPK1	Cancer cell lines	actin dynamics, pAkt	[354]
miR 15-5p	FGF2, VEGF	Endothelial (HUVECs)	anti-angiogenic/migration/differentiation	[356]
miR 15a-5p	indirect	Endothelial (RECs)	anti-TGFβ3 /VEGF signals	
& 16-5p			increase key tight junction proteins	[358]
	BCL-2	Cancer cell lines	tumour suppressor/CCND1/WNT3A	[383]
	Bmi-1	EOC cell line/tissue	tumour-suppressor anti-proliferation	[359]
	BCL-2	Leukemic cell line	pro-apoptotic	[361]
	VEGF-A	Multiple myeloma	anti-angiogenic, anti-tube formation	
			anti-migration/differentiation	[357]
miR-497-5p	BCL-2	Endothelial (HUVECs)	anti-proliferation via Bcl-2/	
	CCND2		Bax-Casp9-Casp3 and Cyclin D2	[364]
	BCL-2/IFFβ	Cancer cell lines	tumour suppressor	[365]
	VEGFRA			
miR 381-3p	indirect	Endothelial (LEC)	anti-bFGF/VEGFC expression	
			anti-BFGF-promoted tube formation	[362]
	YY1	EOC line	anti-cancer progression	
			and miR381/YY1/Wnt signalling	[363]
	MDR1	Breast cancer	anti-chemoresistance,pro-apoptotic	[384]
	FYN	Breast cancer	pro-chemosensitivity	[385]
	LHR01	Osteosarcoma	anti-LHR01/Wnt/B-catenin pathway	
			pro-caspase 3/9, Bax/Bcl-2 and p53	[386]
miR 93-5p	EPLIN	Endothelial (HUVECS)	pro-proliferative/migration/angiogenesis	[366]
	PTEN	Endothelial	anti-apoptotic miR93-5p/PTEN/pAkt	[368]
	RhoC	OC lines	pro-apoptotic, anti-migration/invasion	[369]
	IL8	Neuroblastoma	anti-angiogenic	[367]
	VEGF	Neuroblastoma	anti-angiogenic	[367]
miR 29a-3p	Lypla	Endothelial (arterioles)	promotes normal Nitric Oxide production	[370]
	SIRT1	EOC lines	anti-proliferation/migration/invasion	[373]
miR29b-3p	Lypla	Endothelial (arterioles)	promotes normal Nitric Oxide production	[370]
	indirect	Endothelial (HUVEC)	pro-inflammation/apoptosis	
			pro-NF-$\kappa\beta$ and JNK pathways	[371]
	MCL-1	Fibroblasts	anti-fibrotic miR-29/IL-6 axis	
			anti-TGF-β-mediated collagen up-reg.	[387]
	indirect	EOC cell lines	pro-chemosensitivity, inihibits ERK1/2	[388]
	AKT2/	EOC lines	regulates glucose transporter gene	
	AKT3		metabolism, tumour progression	[372]
miR-19a-3p	KLF10	Endothelial (rat VEC)	anti-apoptotic, pro-proliferation	
			Klf10 dependent TGF-β1/Smad signalling	[378]
	PTEN	EOC lines	pro-proliferation/differentiation	
			anti-apoptotic(PI3K)/AKT	[379]
miR-19b-3p	Apaf1	Endothelial (HUVECs)	anti-TNF-α-induced EC apoptosis	[377]
	Casp7		,Apaf1/caspase-dependent pathway	[377]
miR-144-3p	Meis1	Embryotic (Zebrafish)	decreases runx-1,c-myc,haematoepeoeisis	[389]
	SRF	Endothelial (HUVECs)	anti-proliferative, pro-apoptotic	[390]
	RUNX-1	EOC line	anti-proliferation anti-migration	[391].
	PAX-8	Papilliary thyroid	pro-proliferative/metastatic	
		carcinoma	via Akt and c-Jun N-terminal kinase	[392]
miR 23a-3p	ZO-2	Endothelial (HUVECs)	inhibit permeability	[393]
miR-23b-3p	JAM-C	Endothelial (HUVECs)	pro-angiogenic, increase permeability	[393]

EOC=Epithelial ovarian cancer EMT=Epithelial-to-Mesenchymal Transition
HUVEC=Human umbilical vascular ECs HUAEC=Human umbilical artery ECs

Principle component analysis results identified variation attributed to inflammation and cancer-infiltration.

The results of the PCA analysis show that most variation between samples could be accounted for by PCA component 1 and PCA component 2 3.19F. The miRNA that contributed the most to PCA1 and PCA2 can be seen in Table 3.11. PC1 shows a broad range of miRNA with many that were not identified as altered between groups of inflamed/non-inflamed LVs. The results may differ because PCA identifies variation between all the samples. For example, miR-20 varies a lot between the patient samples, however if the variation is spread between cancer containing LVs and normal LVs, the mean fold-difference between groups is unlikely to show a significant change. Of the top 16 miRNA whose expression contributed the most to PCA1, only 4 were were identified in the fold-change analysis. All 4 miRNA were up-regulated in cancer-containing LVs. In contrast, 75% of the top 16 miRNA that contributed the most to PC2 were also identified in the comparison of cancer containing and non-cancer containing vessels and inflamed versus non-inflamed LVs. The top 7 influential miRNA that contributed to PCA2, were identified as down-regulated in inflamed or cancerous vessels and 4 miRNA as up-regulated. Therefore, variation over PCA2 should differentiate cancer-containing samples and non cancer-containing samples.

Table 3.11: The contribution of miRNA to PCA component 1 and 2. The weighting is referred to as a load and an array of loads (eigenvector) is used to calculate each principle component. The 16 miRNA with the highest loads in the calculation of PCA1 and PCA2 are shown here. Micro RNA that were identified as differentially expressed in the earlier fold-change analysis between cancer-containing or inflamed LVs and non-cancer-containing or non-inflamed vessels are shown in bold. PC1 contained identified up-regulated miRNA and PC2 contained primarily down-regulated miRNA.

miRNA	PC1 load	miRNA	PC2 load
hsa-miR-20a-5p	0.183	**hsa-let-7c-5p**	0.216
hsa-miR-545-3p	0.176	**hsa-let-7d-5p**	0.213
hsa-miR-128-3p	0.174	**hsa-miR-202-3p**	0.193
hsa-miR-17-5p	0.164	**hsa-let-7b-5p**	0.186
hsa-miR-30b-5p	0.159	**hsa-let-7e-5p**	0.177
hsa-miR-93-5p	0.158	**hsa-miR-23a-3p**	0.175
hsa-miR-106b-5p	0.158	**hsa-miR-186-5p**	-0.171
hsa-miR-181c-5p	0.156	**hsa-miR-29b-3p**	-0.172
hsa-miR-340-5p	0.155	hsa-let-7f-5p	0.170
hsa-miR-30c-5p	0.154	hsa-miR-145-5p	-0.169
hsa-miR-101-3p	0.153	hsa-let-7a-5p	0.153
hsa-miR-125a-5p	0.150	**hsa-miR-181d-5p**	0.152
hsa-miR-20b-5p	0.148	**hsa-miR-19b-3p**	-0.150
hsa-miR-30d-5p	0.147	**hsa-miR-19a-3p**	-0.146
hsa-miR-16-5p	0.145	hsa-miR-15b-5p	0.145
hsa-miR-30a-5p	0.143	**hsa-miR-15a-5p**	-0.140

Figure 3.19 shows the variation between samples, over PCA1 and PCA2. Samples that express the most similar miRNA profiles cluster together. In all the figures represented, there is more separation between sample groups in the y-axis (PCA2) than in the x-axis (PCA-1), which is consistent with the results of the fold-change analysis. Inflamed and non-inflamed vessels vary similarly over PCA1 and PCA2 but can be divided more over PCA-1 (A). Cancer-containing LVs present with a more similar profile over PCA1 and PCA2 than non-cancer containing cells, whilst LVs samples from patients that did not relapse can be separated by the PCA-1 axis only. Figure 3.19 shows that variance in cancer containing cells is accounted for by both PCA1 and PCA2, but variation in cancer containing LV samples and samples from patients show similar profiles in PC1 only. Overall, considering the variation in miRNA expression across all patient samples, cancer-containing LVs present with more similar transcription profiles than non-cancer containing LVs. Inflamed LVs show more clustering along PCA2, meaning that they can be differentiated from non-inflamed vessels by the expression of miRNAs that relatively contribute most to PCA2. These are the down-regulated let-7 family, 202-3p, up-regulated miR19a, miR19b, miR15a, miR15b and 181d-5p, amongst others.

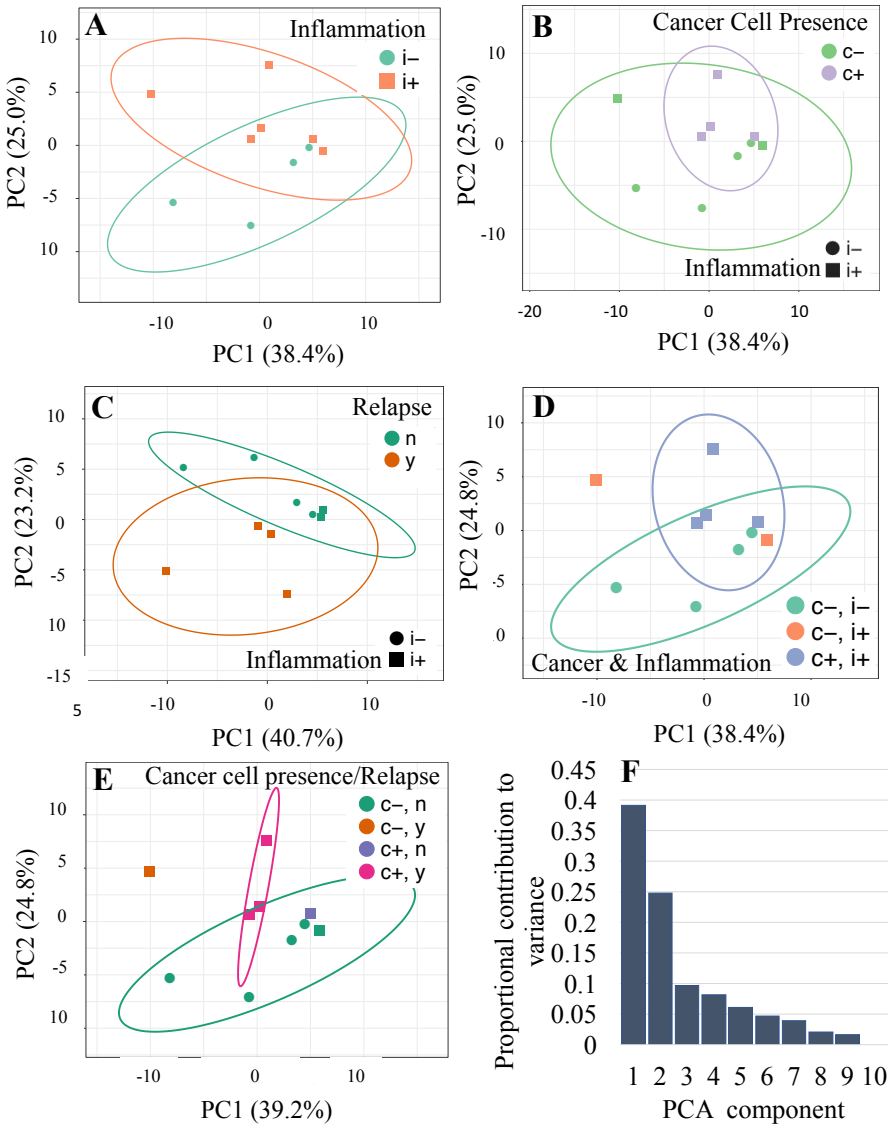

FIGURE 3.19: The results of a Principle Component Analysis. The miRNA expression driving PC1 and PC2 contributed to greatest variation between sample groups (Table 3.11) . Samples with most similar miRNA expression profile cluster together. A. Inflamed samples showed more variance in PC2. B. Samples with cancer-cell presence clustered more closely with less variation in miRNA expression than non-cancer-containing samples. C. Non-cancerous and non-inflamed LVs varied more over PC1 than PC2, whilst cancer-containing LVs varied more over PC2. Overall, expression overlapped between groups. D. Samples that relapsed show a broad expression profile and non-relapse samples showed less variation over PC2. E . Samples that were inflamed, cancer containing and relapse showed a similar transcription profile. F. A PCA scree plot to ensure the two primary principle components accounted for much of the variation. PCA figures produced with ClustVis [344].

Pathway analysis showed dysregulated miRNA involvement in maintaining LV integrity .

When analysing the six significantly up-regulated miRNA in the cancer containing vessels, commonly identified pathways were the proteoglycan path-way and the fatty acid bio-synthesis pathway, with repeated occurrence highlighted (purple) within the three analyses performed (Table 3.12). The pair of up-regulated genes, miR-16-5p and miR-497-5p, were noted to be part of the same miRNA family, and have both been found to target anti-apoptotic gene BCl-2. The analysis with the database Micro-CT-DS identified a group of four miRNA, miR-497-5p and miR-16-5, miR-144 and miR-381 involved in the proteoglycan pathway.Two of these miRNA miR16-5p and miR-381 are known to inhibit VEGF and VEGF-C secretion respectively. Pathway analysis of all up-regulated genes (>1.8 fold) show a similar pattern with the proteoglycan pathway again represented, along with the Extra-Cellular Matrix (ECM)-receptor interaction pathway and TBF-beta pathway (Table 3.12). Pathway analysis of down-regulated miRNA showed slightly different pathways with the identification of the Cell Cycle pathway, Transcriptional mis-regulation in cancer and Glycosaminoglycan biosynthesis pathway amongst others (Table 3.12). Results of the pathway analysis for miRNA differentially expressed in LVs that showed high and low inflammation can be found in Appendix B.2.

TABLE 3.12: Pathway analysis using significantly up-regulated miRNAs in cancer-infiltrated LVs. The first analysis used only miRNA identified as significantly different, meaning only up-regulated miRNA were analysed.

	KEGG pathway	p-value	#genes	#miRNAs	
TARBASE*	Proteoglycans in cancer	3.02E-15	96	5	
	Adherens junction	3.09E-09	44	5	
	Prion diseases	3.09E-09	14	5	
	Viral carcinogenesis	1.64E-08	91	5	
	Hippo signaling pathway	2.37E-08	68	5	
	TGF-beta signaling pathway	9.56E-08	41	5	
TARGETSCAN	Fatty acid biosynthesis	7.90E-38	2	2	
	Fatty acid metabolism	8.15E-15	3	2	Mir-154 family
	Metabolism of xenobiotics by cytochrome P450	7.48E-06	2	2	miR16-5p miR-497-5p
	Signaling pathways regulating pluripotency of stem cells	6.26E-05	11	3	
	TGF-beta signaling pathway	0.0387	5	3	
MICRO-CT-DS	Fatty acid biosynthesis	7.9E-38	5	2	
	Fatty acid metabolism	8.15E-15	11	2	
	Signaling pathways regulating pluripotency of stem cells	3.74E-12	47	3	miR-144-3p miR-381-3p
	Hippo signaling pathway	2.06E-06	29	2	miR-497-5p
	Proteoglycans in cancer	2.70E-06	59	4	miR-16-5p

TABLE 3.13: Pathway analysis using miRNA up-regulated >1·8 fold in cancer-infiltrated LVs.

	KEGG pathway	p-value	#genes	#miRNAs
TARBASE	Proteoglycans in cancer	6.83E-19	139	17
	Viral carcinogenesis	6.07E-13	138	17
	Cell cycle	8.89E-11	93	17
	TGF-beta signaling pathway	3.20E-10	60	17
	ECM-receptor interaction	8.00E-10	48	16
	Hippo signaling pathway	2.07E-09	98	17
	Protein processing in endoplasmic reticulum	6.09E-09	117	17
	Adherens junction	6.58E-09	58	17
TARGETSCAN	ECM-receptor interaction	7.54E-20	44	16
	Proteoglycans in cancer	8.22E-15	113	18
	Fatty acid biosynthesis	5.59E-13	8	11
	TGF-beta signaling pathway	1.86E-09	50	16
	Signaling pathways regulating pluripotency of stem cells	1.07E-08	80	19
MICRO-CT-DS	ECM-receptor interaction	1.00E-17	44	18
	Proteoglycans in cancer	3.30E-16	117	19
	Fatty acid biosynthesis	2.01E-12	8	11
	TGF-beta signaling pathway	2.33E-09	51	16
	Signaling pathways regulating pluripotency of stem cells	1.88E-08	81	19
	Axon guidance	1.06E-06	69	19
	Pathways in cancer	1.06E-06	191	19
	Focal adhesion	1.09E-06	113	19

TABLE 3.14: Pathway analysis using miRNA down-regulated >1·8-fold in cancer-infiltrated LVs.

	KEGG pathway	p-value	#genes	#miRNAs
TARBASE	Fatty acid biosynthesis	6.37E-10	4	6
	Cell cycle	3.03E-07	52	6
	TGF-beta signaling pathway	6.77E-06	30	7
	Viral carcinogenesis	8.69E-06	61	6
	Protein processing in endoplasmic reticulum	9.18E-06	61	7
	Endocytosis	9.18E-06	70	7
TARGETSCAN	Signaling pathways regulating pluripotency of stem cells	0.00057	8	7
	Valine, leucine and isoleucine biosynthesis	0.00145	1	6
	Mucin type O-Glycan biosynthesis	0.00145	1	7
MICRO-CT-DS	ECM-receptor interaction	9.41E-14	17	8
	Transcriptional misregulation in cancer	0.000373	38	8
	Glycosaminoglycan biosynthesis - chondroitin sulfate / dermatan sulfate	0.000465	7	7
	Signaling pathways regulating pluripotency of stem cells	0.001108	38	8
	Proteoglycans in cancer	0.001700	41	8
	TGF-beta signaling pathway	0.002738	21	8

Analysis of LV miRNA expression in patients who relapsed

Analysis of miRNA expression in LV samples from patients that relapsed and patients that did not relapse showed that many upregulated miRNA in cancer containing and inflamed vessels were also up-regulated in the relapse samples (Figure 3.20, Appendix B3, Table B.5). This was to be expected as inflammation and cancer-containing vessels correlated to relapse. 70% of the miRNA down-regulated in cancer containing vessels were also down-regulated in the relapse and inflamed vessels, all of which were members of the let-7 family. Pathway analysis was also performed using the up-regulated and down-regulated in the LVs from patients that relapsed. This revealed the most common KEGG pathways that the dysregulated miRNA have known involvement in to be the proteoglycans in cancer, adherens junctions and TGFβ signalling pathways (Appendix B3 B.6).

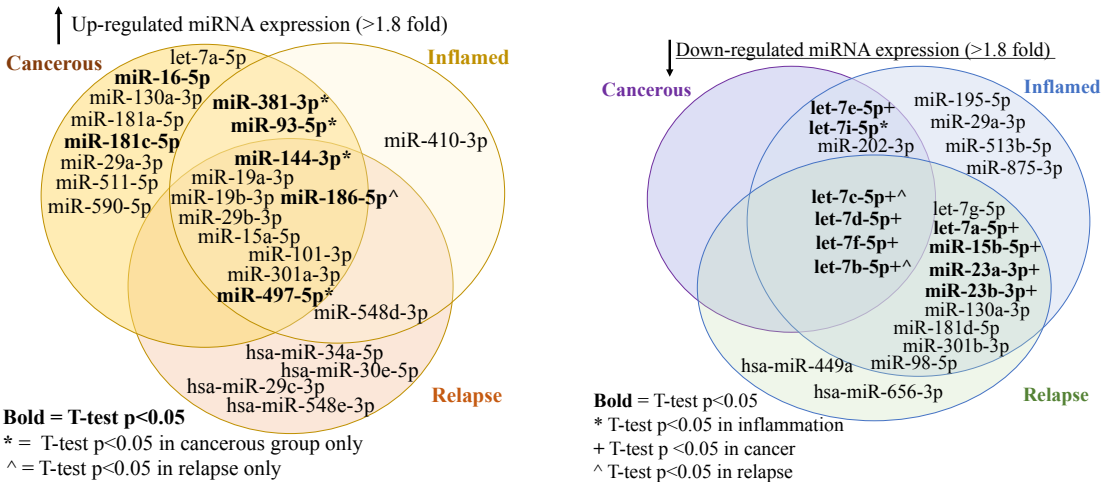

(A) (B)

FIGURE 3.20: Overlap in differential expression of miRNA in inflamed, cancer-infiltrated and relapse-associated LVs.The (a) up-regulated and (b) down-regulated miRNA identified in three separate comparisons. In the first group LVs with cancer cells present in them were compared with LVs without cancer cells present. In the second group LVs showing high inflammation were compared to those with low inflammation. In the 3rd group miRNA expression in LVs from patients who relapsed during the study duration was compared to miRNA expression in LVs from those who did not relapse.

3.4 Discussion

3.4.1 Patient relapse is associated with highly inflamed LVs that show differential miRNA expression.

The staging of LNs is routinely used to quantify cancer progression. However, cancer cell detection in LVs at the time of surgery, away from both the tumour micro-environment and the draining LN has not previously been investigated. A novel finding was that the presence on highly inflamed LV, identified at the time of surgery, correlated to patient relapse, and inflamed LVs (Medium or High inflammation) showed a moderate agreement with relapse (Table 3.7). Overall this implies that systemic changes occur in the LVs during ovarian cancer with potentially greater sensitivity to patient prognosis than LN presentation. The alterations could be the result of disease progression that makes relapse more likely, and may effect the patient response to cancer-cell infiltration, that did not correlate significantly with relapse. Alternatively, the changes induced by inflammation may contribute to the likelihood of relapse.

Significant changes in the miRNA expression were noted in the subgroups of cancer-containing versus cancer-free vessels and inflamed versus non-inflamed LVs. As the state of the LV correlates to relapse, the underlying miRNA expression changes that accompany the LV state can also be linked to relapse. The contribution of each miRNA to the total variation in miRNA expression amongst the LVs, was assessed using a principle component analysis (PCA). The first and second PCA axis account for as much variation in the data as possible. The expression of each miRNA contributes to the calculation of each axis, with weightings that represent their influence. Most of the miRNA that contributed to the first PCA axis, had not been identified as differential expressed in cancer-containing or inflamed LVs. The remaining 25% of miRNA were up-regulated in cancer-containing compared to non-cancer-containing LVs. Due to patient variability, it is expected that many miRNA vary from patient to patient without any clear link to disease processes. In the second PCA axis, 87% of the variation between the LVs was contributed to by miRNA that were differentially expressed between cancer-containing or inflamed Ls and the non-inflamed LVs. 37% of these were let-7 family members. This showed that the differential

miRNA expression between cancer-containing and/or inflamed LVs and non-cancer-containing and/or non-inflamed LVs was significant enough to stand out from the total variation amongst the patient samples.

As the high inflammation of LVs correlated with relapse and cancer-cell presence showed a moderate agreement with relapse, the miRNA expression changes could be an effect of processes associated with relapse. This includes LV inflammation and cancer-cell infiltration. Alternatively, the miRNA changes may contribute to, or drive the processes that make inflammation or cancer-cells presence more likely. The pattern of miRNA expression change could present as a useful prognostic indicator. Micro RNA are transcriptional regulators that control the expression of a network of genes. If the miRNA changes affect LV function in a way that promotes relapse, their expression may also present as targets for future therapeutics.

3.4.2 Dysregulated miRNA affect endothelial cell processes in ways that may be beneficial or detrimental in the LVs

The observed alterations in the LV miRNA expression are associated with a variety of different and relevant pathways in LVs that could influence cancer-cell survival and transport. Some of the changes in the miRNA are likely to produce detrimental effects in the LVs. For example, up-regulation of miR-181a-5p and miR-144-3p may result in the loss of normal LEC phenotypes and the gain of VEC characteristics, is likely to affect LV permeability and normal immune cell transport. Changes in the permeability of the transporting LVs are important as this could affect the ability of tumour cells to enter and exit LVs. Changes to secretion of cytokines, caused by alteration in miRNA, such as the let-7 family, can also impact LV permeability and immune response, both in the LVs and at the draining LN. Cytokines and increased permeability, along with other miRNA alterations that affect LV contraction can contribute to altered lymphatics flow. This could disrupt transport of both tumour cells and immune cells to the LN, impairing the ant-tumour response, and allowing cancer cells more time to proliferate and/or escape from the LVs.

Some observed miRNA changes may have a beneficial effect on the cancer-containing LV, such as those involved in inhibition of LV fibrosis. Fibrosis is defined as 'excessive deposition' of ECM products, including collagen, and can occur in the LVs themselves and surrounding tissue. The myo-fibroblast is a key mediator of fibrosis, which is generated from several sources including mesenchymal, epithelial and endothelial cells in the endMT or EMT transition, in addition to circulating fibro-blast-like cells [394]. The effects of fibrosis in the surrounding tissue contribute to decreased lymphatic function and lymphedema is associated with tissue fibrosis [26, 395, 396]. Thickening and fibrosis of specifically LVs distal to lymphedema site has also been observed [25]. Furthermore, in a mouse model of lymphedema, decreased fibrosis was accompanied by increased lymphangiogenesis, improved lymphatic function, and decreased inflammation [397]. Decreasing fibrosis may also aid the pumping function of LVs as the drug Pirfenidone decreases fibrosis and improved lymphatic function in mouse models of secondary lymphedema [398]. However, whether Pirfenidone targets specifically and/or primarily LV fibrosis or tissue fibrosis remains unclear.

Similarly, during would healing, tissue fibrosis and scarring is associated with accompanying specific LV fibrosis and thickening, with increased collagen deposition around the vessels and increased LEC co-expression of myo-fibroblast marker smooth muscle actin. [26]. The effect of fibrosis on LV contractility is unknown but fibrosis in vascular tissues is known to increase stiffness and impair contraction, which could translate to impaired contractility of collecting lymphatics. Additionally, fibrosis of LVs may interfere with the uptake of interstitial fluid , as distention of the ECM, after accumulation of interstitial fluid usually results in lymphatic capillary dilation and uptake is inhibited by stiffness accompanying fibrosis [26]. In conclusion, miRNA inhibition of fibrosis pathways in the LVs could present as beneficial by counteracting inflammation-induced changes in permeability and helping to maintain normal lymphatic fluid transport.

Several of the dysregulated miRNA, (miR-19a,miR-19b, miR-29b, miR-15a and let7e) have known involvement in inhibition of the EMT pathway via inhibition of TGFβ-signalling. Promotion of EMT in epithelial cells is associated with tissue

re-modelling and fibrosis in VECs. In LECS, treatment with TGBβ2, or depletion of basic fibroblast growth factor (FGF2) enhanced EMT marker expression and resulted in increased LEC permeability [399]. Therefore, miRNA inhibition of the EMT pathway is likely to be beneficial in the cancer-containing LVs by inhibiting fibrotic pathways and reducing LV permeability.

The expression of Vascular Endothelial Growth factor (VEGF), and thus lymphangiogenesis, was inhibited both directly and indirectly through inhibition of *Bcl-2*. VEGF is produced at the tumour site and can drain into the LVs to LNs. VEGF promotes LEC proliferation and aids repair of LVs but VEGF also induces lymphangiogenesis at both the tumour site and the LN, which is associated with poor prognosis. Consequently, a reduction in VEGF expression in the cancer-containing vessels may be a response to the detection of already increased levels, and likely to be of benefit.
The predicted likely effects of dyregulation in LVs, discussed further in the following section, are based on the the known effects in LECs, where data is available, or vascular or retinal endothelial cells. The role of the miRNA in ovarian cancer cells was also recorded (Table3.10), as any therapeutic intervention targeting LVs, is also likely to access the tumour-micro-environment (TME).

TABLE 3.15: Summary of dysregulated miRNA roles. Several of the dysregulated miRNA are involved in similar processes in ovarian cancer (OC) or endothelial cells (EC), including lymphatic, vascular and retinal endothelial cells (See complete results in Table 3.10). Some of the effects of the dysregulated expression may be more likely to present beneficial or detrimental actions in the LVs of cancer patients. The effect of some dysregulation, such as increased nitric oxide (NO), is uncertain as not enough information is known regarding the baseline expression of NO in LVs from cancer patients.

	miRNA	Function in OC or ECs	Likely effect of altered expression
Detrimental	↓let-7 family	Promote anti-inflammatory pathways, target cytokines, inhibit EMT	Increased EMT, increased expression of inflammatory cytokines and increased LV permeability
	↑miR-181, miR-144	Target genes that maintain LEC phenotype	Gain of Blood EC characteristics and infiltration of blood cells
	↑↓miR-29a, miR-29b, miR-19a, miR-19b	Promote NO production. Inhibit TGFβ/smad path.	Maintained/decreased LV pumping. Decreased EMT. Anti-fibrotic
Beneficial	↑ miR-16- 5p, miR-15-5p, miR-93p, miR-381	Target (inhibit) VEGF and VEGF receptors	Reducde LEC proliferation and changes associated with lymphangiogenesis
	↑ miR-497-5p, miR-15-5p, miR-16-5p	Target anti-apoptotic factor BCL-2, indirectly target VEGF	Increased apoptosis, reduced lymphangiogenesis

3.4.3 Down-regulation of let-7 miRNA in inflamed LVs could altered LV permeability and immune responses.

In the inflamed LVs, 75% of the let-7 family were consistently significantly down-regulated. Although some down-regulation was also observed in cancer-infiltrates vessels, it was not significant in comparative t-tests. In OC, the let-7 family behave as tumour suppressors by targeting oncogenes *HMAG2* and *RAS* and inhibiting Ras/MAPK signalling [345, 346]. The down-regulation of let-7 family members in OC is reported in multiple studies, and associated with poor prognosis and increased chemo-resistance [308, 309, 311, 314, 317, 345, 346]. Loss of let-7 is also associated with the development of aggressive cancers [400]. A meta-analysis of 31 studies that analysed let-7 expression in a range of tumour-types, identified let-7 as a prognostic factor for better overall survival and disease free survival type [401].Therefore, the down-regulation of let-7 expression in the inflamed vessels which were associated with patient relapse, was consistent with the effects reported at the tumour site. In addition, expression of multiple let-7 members were reduced, not just one or two miRNA. Together, this suggests that down-regulation of let-7 may be useful biomarkers of prognosis,

The let-7 family can also target cytokines. For example, in malignant epithelial cells of the bile duct, let-7-a targets the inflammatory cytokine IL-6 [382]. This contributed to cancer-cell apoptosis by reducing the expression of a IL-6-dependent transcription-factor. In allergic asthma, expression of lymphocyte let-7f can produce an anti-inflammatory action by inhibiting the expression of IL-13 [351]. Inflammation in smooth muscle is ameliorated by let-7g that targets receptor LOX-1.[380]. In HIV, expression of let-7f inhibited IL-10 expression in $CD4^+$ TCs, and down-regulation was observed in the HIV-positive TCs [381]. However, let-7 can sometimes increase inflammation. For example, auto-immune encephalomyelitis is aggravated by let-7e inhibition of *IL-10* expression in TH1 and TH17 TCs [349, 350].

MiRNA-mediated alterations in LV cytokine expression could affect immune cells in transit and immune cells that reside on the LV walls [281–283]. Cytokines also affect the LVs themselves. For example, by inducing up-regulation of MHCII surface receptors that may cross-present to $CD4^+$ and DCs [66–68].

Cytokines, including IL-6, can increase the permeability of the LVs by inducing barrier dysfunction [402]. Cytokines IL-1β, TNF-α, and IL-6 may decrease lymphatic pulsing frequency and velocity [403]. Therefore, the down-regulation of let-7a, that may increase expression of target IL-6, could contribute to increased LV permeability and decreased LV pumping. In addition, cytokines secreted by LVs can be transported in the lymph. Therefore down-regulation of let-7, that may increase secretion of inflammatory cytokines IL-13 and IL-10, may also impact the anti-tumour immune response in the draining LN.

Down-regulation of let-7 family members in endothelial cells is also associated with the promotion of the EMT. In VECS inhibition of let-7e resulted in increased levels of TGFβ signalling, which then promoted the EMT. This is likely to increase blood vessel permeability and interfere in leukocyte transmigration [348]. In a separate study let-7e expression in VECs inhibited IκBβ expression. This promoted NF-κB activation and translocation to the nucleus, that led to increased expression of inflammatory and adhesion molecules [347]. In LECS, NF-κB activation has been associated with promotion of the EMT, and lymphangiogenesis [70, 347, 404]. Therefore, down-regulation of let-7 in LVs is likely to promote the EMT pathway via TGFβ signalling. However, confirmation is needed, as indirect pathways could counteract this.

3.4.4 Cancer-containing LVs show dysregulated miRNA involved maintaining LEC phenotypes

The miR-181a-5p, which was up-regulated in cancer-containing LVs, is known to inhibit Prox-1 in LECs. This is significant because mature LECs require constant expression of *Prox-1* to maintain a LEC phenotype. [352]. During development, LECs differentiate from a precursor pool of blood ECs [319, 320]. In adult and embryonic LECs, inhibition of *Prox-1* causes LECs to de-differentiate into blood endothelial cells [352]. The LECs lose typical lymphatic cell junction characteristics and gain features associated with blood vessels. Inhibition of *Prox-1* at both embryonic and post-natal time-points resulted in blood-filled LVs. This was due to infiltration of blood cells through the vessel walls rather than by forming connections to vascular vessels. LECs can also trans-differentiate into fibro-blasts, and expression of VEGF-C/VEGF-R-3 and *Prox-1* helps LECs to

maintain their endothelial state [405]. The miRNA miR-144 was up-regulated in cancer-containing LVs and is also involved in differentiation between LECs and BECs. In EOC, miR-144 targets *RUNX1*, suppressing cancer cell migration and proliferation [391]. During development, in zebra fish, miR-144 regulates expression of the homologue runx-1 and c-myb. Over-expression of miR-144 inhibited hematopoiesis which resulted in abnormal vascular development [389]. Mice deficient in homologue *Runx1* develop blood-filled LVs at specific embryonic time points (rev [406]). Therefore up-regulation of miR-181a-5p and miR-144 could contribute to the loss of LEC phenotype though inhibition of *Prox-1* and disruption of processes that maintain the LEC and BEC differentiation. Loss of LEC phenotype could have serious implication during cancer. If LVs no longer filter out blood cells and LVs transport routes become compromised, the immune response at the LN is likely to be impaired. Disruption of normal fluid transport could also result in the leakage of cytokines and cancer cells that may have drained from the tumour site into surrounding tissue, aiding metastasis.

3.4.5 Dysregulated expression of miR-29a, miR-29b, miR-19a and miR-19b, may impact fibrosis pathways and the secretion of NO in LVs.

The contractile LVs, that carry fluid from initial lymphatics to LNs, require NO to undergo vasodilation and maintain regular LV pumping (rev [407]). LECs secrete endothelial Nitric Oxide Synthase (eNOS), that allows generation of NO in the endothelial cells. Additional NO inhibits lymphatic pumping because the normal flow dependent eNOS pattern is disrupted and also increases the permeability of the LVs [408, 409]. The miRNA, miR-29b and miR-29a, are both involved in maintenance of normal endothelial cell function and NO production in arterioles [370]. The gene *Lylpla*, which relates to NO production, is a direct target of miR-29b and miR-29a. In the arterioles of patients with type 2 diabetes mellitus, over-expression of *Lypla* reduced the NO-promoting effects of miR-29 expression. Correspondingly, miR-29 mimics restored normal endothelium-dependent vasodilation that was otherwise impaired. MiR-29b was upregulated in both cancer-containing and inflamed LV and miR-29a in cancer containing LVs only. This is likely to increase NO production and therefore increased LV permeability. The effect on the pumping activity would depend on whether the

increased NO production act to return NO expression to normal levels, or results in over-production that could reduce pumping. Reduction in lymphatic pump-activity is significant in cancer, as this could reduce immune-cell transport rate and impair anti-tumour response at the LN. Reduced lymphatic flow could also reduce cancer cell transport rate, potentially aiding arrest in LVs, and allowing further proliferation and development before reaching the less hospitable LN.

The miR-29 family is also associated with fibrosis in organs such as the liver, kidney arterioles and intestines [378, 387, 410, 411]. Expression of miR-29b expression inhibited scar formation, and thus tissue fibrosis, in murine epithelium by targeting TGF-β1/Smad and connective tissue growth factor signalling pathway [412]. Similarly, in Crohn's disease, intestinal miR-29b suppression facilitated TGF-β-mediated up-regulation of collagen in fibroblasts. This then promoted anti-fibrotic behaviour by increasing IL-6 and IL8 expression [387]. Micro RNA miR-19a and miR-19b belong to the miR-17-92 cluster. In mice, enhancing expression of the miR17-92 cluster in the lungs reduced the expression of fibrotic genes [413]. In rats VECs, miR-19b expression also inhibited a TGF-β1/Smad signalling pathway and reduced VEC apoptosis [378].

In LECs, the role of miR-29a/b and miR-19a/b has not confirmed. However, FGF2 signalling that resulted in suppression of TGFβ, maintained LEC identity by preventing gain of fibroblastic features and reducing ENdMT [414]. Therefore, miR-29 and miR-19 appear to be involved in inhibition of the TGFβ1/Smad signalling pathway, and inhibition of LV fibrosis. Fibrosis of the LVs can reduce permeability, is associated with decreased lymphatic function and reduced lymphatic-regeneration after damage. Therefore, the upregulation of miR-29 and miR-19 may be beneficial responses that help to maintain normal LV state.

The expression of miR-29b-3p and miR-19b-3p may act contrastingly to promote and inhibit TNFα induced apoptosis. In HUVECs, miR-29b over-expression was required for increased secretion of TNFα, IL-1α [371]. This aggravated LPS-induced inflammation and apoptosis. It also increased the activity of NFκB, which promotes EMT and inflammatory cytokine production in LECs [70]. On

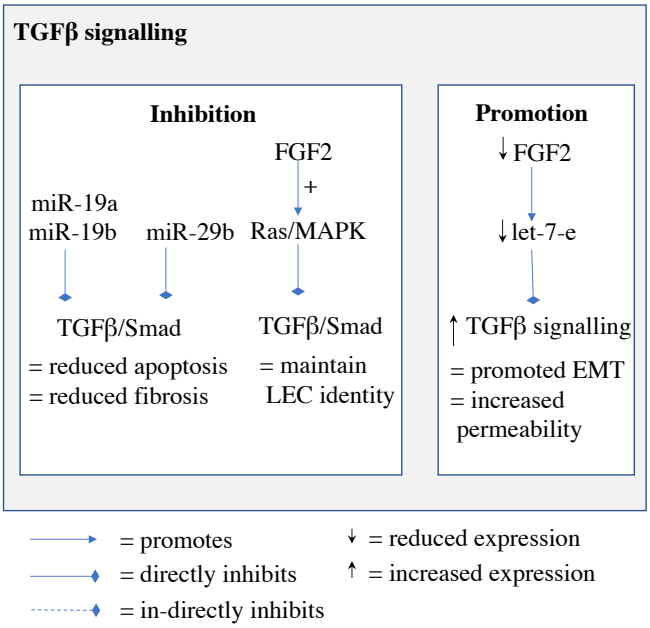

FIGURE 3.21: Dysregulated miRNA that affect TGF-β signalling in the LECs. The miR-19 and miR-29 up-regulation may be beneficial as they are known to inhibit TGF-β induced LV fibrosis and LEC apoptosis. Inhibition of TGFβ signalling has also been shown to help to maintain a normal LEC phenotype. Contrastingly, down-regulation of let-7-e may negatively impact the LV, as this results in less inhibition of the EMT pathway.

the other hand , miR-19b helped to inhibit TNFα-induced endothelial cell apoptosis in VECs. MiR-19b was also identified as up-regulated in inflamed rat LVs treated with TNFα [70, 377]. Therefore, the upregulation of miR-19b could be a direct response to increased TNFα that is promoted by miR-29 expression. This emphasises that miRNA changes may be beneficial or detrimental.

3.4.6 Several up-regulated miRNA in cancer containing and inflamed LVs target VEGF.

In LECs miR-381-3p indirectly inhibited VEGF-C expression by preventing FGF2 induction of VEGF-3, which led to prevention of tube formation (the early stage of lymphangiogenesis) [362]. In VECS, miR-15a-5p directly targets FGF2 and VEGF resulting in inhibition of angiogenesis[356]. In endothelial retinal cells, miR15a-5p indirectly inhibits TGFβ and VEGF expression [358]. Both miR-15a-5p and miR-16-5p express complementary binding sites to target gene *VEGF* and directly target VEGF-A in multiple myeloma.[357]. The miR-497-5p has

also been show to target VEGF-A and receptor VEGFR-2 in several types of cancers acting as a tumour suppressor [365]. Computational analysis of RNA sequences has also predicted that miR-93-5p targets VEGF and IL-8, a chemokine (CXCL8) that also promotes lymphangiogenesis [367]. This was confirmed in neuroblastoma cells.

VEGF drives lymphangiogenesis and LEC proliferation. As LVs can transport VEGF from the TME to the LN, inhibition of VEGF secretion by miRNAs may be in response to detection of increased VEGF in the lymph. VEGF induces lymphangiogenesis and LEC proliferation. Increased levels of VEGF at the TME and draining LN can induce lymphangiogenesis which is associated with poor prognosis [89–91, 415]. Therefore VEGF inhibition could be beneficial, by reducing LN lymphangiogenesis. However, a decrease in VEGF expression could result in less efficient repair of LV damage due to diminished LEC proliferation.

VEGF also play roles in LV contractility as application of VEGF-C to mesenteric LV of rats increased the contractile pumping of LVs [416]. VEGF-C application to LVs also altered the barrier function suggesting elevated permeability occurred [417]. However, whether a reduction in VEGF-C below normal levels has any effect is unknown. In addition, the VEGF concentration in the lymph may already be higher in cancer patients due to production at the tumour site. Therefore the reduction in VEGF secretion remains likely to have beneficial effects on returning contraction and permeability to normal levels.

3.4.7 MicroRNA that target anti-apoptotic factor BCL-2 were upregulated in cancer-containing LVs

In the cancer-infiltrated LVs, miR-497-5p, miR-15-5p and miR-16-5p, were upregulated and have all been shown to target the anti-apoptopic factor Bcl-2 (3.10. In EOC, BCL-2 expression decreases as the disease progresses, and apoptosis is augmented by inhibition of Bcl-2 [419]. Expression of Bcl-2 in endothelial cells has also been shown to influence regulation of extra-cellular-matrix, cell adhesion and migration processes [420–422]. In vascular tissue, modulation of Bcl-2 is involved in angiogenesis and Bcl-2 expression can induce VEGF expression and inhibit endothelial cell apoptosis [420, 423–426]. In VECs of the retina, a lack of Bcl-2 resulted in both increased endothelial cell apoptosis

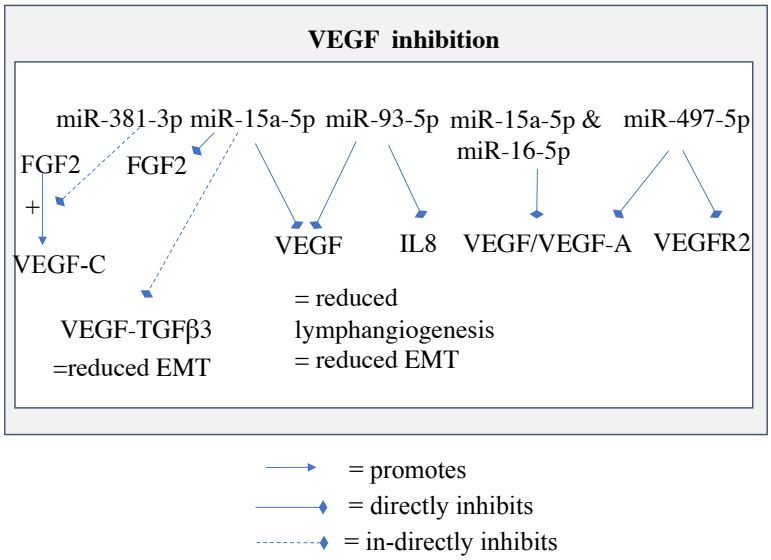

FIGURE 3.22: Dysregulated miRNA that target VEFG. Several of the miRNA up-regulated in cancer-containing LVs act to inhibit endothelial expression of VEGF or the expression of corresponding receptors. This is likely to result in less LEC proliferation and inhibit lymphangiogenesis. IL-8 (also known as CXCL8) is a chemokine that also promotes lymphangiogenesis, suggesting the effects are likely to be similar [418].

and proliferation alongside reduced branching [420]. Bcl-2 is constitutively expressed in abdominal LN, the spleen and ileac lymphoid tissue but future studies are required to assess whether Bcl-2 inhibition may similarly decrease VEGF expression in the LECs [427]. As before, VEGF inhibition in the LVs is likely to be of benefit at the draining LN, however inhibition of VEGF-mediated lymphangiogenesis and increased apoptosis would be unfavourable in damaged LVs.

3.4.8 Analysis of differentially expressed miRNA revealed common roles in KEGG pathways associated with LV structure and integrity.

The dysregulated miRNA are involved in KEGG pathways related to the TGFβ pathway, proteoglycans in cancer, glycosaminoglycan synthesis and glycan biosynthesis as well as the 'Extra-Cellular-Matrix (ECM) receptor interactions' pathway and 'adherens junction pathway'. Involvement in the TGFβ pathway is consistent with the discussed roles of individual miRNA in endothelial cells.

Changes in the remaining pathways may affect the integrity of the LV wall as LECs on the LV lumen present with a thick glycocalx which is composed of glycoprotein side chains, a backbone that includes adhesion molecules, and a proteoglycan core [272].

The function of the glycocalx in the LVs is multi-faceted and includes aiding lymphocyte rolling to preventing immune cells from sticking to the LV walls, regulating exchange between LV interstitium and surrounding interstitium and involvement in cytokine/chemokine gradient formation [272, 428]. A study by Zolla *et al* 2015 showed aged collecting LVs presented with a thinner endothelial cell glycocalyx and a loss of gap junction proteins compared to vessels from younger animals (rats) [271]. Functionally this resulted in hyper-permeability of the LVs, that allowed pathogen to escape into surrounding tissue. It also contributing to reduced control of tissue fluid homeostasis. Therefore, alterations in the proteoglycan pathway and the ECM pathway may impact LV permeability. This is consistent with the effects of the individual miRNA in VECs.

3.4.9 Experimental limitations

The miRNA was extracted from the entire LV which, although manually stripped of surrounding tissue, meant that there was possible contamination with miRNA from infiltrated cells. However, the number of infiltrated cells was very small compared to the overall number of LV cells. The LV cells were a mixture of LECs and smooth muscle cells, thus miRNA changes may be attributed to either or both cell types. Omission of cell sorting reduced the time to RNA extraction, as it was necessary to transport and dissect samples without a RNA-protective buffer, due to potential interference with epitope-structures required for immuno-histochemical-staining needed to quantify LV state. Furthermore, the goal of the study was to identify changes in the entire LV as present in the patient, rather than homogenous cell populations, when SMC and LEC proportion may differ between patients. This allows direct clinical correlation of the patients LVs and miRNA expression without cell sorting. Additionally, changes in both SMC and LECs will affect the surrounding micro-environment. Furthermore, if LV miRNA expression is to be used as a biomarker in future, minimising processing steps is key. Investigation of miRNA expression in homogenous cells

without clinical correlation can also be carried out in cell culture, for example, by tracking specific miRNA expression in LECs after application of inflammatory agents [70]. To further delineate the function of identified dys-regulated miRNA, follow up studies could also include micro-dissection of the LV to distil the source cell type, and/or compare expression with the limited LV screening [324].
Samples were isolated from ovarian cancer patients which meant that only changes associated with inflammation and cancer containing LVs were identified, rather than the systemic OC changes that could occur in all patients, regardless of prognosis. This is of benefit when attempting to identify factors that can aid prognosis. The miRNA expression of non-cancer containing and non-inflamed LVs was used as a comparative control.

It was not possible to completely isolate the effects of inflammation alone, as most, but not all, cancer-containing LVs were also inflamed. A larger trial may allow greater numbers of only cancer containing LVs and in addition to confirmation of the trends observed here. The lack of isolated effects supported a link between systemic inflammation and cancer cell spread. A comparison of inflamed versus non-inflamed and cancer-containing versus non-cancer containing LVs in separate analyses allowed the overlap in the miRNA changes to be considered when interpreting the data.

Finally, unlike mice and cell lines, patient samples varied due to both natural variation in miRNA expression and variation in the size of the LV extracted. The RNA degradation rate and therefore RNA extraction quality was also likely to vary due to variation in the time-point within surgery that the sample was taken, as the surgical procedure of varying length was prioritized over sample extraction. Normalization of RNA expression to expression of control housekeeping genes in each sample aimed to minimize the variation due to sample quality.

3.4.10 Summary

The results suggest that LVs can respond systemically to ovarian cancer. The presence of high inflammation in the LVs away from the tumour-site correlated to relapse, implying that the differences in the state of the LV are linked to patient outcome. The presence of cancer-cell infiltration showed moderate agreement with relapse but insignificant association. However inflammation and cancer-infiltration were more likely to be observed together, indicating potentially interlinked effects that require a larger sample size to further investigate. The underlying changes in miRNA expression in inflamed LVs and cancer-containing LVs overlapped. This suggests that the changes associated with inflammation and cancer-cell metastases are intertwined, and either could promote the other.

The likely effects of the miRNA expression changes can be detrimental or beneficial. For example, miRNA expression changes that result in increased inflammatory cytokines and loss of normal LEC phenotype is detrimental, whilst miRNA regulation that inhibits VEGF expression and LV fibrosis may be beneficial responses. A key alteration was the down-regulation of many members of the let-7 family in cancer-containing and/or inflamed LVs, which is also observed in ovarian cancer tumours, and correlates with poor prognosis. The variation on let-7 expression was also significant enough to be identified as a strong contributor to variation between all LVs by PCA analysis. This means that the dysregulation can stand out amongst the normal patient variability. Therefore, let-7 expression presents as a promising target as a diagnostic measure. However, although the results are encouraging, further development and application as a diagnostic would require significant investment in clinical trials. The expression of let-7 is already the subject of studies assessing a role in prevention of chemo-sensitivity in EOC [314, 429]. To determine whether increased expression of let-7 in LVs is a suitable therapeutic aim, confirmation of a role for the let-7 family as regulators of the EMT and anti-inflammation in LECs is required.

In summary, LVs undergo changes in inflammatory state and miRNA expression that correlate with relapse. These changes may present as useful prognostic markers, can be detrimental but may also occur as a feedback-response to maintain a non-pathogenic LV state. This strongly supports the evidence that LVs are not passive transport channels.

Chapter 4

Future work

4.0.1 Key Contributions

The modelling work presented in this thesis produced results that disprove the hypothesis that LN swelling does not impact TC response. Analysis of simulation results indicated that LN swellings aids in TC activation and can help subsequent effector production. However, conversely, promoting LN swelling may impair production and timely exit of effector cells when too much swelling occurs before sufficient stimulation and proliferation of CD8+ TCs (Figure 4.1). The definition of sufficient proliferation appeared to vary with the maximal swelling, and the point at which half maximal swelling is reached.

The contribution of this modelling conclusion, seemed initially at odds with previous work regarding the swelling of LNs in-vivo, which suggested that swelling aided effector TC proliferation [60]. However, a key differences between the model and the *in-vivo* study was that, in the simulated response, physiological levels of cognate TCs amongst the naïve TC pool were used, while *in-vivo*, there was an artificially high cognate frequency as LNs were pre-injected with antigen-specific TCs. Therefore, the initial proliferative response was likely to result in higher TC numbers much more quickly. The simulation results indicate that early proliferation, that results in rapid TC expansion sooner, would mean that the point at which swelling is helpful begins much earlier. In the aforementioned scenario, the simulation results therefore suggest that any swelling would likely aid response, which is in-line with the *in-vivo* observations. Previous modelling work, has also looked at TC-DC interaction scanning efficiency, TC-DC priming, chemotaxis effects on interaction and uncoupling of peptides from MHC molecules to name but a few aspects, but no-known studies have

focused on the contribution of swelling to TC response [46, 178, 180, 205]. Therefore, the observation that LN swelling aids TC activation but can impair effector production when there is insufficient TC response is a novel finding, that aids our understanding of why LNs are not simply larger to start with and offers the manipulation of LN swelling to modulate response.

The modelling work also highlighted several accompanying features of LN swelling that likely impact effector TC production, but characterisation remains uncertain. The simulation results showed that LN swelling was accompanied by large alterations in TC egress and indicated that early swelling may be detrimental to subsequent effector response by encouraging TCs to exit through increased access to exit areas before undergoing optimal proliferative expansion. Previous *in-vivo* work has not concluded whether TCs exit in hotspots or through cell junction and how these exit points may vary with swelling [107, 108, 110] (Figure 1.4). The importance of alterations in egress likelihood emphasise that better understanding how egress areas function and alter with swelling remains a vital area to further focus on due to the observed increased exit and detrimental effects.

The effect of blocking $S1P_1r$ expression to prevent the egress of effector TCs out of the LN and into the brain is currently the underlying mechanism of Multiple Sclerosis drug, Fingolimod (FTY720), but the simulation results suggested that temporary $S1P_1r$ down-regulation may aid effector TC response (rev. [235]). The extent of $S1P_1r$ re-expression on newly differentiated effectors TCs was varied, and the simulation results showed that prolonging $S1P_1r$ down-regulation on a small subset of cells (those having undergone 4-6 proliferations), had a large impact on the resulting effector TC response (see 2.3.4). Firstly, this suggested that temporary $S1P_1r$ down-regulation could restore or increase effector TC responses, particularly in enlarged LNs. Secondly, this highlighted the importance of retentive influence and regulation of trafficking on the effector TC production. There has been much work regarding $S1P_1r$, for example $S1P_1r$ blockade prior to the development of Fingolimod, but limited work exists involving temporary $S1P_1r$ down-regulation, perhaps due difficulty of implementation *in-vivo* (Figure 4.1). Work by Benechet *et al* 2016, temporarily inhibited $S1P_1r$ expression on effector TCs only, but this altered all subsequent effectors [116].

The novel insight into the importance of temporary retention, provided by the simulation results, warrants further investigation, particularly of other influences such as chemokine concentration. Currently knowledge regarding chemokine diffusion in the LN in limited, with ABM and ODE based descriptions producing contrasting reports regarding the effectiveness on TC/DC interaction (see 2.1.7) [177–179]. However, as the *in-silico* modelling results showed that retention of early effector TCs can have a strong impact on the immune response, chemokine diffusion changes are also likely to be significant. As such future work should be carried out to better understand the effects of alternative retentive features that could influence retention, including more accurate descriptions of chemokine diffusion using computational fluid dynamics, with a focus on flow and chemokine diffusion having shown that fluid flow helps to shape the chemokine gradients [182]. The contributions and remaining key unknowns regarding the modelling of LN swelling to investigate the effects on TC response are summarised in Figure 4.1.

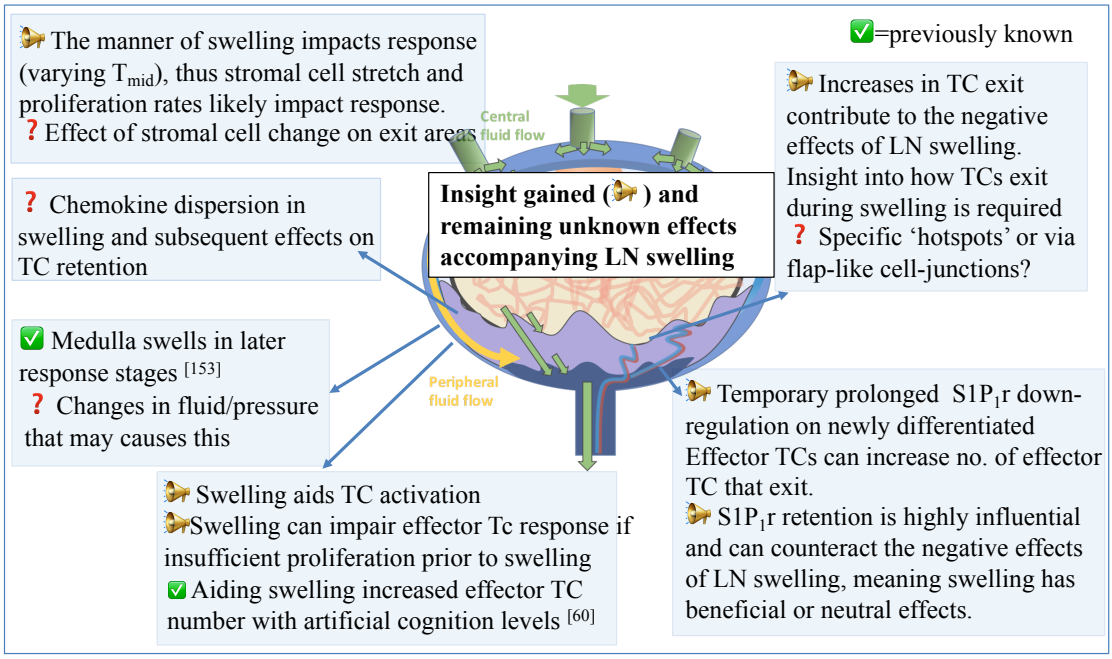

FIGURE 4.1: Key contributions and remaining unknowns regarding LN swelling. The results of the model revealed the possibility for swelling to both aid and hinder effector TC production and highlighted the importance of selective retention at key stages of TC response.

The miRNA experiments discussed in Chapter 3, contributed to the state-of-the-art research by showing, firstly, that the draining LVs, away from the tumour micro-environment, can undergo changes in inflammatory status during ovarian cancer. Secondly, the presence of highly inflamed LVs clinically correlated to patient relapse with significance (p=0.03) whilst the presence of any inflammation correlated with patient relapse with significance (p=0.07). Thirdly, during ovarian cancer, miRNA expression changes are differentially expressed between cancer-containing and non-cancer containing and inflamed versus non-inflamed vessels. Cancer-cell infiltration was also detected in some of the LVs but did not correlate with relapse suggesting that patient response to cancer-infiltration could be more important.

Previous work had shown that changes in miRNA and RNA expression occurs in tumours, with some changes specific to induction of lymphangiogenesis and secretion of VEGF from blood vessels and lymphatics (see 3.1.3). Primary LECs isolated from fibrosarcomas and that metastatic LNs presented with differential gene expression (see 3.1.5)[94, 327]. Previous work regarding alterations in the draining LVs is limited but *in-vitro* models of gastric cancer using LECs that could represent draining LVs or LVs have shown miRNA expression alterations do occur[86]. Gene expression alterations have also been show to occur in LECs draining a metastatic gastric cancer in a rat model [328]. This work confirmed that, in humans, functional LVs in the draining LVs underwent changes associated with inflammation or relapse

Analysis of the miRNA alterations in the inflamed or cancer-infiltrated LVs showed that LEC secretion of cytokines, chemokines, and VEGF were likely to be affected. These molecules can be transported in the lymph and impact the draining LN. Several forms of VEGF (VEGF-A,VEGF-C,VEGF-D) promote LN lymphangiogenesis, which is associated with metastasis and frequently accompanied by LN enlargement [89–91]. It is already known that LNs located downstream of tumours often display an impaired anti-tumour response, which may partly be driven by exposure to cytokines and signalling molecules from both the tumour and the LV and thus may also be impacted by changes in the LVs that affect VEGF and cytokine secretion. Additionally, changes in inflammation of the LVs could also impact the permeability and contraction of vessels, that

may impact lymphatic flow. As the modelling simulations showed, any of these changes that facilitate LN swelling at sub-optimal TC numbers could impair immune responses.

To confirm the prognostic potential of miRNA expression changes in LVs and assess the impact of dysregulation on the immune response at the LN, more studies are needed. The following section outlines suggestions for future work to tackle some of these points.

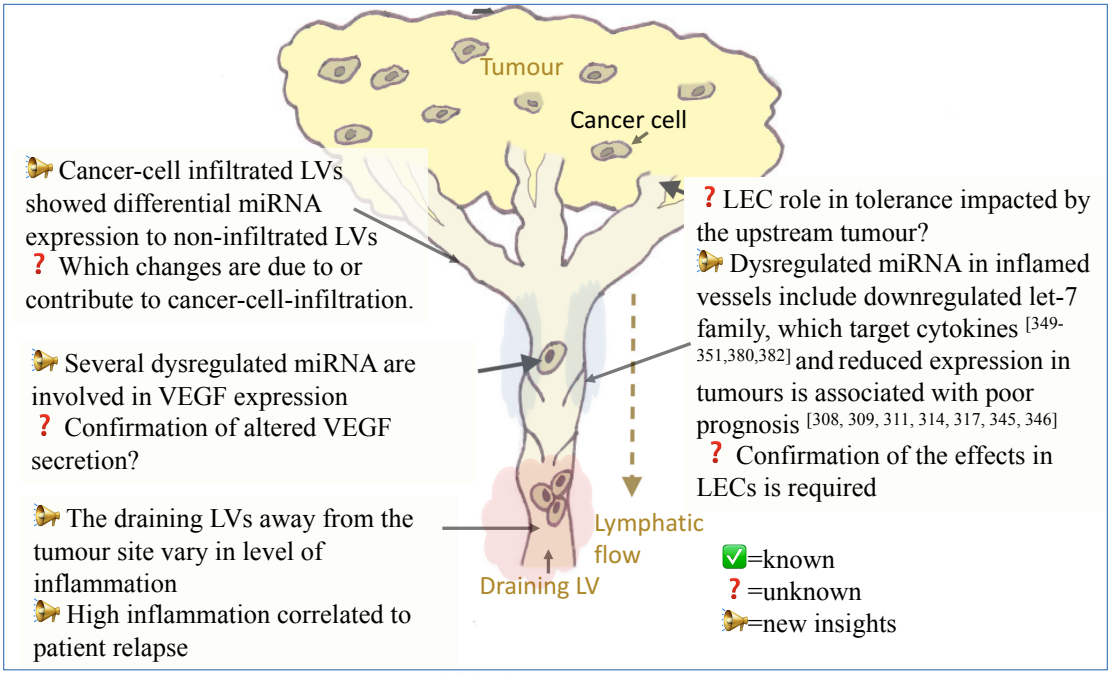

FIGURE 4.2: Key contributions and remaining unknowns regarding draining LVs state in ovarian cancer. This study showed for the first time that human LVs undergo alterations away from the tumour microenviroment, and patients with highly inflamed LVs are more likely to relapse

4.0.2 Further investigate the use of inflammation and let-7 as a marker of prognosis

Cancer-containing and inflamed LVs correlate with relapse suggesting that the associated miRNA expression could be a novel marker of prognosis. During primary debulking surgery, samples of bulky LNs are removed at the time of surgery and dissected for routine staging. The presence of inflammation could also be used as a diagnostic tool. A possible experimental set up would involve staining the cross-section of the fatty tissue sample with a LV marker (to identify LV presence in the tissue) and an inflammatory marker. The level of inflammation associated with LVs identified in a cross section could then be quantified, eliminating the need for LV or LN isolation. As a further refinement of prognosis, the expression of let-7 family members could be assessed, as RNA extraction requires only a small amount of LV sample. The let-7 family present as strong candidates due to the significant down-regulation in cancer-containing and inflamed LV (see 3.3.1). Additionally, principal component analysis showed that the expression of the let-7 miRNA contributed highly to the LV sample variation. This showed that the variation in let-7 expression, prior to identification of LV state, was substantial enough to be noticeable amongst the normal patient variation. This is important because it showed that let7 down-regulation presents as a strong signal, allowing reliable detection of expression.

4.0.3 Confirm let-7 roles *in-vitro*, to assess therapeutic potential

.

Down-regulation of let-7 in endothelial cells is associated with inhibition of cytokine IL-6 and promotion of the EMT pathway. Application of IL-6 to LVs is known to increase LV permeability. However, the direct action of let-7 inhibition or over-expression in LECs is unconfirmed. As let-7 is also known act as an anti-inflammatory agent in TCs, a set of *in-vitro* experiments is required to determine the effect of let-7 modulation in LEC. Specific let-7 mimics and inhibitors could be applied to LEC cell culture. The inflammatory response and maintenance of LEC phenotype could then be evaluated by measuring different types of cytokine expression and EMT markers. Changes in permeability could

also be assessed by using a monolayer of cells and fluorescent tracers in a specially designed fluidic device, such as that described by Young et al 2010 [430]. The device also allows consideration of the effects of shear-stress and has been used to characterize the permeability of blood vessel endothelium.

To investigate whether let-7 down-regulation is directly triggered by inflammation, let-7 expression should be measured with and without the application of an inflammatory stimuli. A study of miRNA expression in rat LVs and LECs after application of inflammatory cytokine TNFα did not report let 7 down-regulation [70]. However, it would be necessary to identify any baseline changes to then assess alteration after modulation of let-7 directly.

Finally, inhibition and over-expression of let-7 should be combined with the application of an inflammatory stimuli. The cytokine expression, EMT status, and permeability could then be assessed, providing insight into whether let-7 modulation ameliorates or exacerbates the effects of inflammation.

4.0.4 Assess miRNA expression in LNs

The miRNA expression of the LN may differ to that of the LVs, as they contain a dense blood vessel network and a complex architecture built of many types of stromal cells. However, targeting the miRNA expression of LVs would also be likely to impact the connecting LNs. Further studies would be desirable to assess the miRNA expression changes in inflamed and cancer containing LNs compared to non-inflamed and non-cancerous LNs. This would allow assessment of whether the changes identified in the LVs are also observed in the LNs, while also permitting a more general investigation of LNs miRNA expression profile changes. It would then be possible to predict whether targeting altered LVs would negatively or positively impact the LNs. In addition, new miRNA targets to modulate immune response during cancer could be identified.

4.0.5 Assess miRNA modulation that may inhibit VEGF expression in LECs

The results detailed in Chapter 3 showed that several miRNA (miR-16-5p, miR-15-5p, miR-93p and miR-381-3p, miR497-5p) that inhibit VEGF or VEGF secretion in endothelial cells were up-regulated in the inflamed and cancer-containing LVs. It was postulated that the inhibition of VEGF could be a response to detection of higher circulating concentrations of VEGF transported in the lymph from the tumour. Proliferation of LECs is promoted by VEGF and increased VEGF expression is associated with lymphangiogenic and pre-metastatic LNs. Induced increased secretion of VEGF by B cells in the LN resulted in both LN enlargement and impaired immune responses [431]. Several studies have also shown that VEGF can inhibit immune cell responses (rev. [432]). Therefore miRNA modulation to reduce VEGF concentration in the LVs and downstream LN may be a potential therapeutic target, to reduce excessive swelling and promote the TC response. However several further studies are required before pursuing this goal.

Firstly, varying concentration of VEGF could be applied to LECs culture and the expression of the miRNA analysed using qPCR, as described in Chapter 3. Comparison of the miRNA expression and the VEGF concentration would provide insight into whether miRNA upregulation occurs as a feedback mechanism to increased levels of VEGF.

Secondly, several of the studies that identified VEGF and VEGF receptors as the target of these miRNA were carried out in VECs and cancers [356, 357, 365, 367]. Therefore, it remains to be confirmed that the miRNA modulate VEGF secretion of LVs. This could be carried out by applying miRNA mimics and inhibitors to LEC culture and measuring VEGF concentrations. The use of a microfluidic device, or a parallel plate flow chamber, to simultaneously apply a shear stress across a monolayer of cells whilst applying the mimic/inhibitor would more closely match the conditions in LVs.

4.0.6 Assess permeability of inflamed EOC LV samples

Many of the miRNA alterations associated with inflamed and/or cancer-containing LVs may increase LV permeability. To confirm this, LVs from ovarian cancer patients could be isolated in a similar manner as described in Chapter 3. The method developed by Chooi et al 2016, to measure water flux across an *ex-vivo* arterial segment, could be adapted to assess the permeability of LVs [433]. Arterial vessels were isolated, cannulated and pressurised as part of the process to calculate conductance, and image-derived data used to obtain vessel geometries and distribution of smooth muscle and extracellular matrix. Numerical methods were then used to calculate water-flux from the *ex-vivo* data collected. Previously, our group has cannulated and pressurised the LVs to characterise the passive biomechanical behaviour [434]. Therefore, it should be possible to apply this method to LVs. By processing a portion of each LV for subsequent immunohistochemical staining with inflammatory markers (as described in Chapter 3), the corresponding inflammatory state of each LV could be quantified. This would allow a comparison of the LV inflammation and the permeability in the LVs of ovarian cancer patients. Increased permeability is likely to increase the afferent lymph flow rate, which could result in higher pressure and/or swelling in the draining LN.

4.0.7 Improve the model by incorporating fluid dynamics

To understand how pressure and fluid flow in the LN may impact the immune cell trafficking, the ABM model, described in Chapter Two, should be linked to a corresponding model of fluid flow. The ABM divides the environment into grids the size of T cells, whilst to describe fluid flow, the LN geometry is divided into a computational mesh of varied sizes optimised to solve fluid and mass transport equations in the LN domain [182, 435]). Using interpolation, it would be possible to link the geometries of the models. The ABM can describing the TC activation and proliferation in response to stimuli, the TC trafficking and providing information regarding TC number, TC crowding and strength of stimuli. The new LN volume would be calculated in the ABM, using information regarding TC number, the present volume and fluid and pressure from the previous

step. The ABM then defines the new volume of the LN and the boundaries of the compartments. The location of the new boundaries could then be fed back into the fluid dynamic model by expanding the corresponding domains and using well-established methods of moving boundary and if needed re-meshing to update the mesh. The fluid flow, pressure and chemokine gradients could be recalculated incorporating the information regarding the number of TCs and new volume. This information would be returned to the LN to influence TC egress and to be included in the next iteration of calculation of LN swelling.

Previously, our laboratory group has published a study regarding alterations in fluid transport to and from the specialised blood vessels in the paracortex under different pressure conditions [182]. It therefore could also be possible to consider the effects of fluid-transport gradients from the blood to the paracortex on the recruitment rate of TCs across high-endothelial venules. One challenge is consistent incorporation of changes in the geometry of the LN domain in the CFD model.

4.0.8 Investigate whether facilitating LN stretch alters TC response.

The *in-silico* work discussed in Chapter 3 also showed that swelling can aid response under some conditions but early swelling inhibits $CD8^+$ TC response. To modulate LN swelling, the stromal cells of the LN can be targeted. Although the application of VEGF has been shown to result in LN enlargement, VEGF also targets immune cells. This means that it affects too many variables to modulate the swelling alone.

At homeostasis, fibro-blastic-reticular cells (FRCs) of the LN express surface protein Podoplanin (PDPN), which help to maintain FRC contractility and LN architecture. The interaction between the surface receptor CLEC-2 expressed on migrating DCs and PDDN results in sequestration of PDPN and relaxation of FRC cells [58, 60, 146]. This facilitates LN swelling, by allowing the paracortical reticular network to stretch (Figure 4.3). The PDPN-CLEC-2 interaction can also promote the proliferation of LECs [436, 437]. In mice, inhibition of DC expression of CLEC-2, resulted in less swelling and a smaller proliferative response. However, loss of DC CLEC-2 expression also resulted reduced

agDCs migration into the LN, therefore the reduced swelling was not an independent effect of reduced elasticity. Application of anti-PDPN can reduce FRC contractility directly and results in enlarged LNs at homeostasis. Transferring pre-immunized ovalbumin-specific $CD8^+$ TCs and applying anti-PDPN resulted in more LN swelling and increased proliferative response to application of inflammatory stimuli LPS.

Future work could adapt this experiment to investigate the effect of facilitated swelling when there is not a large-subset of pre-stimulated cognate TCs. For example, by applying agDCs without transferring specific cognate TCs, combined with injection of CLEC-2 (CLEC-2 protein bound to the tail region of an antibody). The application of CLEC-2 could ensure that maximal relaxation of the FRCs is achieved in addition to promoting LEC proliferation to support expansion. The number of agDCs applied could also be incrementally reduced and the proliferative response recorded with and without anti-PDPN and CLEC-2-facilitated swelling. This would allow confirmation of whether swelling can switch from beneficial to detrimental, as observed *in-silico*.

4.0.9 Modulate murine TC expression of S1P1r early on specific effector TCs.

The in-silico down-regulation of $S1P_1r$ on early TCs (effector TCs that have undergone 4-6 proliferations) showed a strong impact on the number of effector TCs produced overall (See 3.3.3). As naïve T cells become activated and proliferate they undergo several changes in receptor expression. This includes the re-expression of S1P1r, down-regulation of CCR7, and down-regulation of CD69 [116, 207, 438, 439]. The changes also become significant at around 4 proliferations. This is the point that activated TCs are likely to be fully differentiated into effector TCs, and the point that 'early' effector TCs appear. The $S1P_1r$ receptor is already a confirmed therapeutic target. The multiple sclerosis drug fingolimod FTY720 achieves abolishment of $S1P_1r$ expression on all TCs to prevent effector TC migration to the brain as part of the autoimmune responses [440]. Conditional and temporal deletion of effector TC $S1P_1r$ has also been carried out in mice, retaining the effector TCs at a chosen timepoint [116]. However, the $S1P_1r$ could not be re-expressed as the effector cells continued to

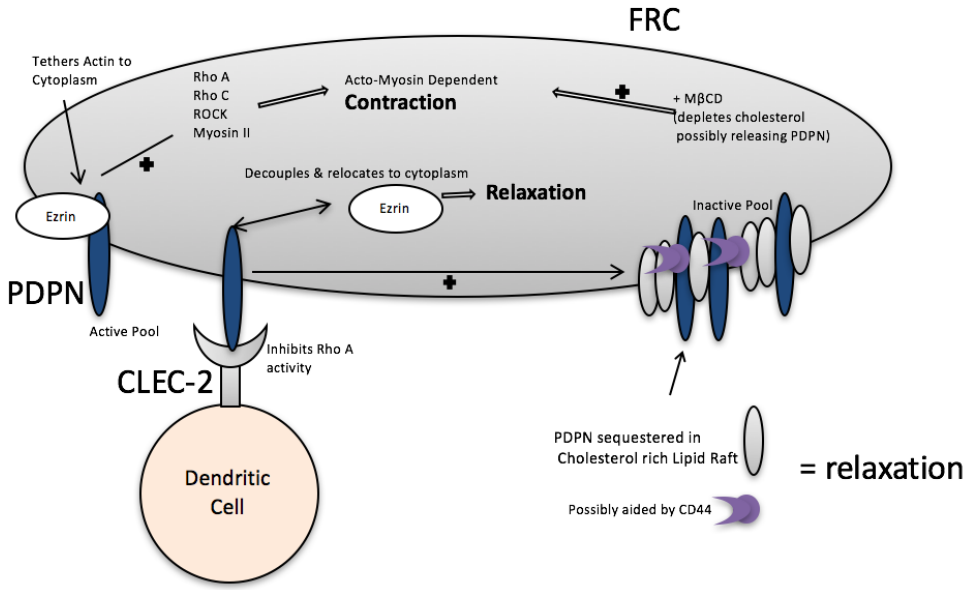

FIGURE 4.3: A summary of molecular mechanisms that allow LN stromal cell stretch. The receptor Clec-2 is expressed on migrating DCs that carry antigen into the LN. Fibroblastic reticular cells that support the LN architecture express surface protein Podoplanin (PDPN) helps to maintain FRC contractility. Interaction of PDPN and CLEC-2 results in sequestration of PDPN into lipid rafts and relaxation of the FRCs. This facilitates LN swelling by increasing the elasticity of the LN. A combination of anti-PDPN application and CLEC-2 protein application alongside decreasing amounts of agDCs could confirm the point at which swelling becomes detrimental.

---

proliferate. Ideally, future studies would involve temporary conditional deletion of $S1P_1r$ that would not impact the progeny.

Therapeutic targeting of $S1P_1r$ on only newly differentiated effector TCs could prove to be challenging. An alternative approach could be to manipulate effector TC retention via modulation of chemokine secretion. As effector TCs continue to proliferate, they reduce their expression of CCR7, resulting in diminished sensitivity to chemotactic retention [109, 116]. By increasing secretion of chemokine CCL20 or CCL19, TCs may be retained for longer. To gain an improved understanding of how chemotactic influence may change during LN swelling, chemokines could be incorporated into a multi-scale model of immune response in the LN, linking together a CFD and ABM model, as described in 4.0.7. Chemokine diffusion could be modelled to predict chemokine influence on TC retention as the LN swells. This would provide insight into whether

modulation of chemokine secretion can be implemented as a novel handle on immune response.

4.0.10 Gain insight into the relationship between TC egress and LN swelling

The results of the *in-silico* model emphasised that TC egress changes can abate the proliferative response. Yet little is known about the changes in TC egress during LN swelling. Studies in mice, sheep and rats showed an initial drop in egress in the initial 24 hours, followed by a 3-5fold increase in TC egress [164, 185, 232]. However, the corresponding volume of the LN was not recorded. A study by Tan *et al* 2012, showed that preferential expansion of cortical and medullary sinuses of the LN occurred during prolonged inflammation. TC egress rate showed a decreased level at day 4 and a return to baseline levels at day 14 [154]. *In-vivo* live-imaging of the TC egress into cortical and medullary sinuses has also been carried out in mice but the invasive experimental technique means that a normal swelling can't be recorded [110, 116]. To gain a better insight into the relationship between LN swelling and TC egress, *in-vivo* experiments could be performed in mice at more frequent intervals. Fluorescently tagged cognate TCs could be injected into the popliteal LN and an inflammatory agent injected into the hindpad. Samples of efferent lymph could be taken prior to removal of the LN to measure volume. Ideally measurements would be taken every two or three days for 10 days. Alternate methods of LN imaging *in-vivo* include PET, CT, and ultrasound scans, which could also be used to track the same mouse without sacrifice [249, 441, 442]. There is likely to be natural variation in LN swelling that can be compared to TC egress changes, but CLEC-2 protein or anti-PDPN could be used to artificially promote swelling. The difficulty of *in-vivo* experiments highlights the benefit of developing a multi-scale model, where egress rates and fluid pressures can be modelled and varied in a time and cost-efficient manner.

4.0.11 Summary

The analysis of miRNA expression in LVs from ovarian cancer patients, as discussed in Chapter 3, presented with promising results. The expression of several miRNA identified as potential therapeutic targets and/or prognostic factors, amongst the 74 screened for. These included down-regulated let-7 family members and VEGF-inhibiting miR-15-5p, miR-16-5p, mir-497-5p, miR-381-5p and miR-93p. These can now be further investigated with focused functional studies in LECs. The correlation of systemic LV inflammation with patient relapse was an additional novel finding. Several of the predicted changes in LVs, such as increased permeability, could be tested in *ex-vivo* samples but are also likely to impact fluid flow to the LN, potentially promoting swelling. The *in-silico* work presented in this thesis predicted that increased early swelling could inhibit immune response, if the swelling occurs before sufficient TC stimulation and response. The retention of newly differentiated effector TCs, for only two further proliferations, had a strong influence on the number of effector TCs produced, which could counteract the effects of early swelling. Specific modulation of only this subset of effector TCs would be difficult to carry out *in-vivo*, therefore this is an example of the novel insights that modelling can achieve.

To further investigate how retentive influences and changes in fluid flow affect TC trafficking and response, the ABM could be coupled to a computational fluid dynamic model. This would allow consideration of changes in upstream fluid velocity and LN pressure due to changes in LVs that could affect LN swelling and TC egress. It would also provide an economical method to further investigate TC retention by allowing incorporation of chemokine diffusion. In conclusion, an improved understanding of immune reactions in both the LNs and LVs was achieved. It was confirmed that changes in LVs from EOC cancer patients can correlate with relapse, therefore presenting as new targets for therapeutics. It was also shown that LN swelling that occurs before sufficient TC proliferation can inhibit effector TC response, with retention of a small subset of newly differentiated effector TCs able to counteract this effect. The temporary retention of effector TCs may therefore present as a future method to modulate immune responses in enlarged LNs.

Appendix A

Supplementary Data for Chapter 2

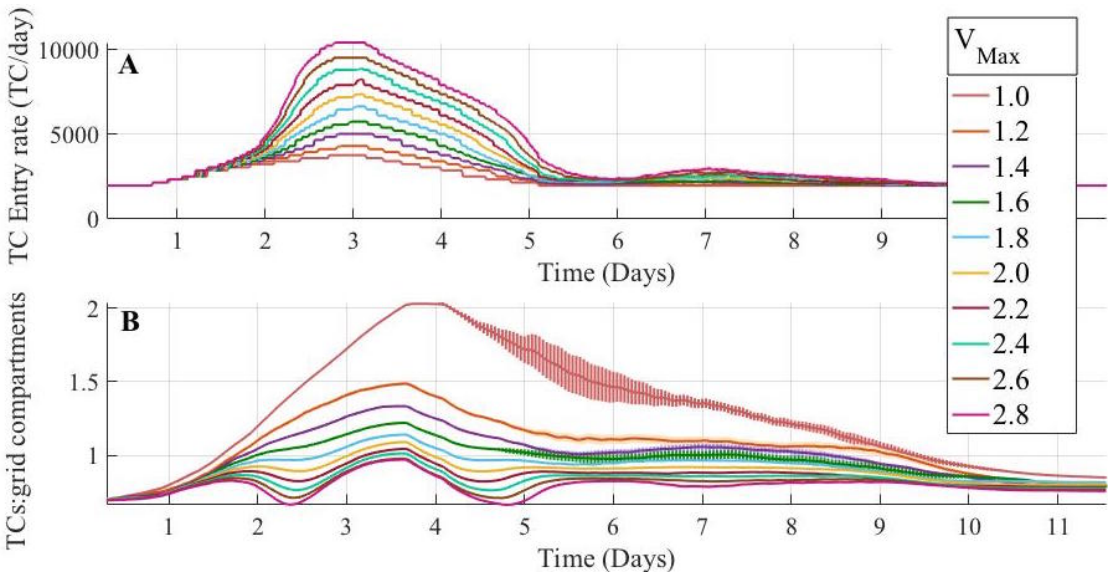

FIGURE A.1: TC recruitment rate and TC to grid ratio whilst varying V_{Max}. TC recruitment increased relative to the size of the LN (A), but the TC to grid ratio decreased with paracortical expansion. The TC to grid ratio under non-expanding conditions is higher than physiologically possible suggesting there should be a greater probability of egress when TC crowding reaches more than 1 TC per compartment.

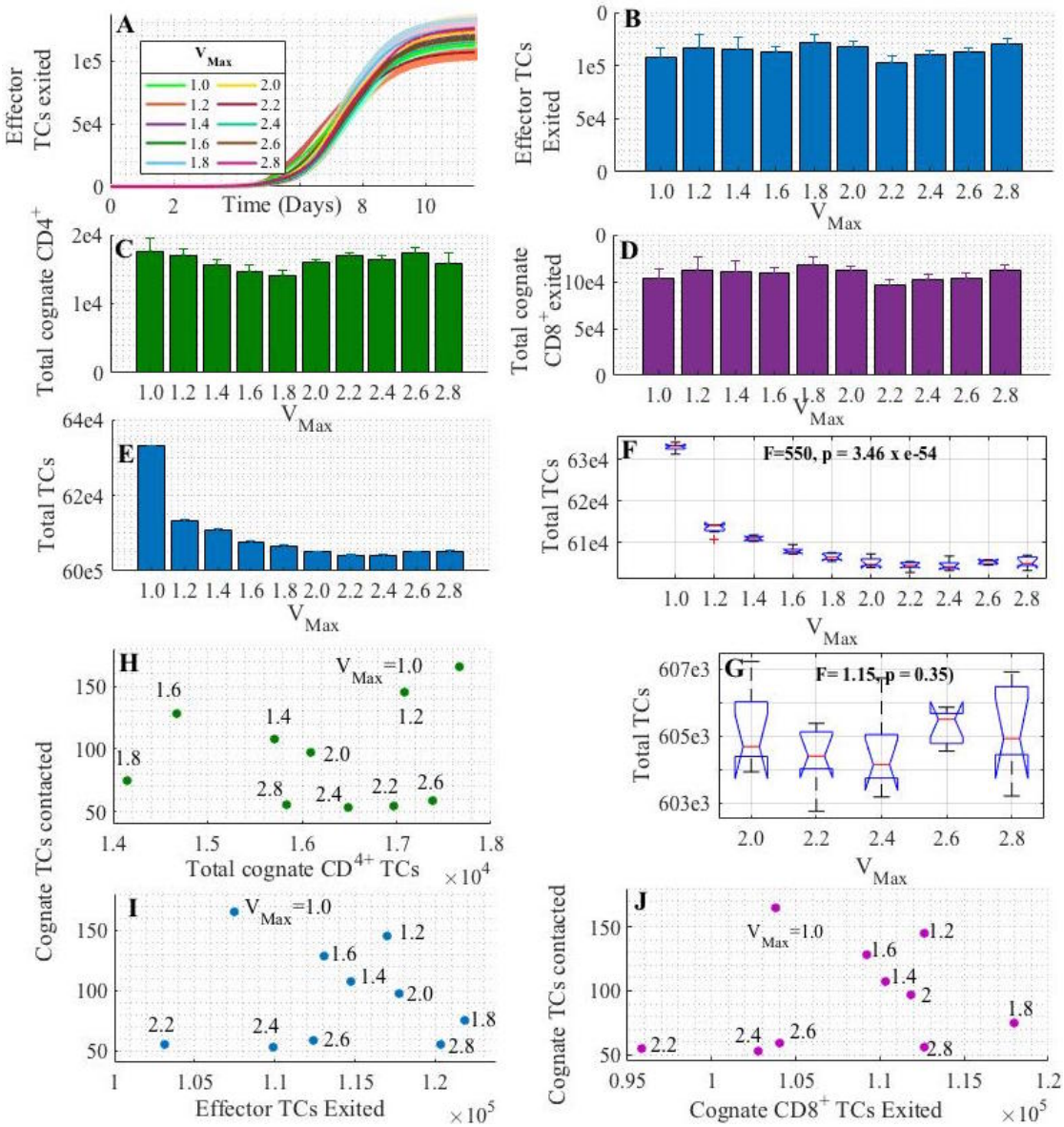

FIGURE A.2: Additional data when V_{Max} was varied with T_{mid}=10e4 TCs. A/B. No significant difference was apparent when the effector TCs and effector TCs exited were plotted over time. C. The total TCs present in the paracortex did not vary with V_{Max}. D. Effector TCs exited. E. Total cognate $CD4^+$ TCs in the paracortex. F. Total $CD8^+$ TCs that exited the paracortex.

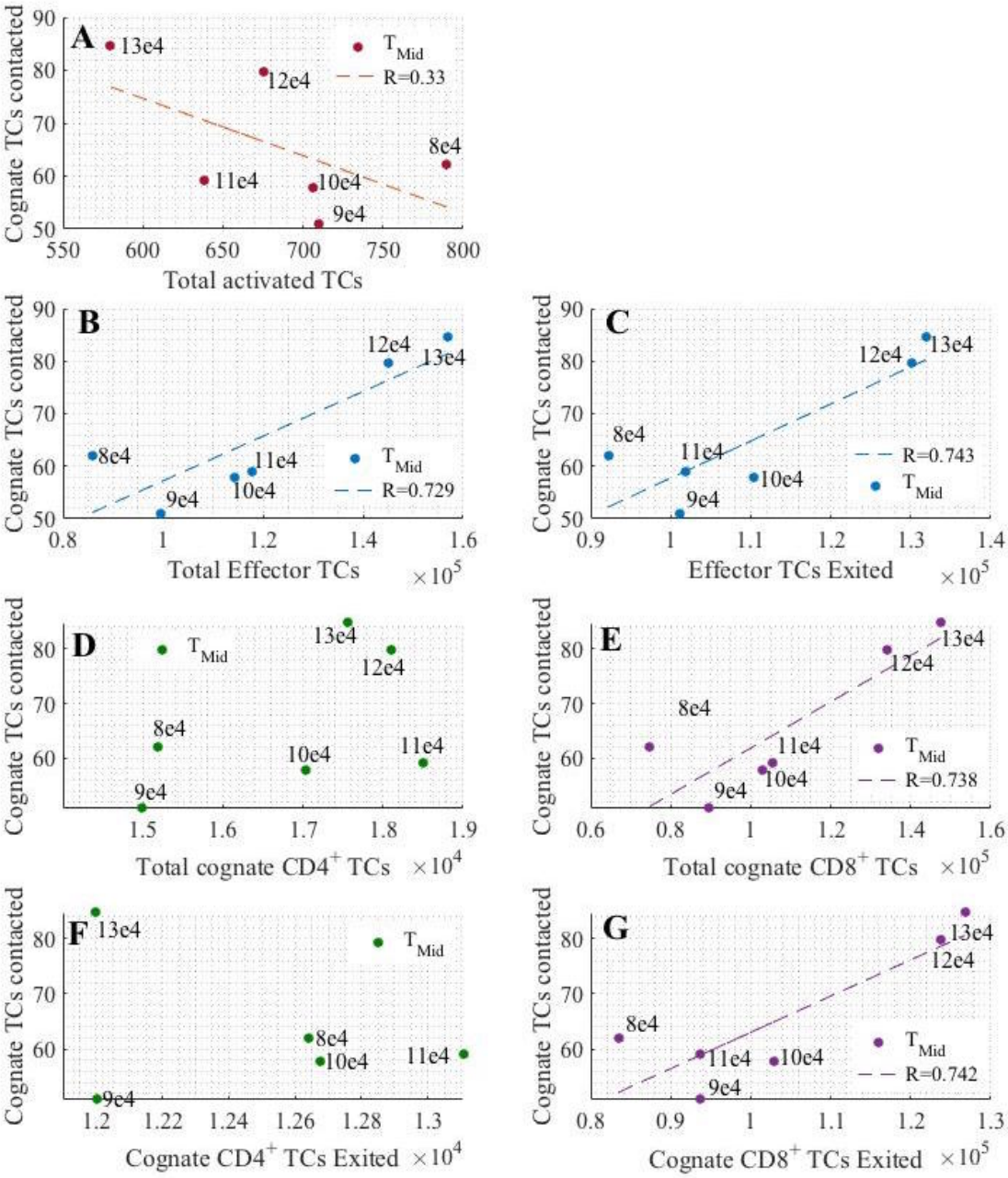

FIGURE A.3: Contact between TC-DCs, and TC response with varying T_{mid} value and a large swelling. At large paracortical swelling (V_{max}=2.5), increasing the values of T_{mid}, resulted in more TCs contacted, less activated TCs present (p=0.234) but more effector TCs exited (p=0.0305). CD4+ TCs exited and present showed no correlation with TCs contacted. However as Tmid was increased, and more TCs were contacted by DCs, the number of CD8+ exited (p=0.0275) and the number present increased (p=0.0285).

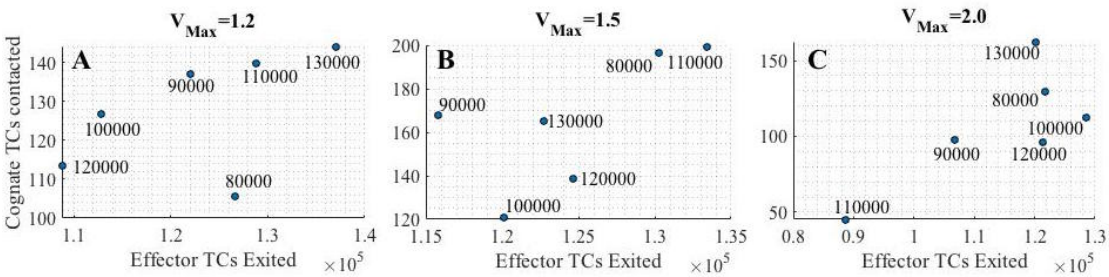

FIGURE A.4: Contact between TC-DCs and effector TCs exited with varying T_{mid}. When V_{max} was varied at different T_{mid} values, there was no correlation between effector TCs exited and mean no. of TCs contacted by DCs at 30-60hrs post stimuli. Pearson's correlation coefficient (V_{max}=1.2,1.5, 2,0, p= 0.65 p=0.16,p=0.08)

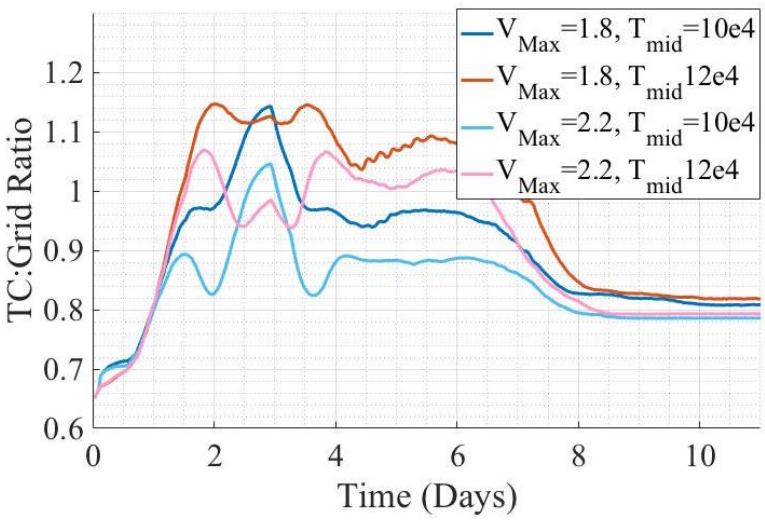

FIGURE A.5: Increasing T_{mid} increases the TC to grid ratio earlier in the response.

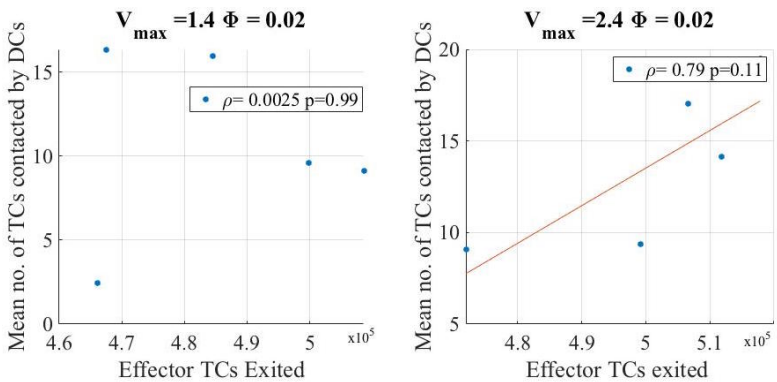

FIGURE A.6: At a low agDC application, effector TCs exited showed some correlation with TC-DC contact at larger swelling values.

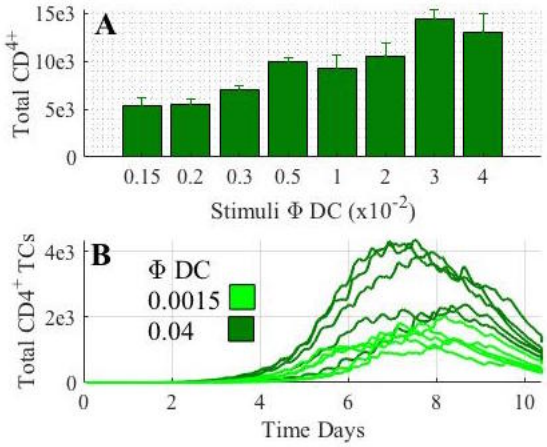

FIGURE A.7: When the DC stimuli was reduced, CD4+ TCs did not show all-or-nothing behaviour.

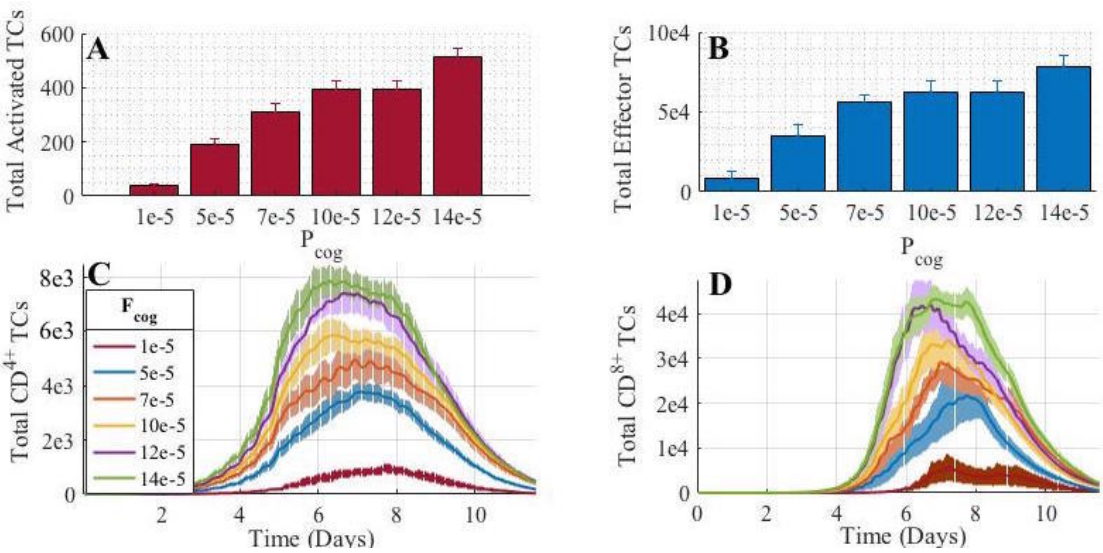

FIGURE A.8: Further effects of reducing probability of TC cognition. Both the number of activated TCs present (A) and the total number of effector TCs (B) responded proportionally to the response. Both CD4+ and CD8+ TCs responded similarly on average.

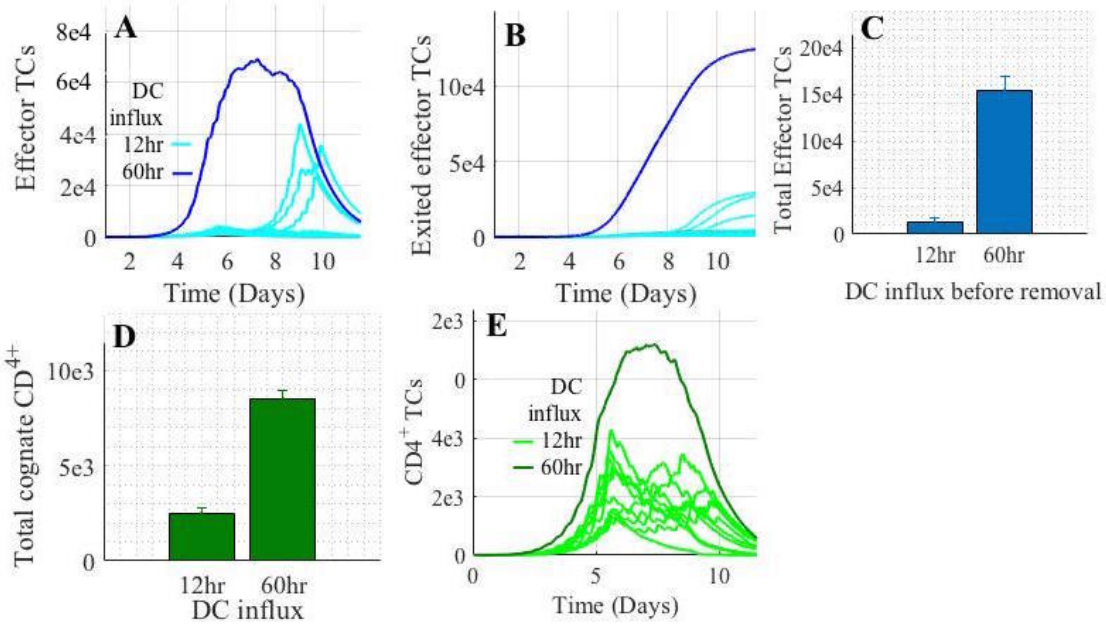

FIGURE A.9: Individual simulation results when curtailing the stimuli. When the DC stimuli was abruptly removed at 12 hours the total number of effector TCs was reduced 90% but individual simulations showed an all or nothing response (A,B,C). In some simulations,the number of effector TCs produced reached 25% of the original response to 60hours simulation, whereas half the simulations produced <1%. (D,E). The CD4+ response was reduced 80% but all the simulations showed a measurable response.

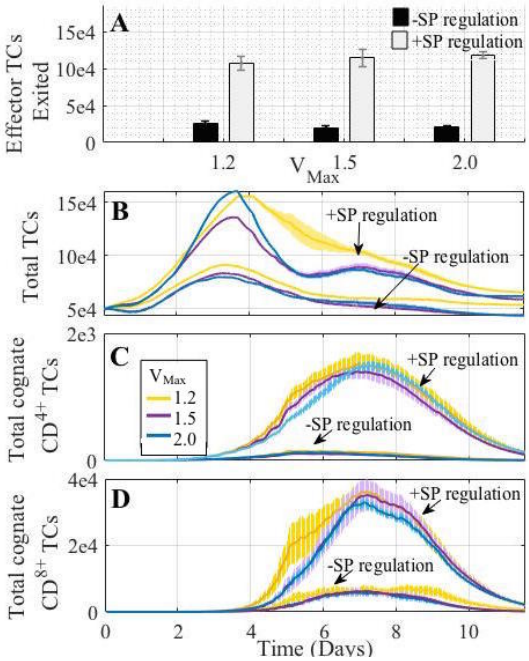

FIGURE A.10: Inhibition TC S1P1r expression at different maximal swellings. The removal of S1P1 down-regulation on activated TCs inhibited the number of effector TCs produced at all values of maximal swelling and variance between simulations at different values of V_{max} was much less than the difference between +/- S1P1 down-regulation.

Appendix B

Supplementary Data for Chapter 3

B.1 Normalisation techniques

GeNorm.

GeNorm ranks the genes in order of stability but recommends using the average of 2 or more stable genes. To determine how many genes should be used, the normalisation factors that would result from using n,n+1,n+2 to n+10 genes, where n is the most stable gene, are calculated. This results in normalisation factors NF_n, NF_{n+1}... NF_{10}. The variation between adjacent pairs of these normalisation factors is calculated as value V, using the standard deviation of the variation across samples (see Figure B.1. Once V $<$ 0.15, an additional stable reference gene is giving no additional value to the stability of the normalization factor so 'n' is the optimal number of reference genes to be used.

V= variation between pairwise comparison of the normalisation factor calculated from top **n** most stable genes.

	NF_n	NF_{n+1}	
Sample1	a1	b1	Log2(a1/b1)
Sample2	a2	b2	Log2(a2/b2)
Sample3	a3	b3	Log2(a3/b3)
Sample4	a4	b4	Log2(a4/b4)

SD= V

FIGURE B.1: Finding the optimal number of genes to normalise data. Variation between the results of normalising using n or n+1 genes are compared. If V>0.15, the result of normalising between n+1 or n+2 genes will be compared. This process repeats until V<0.15.

Normfinder

Normfinder applies a model-based approach to identify stable genes. In an experiment there are k genes and G groups with n_g samples per group. The number of genes are $1...k$ and the number of samples $j..n_g$ for each group g.
y is calculated representing gene expression for gene i for sample j of group g using three terms.

α_{ig} represents general expression level for candidate genes i in group g.

β_{gj} represents the amount of miRNA in the sample j.

ϵ_{igj} represents the random variation caused by biological and experimental factors and is assumed to have a mean of zero and variance σ^2 of all genes in the group.

$$y_{igj} = \alpha_{ig} + \beta_{gj} + \epsilon_{igj} \tag{B.1}$$

Intra-group variation is then estimated. The residuals from the initial steps in a standard calculation of variance using the additive method,$(x - \bar{x})$ where x is gene expression and $\bar{x}$ is the mean, are squared and then summed over the samples belonging to one group. The sum is then divided by $(n_g - 1)(1 - \frac{2}{k})$ to give s^2_{ig} which represents the variance for genes in one group.

$$s^2_{ig} = \frac{\sum_{i=1}^{k} (x_{ig} - \bar{x_g})}{(n_g - 1)(1 - \frac{2}{k})} \tag{B.2}$$

An unbiased estimation of the standard deviation for genes in group g is then calculated as:

$$\hat{\sigma}^2_{ig} = s^2_{ig} - \frac{1}{k(k-1)} \sum_{v=1}^{k} s^2_{vg} \tag{B.3}$$

Intergroup variation is then estimated. Z_{ig} is defined as the average of y_{igj} over all samples in group g. The value of θg is the average of β_{igj}, which is the average amount of miRNA, over all samples in group g. Therefore the mean of Z_{ig} = $\alpha_{ig} + \theta_g$ and the variance with respect to inter-group variation is σ^2_{ig}/n_g.

The variation of $Z_{ig} - \theta_g$ where $g = 1...G$, defines whether a gene is suitable as a control gene.

The next step is to combine the estimates for intra-group and inter-group variation into a stability value, adding the 2 sources of variation to give a practical measure of systematic error that will then be including when using the investigated gene.

The final step is to consider α_i as the mean expression for each group. Then in future experiments Z_{ig}-$\theta_g - \alpha_i$ defines the stability of a gene.However a distribution like this is impractical, therefore it is reduced to a one dimensional value ρ_{ig} to be the absolute value of the mean plus one standard deviation. To obtain a single value for gene i , ρ_i is the average of ρ_{ig}, $g = 1..G$. The genes in each group now have a stability value which are ranked. Further statistical details can be found at .

B.2 Imaging Results

B.2.1 Haematoxylin and Eosin Samples

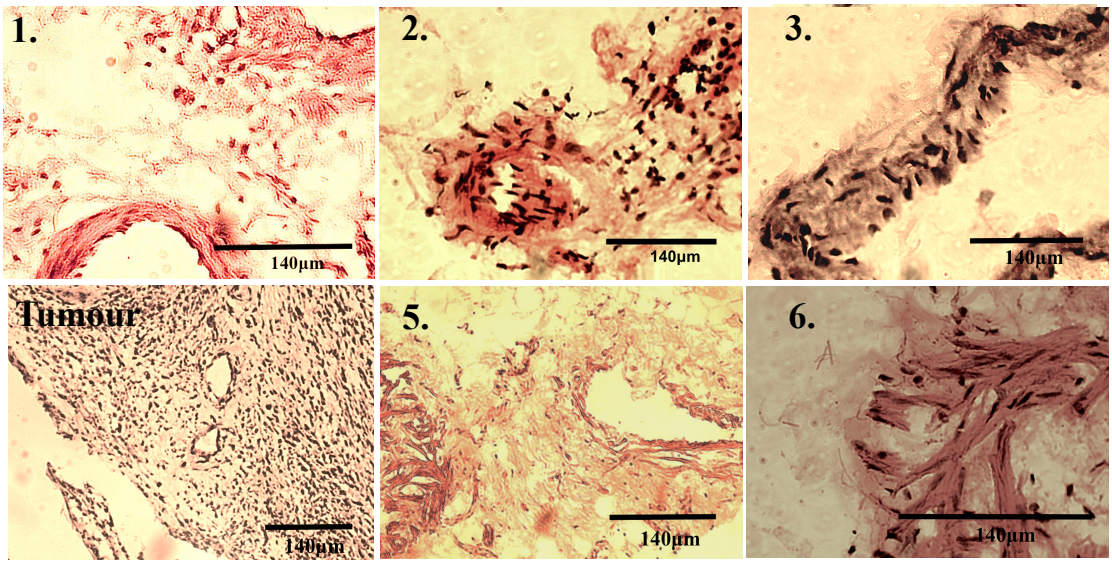

FIGURE B.2: A selection of H and E stained lymphatic vessel samples. Sample 6 shows signs of cryogenic damage but for the purpose of detecting cancer cell presence, maintenance of structure was sufficient.

B.2.2 Myeloperoxidase

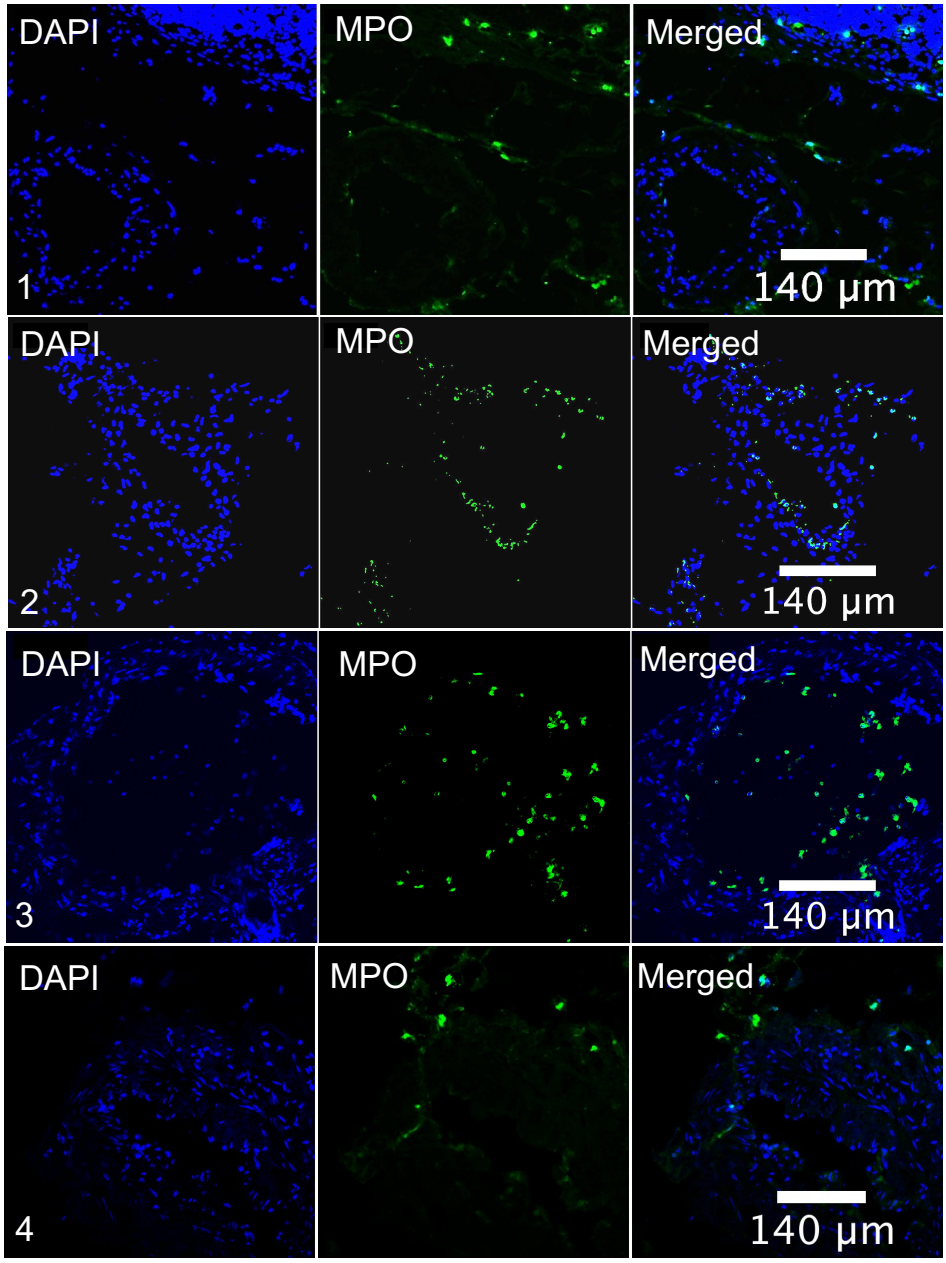

FIGURE B.3: Inflammatory marker myeloperoxidase (MPO) and nuclear marker DAPI for samples 1 to 4.

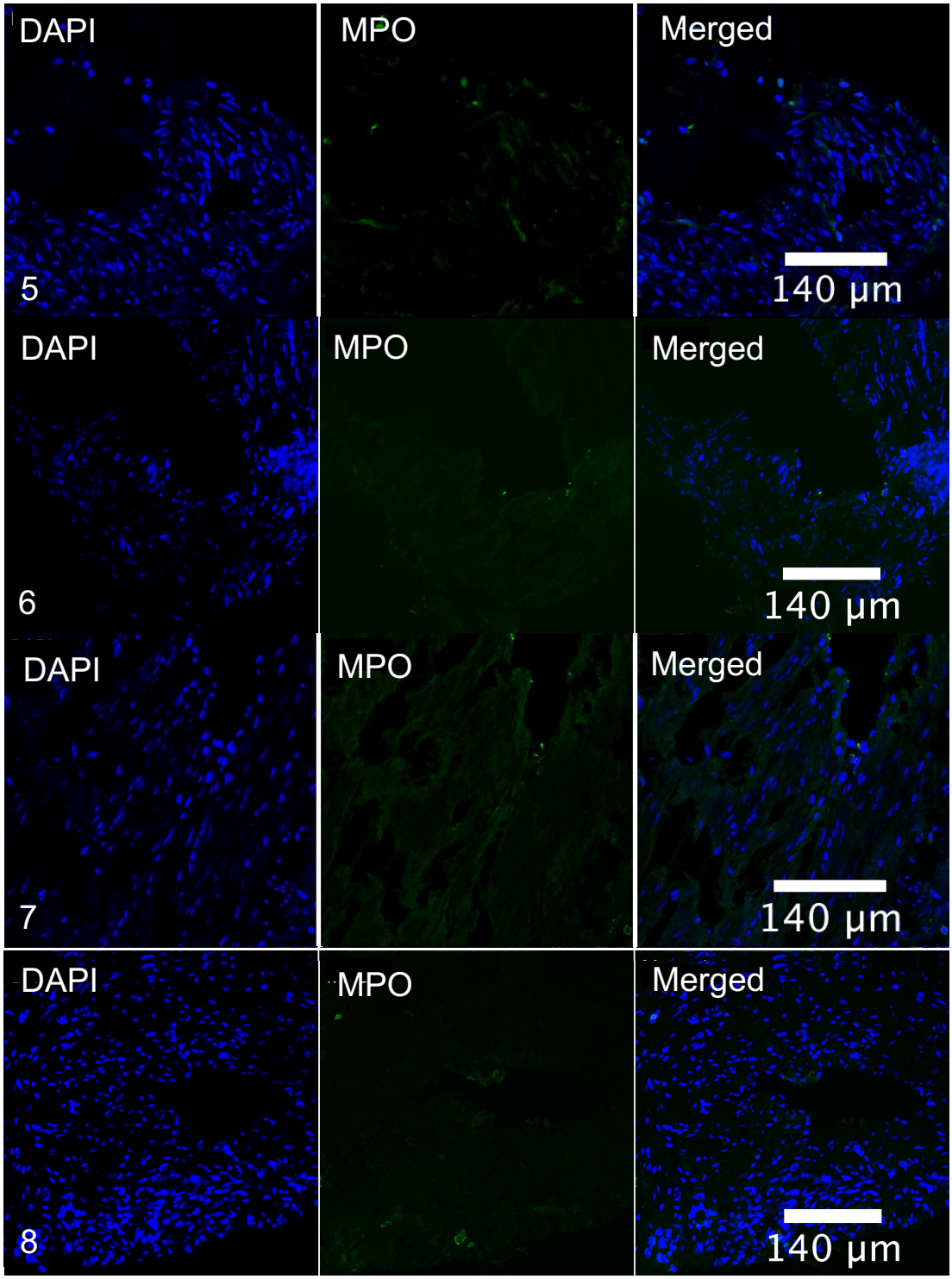

FIGURE B.4: Inflammatory marker myeloperoxidase (MPO) and nuclear marker DAPI for samples 5 to 8.

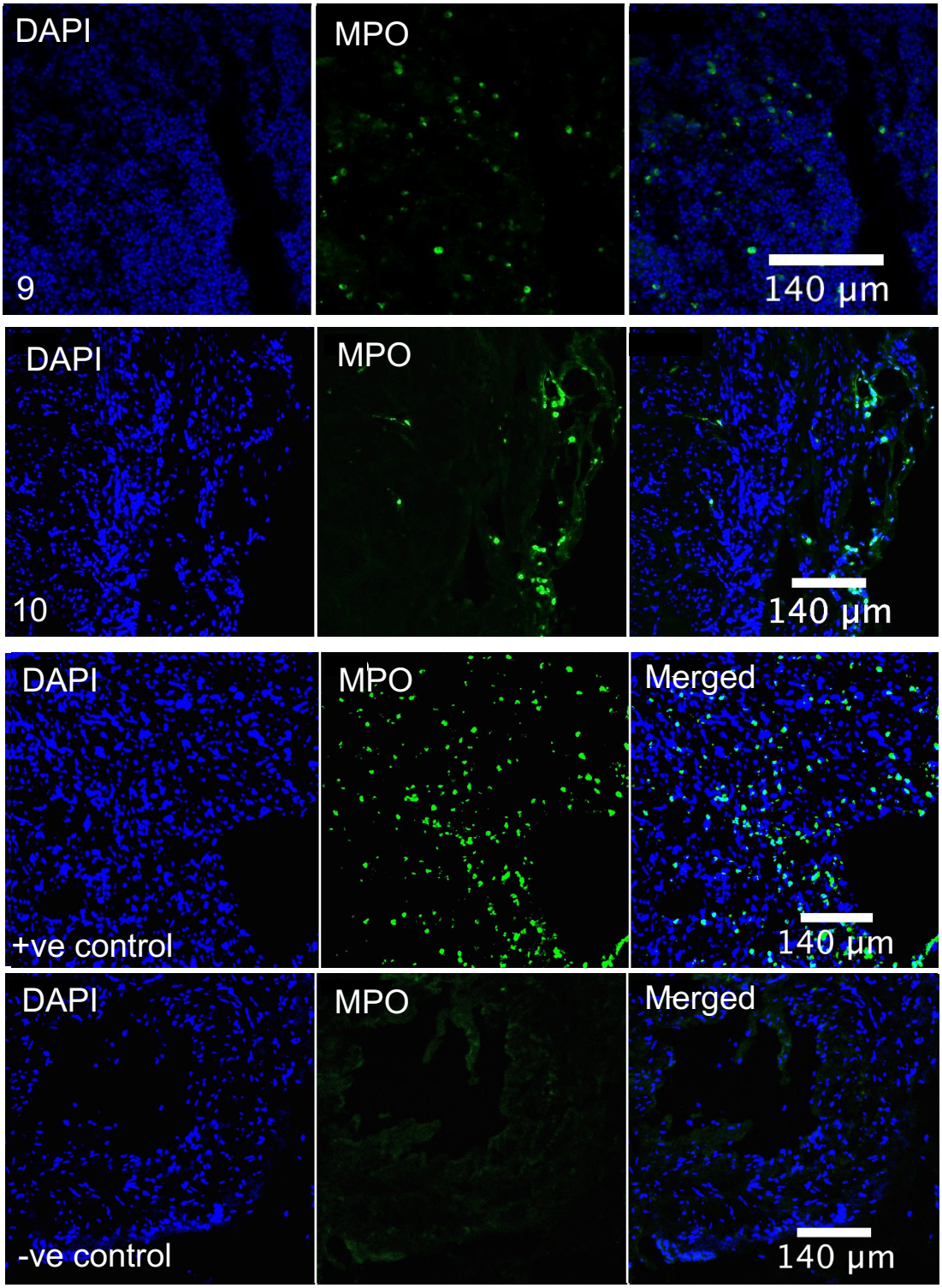

FIGURE B.5: Inflammatory marker myeloperoxidase (MPO) and nuclear marker DAPI for samples 9,10 and controls

B.2.3 Wilms Tumour-1

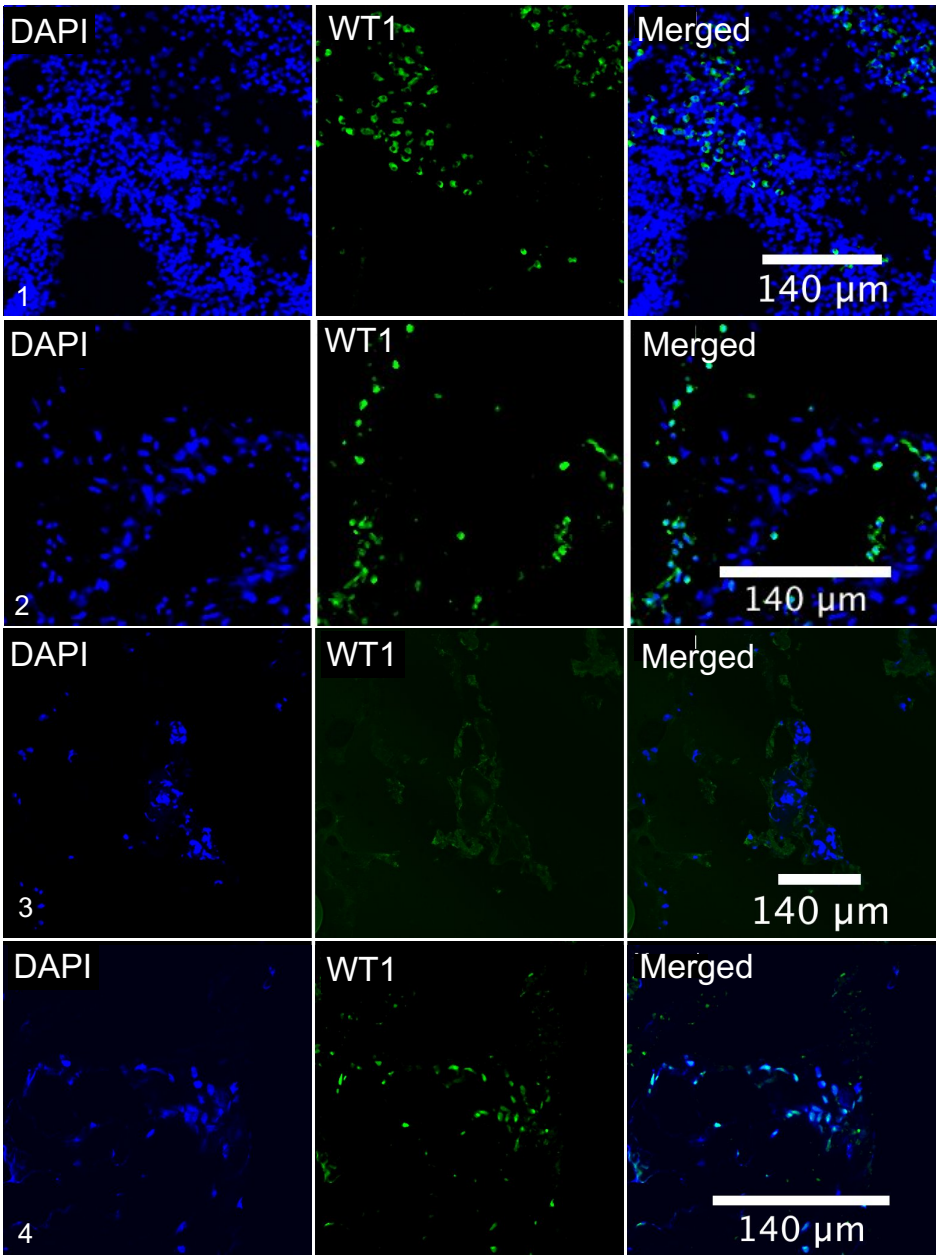

FIGURE B.6: Cancer-cell marker Wilms-Tumour-1 (WT1) and nuclear marker DAPI for sample 1-4.

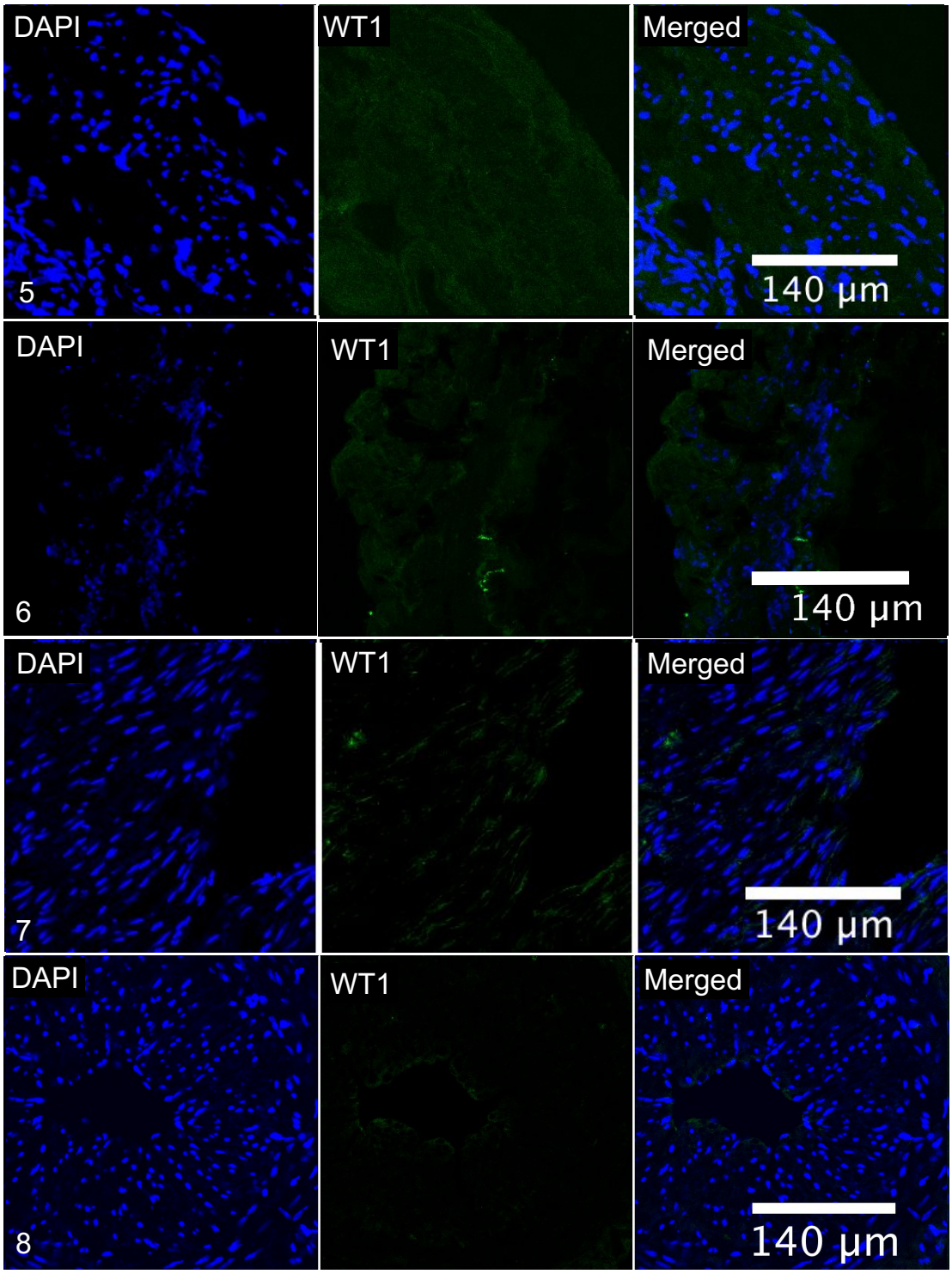

FIGURE B.7: Cancer-cell marker Wilms-Tumour-1 (WT1) and nuclear marker DAPI for sample 5-8.

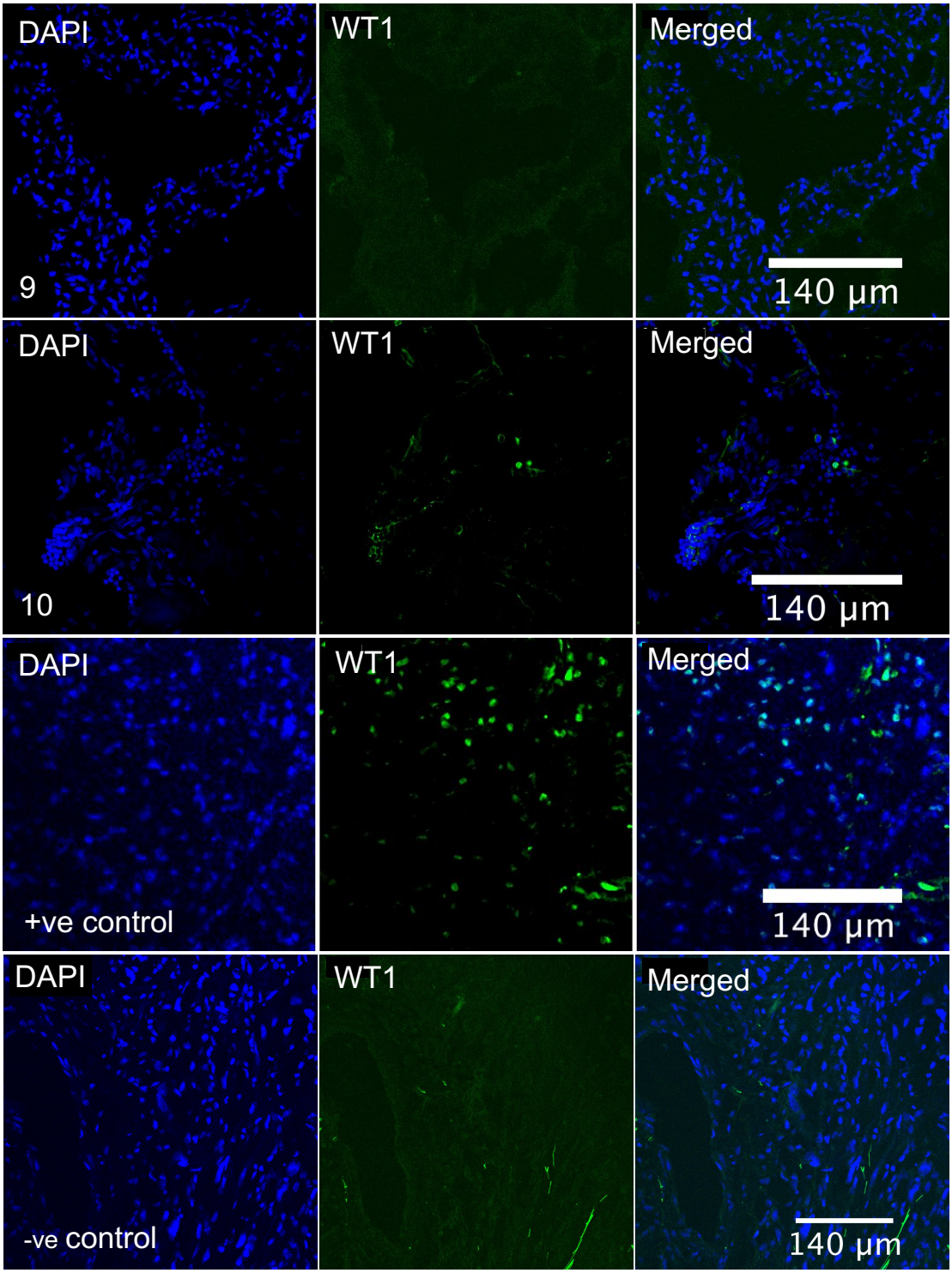

FIGURE B.8: Cancer-cell marker Wilms-Tumour-1 (WT1) and nuclear marker DAPI for sample 9,10 and controls.

B.2.4 Pax-8

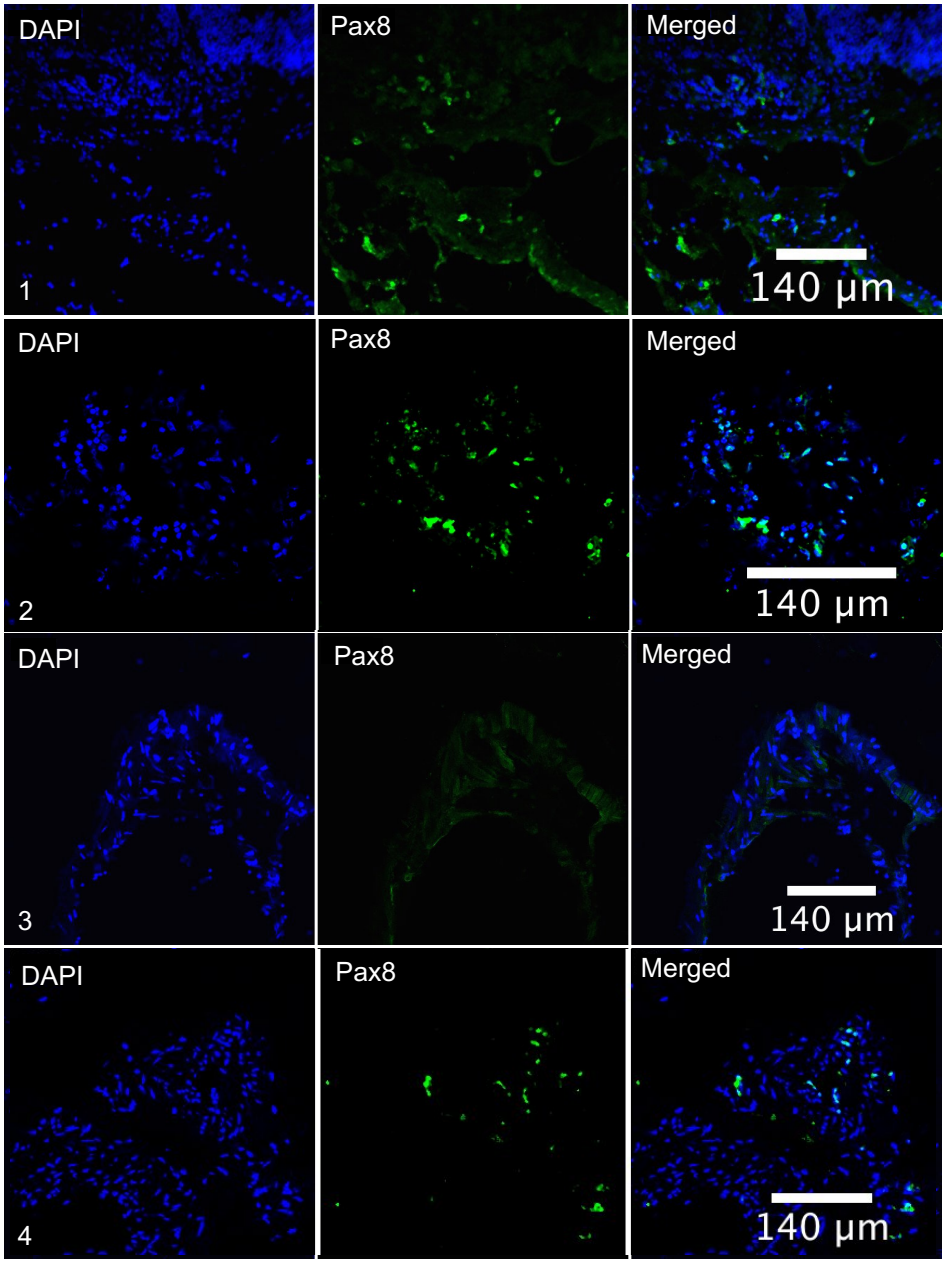

FIGURE B.9: Cancer-cell marker Pax-8 and nuclear marker DAPI for sample 1-4.

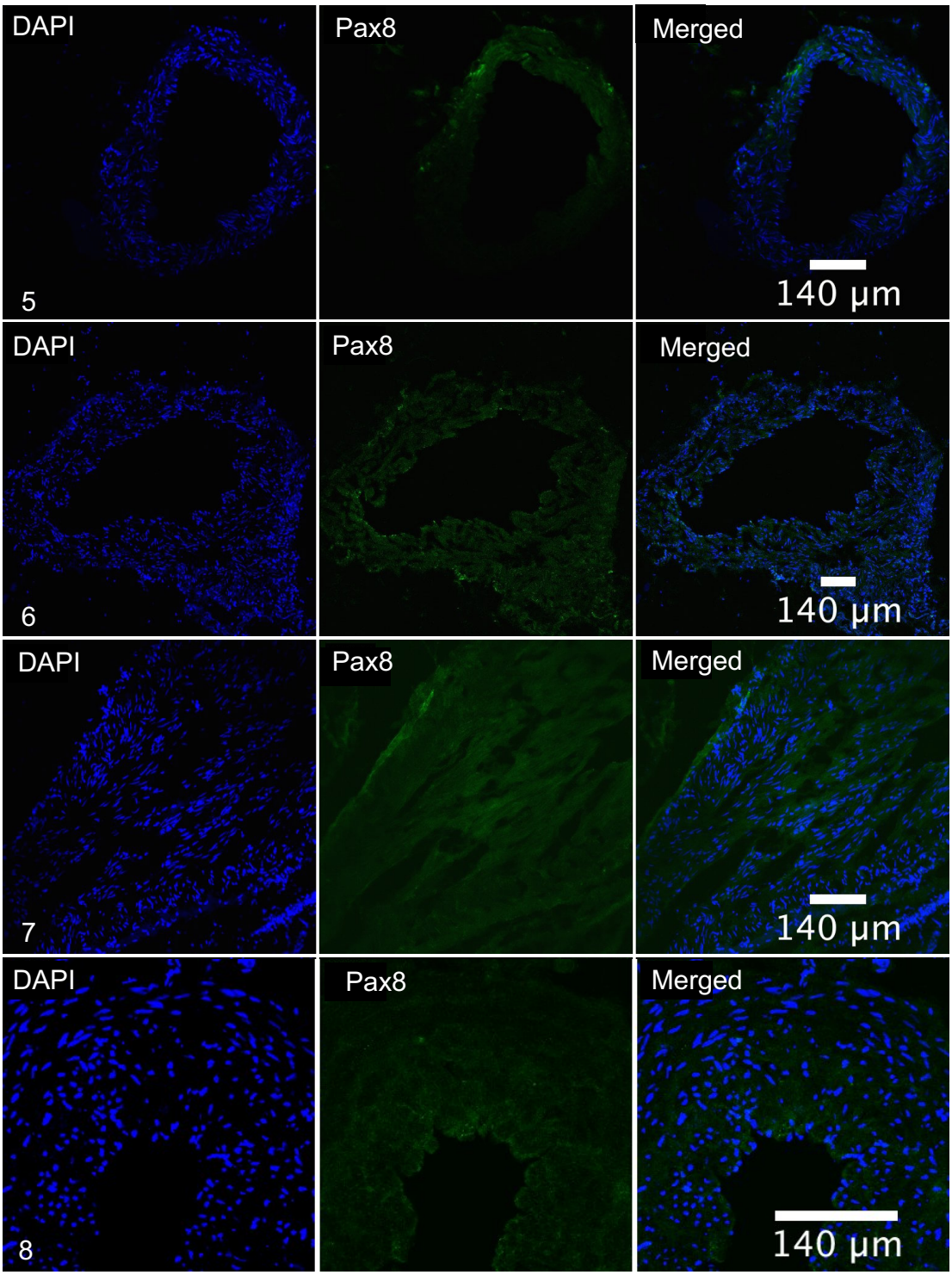

FIGURE B.10: Cancer-cell marker Pax-8 and nuclear marker DAPI for sample 5-8.

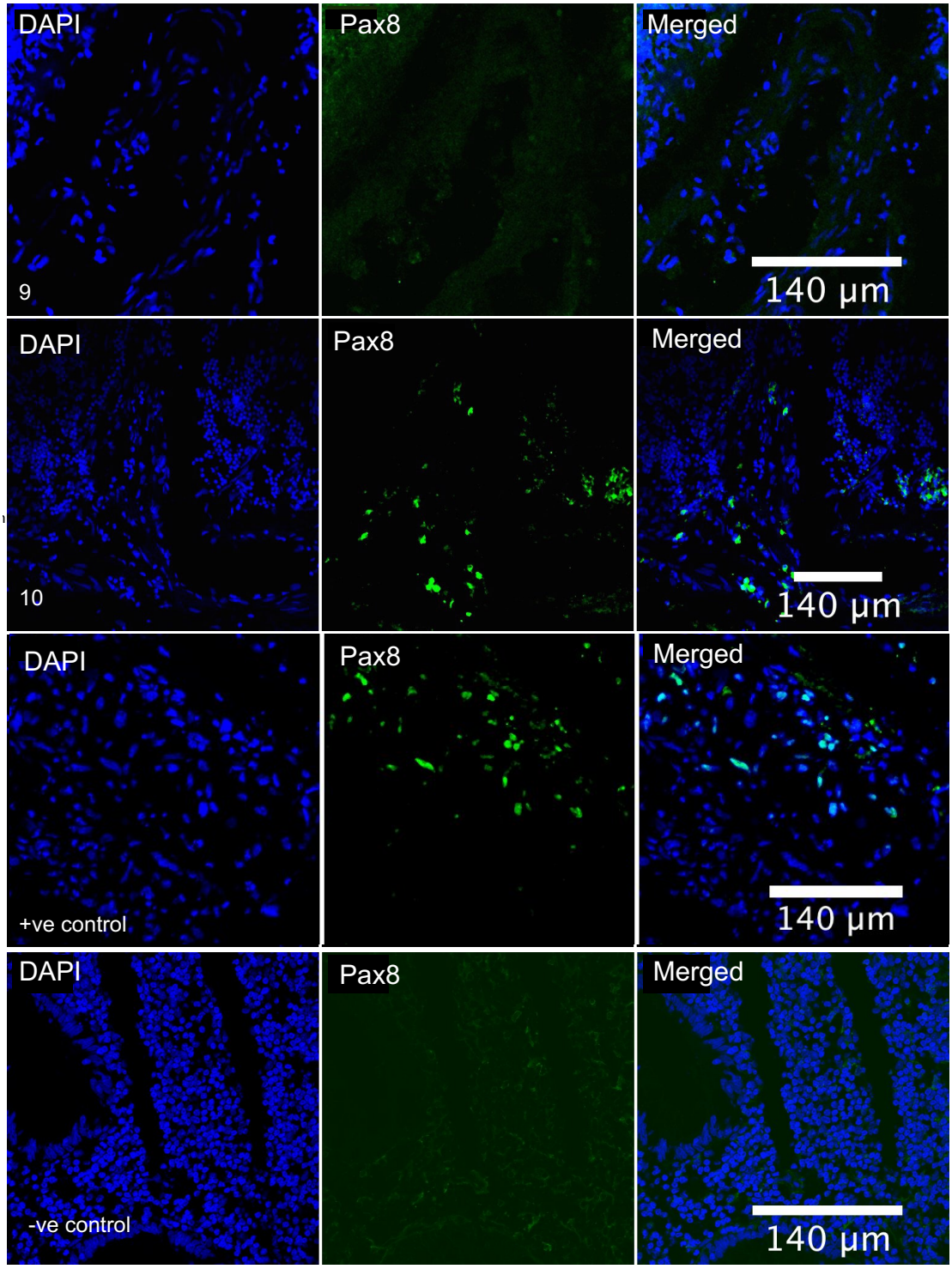

FIGURE B.11: Cancer-cell marker Pax-8 and nuclear marker DAPI for sample 9,10 and controls.

B.2.5 Podoplanin

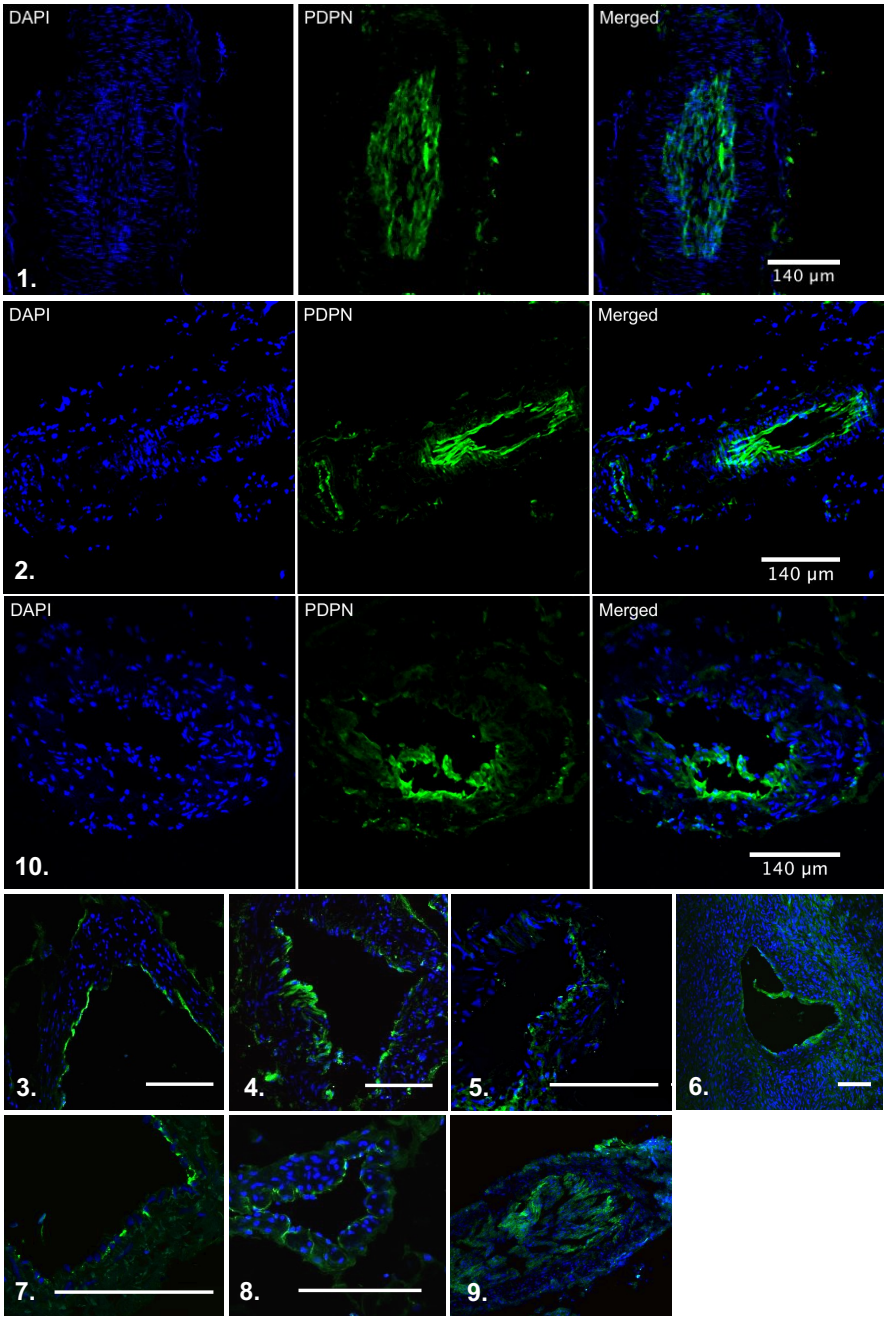

FIGURE B.12: Lymphatic endothelial cell marker Podoplanin (Green)

B.2.6 Additional miRNA expression data

Table B.1: The non-expressed miRNA in the LVs.

Non-Expressed miRNA
hsa-miR-1324
hsa-miR-300
hsa-miR-302b-3p
hsa-miR-34c-5p
hsa-miR-372-3p
hsa-miR-373-3p
hsa-miR-513b-5p
hsa-miR-519c-3p
hsa-miR-519d-3p
hsa-miR-520e
hsa-miR-524-5p
hsa-miR-548c-3p
hsa-miR-548d-3p
hsa-miR-655-3p
hsa-miR-875-3p

TABLE B.2: Pathway analysis results using the miRNAs identified when comparing inflamed LVs to non-inflamed LVs. The first analysis used only miRNA identified as significantly different, meaning only down-regulated miRNA were analysed because no miRNA were significantly up-regulated.

	KEGG pathway	p-value	#genes	#miRNAs
TARBASE	Adherens junction	5.86E-13	52	8
	Proteoglycans in cancer	5.86E-13	107	8
	TGF-beta signaling pathway	3.29E-09	49	8
	Viral carcinogenesis	5.77E-09	99	8
	Hippo signaling pathway	1.24E-07	74	8
TARGETSCAN	Fatty acid biosynthesis	2.92E-53	3	1
	Fatty acid metabolism	1.03E-21	4	1
	Signaling pathways regulating pluripotency of stem cells	2.58E-09	17	7
	Metabolism of xenobiotics by cytochrome P450	8.99E-07	3	3
	N-Glycan biosynthesis	0.00466	5	3
MICRO-CT-DS	Fatty acid biosynthesis	7.39E-26	6	9
	ECM-receptor interaction	3.21E-07	17	9
	Signaling pathways regulating pluripotency of stem cells	1.01E-06	43	9
	Mucin type O-Glycan biosynthesis	5.38E-06	9	9
	Proteoglycans in cancer	2.34E-05	53	9
	p53 signaling pathway	3.13E-05	27	9

Table B.3: Pathway analysis of miRNA up-regulated >1.8 fold in inflamed versus non-inflamed LVs.

	KEGG pathway	p-value	#genes	#miRNAs
TARBASE	Proteoglycans in cancer	1.27E-14	109	11
	Viral carcinogenesis	1.81E-13	110	11
	Adherens junction	6.85E-10	50	11
	Prion diseases	5.87E-09	16	10
	TGF-beta signaling pathway	5.87E-09	47	11
	Hippo signaling pathway	5.87E-09	76	11
	Protein processing in endoplasmic reticulum	1.75E-07	92	11
TARGETSCAN	ECM-receptor interaction	1.76E-41	12	1
	Fatty acid biosynthesis	1.28E-38	3	2
	Metabolism of xenobiotics by cytochrome P450	2.68E-09	4	4
	Fatty acid metabolism	2.82E-09	4	2
	Signaling pathways regulating pluripotency of stem cells	0.000152 308	18	7
	Protein digestion & absorption	0.00041	17	3
	Focal adhesion	0.00878	25	8
MICRO-CT-DS	Proteoglycans in cancer	1.92E-18	123	13
	Fatty acid biosynthesis	1.83E-11	8	9
	Signaling pathways regulating pluripotency of stem cells	5.31E-11	87	13
	ECM-receptor interaction	7.74E-11	43	13
	Hippo signaling pathway	2.88E-09	87	13
	TGF-beta signaling pathway	3.62E-09	49	12

Table B.4: Pathway analysis of all miRNA down-regulated >1.8 fold when comparing inflamed versus non-inflamed LVs.

	KEGG pathway	p-value	#genes	#miRNAs
TARBASE	Proteoglycans in cancer	9.07E-16	128	14
	Viral carcinogenesis	1.74E-13	125	13
	Adherens junction	2.50E-10	54	13
	TGF-beta signaling pathway	2.50E-10	57	14
	Renal cell carcinoma	2.02E-08	48	12
	Hippo signaling pathway	2.02E-08	83	14
	Glycosaminoglycan biosynthesis - keratan sulfate	3.55E-07	11	11
	ECM-receptor interaction	7.26E-07	42	13
TARGETSCAN	Proteoglycans in cancer	5.38E-15	118	15
	Viral carcinogenesis	2.95E-13	114	10
	TGF-beta signaling pathway	4.27E-10	53	15
	Adherens junction	8.73E-09	50	14
	Hippo signaling pathway	1.26E-08	77	15
	Renal cell carcinoma	1.64E-08	45	9
	ECM-receptor interaction	1.88E-07	39	14
MICRO-CT-DS	ECM-receptor interaction	4.39E-17	30	19
	Fatty acid biosynthesis	8.08E-14	6	15
	Proteoglycans in cancer	1.16E-09	91	19
	Signaling pathways regulating pluripotency of stem cells	2.27E-08	72	19
	Hippo signaling pathway	1.59E-07	65	19
	Glycosaminoglycan biosynthesis - heparan sulfate / heparin	9.10E-06	14	16

TABLE B.5: Differentially expressed LV miRNA in relapse patients. Expression of miRNA in LVs samples from patients who relapsed or remained disease-free during the study duration. (13.2±3.6months)

Non-Relapse vs Relapse		
miRNA	**Fold Regulation**	**p value**
hsa-miR-144-3p	5.069	0.091
hsa-miR-186-5p	4.930	**0.029**
hsa-miR-301a-3p	3.750	0.458
hsa-miR-19b-3p	3.267	0.204
hsa-miR-19a-3p	3.183	0.263
hsa-miR-15a-5p	2.975	0.167
hsa-miR-29b-3p	2.609	0.186
hsa-miR-29c-3p	2.475	0.407
hsa-miR-497-5p	2.295	0.067
hsa-miR-101-3p	2.117	0.256
hsa-miR-34a-5p	2.089	0.083
hsa-miR-548d-3p	2.009	0.614
hsa-miR-30e-5p	-1.827	0.318
hsa-miR-548e-3p	-1.917	0.287
hsa-let-7g-5p	-1.938	0.178
hsa-let-7f-5p	-1.954	0.433
hsa-miR-23a-3p	-2.769	0.114
hsa-miR-449a	-3.197	0.395
hsa-miR-15b-5p	-3.302	0.110
hsa-miR-98-5p	-3.430	0.067
hsa-let-7d-5p	-3.681	0.064
hsa-miR-181d-5p	-4.029	0.177
hsa-miR-130a-3p	-4.306	0.510
hsa-let-7c-5p	**-4.335**	**0.039**
hsa-miR-301b-3p	-4.776	0.151
hsa-let-7b-5p	**-6.940**	**0.038**
hsa-miR-23b-3p	**-8.529**	**0.028**
hsa-miR-656-3p	-16.377	0.314
hsa-let-7a-5p	-42.416	0.237

Up-regulation Down-regulation
bold =p<0.05

TABLE B.6: Pathway analysis results of miRNA that showed a up-regulation >1·8 fold-change in LV samples of patients who relapsed. (13.mnths±3.6).

	KEGG pathway	p-value	#genes	#miRNAs
TARBASE	Cell cycle	6.76E-11	94	12
	Proteoglycans in cancer	1.76E-10	129	12
	Adherens junction	2.56E-10	57	12
	Pancreatic cancer	2.98E-09	54	11
	Colorectal cancer	3.12E-08	50	12
	Prostate cancer	9.54E-08	67	12
	Hippo signaling pathway	1.37E-07	90	12
	Pathways in cancer	1.90E-07	229	12
	p53 signaling pathway	1.94E-07	54	12
TARGETSCAN	Proteoglycans in cancer	5.81E-21	127	13
	Fatty acid biosynthesis	2.01E-15	10	8
	ECM-receptor interaction	1.34E-10	46	13
	TGF-beta signaling pathway	8.96E-09	50	12
	Axon guidance	1.39E-08	76	13
	ErbB signaling pathway	7.32E-08	59	13
	Pathways in cancer	2.41E-07	206	13
	Signaling pathways regulating pluripotency of stem cells	3.35E-07	82	13
MICRO-CT-DS	Proteoglycans in cancer	3.78E-19	124	12
	Fatty acid biosynthesis	8.55E-16	10	8
	TGF-beta signaling pathway	1.18E-08	49	12
	Axon guidance	1.18E-08	75	12
	ECM-receptor interaction	1.18E-08	45	12
	ErbB signaling pathway	1.05E-07	58	12
	Signaling pathways regulating pluripotency of stem cells	1.05E-07	82	13
	Pathways in cancer	1.62E-07	203	13

TABLE B.7: Pathway analysis results of miRNA that showed a down-regulation >1·8 fold-change in LV samples of patients who relapsed. (13.2mnths±3.6).

	KEGG pathway	p-value	#genes	#miRNAs
TARBASE	Proteoglycans in cancer	1.17E-14	118	9
	Adherens junction	5.58E-09	51	9
	Cell cycle	7.96E-09	81	9
	TGF-beta signaling pathway	7.96E-09	51	9
	Prostate cancer	2.26E-08	62	9
	Renal cell carcinoma	3.46E-07	45	9
	Protein processing in endoplasmic reticulum	1.65E-06	97	9
	Chronic myeloid leukemia	2.39E-06	49	9
	Pathways in cancer	2.77E-06	203	9
TARGETSCAN	Proteoglycans in cancer	1.71E-11	124	
	Adherens junction	2.57E-09	54	
	TGF-beta signaling pathway	6.71E-09	55	
	Cell cycle	4.34E-08	83	
	Prostate cancer	3.39E-07	63	
	Pathways in cancer	1.11E-06	218	
	Renal cell carcinoma	1.11E-06	46	19
	Oocyte meiosis	2.78E-06	68	15
MICRO-CT-DS	Fatty acid biosynthesis	2.56E-42	4	2
	Fatty acid metabolism	2.68E-11	5	2
	Signaling pathways regulating pluripotency of stem cells	2.17E-06	22	11
	Glycosphingolipid biosynthesis - lacto and neolacto series	1.04E-05	2	1
	Metabolism of xenobiotics by cytochrome P450	1.32E-05	4	5
	Mucin type O-Glycan biosynthesis	0.000175151	3	9

Bibliography

1. Louveau, A. *et al.* Structural and functional features of central nervous system lymphatic vessels. *Nature* **523,** 337 EP – (June 2015).
2. Crivellato, E, Travan, L & Ribatti, D. The Hippocratic treatise 'On glands': the first document on lymphoid tissue and lymph nodes. *Leukemia* **21,** 591 EP – (Mar. 2007).
3. Natale, G., Bocci, G. & Ribatti, D. Scholars and scientists in the history of the lymphatic system. *Journal of Anatomy* **231,** 417–429 (2017).
4. Ambrose, C. T. Immunology as first priority dispute: An account of the 17th-century Rudbeck-Bartholin feud. *Cellular Immunology* **242,** 1 –8 (2006).
5. Goss, C. M. Galen on the usefulness of the parts of the body. Translated from the Greek with an Introduction and Commentary. By Margaret Talladge May. 1968. xv + 802 pages in 2 volumes. $25.00. Cornell University Press, Ithaca, New York. *The Anatomical Record* **163,** 135–137 (1968).
6. Loukas, M *et al.* The lymphatic system: a historical perspective. *Clin Anat* **24,** 807–16 (July 2011).
7. Chikly, B. Who discovered the lymphatic system. *Lymphology* **4,** 186–93 (Dec. 1997).
8. Riva, M., Benedetti, M & Vaglienti, F. Guglielmo Riva (1627-1677) and the end of hepatocentrism: a 17th-century painting. *Vesalius* **20** (1921).
9. Mieli, A. Gli Scienziati Italiani dall?inizio del medioevo ai nostri giorni. *Dott. Attilio Nardecchia Editore* **1** (1921).
10. Scallan, J, Huxley, V. & Korthuis, R. *Capillary Fluid Exchange: Regulation, Functions, and Pathology* (Morgan and Claypool Life Sciences, 2010).

11. Von der Weid, P.-Y. & Zawieja, D. C. Lymphatic smooth muscle: the motor unit of lymph drainage. *The International Journal of Biochemistry and Cell Biology* **36,** 1147 –1153. ISSN: 1357-2725 (2004).

12. Von Andrian, U. H. Intravital Microscopy of the Peripheral Lymph Node Microcirculation in Mice. *Microcirculation* **3,** 287–300. ISSN: 1549-8719 (1996).

13. Baluk, P. *et al.* Functionally specialized junctions between endothelial cells of lymphatic vessels. *The Journal of experimental medicine* **204,** 2349–2362 (Oct. 2007).

14. Miller, N. E. *et al.* Secretion of adipokines by human adipose tissue in vivo: partitioning between capillary and lymphatic transport. *American Journal of Physiology-Endocrinology and Metabolism* **301.** PMID: 21750269, E659–E667 (2011).

15. Wiig, H. & Swartz, M. A. Interstitial Fluid and Lymph Formation and Transport: Physiological Regulation and Roles in Inflammation and Cancer. *Physiological Reviews* **92.** PMID: 22811424, 1005–1060 (2012).

16. Leak, L. V. Studies on the permeability of lymphatic capillaries. *The Journal of cell biology* **50,** 300–323 (Aug. 1971).

17. Albertine, K. H. & O'Morchoe, C. C. Renal lymphatic ultrastructure and translymphatic transport. *Microvascular Research* **19,** 338 –351. ISSN: 0026-2862 (1980).

18. Randolph, G. J., Ivanov, S., Zinselmeyer, B. H. & Scallan, J. P. The Lymphatic System: Integral Roles in Immunity. *Annual review of immunology* **35,** 31–52 (Apr. 2017).

19. Schmid-Schonbein, G. W. Microlymphatics and lymph flow. *Physiological Reviews* **70.** PMID: 2217560, 987–1028 (1990).

20. Ono, N., Mizuno, R. & Ohhashi, T. Effective permeability of hydrophilic substances through walls of lymph vessels: roles of endothelial barrier. *American Journal of Physiology-Heart and Circulatory Physiology* **289.** PMID: 15964919, H1676–H1682 (2005).

21. Scallan, J. P. & Huxley, V. H. In vivo determination of collecting lymphatic vessel permeability to albumin: a role for lymphatics in exchange. *The Journal of Physiology* **588,** 243–254 (2010).

22. Davis, M. J. *et al.* Intrinsic increase in lymphangion muscle contractility in response to elevated afterload. *American journal of physiology. Heart and circulatory physiology* **303,** H795–H808 (Oct. 2012).

23. Scallan, J. P., Zawieja, S. D., Castorena-Gonzalez, J. A. & Davis, M. J. Lymphatic pumping: mechanics, mechanisms and malfunction. *The Journal of physiology* **594,** 5749–5768 (Oct. 2016).

24. Scallan, J. P. *et al.* Independent and interactive effects of preload and afterload on the pump function of the isolated lymphangion. *American journal of physiology. Heart and circulatory physiology* **303,** H809–H824 (Oct. 2012).

25. Suami, H, Pan, W. & Taylor, G. Changes in the lymph structure of the upper limb after axillary dissection: Radiographic and anatomical study in a human cadaver. *Plast Reconstr Surg,* 982—991 (2007).

26. Avraham, T *et al.* Fibrosis Is a Key Inhibitor of Lymphatic Regeneration. *Plastic and Reconstructive Surgery* **124,** 438–450 (Aug. 2009).

27. Clark, B, Sitzia, J & Harlow, W. Incidence and risk of arm oedema following treatment for breast cancer: A three-year follow-up study. *QJM : monthly journal of the Association of Physicians* **98,** 343–8 (May 2005).

28. Rajasekaran, S., Rajamanickam, A., Gurusamy, M. & Bethunaickan, R. An overview of Lymphatic Filariasis Lymphedema. *Lymphology* **50** (Apr. 2018).

29. Bockarie, M. J. & Molyneux, D. H. The end of lymphatic filariasis? *BMJ* **338.** ISSN: 0959-8138. doi:10.1136/bmj.b1686. eprint: https://www.bmj.com/content. https://www.bmj.com/content/338/bmj.b1686 (2009).

30. *World Health Organisation Fact Sheet Lymphatic filarisis* https://www.who.int/news-room/fact-sheets/detail/lymphatic-filariasis (2018).

31. Leduc, O. & Leduc, A. Rehabilitation protocol in upper limb lymphedema. *Annali italiani di chirurgia* **73,** 479–84 (Sept. 2002).

32. Trombetta, E. & Mellman, I. CELL BIOLOGY OF ANTIGEN PROCESSING IN VITRO AND IN VIVO. *Annual Review of Immunology* **23.** PMID: 15771591, 975–1028 (2005).

33. Steinman, R. M. & Hemmi, H. Dendritic cells:translating innate to adaptive immunity. *Curr Top Microbiol Immunol* **311,** 17–58. ISSN: 0022-1007 (2006).

34. Braun, A. *et al.* Afferent lymph-derived T cells and DCs use different chemokine receptor CCR7-dependent routes for entry into the lymph node and intranodal migration. *Nat. Immunol.* **12,** 879–87 (2011).

35. Nibbs, R. J. *et al.* The beta-chemokine receptor D6 is expressed by lymphatic endothelium and a subset of vascular tumors. *The American journal of pathology* **158,** 867–877 (Mar. 2001).

36. Girard, J. P., Moussion, C. & Förster, R. HEVs, lymphatics and homeostatic immune cell trafficking in lymph nodes. *Nat. Rev. Immunol.* **12,** 762–73 (2012).

37. Laouini, D. *et al.* VI2 T Cell Repertoire of CD8+ Splenocytes Selected on Nonpolymorphic MHC Class I Molecules. *The Journal of Immunology* **165,** 6381–6386. ISSN: 0022-1767 (2000).

38. Blattman, J. N. *et al.* Estimating the Precursor Frequency of Naive Antigen-specific CD8 T Cells. *The Journal of Experimental Medicine* **195,** 657–664 (Mar. 2002).

39. Nelson, R. W. *et al.* T cell receptor cross-reactivity between similar foreign and self peptides influences naïve cell population size and autoimmunity. *Immunity* **42,** 95–107 (Jan. 2015).

40. Jenkins, M. K. & Moon, J. J. The role of naïve T cell precursor frequency and recruitment in dictating immune response magnitude. *Journal of Immunology (Baltimore, Md. : 1950)* **188,** 4135–4140 (May 2012).

41. Chaplin, D. D. Overview of the immune response. *The Journal of allergy and clinical immunology* **125,** S3–S23 (Feb. 2010).

42. Depillis, L., Gallegos, A. & Radunskaya, A. A model of dendritic cell therapy for melanoma. *Frontiers in oncology* **3,** 56–56 (Mar. 2013).

43. Harris, T. H. *et al.* Generalized Lévy walks and the role of chemokines in migration of effector CD8+ T cells. *Nature* **486,** 545 EP – (May 2012).

44. Banigan, E. J., Harris, T. H., Christian, D. A., Hunter, C. A. & Liu, A. J. Heterogeneous CD8+ T Cell Migration in the Lymph Node in the Absence of Inflammation Revealed by Quantitative Migration Analysis. *PLOS Computational Biology* **11,** 1–20 (Feb. 2015).

45. Textor, J. *et al.* Random Migration and Signal Integration Promote Rapid and Robust T Cell Recruitment. *PLOS Computational Biology* **10,** 1–16 (Aug. 2014).

46. Beltman, J. B., Marée, A. F., Lynch, J. N., Miller, M. J. & de Boer, R. J. Lymph node topology dictates T cell migration behavior. *Journal of Experimental Medicine* **204,** 771–780. ISSN: 0022-1007 (2007).

47. Bogle, G. & Dunbar, P. R. Simulating T-cell motility in the lymph node paracortex with a packed lattice geometry. *Immunol Cell Biol* **86,** 676–687 (Aug. 2008).

48. Bogle, G. & Dunbar, P. R. Agent-based simulation of T-cell activation and proliferation within a lymph node. *Immunol Cell Biol* **88,** 172–179 (Nov. 2009).

49. Fletcher, A. L., Acton, S. E. & Knoblich, K. Lymph node fibroblastic reticular cells in health and disease. *Nature reviews. Immunology* **15,** 350–361 (June 2015).

50. Lukacs-Kornek, V. *et al.* Regulated release of nitric oxide by nonhematopoietic stroma controls expansion of the activated T cell pool in lymph nodes. *Nature Immunology* **12,** 1096 EP – (Sept. 2011).

51. Siegert, S. *et al.* Fibroblastic reticular cells from lymph nodes attenuate T cell expansion by producing nitric oxide. *PloS one* **6,** e27618–e27618 (Nov. 2011).

52. Khan, O. *et al.* Regulation of T Cell Priming by Lymphoid Stroma. *PLOS ONE* **6,** 1–12 (Nov. 2011).

53. Katakai, T. Marginal reticular cells: a stromal subset directly descended from the lymphoid tissue organizer. *Frontiers in Immunology* **3,** 200. ISSN: 1664-3224 (2012).

54. Heesters, B. A., Myers, R. C. & Carroll, M. C. Follicular dendritic cells: dynamic antigen libraries. *Nature Reviews Immunology* **14,** 495 EP – (June 2014).

55. Ohl, L, Mohaupt, M, Czeloth, N, Hintzen, G & Kiafard, Z. CCR7 governs skin dendritic cell migration under inflammatory and steady-state conditions. *Immunity* (2004).

56. Ulvmar, M., Werth, K, Braun, A, Kelay, P & Hub, E. The atypical chemokine receptor CCRL1 shapes functional CCL21 gradients in lymph nodes. *Nature Imm.* doi:10.1038/ni.2889 (2014).

57. Tamburini, B. A., Burchill, M. A. & Kedl, R. M. Antigen capture and archiving by lymphatic endothelial cells following vaccination or viral infection. *Nature Communications* **5,** 3989 EP – (June 2014).

58. Acton, S. E. *et al.* Dendritic cells control fibroblastic reticular network tension and lymph node expansion. *Nature* **514,** 498–502 (Oct. 2014).

59. Kumar, V, Chyou, S, Stein, J. & Lu, T. Optical projection tomography reveals dynamics of HEV growth after immunization with protein plus CFA and features shared with HEVs in acute. *Frontiers in immunology* (2012).

60. **.Astarita, J. L. et al. The CLEC-2-podo... Nature Imm. 16, 75–84 (2015)**

61. Yao, L.-C., Baluk, P., Srinivasan, R. S., Oliver, G. & McDonald, D. M. Plasticity of button-like junctions in the endothelium of airway lymphatics in development and inflammation. *The American journal of pathology* **180,** 2561–2575 (June 2012).

62. Swartz, M. A. & Lund, A. W. Lymphatic and interstitial flow in the tumour microenvironment: linking mechanobiology with immunity. *Nature Reviews Cancer* **12,** 210 EP – (Feb. 2012).

63. Redmond, W. L. & Sherman, L. A. Peripheral Tolerance of CD8 T Lymphocytes. *Immunity* **22,** 275 –284. ISSN: 1074-7613 (2005).

64. Lucas, E. D. & Tamburini, B. A. J. Lymph Node Lymphatic Endothelial Cell Expansion and Contraction and the Programming of the Immune Response. *Frontiers in Immunology* **10,** 36. ISSN: 1664-3224 (2019).

65. Cohen, J. N. *et al.* Tolerogenic Properties of Lymphatic Endothelial Cells Are Controlled by the Lymph Node Microenvironment. *PLOS ONE* **9,** 1–13 (Feb. 2014).

66. Malhotra, D. *et al.* Transcriptional profiling of stroma from inflamed and resting lymph nodes defines immunological hallmarks. *Nature Immunology* **13,** 499 EP – (Apr. 2012).

67. Rouhani, S. J., Eccles, J. D., Tewalt, E. F. & Engelhard, V. H. Regulation of T-cell Tolerance by Lymphatic Endothelial Cells. *Journal of clinical and cellular immunology* **5,** 1000242 (2014).

68. Clement, C. C. & Santambrogio, L. The lymph self-antigen repertoire. *Frontiers in immunology* **4,** 424; 424–424 (Dec. 2013).

69. Dubrot, J. *et al.* Lymph node stromal cells acquire peptide–MHCII complexes from dendritic cells and induce antigen-specific CD4+ T cell tolerance. *Journal of Experimental Medicine* **211,** 1153–1166. ISSN: 0022-1007 (2014).

70. Chakraborty, S., Zawieja, D. C., Davis, M. J. & Muthuchamy, M. MicroRNA signature of inflamed lymphatic endothelium and role of miR-9 in lymphangiogenesis and inflammation. *American Journal of Physiology - Cell Physiology* **309,** C680–C692 (Nov. 2015).

71. Liao, S. *et al.* Impaired lymphatic contraction associated with immunosuppression. *Proceedings of the National Academy of Sciences of the United States of America* **108,** 18784–18789 (Nov. 2011).

72. Liao, S. & von der Weid, P. Y. Lymphatic system: an active pathway for immune protection. *Seminars in cell and developmental biology* **38,** 83–89 (Feb. 2015).

73. Padera, T. P., Meijer, E. F. J. & Munn, L. L. The Lymphatic System in Disease Processes and Cancer Progression. *Annual review of biomedical engineering* **18,** 125–158 (July 2016).

74. Jones, D., Pereira, E. R. & Padera, T. P. Growth and Immune Evasion of Lymph Node Metastasis. *Frontiers in oncology* **8,** 36; 36–36 (Feb. 2018).

75. Bachmann, C., Bachmann, R., Fend, F. & Wallwiener, D. Incidence and Impact of Lymph Node Metastases in Advanced Ovarian Cancer: Implications for Surgical Treatment. *Journal of Cancer* **7,** 2241–2246 (2016).

76. Lund, A. W. *et al.* Lymphatic vessels regulate immune microenvironments in human and murine melanoma. *The Journal of Clinical Investigation* **126,** 3389–3402 (Sept. 2016).

77. Karaman, S. & Detmar, M. Mechanisms of lymphatic metastasis. *The Journal of clinical investigation* **124,** 922–928 (Mar. 2014).

78. Pereira, E. R. *et al.* Lymph node metastases can invade local blood vessels, exit the node, and colonize distant organs in mice. *Science* **359,** 1403–1407. ISSN: 0036-8075 (2018).

79. Christiansen, A. & Detmar, M. Lymphangiogenesis and Cancer. *Genes and Cancer* **2,** 1146–1158 (Dec. 2011).

80. Dieterich, L. C. *et al.* Tumor-Associated Lymphatic Vessels Upregulate PDL1 to Inhibit T-Cell Activation. *Frontiers in immunology* **8,** 66; 66–66 (Feb. 2017).

81. Tewalt, E. F. *et al.* Lymphatic endothelial cells induce tolerance via PD-L1 and lack of costimulation leading to high-level PD-1 expression on CD8 T cells. *Blood* **120,** 4772–4782. ISSN: 0006-4971 (2012).

82. Kwon, S., Agollah, G. D., Wu, G., Chan, W. & Sevick-Muraca, E. M. Direct visualization of changes of lymphatic function and drainage pathways in lymph node metastasis of B16F10 melanoma using near-infrared fluorescence imaging. *Biomedical optics express* **4,** 967–977 (May 2013).

83. Thelmo, M. M. C. *et al.* Micrometastasis to In-Transit Lymph Nodes From Extremity and Truncal Malignant Melanoma. *Annals of Surgical Oncology* **8,** 444–448 (2001).

84. Vigl, B. *et al.* Tissue inflammation modulates gene expression of lymphatic endothelial cells and dendritic cell migration in a stimulus-dependent manner. *Blood* **118,** 205–215. ISSN: 0006-4971 (2011).

85. Lachance, P.-A., Hazen, A. & Sevick-Muraca, E. M. Lymphatic Vascular Response to Acute Inflammation. *PLoS ONE* **8,** e76078 (2013).

86. Yang, B. *et al.* Identification of microRNAs associated with lymphangiogenesis in human gastric cancer. **16** (July 2013).

87. Das, S. *et al.* Tumor cell entry into the lymph node is controlled by CCL1 chemokine expressed by lymph node lymphatic sinuses. *The Journal of experimental medicine* **210,** 1509–1528 (July 2013).

88. Maby-El Hajjami, H. & Petrova, T. V. Developmental and pathological lymphangiogenesis: from models to human disease. *Histochemistry and Cell Biology* **130,** 1063–1078. ISSN: 1432-119X (Dec. 2008).

89. Lee, E., Pandey, N. B. & Popel, A. S. Pre-treatment of mice with tumor-conditioned media accelerates metastasis to lymph nodes and lungs: a new spontaneous breast cancer metastasis model. *Clinical and experimental metastasis* **31,** 67–79 (Jan. 2014).

90. Harrell, M. I., Iritani, B. M. & Ruddell, A. Tumor-induced sentinel lymph node lymphangiogenesis and increased lymph flow precede melanoma metastasis. *The American journal of pathology* **170,** 774–786 (Feb. 2007).

91. Hirakawa, S. *et al.* VEGF-A induces tumor and sentinel lymph node lymphangiogenesis and promotes lymphatic metastasis. *The Journal of experimental medicine* **201,** 1089–1099 (Apr. 2005).

92. Chen, D. S. & Mellman, I. Elements of cancer immunity and the cancer–immune set point. *Nature* **541,** 321 EP – (Jan. 2017).

93. Padera, T. P. *et al.* Lymphatic Metastasis in the Absence of Functional Intratumor Lymphatics. *Science* **296,** 1883–1886. ISSN: 0036-8075 (2002).

94. Kim, T.-J. *et al.* Gene expression profiling for the prediction of lymph node metastasis in patients with cervical cancer. *Cancer Science* **99,** 31–38.

95. Feng, L. *et al.* Role of microRNA-141 in colorectal cancer with lymph node metastasis. *Experimental and Therapeutic Medicine* **12,** 3405–3410 (Nov. 2016).

96. Gong, C. *et al.* Predicting lymph node output efficiency using systems biology. *Journal of Theoretical Biology* **335,** 169 –184 (2013).

97. Gong, C., Linderman, J. & Kirschner, D. Harnessing the Heterogeneity of T Cell Differentiation Fate to Fine-Tune Generation of Effector and Memory T Cells. *Frontiers in Immunology* **5,** 57. ISSN: 1664-3224 (2014).

98. Cordelia Ziraldo Chang Gong, D. E.K.J. J. Strategic Priming with Multiple Antigens can Yield Memory Cell Phenotypes Optimized for Infection with Mycobacterium tuberculosis: A Computational Study. *Frontiers in Microbiology* **6.** doi:10.3389/fmicb.2015.01477. https://www.ncbi.nlm.nih.gov/pmc/articles/PMC4701940/ (2015).

99. V Baldazzi P Paci, M. B.F. C. Modeling lymphocyte homing and encounters in lymph nodes. *BMC Bioinformatics* **10,** 387. ISSN: 0264-410X (2009).

100. Cyster, J. G. Chemokines, sphingosine-1-phosphate, and cell migration in secondary lymphoid organs. *Annu. Rev. Immunol.* **23,** 127–59. ISSN: 0732-0582 (2005).

101. Andrian, U. H. v. & Mempel, T. R. Homing and cellular traffic in lymph nodes. *Nature reviews. Immunology* **3,** 867–78. ISSN: 1474-1733 (Mar. 2003).

102. Förster, R, Braun, A & Worbs, T. Lymph node homing of T cells and dendritic cells via afferent lymphatics. *Trends in immunology* (2012).

103. Girard, J. & Springer, T. High endothelial venules (HEVs): specialized endothelium for lymphocyte migration. *Immunology today* (1995).

104. Butcher, E. C. & Picker, L. J. Lymphocyte Homing and Homeostasis. *Science* **272,** 60–67. ISSN: 0036-8075 (1996).

105. Matloubian, M, Lo, C., Cinamon, G, Lesneski, M. & Xu, Y. Lymphocyte egress from thymus and peripheral lymphoid organs is dependent on S1P receptor 1. *Nature.* doi:10.1038/nature02284 (2004).

106. Lo, C., Xu, Y, Proia, R. & Cyster, J. Cyclical modulation of sphingosine-1-phosphate receptor 1 surface expression during lymphocyte recirculation and relationship to lymphoid organ transit. *Journal of Experimental Medicine.* doi:10.1084/jem.20041509 (2005).

107. Cyster, J. & Schwab, S. Sphingosine-1-phosphate and lymphocyte egress from lymphoid organs. *Annual review of immunology.* doi:10.1146/annurev-immunol-020711-075011 (2012).

108. Schwab, S. & Cyster, J. Finding a way out: lymphocyte egress from lymphoid organs. *Nature immunology.* doi:10.1038/ni1545 (2007).

109. Pham, T., Okada, T, Matloubian, M, Lo, C. & Cyster, J. S1P 1 receptor signaling overrides retention mediated by Gi-coupled receptors to promote T cell egress. *Immunity* (2008).

110. Grigorova, I., Schwab, S., Phan, T. & Pham, T. Cortical sinus probing, S1P1-dependent entry and flow-based capture of egressing T cells. *Nature Imm.* doi:10.1038/ni.1682 (2009).

111. Grigorova, I. L., Panteleev, M. & Cyster, J. G. Lymph node cortical sinus organization and relationship to lymphocyte egress dynamics and antigen exposure. *Proc. Natl. Acad. Sci. U.S.A.* **107,** 20447–52. ISSN: 0027-8424 (2010).

112. Hunter, M., Teijeira, A & Halin, C. T cell trafficking through lymphatic vessels. *Frontiers in Immunology* (2016).

113. Lee, M.-J. *et al.* Sphingosine-1-Phosphate as a Ligand for the G Protein-Coupled Receptor EDG-1. *Science* **279,** 1552–1555. ISSN: 0036-8075 (1998).

114. Shiow, L., Rosen, D., BrdiÄková, N, Xu, Y & An, J. CD69 acts downstream of interferon-I/I2 to inhibit S1P1 and lymphocyte egress from lymphoid organs. *Nature.* doi:10.1038/nature04606 (2006).

115. Banchereau, J, Briere, F & Caux, C. Immunobiology of dendritic cells. *Annual review of Immunology.* doi:10.1146/annurev.immunol.18.1.767 (2000).

116. Benechet, A. P. *et al.* T cell-intrinsic S1PR1 regulates endogenous effector T-cell egress dynamics from lymph nodes during infection. *Proceedings of the National Academy of Sciences of the United States of America* **113,** 2182–2187 (Feb. 2016).

117. Pennock, N. D. *et al.* T cell responses: naïve to memory and everything in between. *Advances in Physiology Education* **37,** 273–283 (Dec. 2013).

118. Prlic, M., Hernandez-Hoyos, G. & Bevan, M. J. Duration of the initial TCR stimulus controls the magnitude but not functionality of the CD8+ T cell response. *Journal of Experimental Medicine* **203,** 2135–2143. ISSN: 0022-1007 (2006).

119. Von Andrian, U. & Mackay, C. T-cell function and migration, two sides of the same coin. *New England Journal of Medicine* (2000).

120. Hugues, S. *et al.* Distinct T cell dynamics in lymph nodes during the induction of tolerance and immunity. *Nature Immunology* **5,** 1235 EP – (Oct. 2004).

121. Mempel, T. R., Henrickson, S. E. & Von Andrian, U. H. T-cell priming by dendritic cells in lymph nodes occurs in three distinct phases. *Nature* **427,** 154–9. ISSN: 0028-0836 (2004).

122. Stoll, S, Delon, J, Brotz, T. & Germain, R. Dynamic imaging of T cell-dendritic cell interactions in lymph nodes. *Science.* doi:10.1126/science.1071065 (2002).

123. Bousso, P. T-cell activation by dendritic cells in the lymph node: lessons from the movies. *Nature Reviews Immunology* **8,** 675 EP – (Sept. 2008).

124. Miller, M. J., Hejazi, A. S., Wei, S. H., Cahalan, M. D. & Parker, I. T cell repertoire scanning is promoted by dynamic dendritic cell behavior and random T cell motility in the lymph node. *Proc. Natl. Acad. Sci. U.S.A.* **101,** 998–1003. ISSN: 0027-8424 (2004).

125. Germain, R. N. & Stefanová, I. THE DYNAMICS OF T CELL RECEPTOR SIGNALING: Complex Orchestration and the Key Roles of Tempo and Cooperation. *Annual Review of Immunology* **17,** 467–522 (July 1999).

126. Rachmilewitz, J. & Lanzavecchia, A. A temporal and spatial summation model for T-cell activation: signal integration and antigen decoding. *Trends in Immunology* **23,** 592–595 (2002).

127. Lanzavecchia, A. & Sallusto, F. Progressive differentiation and selection of the fittest in the immune response. *Nature Reviews Immunology* **2,** 982 EP – (Dec. 2002).

128. Youngblood, B. *et al.* Effector CD8 T cells dedifferentiate into long-lived memory cells. *Nature* **552,** 404 EP – (Dec. 2017).

129. Wherry, E. J. & Ahmed, R. Memory CD8 T-Cell Differentiation during Viral Infection. *Journal of Virology* **78,** 5535–5545 (2004).

130. Van Stipdonk, M. J. B., Lemmens, E. E. & Schoenberger, S. P. Naïve CTLs require a single brief period of antigenic stimulation for clonal expansion and differentiation. *Nature Immunology* **2,** 423 EP – (May 2001).

131. Bevan, M. J. Helping the CD8+ T-cell response. *Nature Reviews Immunology* **4,** 595 EP – (Aug. 2004).

132. Schrum, A. G., Palmer, E. & Turka, L. A. Distinct temporal programming of naive CD4(+) T cells for cell division versus TCR-dependent death susceptibility by antigen-presenting macrophages. *European journal of immunology* **35,** 449–459 (Feb. 2005).

133. Wong, P. & Pamer, E. G. Cutting Edge: Antigen-Independent CD8 T Cell Proliferation. *The Journal of Immunology* **166,** 5864–5868. ISSN: 0022-1767 (2001).

134. Kaech, S. M. & Ahmed, R. Memory CD8+ T cell differentiation: initial antigen encounter triggers a developmental program in naïve cells. *Nature Immunology* **2,** 415 EP – (May 2001).

135. Shaulov, A. & Murali-Krishna, K. CD8 T Cell Expansion and Memory Differentiation Are Facilitated by Simultaneous and Sustained Exposure to Antigenic and Inflammatory Milieu. *The Journal of Immunology* **180,** 1131–1138. ISSN: 0022-1767 (2008).

136. Mueller, S. & KA, H. Regulation of homeostatic chemokine expression and cell trafficking during immune responses. *Science.* doi:10.1126/science.1144830 (2007).

137. Sallusto, F, Lenig, D, Förster, R, Lipp, M & Lanzavecchia, A. Two subsets of memory T lymphocytes with distinct homing potentials and effector functions. *Nature.* doi:10.1038/44385 (1999).

138. Weninger, W, Crowley, M. & Manjunath, N. Migratory properties of naive, effector, and memory CD8+ T cells. *J. of Exp. Med.* (2001).

139. Manjunath, N, Shankar, P & Wan, J. Effector differentiation is not prerequisite for generation of memory cytotoxic T lymphocytes. *J. Clinical Exp.* doi:10.1172/JCI13296 (2001).

140. Mueller, S. N. & Germain, R. N. Stromal cell contributions to the homeostasis and functionality of the immune system. *Nature Reviews Immunology* **9,** 618 EP – (July 2009).

141. Roozendaal, R. & Mebius, R. E. Stromal Cells Immune Cell Interactions. *Annual Review of Immunology* **29.** PMID: 21073333, 23–43 (2011).

142. Bajénoff, M. *et al.* Stromal cell networks regulate lymphocyte entry, migration, and territoriality in lymph nodes. *Immunity* **25,** 989–1001. ISSN: 1074-7613 (2006).

143. Katakai, T., Hara, T., Sugai, M., Gonda, H. & Shimizu, A. Lymph Node Fibroblastic Reticular Cells Construct the Stromal Reticulum via Contact with Lymphocytes. *The Journal of Experimental Medicine* **200,** 783–795 (Sept. 2004).

144. Link, A. *et al.* Fibroblastic reticular cells in lymph nodes regulate the homeostasis of naive T cells. *Nat. Immunol.* **8,** 1255–65. ISSN: 1529-2908 (2007).

145. Chyou, S. *et al.* Fibroblast-type reticular stromal cells regulate the lymph node vasculature. *Journal of immunology (Baltimore, Md. : 1950)* **181,** 3887–96 (Aug. 2008).

146. Acton, S. E. *et al.* Podoplanin-rich stromal networks induce dendritic cell motility via activation of the C-type lectin receptor CLEC-2. *Immunity* **37,** 276–289 (Aug. 2012).

147. Herzog, B. H. *et al.* Podoplanin maintains high endothelial venule integrity by interacting with platelet CLEC-2. *Nature* **502,** 105 EP – (Sept. 2013).

148. Fletcher, A. L., Malhotra, D. & Turley, S. J. Lymph node stroma broaden the peripheral tolerance paradigm. *Trends in immunology* **32,** 12–18 (Jan. 2011).

149. Onder, L. *et al.* IL-7–producing stromal cells are critical for lymph node remodeling. *Blood* **120,** 4675–4683. ISSN: 0006-4971 (2012).

150. Estes, J. *et al.* Collagen deposition limits immune reconstitution in the gut. *The Journal of infectious diseases* **198,** 456–464 (Aug. 2008).

151. Zeng, M. *et al.* Cumulative mechanisms of lymphoid tissue fibrosis and T cell depletion in HIV-1 and SIV infections. *The Journal of clinical investigation* **121,** 998–1008 (Mar. 2011).

152. Estes, J. D. *et al.* Antifibrotic therapy in simian immunodeficiency virus infection preserves CD4+ T-cell populations and improves immune reconstitution with antiretroviral therapy. *The Journal of infectious diseases* **211,** 744–754 (Mar. 2015).

153. Estes, J. D. Pathobiology of HIV/SIV-associated changes in secondary lymphoid tissues. *Immunological reviews* **254,** 65–77 (July 2013).

154. Tan, K. W. *et al.* Expansion of Cortical and Medullary Sinuses Restrains Lymph Node Hypertrophy during Prolonged Inflammation. *The Journal of Immunology* **188,** 4065–4080. ISSN: 0022-1767 (2012).

155. T., P. S. *et al.* MRI and Quantification of Draining Lymph Node Function in Inflammatory Arthritis. *Annals of the New York Academy of Sciences* **1117,** 106–123.

156. Manzo, A. *et al.* Subclinical remodelling of draining lymph node structure in early and established rheumatoid arthritis assessed by power Doppler ultrasonography. *Rheumatology* **50,** 1395–1400 (2011).

157. Chyou, S. *et al.* Coordinated regulation of lymph node vascular-stromal growth first by CD11c+ cells and then by T and B cells. *Journal of immunology (Baltimore, Md. : 1950)* **187,** 5558–67 (Nov. 2011).

158. Yang, C.-Y. Y. *et al.* Trapping of naive lymphocytes triggers rapid growth and remodeling of the fibroblast network in reactive murine lymph nodes. *Proceedings of the National Academy of Sciences of the United States of America* **111,** E109–18. ISSN: 0027-8424 (2014).

159. Kumar, V. *et al.* Global lymphoid tissue remodeling during a viral infection is orchestrated by a B cell–lymphotoxin-dependent pathway. *Blood* **115,** 4725–4733. ISSN: 0006-4971 (2010).

160. Webster, B. *et al.* Regulation of lymph node vascular growth by dendritic cells. *J. Exp. Med.* **203,** 1903–13. ISSN: 0022-1007 (2006).

161. Tzeng, T.-C. *et al.* CD11chi Dendritic Cells Regulate the Re-establishment of Vascular Quiescence and Stabilization after Immune Stimulation of Lymph Nodes. *The Journal of Immunology* **184,** 4247–4257. ISSN: 0022-1767 (2010).

162. Tedla, N, Wang, H. & HP, M. Regulation of T lymphocyte trafficking into lymph nodes during an immune response by the chemokines macrophage inflammatory protein (MIP)-1 and MIP-1I2. *The Journal of Imm.* (1998).

163. Ottaway, C. A. & Parrott, D. M. Regional blood flow and its relationship to lymphocyte and lymphoblast traffic during a primary immune reaction. *Journal of Experimental Medicine* **150,** 218–230. ISSN: 0022-1007 (1979).

164. Hay, J. B. & Hobbs, B. B. The flow of blood to lymph nodes and its relation to lymphocyte traffic and the immune response. *Journal of Experimental Medicine* **145,** 31–44. ISSN: 0022-1007 (1977).

165. Soderberg, K. A. *et al.* Innate control of adaptive immunity via remodeling of lymph node feed arteriole. *Proceedings of the National Academy of Sciences of the United States of America* **102,** 16315–16320. ISSN: 0027-8424 (May 2005).

166. Cahill, R., Frost, H & Trnka, Z. The effects of antigen on the migration of recirculating lymphocytes through single lymph nodes. *J. Exp. Med.* doi:10.1084/jem.143.4.870 (1976).

167. Ottaway, C. A. & Parrott, D. M. Regional blood flow and its relationship to lymphocyte and lymphoblast traffic during a primary immune reaction. *Journal of Experimental Medicine* **150,** 218–230. ISSN: 0022-1007 (1979).

168. Herman, P. G., Yamamoto, I. & Mellins, H. BLOOD MICROCIRCULATION IN THE LYMPH NODE DURING THE PRIMARY IMMUNE RESPONS. *TJ Exp Med* **136,** 697–714. ISSN: 0022-1007 (1972).

169. J, A., Matt, L. R. & Cyster, J. D. Response in Distant Lymph Nodes of Mice to Infection in the Hind Footpad with Mycobacterium Marino. *Infection and Immunity* **28,** 225–229 (Apr. 1980).

170. Gregory, J. L. *et al.* Infection Programs Sustained Lymphoid Stromal Cell Responses and Shapes Lymph Node Remodeling upon Secondary Challenge. *Cell Reports* **18,** 406 –418. ISSN: 2211-1247 (2017).

171. Reynolds, J., Coles, M., Lythe, G. & Molina-París, C. Mathematical Model of Naive T Cell Division and Survival IL-7 Thresholds. *Frontiers in immunology* **4,** 434–434 (Dec. 2013).

172. Choo, D. K., Murali-Krishna, K., Anita, R. & Ahmed, R. Homeostatic Turnover of Virus-Specific Memory CD8 T Cells Occurs Stochastically and Is Independent of CD4 T Cell Help. *The Journal of Immunology* **185,** 3436–3444. ISSN: 0022-1767 (2010).

173. Su, B, Zhou, W, Dorman, K. & Jones, D. Mathematical Modelling of Immune Response in Tissues. *Computational and Mathematical Methods in Medicine* **10,** 9–38 (2009).

174. Cheong, R. *et al.* Transient IkB Kinase Activity Mediates Temporal NF-KB Dynamics in Response to a Wide Range of Tumor Necrosis Factor-alpha Doses. *Journal of Biological Chemistry* **281,** 2945–2950 (2006).

175. Fricke, G. M., Letendre, K. A., Moses, M. E. & Cannon, J. L. Persistence and Adaptation in Immunity: T Cells Balance the Extent and Thoroughness of Search. *PLOS Computational Biology* **12,** 1–23 (Mar. 2016).

176. Donovan, G. M. & Lythe, G. T-cell movement on the reticular network. *Journal of Theoretical Biology* **295,** 59 –67. ISSN: 0022-5193 (2012).

177. Graw, F. & Regoes, R. R. Influence of the Fibroblastic Reticular Network on Cell-Cell Interactions in Lymphoid Organs. *PLOS Computational Biology* **8,** 1–9 (Mar. 2012).

178. Riggs, T. *et al.* A comparison of random vs. chemotaxis-driven contacts of T cells with dendritic cells during repertoire scanning. *Journal of theoretical biology* **250,** 732–751 (Feb. 2008).

179. Bogle, G. & Dunbar, P. R. On-lattice simulation of T cell motility, chemotaxis, and trafficking in the lymph node paracortex. *PloS one* **7,** e45258 (2012).

180. Brown, L. V., Gaffney, E. A., Wagg, J. & Coles, M. C. An in silico model of cytotoxic T-lymphocyte activation in the lymph node following short peptide vaccination. *Journal of the Royal Society, Interface* **15,** 20180041 (Mar. 2018).

181. Celli, S. *et al.* How many dendritic cells are required to initiate a T-cell response? *Blood* **120,** 3945–3948. ISSN: 0006-4971 (2012).

182. Jafarnejad, M., Woodruff, M. C., Zawieja, D. C., Carroll, M. C. & Moore, J. Modeling Lymph Flow and Fluid Exchange with Blood Vessels in Lymph Nodes. *Lymphat Res Biol* **13,** 234–247. ISSN: 1539-6851 (2015).

183. Kuka, M. & Iannacone, M. The role of lymph node sinus macrophages in host defense. *Annals of the New York Academy of Sciences* **1319,** 38–46 (2014).

184. Smith, J. B., McIntosh, G. H. & Morris, B. The traffic of cells through tissues: a study of peripheral lymph in sheep. *Journal of Anatomy* **107,** 87–100 (July 1970).

185. Hall, J. & Morris, B. The immediate effect of antigens on the cell output of a lymph node. *British journal of experimental pathology* (1965).

186. Latif, R. *et al.* Reversal of the CD4(+)/CD8(+) T-Cell Ratio in Lymph Node Cells upon In Vitro Mitogenic Stimulation by Highly Purified, Water-Soluble S3-S4 Dimer of Pertussis Toxin. *Infection and Immunity* **69** (ed Clements, J. D.) 3073–3081 (May 2001).

187. Hernandez, O., Oweity, T. & Ibrahim, S. Is an increase in CD4/CD8 T-cell ratio in lymph node fine needle aspiration helpful for diagnosing Hodgkin lymphoma? A study of 85 lymph node FNAs with increased CD4/CD8 ratio. *CytoJournal* **2,** 14–14 (2005).

188. Park, E., Peixoto, A, Imai, Y, Goodarzi, A & Cheng, G. Distinct roles for LFA-1 affinity regulation during T-cell adhesion, diapedesis, and interstitial migration in lymph nodes. *Blood* (2010).

189. Boscacci, R., Pfeiffer, F, Gollmer, K & Sevilla, A. Comprehensive analysis of lymph node stroma-expressed Ig superfamily members reveals redundant and nonredundant roles for ICAM-1, ICAM-2, and VCAM-1 in lymphocyte homing. *Blood* (2010).

190. Park, C, Hwang, I., Sinha, R. & Kamenyeva, O. Lymph node B lymphocyte trafficking is constrained by anatomy and highly dependent upon chemoattractant desensitization. *Blood* (2012).

191. Miller, M. J., Wei, S. H., Parker, I. & Cahalan, M. D. Two-photon imaging of lymphocyte motility and antigen response in intact lymph node. *Science* **296,** 1869–73. ISSN: 0036-8075 (2002).

192. Miller, M. J., Wei, S. H., Cahalan, M. D. & Parker, I. Autonomous T cell trafficking examined in vivo with intravital two-photon microscopy. *Proc. Natl. Acad. Sci. U.S.A.* **100,** 2604–9. ISSN: 0027-8424 (2003).

193. Bousso, P & Robey, E. Dynamics of CD8+ T cell priming by dendritic cells in intact lymph nodes. *Nature immunology* (2003).

194. Cella, M. *et al.* Maturation, Activation, and Protection of Dendritic Cells Induced by Double-stranded RNA. *The Journal of Experimental Medicine* **189,** 821–829 (Mar. 1999).

195. Kukutsch, N. A., RoÃner, S., Austyn, J. M., Schuler, G. & Lutz, M. B. Formation and Kinetics of MHC Class I-Ovalbumin Peptide Complexes on Immature and Mature Murine Dendritic Cells. *Journal of Investigative Dermatology* **115,** 449 –453. ISSN: 0022-202X (2000).

196. Cella, M., Engering, A., Pinet, V., Pieters, J. & Lanzavecchia, A. Inflammatory stimuli induce accumulation of MHC class II complexes on dendritic cells. *Nature* **388,** 782 EP – (Aug. 1997).

197. Baumgartner, C., Ferrante, A., Nagaoka, M., Gorski, J. & Malherbe, L. P. Peptide-MHC Class II Complex Stability Governs CD4 T Cell Clonal Selection. *Journal of immunology (Baltimore, Md. : 1950)* **184,** 573–581 (Jan. 2010).

198. Nitschké, M. *et al.* Differential requirement for ROCK in dendritic cell migration within lymphatic capillaries in steady-state and inflammation. *Blood* **120,** 2249–2258. ISSN: 0006-4971 (2012).

199. Paharkova-Vatchkova, V., Maldonado, R. & Kovats, S. Estrogen Preferentially Promotes the Differentiation of CD11c+ CD11bintermediate Dendritic Cells from Bone Marrow Precursors. *The Journal of Immunology* **172,** 1426–1436. ISSN: 0022-1767 (2004).

200. Obst, R. The Timing of T Cell Priming and Cycling. *Frontiers in Immunology* **6,** 563 (2015).

201. Smith, C. M. *et al.* Cognate CD4+ T cell licensing of dendritic cells in CD8+ T cell immunity. *Nature Immunology* **5,** 1143 EP – (Oct. 2004).

202. De Boer, R. J., Homann, D. & Perelson, A. S. Different Dynamics of CD4+ and CD8+ T Cell Responses During and After Acute Lymphocytic Choriomeningitis Virus Infection. *The Journal of Immunology* **171,** 3928–3935. ISSN: 0022-1767 (2003).

203. Foulds, K. E. *et al.* Cutting Edge: CD4 and CD8 T Cells Are Intrinsically Different in Their Proliferative Responses. *The Journal of Immunology* **168,** 1528–1532. ISSN: 0022-1767 (2002).

204. Tubo, N. J. *et al.* Single Naive CD4$^+$ T Cells from a Diverse Repertoire Produce Different Effector Cell Types during Infection. *Cell* **153,** 785–796.

205. Linderman, J. J. *et al.* Characterizing the Dynamics of CD4+ T Cell Priming within a Lymph Node. *The Journal of Immunology* **184,** 2873–2885. ISSN: 0022-1767 (2010).

206. Obar, J. J., Khanna, K. M. & Lefrançois, L. Endogenous naive CD8+ T cell precursor frequency regulates primary and memory responses to infection. *Immunity* **28,** 859–869 (June 2008).

207. Garris, C. S., Blaho, V. A., Hla, T. & Han, M. H. Sphingosine-1-phosphate receptor 1 signalling in T cells: trafficking and beyond. *Immunology* **142,** 347–353 (July 2014).

208. Habenicht, L. M., Albershardt, T. C., Iritani, B. M. & Ruddell, A. Distinct mechanisms of B and T lymphocyte accumulation generate tumor-draining lymph node hypertrophy. *Oncoimmunology* **5,** e1204505 (Aug. 2016).

209. Battaglia, A. *et al.* Lymphocyte populations in human lymph nodes. Alterations in CD4(+) CD25(+) T regulatory cell phenotype and T-cell receptor VBetarepertoire. *Immunology* **110,** 304–312 (Nov. 2003).

210. Catron, D. M., Itano, A. A., Pape, K. A., Mueller, D. L. & Jenkins, M. K. Visualizing the first 50 hr of the primary immune response to a soluble antigen. *Immunity.* **21,** 341–347. ISSN: 1074-7613 (2004).

211. Tomura, M, Yoshida, N & Tanaka, J. Monitoring cellular movement in vivo with photoconvertible fluorescence protein 'Kaede' transgenic mice. *PNAS.* doi:10.1073/pnas.0802278105 (2008).

212. Sprent, J. & Tough, D. F. T Cell Death and Memory. *Science* **293,** 245–248. ISSN: 0036-8075 (2001).

213. Obst, R., van Santen, H.-M., Mathis, D. & Benoist, C. Antigen persistence is required throughout the expansion phase of a CD4(+) T cell response. *The Journal of experimental medicine* **201,** 1555–1565 (May 2005).

214. Marino, S., Hogue, I. B., Ray, C. J. & Kirschner, D. E. A methodology for performing global uncertainty and sensitivity analysis in systems biology. *Journal of Theoretical Biology* **254,** 178 –196. ISSN: 0022-5193 (2008).

215. Saltelli, A, Chan, K & Scott, E. *Wiley series in probability and statistics: Sensitivity analysis* (Wiley, Chichester, 2000).

216. Moon, J. J. *et al.* Naive CD4(+) T cell frequency varies for different epitopes and predicts repertoire diversity and response magnitude. *Immunity* **27,** 203–213 (Aug. 2007).

217. Martín-Fontecha, A. *et al.* Regulation of Dendritic Cell Migration to the Draining Lymph Node. *Journal of Experimental Medicine* **198,** 615–621. ISSN: 0022-1007 (2003).

218. Gräler, M. H., Huang, M.-C., Watson, S. & Goetzl, E. J. Immunological Effects of Transgenic Constitutive Expression of the Type 1 Sphingosine 1-Phosphate Receptor by Mouse Lymphocytes. *The Journal of Immunology* **174,** 1997–2003. ISSN: 0022-1767 (2005).

219. He, Y. Scanning electron microscope studies of the rat mesenteric lymph node with special reference to high-endothelial venules and hitherto unknown lymphatic labyrinth. *Archivum histologicum Japonicum,* 1–15 (1985).

220. Tough, D. F. & Sprent, J. Life span of naive and memory t cells. *STEM CELLS* **13,** 242–249 (1995).

221. Kamath, A. T., Henri, S., Battye, F., Tough, D. F. & Shortman, K. Developmental kinetics and lifespan of dendritic cells in mouse lymphoid organs. *Blood* **100,** 1734–1741. ISSN: 0006-4971 (2002).

222. Bajénoff, M, Granjeaud, S & Guerder, S. The strategy of T cell antigen-presenting cell encounter in antigen-draining lymph nodes revealed by imaging of initial T cell activation. *Journal of Experimental Med.* doi:10.1084/jem.20030167 (2003).

223. Yoon, H., Legge, K. L., Sung, S.-s. J. & Braciale, T. J. Sequential Activation of CD8+ T Cells in the Draining Lymph Nodes in Response to Pulmonary Virus Infection. *The Journal of Immunology* **179,** 391–399. ISSN: 0022-1767 (2007).

224. Lawrence, C. W. & Braciale, T. J. Activation, Differentiation, and Migration of Naive Virus-Specific CD8+ T Cells during Pulmonary Influenza Virus Infection. *The Journal of Immunology* **173,** 1209–1218. ISSN: 0022-1767 (2004).

225. Demotz, S, Grey, H. & Sette, A. The minimal number of class II MHC-antigen complexes needed for T cell activation. *Science* **249,** 1028–1030. ISSN: 0036-8075 (1990).

226. Lee, W. T., Pasos, G., Cecchini, L. & Mittler, J. N. Continued Antigen Stimulation Is Not Required During CD4+ T Cell Clonal Expansion. *The Journal of Immunology* **168,** 1682–1689. ISSN: 0022-1767 (2002).

227. Arens, R. & Schoenberger, S. P. Plasticity in programming of effector and memory CD8(+) T-cell formation. *Immunological reviews* **235,** 190–205 (May 2010).

228. Butz, E. A. & Bevan, M. J. Massive Expansion of Antigen-Specific CD8(+) T Cells during an Acute Virus Infection. *Immunity* **8,** 167–175 (Feb. 1998).

229. Murali-Krishna, K. *et al.* Counting Antigen-Specific CD8 T Cells: A Reevaluation of Bystander Activation during Viral Infection. *Immunity* **8,** 177–187 (July 1998).

230. Busch, D. H., Pilip, I. M., Vijh, S. & Pamer, E. G. Coordinate Regulation of Complex T Cell Populations Responding to Bacterial Infection. *Immunity* **8,** 353–362 (July 1998).

231. Williams, M. A. & Bevan, M. J. Shortening the Infectious Period Does Not Alter Expansion of CD8 T Cells but Diminishes Their Capacity to Differentiate into Memory Cells. *The Journal of Immunology* **173,** 6694–6702. ISSN: 0022-1767 (2004).

232. Mackay, C., Marston, W & Dudler, L. Altered patterns of T cell migration through lymph nodes and skin following antigen challenge. *European journal of Imm.* doi:10.1002/eji.1830220904 (1992).

233. Corbin, G. A. & Harty, J. T. Duration of Infection and Antigen Display Have Minimal Influence on the Kinetics of the CD4+ T Cell Response to Listeria monocytogenes Infection. *The Journal of Immunology* **173,** 5679–5687. ISSN: 0022-1767 (2004).

234. Rabenstein, H. *et al.* Differential Kinetics of Antigen Dependency of CD4+ and CD8+ T Cells. *The Journal of Immunology* **192,** 3507–3517. ISSN: 0022-1767 (2014).

235. Chun, J. & Hartung, H.-P. Mechanism of action of oral fingolimod (FTY720) in multiple sclerosis. *Clinical neuropharmacology* **33,** 91–101 (Mar. 2010).

236. Huang, J. & LI, C. Requirements for T lymphocyte migration in explanted lymph nodes. *The Journal of Immunology.* doi:10.4049/jimmunol.178.12.7747 (2007).

237. Okada, T & Cyster, J. CC chemokine receptor 7 contributes to Gi-dependent T cell motility in the lymph node. *The Journal of Immunology.* doi:10.4049/jimmunol.178.5.2973 (2007).

238. Worbs, T, Mempel, T. & Bölter, J. CCR7 ligands stimulate the intranodal motility of T lymphocytes in vivo. *Journal of Exp.Med.* doi:10.1084/jem.20061706 (2007).

239. Pietilä, T. E. *et al.* Multiple NF-IB and IFN Regulatory Factor Family Transcription Factors Regulate CCL19 Gene Expression in Human Monocyte-Derived Dendritic Cells. *The Journal of Immunology* **178,** 253–261. ISSN: 0022-1767 (2007).

240. Jelley-Gibbs, D. M., Lepak, N. M., Yen, M. & Swain, S. L. Two Distinct Stages in the Transition from Naive CD4 T Cells to Effectors, Early Antigen-Dependent and Late Cytokine-Driven Expansion and Differentiation. *The Journal of Immunology* **165,** 5017–5026. ISSN: 0022-1767 (2000).

241. Iezzi, G., Karjalainen, K. & Lanzavecchia, A. The Duration of Antigenic Stimulation Determines the Fate of Naive and Effector T Cells. *Immunity* **8,** 89 –95. ISSN: 1074-7613 (1998).

242. Hirakawa, S. *et al.* VEGF-A induces tumor and sentinel lymph node lymphangiogenesis and promotes lymphatic metastasis. *The Journal of experimental medicine* **201,** 1089–1099 (Apr. 2005).

243. Lucas, E. D. *et al.* Type 1 IFN and PD-L1 Coordinate Lymphatic Endothelial Cell Expansion and Contraction during an Inflammatory Immune Response. *The Journal of Immunology* **201,** 1735–1747. ISSN: 0022-1767 (2018).

244. Kataru, R. P. *et al.* Critical role of CD11b+ macrophages and VEGF in inflammatory lymphangiogenesis, antigen clearance, and inflammation resolution. *Blood* **113,** 5650–5659. ISSN: 0006-4971 (2009).

245. Steinman, R. M., Inaba, K., Turley, S., Pierre, P. & Mellman, I. Antigen capture, processing, and presentation by dendritic cells: recent cell biological studies. *Human Immunology* **60,** 562 –567. ISSN: 0198-8859 (1999).

246. Drutman, S. B. & Trombetta, E. S. Dendritic cells continue to capture and present antigens after maturation in vivo. *Journal of immunology (Baltimore, Md. : 1950)* **185,** 2140–2146 (Aug. 2010).

247. Chen, P. *et al.* Dendritic cell targeted vaccines: Recent progresses and challenges. *Human vaccines and immunotherapeutics* **12,** 612–622 (Oct. 2015).

248. Hirakawa, S. *et al.* VEGF-C-induced lymphangiogenesis in sentinel lymph nodes promotes tumor metastasis to distant sites. *Blood* **109,** 1010–1017 (Feb. 2007).

249. Bouta, E. M. *et al.* Power Doppler Ultrasound Phenotyping of Expanding versus Collapsed Popliteal Lymph Nodes in Murine Inflammatory Arthritis. *PLOS ONE* **8,** 1–8 (Sept. 2013).

250. UK, C. R. *Cancer Research UK* `https://www.cancerresearchuk.org/health-professional/cancer-statistics/statistics-by-cancer-type/ovarian-cancer` (2018).

251. Takeshima, N. *et al.* Lymph node metastasis in ovarian cancer: Difference between serous and non-serous primary tumors. *Gynecologic Oncology* **99,** 427 –431. ISSN: 0090-8258 (2005).

252. Panici, P. B. *et al.* Systematic Aortic and Pelvic Lymphadenectomy Versus Resection of Bulky Nodes Only in Optimally Debulked Advanced Ovarian

Cancer: A Randomized Clinical Trial. *JNCI: Journal of the National Cancer Institute* **97,** 560–566 (2005).

253. Aletti, G. D., Dowdy, S., Podratz, K. C. & Cliby, W. A. Role of lymphadenectomy in the management of grossly apparent advanced stage epithelial ovarian cancer. *American Journal of Obstetrics and Gynecology* **195,** 1862 –1868. ISSN: 0002-9378 (2006).

254. HARTER, P. *et al.* Pattern and clinical predictors of lymph node metastases in epithelial ovarian cancer. *International Journal of Gynecological Cancer* **17** (2007).

255. Bachmann, C. *et al.* Prevalence and distribution pattern of nodal metastases in advanced ovarian cancer. *Molecular and Clinical Oncology* **5,** 483–487 (Oct. 2016).

256. Bakkar, R. *et al.* Stage IIIC Ovarian/Peritoneal Serous Carcinoma: A Heterogeneous Group of Patients With Different Prognoses. *International Journal of Gynecological Pathology* **33** (2014).

257. Cancer, T. O. *Target Ovarian Cancer:Stages and Grades* `https://www.targetovariancancer.org.uk/information-and-support/what-ovarian-cancer/stages-and-grades` (2018).

258. Wimberger, P. *et al.* Prognostic factors for complete debulking in advanced ovarian cancer and its impact on survival. An exploratory analysis of a prospectively randomized phase III study of the Arbeitsgemeinschaft Gynaekologische Onkologie Ovarian Cancer Study Group (AGO-OVAR). *Gynecologic Oncology* **106,** 69 –74. ISSN: 0090-8258 (2007).

259. Suh, D. H. *et al.* Improvements to the FIGO staging for ovarian cancer: reconsideration of lymphatic spread and intraoperative tumor rupture. *Journal of Gynecologic Oncology* **24,** 352–358 (Oct. 2013).

260. Abe, A. *et al.* The impact of systematic para-aortic and pelvic lymphadenectomy on survival in patients with optimally debulked ovarian cancer. *Journal of Obstetrics and Gynaecology Research* **36,** 1023–1030 (2013).

261. Nomura, H. *et al.* Lymph Node Metastasis in Grossly Apparent Stages I and II Epithelial Ovarian Cancer. *International Journal of Gynecological Cancer* **20** (2010).

262. Chekerov, R. *et al.* Outcome and Clinical Management of 275 Patients With Advanced Ovarian Cancer International Federation of Obstetrics and Gynecology II to IV Inside the European Ovarian Cancer Translational Research Consortium—OVCAD. *International Journal of Gynecological Cancer* **23** (2013).

263. Carnino, F. *et al.* Significance of Lymph Node Sampling in Epithelial Carcinoma of the Ovary. *Gynecologic Oncology* **65,** 467 –472. ISSN: 0090-8258 (1997).

264. Kim, H. *et al.* Systematic Lymphadenectomy for Survival in Epithelial Ovarian Cancer: A Meta-Analysis. *International Journal of Gynecological Cancer* **20** (2010).

265. Pereira, A. *et al.* The Role of Lymphadenectomy in Node-Positive Epithelial Ovarian Cancer. *International Journal of Gynecological Cancer* **22** (2012).

266. Lund, A. W. & Swartz, M. A. Role of Lymphatic Vessels in Tumor Immunity: Passive Conduits or Active Participants? *Journal of Mammary Gland Biology and Neoplasia* **15,** 341–352. ISSN: 1573-7039 (Sept. 2010).

267. Issa, A., Le, T. X., Shoushtari, A. N., Shields, J. D. & Swartz, M. A. Vascular Endothelial Growth Factor-C and C-C Chemokine Receptor 7 in Tumor Cell–Lymphatic Cross-talk Promote Invasive Phenotype. *Cancer Research* **69,** 349–357. ISSN: 0008-5472 (2009).

268. Sarvaiya, P. J., Guo, D., Ulasov, I., Gabikian, P. & Lesniak, M. S. Chemokines in tumor progression and metastasis. *Oncotarget* **4,** 2171–2185 (Dec. 2013).

269. Tammela, T. *et al.* Photodynamic Ablation of Lymphatic Vessels and Intralymphatic Cancer Cells Prevents Metastasis. *Science Translational Medicine* **3,** 69ra11–69ra11. ISSN: 1946-6234 (2011).

270. Hoshida, T. *et al.* Imaging Steps of Lymphatic Metastasis Reveals That Vascular Endothelial Growth Factor-C Increases Metastasis by Increasing Delivery of Cancer Cells to Lymph Nodes: Therapeutic Implications. *Cancer Research* **66,** 8065–8075. ISSN: 0008-5472 (2006).

271. Zolla, V *et al.* Aging-related anatomical and biochemical changes in lymphatic collectors impair lymph transport, fluid homeostasis, and pathogen clearance. *Aging cell* **14,** 582–594 (Aug. 2015).

272. Reitsma, S., Slaaf, D. W., Vink, H., van Zandvoort, M. A.M. J. & oude Egbrink, M. G. A. The endothelial glycocalyx: composition, functions, and visualization. *Pflugers Archiv : European journal of physiology* **454,** 345–359 (June 2007).

273. Masoumi Moghaddam, S., Amini, A., Morris, D. L. & Pourgholami, M. H. Significance of vascular endothelial growth factor in growth and peritoneal dissemination of ovarian cancer. *Cancer metastasis reviews* **31,** 143–162 (June 2012).

274. Preynat-Seauve, O. *et al.* Extralymphatic Tumors Prepare Draining Lymph Nodes to Invasion via a T-Cell Cross-Tolerance Process. *Cancer Research* **67,** 5009–5016. ISSN: 0008-5472 (2007).

275. Steeg, P. S. Emissaries set up new sites. *Nature* **438,** 750 EP – (Dec. 2005).

276. Stachura, J. *et al.* The dual role of tumor lymphatic vessels in dissemination of metastases and immune response development. *Oncoimmunology* **5,** e1182278 (July 2016).

277. Fankhauser, M. *et al.* Tumor lymphangiogenesis promotes T cell infiltration and potentiates immunotherapy in melanoma. *Science Translational Medicine* **9.** ISSN: 1946-6234 (2017).

278. Yip, L. *et al.* Deaf1 isoforms control the expression of genes encoding peripheral tissue antigens in the pancreatic lymph nodes during type 1 diabetes. *Nature immunology* **10,** 1026–1033 (Sept. 2009).

279. Hirosue, S. *et al.* Steady-state antigen scavenging, cross-presentation, and CD8+ T cell priming: a new role for lymphatic endothelial cells. *Journal of immunology (Baltimore, Md. : 1950)* **192,** 5002–5011 (June 2014).

280. Cohen, J. N. *et al.* Lymph node-resident lymphatic endothelial cells mediate peripheral tolerance via Aire-independent direct antigen presentation. *The Journal of experimental medicine* **207,** 681–688 (Apr. 2010).

281. Chatterjee, V. & Gashev, A. A. Mast cell-directed recruitment of MHC class II positive cells and eosinophils towards mesenteric lymphatic vessels in adulthood and elderly. *Lymphatic research and biology* **12,** 37–47 (Mar. 2014).

282. Chatterjee, V. & Gashev, A. A. Aging-associated shifts in functional status of mast cells located by adult and aged mesenteric lymphatic vessels. *American journal of physiology. Heart and circulatory physiology* **303,** H693–H702 (Sept. 2012).

283. Chakraborty, S. *et al.* Lipopolysaccharide modulates neutrophil recruitment and macrophage polarization on lymphatic vessels and impairs lymphatic function in rat mesentery. *American journal of physiology. Heart and circulatory physiology* **309,** H2042–H2057 (Dec. 2015).

284. Lund, A. *et al.* VEGF-C Promotes Immune Tolerance in B16 Melanomas and Cross-Presentation of Tumor Antigen by Lymph Node Lymphatics. *Cell Reports* **1,** 191 –199. ISSN: 2211-1247 (2012).

285. Lagos-Quintana, M., Rauhut, R., Lendeckel, W. & Tuschl, T. Identification of Novel Genes Coding for Small Expressed RNAs. *Science* **294,** 853–858. ISSN: 0036-8075 (2001).

286. Lujambio, A. *et al.* A microRNA DNA methylation signature for human cancer metastasis. *Proceedings of the National Academy of Sciences of the United States of America* **105,** 13556–13561 (Sept. 2008).

287. Hammond, S. M., Caudy, A. A. & Hannon, G. J. Post-transcriptional gene silencing by double-stranded RNA. *Nature Reviews Genetics* **2,** 110 EP – (Feb. 2001).

288. Ambros, V. microRNAs: Tiny Regulators with Great Potential. *Cell* **107,** 823 –826. ISSN: 0092-8674 (2001).

289. Ha, M. & Kim, V. N. Regulation of microRNA biogenesis. *Nature Reviews Molecular Cell Biology* **15,** 509 EP – (July 2014).

290. Friedman, R. C., Farh, K. K.-H., Burge, C. B. & Bartel, D. P. Most mammalian mRNAs are conserved targets of microRNAs. *Genome Research* **19,** 92–105 (Jan. 2009).

291. Lewis, B. P., hung Shih, I, Jones-Rhoades, M. W., Bartel, D. P. & Burge, C. B. Prediction of Mammalian MicroRNA Targets. *Cell* **115,** 787 –798. ISSN: 0092-8674 (2003).

292. Peng, Y. & Croce, C. M. The role of MicroRNAs in human cancer. *Signal Transduction And Targeted Therapy* **1,** 15004 EP – (Jan. 2016).

293. Kumar, M. S. *et al.* Dicer1 functions as a haploinsufficient tumor suppressor. *Genes and Development* **23,** 2700–2704 (Dec. 2009).

294. Ravi, A. *et al.* Proliferation and Tumorigenesis of a Murine Sarcoma Cell Line in the Absence of DICER1. *Cancer Cell* **21,** 848–855 (June 2012).

295. Merritt, W. M. *et al.* Dicer, Drosha, and Outcomes in Patients with Ovarian Cancer. *The New England journal of medicine* **359,** 2641–2650 (Dec. 2008).

296. Pampalakis, G., Diamandis, E. P., Katsaros, D. & Sotiropoulou, G. Downregulation of dicer expression in ovarian cancer tissues. *Clinical Biochemistry* **43,** 324 –327. ISSN: 0009-9120 (2010).

297. Faggad, A. *et al.* Prognostic significance of Dicer expression in ovarian cancer link to global microRNA changes and oestrogen receptor expression. *The Journal of Pathology* **220,** 382–391 (2009).

298. Coebergh van den Braak, R. R. J. *et al.* Confirmation of a metastasis-specific microRNA signature in primary colon cancer. *Scientific Reports* **8,** 5242 (2018).

299. Ricciardiello, F *et al.* A miRNA signature suggestive of nodal metastases from laryngeal carcinoma. *Acta Otorhinolaryngologica Italica* **37,** 467–474 (Dec. 2017).

300. Volinia, S. *et al.* A microRNA expression signature of human solid tumors defines cancer gene targets. *Proceedings of the National Academy of Sciences* **103,** 2257–2261. ISSN: 0027-8424 (2006).

301. Calin, G. A. & Croce, C. M. MicroRNA signatures in human cancers. *Nature Reviews Cancer* **6,** 857 EP – (Nov. 2006).

302. Network, T. C.G.A. R. *et al.* Integrated genomic analyses of ovarian carcinoma. *Nature* **474,** 609 EP – (June 2011).

303. Sun, Y. *et al.* Key nodes of a microRNA network associated with the integrated mesenchymal subtype of high-grade serous ovarian cancer. *Chinese journal of cancer* **34,** 28–40 (Jan. 2015).

304. Yang, D. *et al.* Integrated analyses identify a master microRNA regulatory network for the mesenchymal subtype in serous ovarian cancer. *Cancer cell* **23,** 186–199 (Feb. 2013).

305. Arora, H., Qureshi, R. & Park, W.-Y. miR-506 regulates epithelial mesenchymal transition in breast cancer cell lines. *PloS one* **8,** e64273; e64273–e64273 (May 2013).

306. Sun, Y. *et al.* MiR-506 inhibits multiple targets in the epithelial-to-mesenchymal transition network and is associated with good prognosis in epithelial ovarian cancer. *The Journal of pathology* **235,** 25–36 (Jan. 2015).

307. Meng, X. *et al.* Diagnostic and prognostic potential of serum miR-7, miR-16, miR-25, miR-93, miR-182, miR-376a and miR-429 in ovarian cancer patients. *British Journal Of Cancer* **113,** 1358 EP – (Sept. 2015).

308. Petrillo, M. *et al.* Identification of high-grade serous ovarian cancer miRNA species associated with survival and drug response in patients receiving neoadjuvant chemotherapy: a retrospective longitudinal analysis using matched tumor biopsies. *Annals of Oncology* **27,** 625–634 (2016).

309. Sorrentino, A. *et al.* Role of microRNAs in drug-resistant ovarian cancer cells. *Gynecologic Oncology* **111,** 478 –486. ISSN: 0090-8258 (2008).

310. Zhang, L. *et al.* Genomic and epigenetic alterations deregulate microRNA expression in human epithelial ovarian cancer. *Proceedings of the National Academy of Sciences* **105,** 7004–7009. ISSN: 0027-8424 (2008).

311. Dahiya, N. *et al.* MicroRNA Expression and Identification of Putative miRNA Targets in Ovarian Cancer. *PLOS ONE* **3,** 1–11 (June 2008).

312. Calura, E. *et al.* miRNA Landscape in Stage I Epithelial Ovarian Cancer Defines the Histotype Specificities. *Clinical Cancer Research* **19,** 4114–4123. ISSN: 1078-0432 (2013).

313. Vang, S. *et al.* Identification of Ovarian Cancer Metastatic miRNAs. *PLOS ONE* **8,** 1–10 (Mar. 2013).

314. Langhe, R. *et al.* A novel serum microRNA panel to discriminate benign from malignant ovarian disease. *Cancer Letters* **356,** 628 –636. ISSN: 0304-3835 (2015).

315. Iorio, M. V. *et al.* MicroRNA Signatures in Human Ovarian Cancer. *Cancer Research* **67,** 8699–8707. ISSN: 0008-5472 (2007).

316. Wyman, S. K. *et al.* Repertoire of microRNAs in Epithelial Ovarian Cancer as Determined by Next Generation Sequencing of Small RNA cDNA Libraries. *PLoS ONE* **4** (ed Dey, S. K.) e5311 (2009).

317. Nam, E. J. *et al.* MicroRNA Expression Profiles in Serous Ovarian Carcinoma. *Clinical Cancer Research* **14,** 2690–2695. ISSN: 1078-0432 (2008).

318. Vaksman, O. *et al.* miRNA profiling along tumour progression in ovarian carcinoma. *Journal of cellular and molecular medicine* **15,** 1593–1602 (July 2011).

319. Leslie Pedrioli, D. M. *et al.* miR-31 Functions as a Negative Regulator of Lymphatic Vascular Lineage-Specific Differentiation In Vitro and Vascular Development In Vivo. *Molecular and Cellular Biology* **30,** 3620–3634 (July 2010).

320. Kazenwadel, J., Michael, M. Z. & Harvey, N. L. Prox1 expression is negatively regulated by miR-181 in endothelial cells. *Blood* **116,** 2395–2401. ISSN: 0006-4971 (2010).

321. Seo, M., Choi, J.-S., Rho, C. R., Joo, C.-K. & Lee, S. K. MicroRNA miR-466 inhibits Lymphangiogenesis by targeting prospero-related homeobox 1 in the alkali burn corneal injury model. *Journal of Biomedical Science* **22,** 3 (2015).

322. Leonov, G *et al.* Suppression of AGO2 by miR-132 as a determinant of miRNA-mediated silencing in human pri- mary endothelial cells. *J Biochem Cell Biol,* 75–84 (2015).

323. Jones, D. *et al.* Mirtron MicroRNA-1236 Inhibits VEGFR-3 Signaling during Inflammatory Lymphangiogenesis. *Arteriosclerosis, Thrombosis, and Vascular Biology* **32,** 633–642 (Mar. 2012).

324. Yee, D., Shah, K. M., Coles, M. C., Sharp, T. V. & Lagos, D. MicroRNA-155 induction via TNF-alpha and IFN-gamma suppresses expression of programmed death ligand-1 (PD-L1) in human primary cells. *The Journal of Biological Chemistry* **292,** 20683–20693 (Dec. 2017).

325. Sasahira, T *et al.* Downregulation of miR-126 induces angiogenesis and lymphangiogenesis by activation of VEGF-A in oral cancer. *British Journal Of Cancer* **107,** 700 EP – (July 2012).

326. Hu, J. *et al.* microRNA-128 plays a critical role in human non-small cell lung cancer tumourigenesis, angiogenesis and lymphangiogenesis by directly targeting vascular endothelial growth factor-C. *European Journal of Cancer* **50,** 2336 –2350. ISSN: 0959-8049 (2014).

327. Clasper, S. *et al.* A Novel Gene Expression Profile in Lymphatics Associated with Tumor Growth and Nodal Metastasis. *Cancer Research* **68,** 7293–7303. ISSN: 0008-5472 (2008).

328. Xu, J. *et al.* Lymphatic endothelial cell-secreted CXCL1 stimulates lymphangiogenesis and metastasis of gastric cancer. *International Journal of Cancer* **130,** 787–797.

329. Tokumoto, M. W. *et al.* Identification of tumour-reactive lymphatic endothelial cells capable of inducing progression of gastric cancer. *British Journal Of Cancer* **113,** 1046 EP – (Sept. 2015).

330. Valente, A. L., Kane, J. L., Ellsworth, D. L., Shriver, C. D. & Ellsworth, R. E. Molecular response of the axillary lymph node microenvironment to metastatic colonization. *Clinical and Experimental Metastasis* **31,** 565–572. ISSN: 1573-7276 (June 2014).

331. Anand, S. *et al.* MicroRNA-132–mediated loss of p120RasGAP activates the endothelium to facilitate pathological angiogenesis. *Nature Medicine* **16,** 909 EP – (Aug. 2010).

332. Cubillos-Ruiz, J. R. *et al.* REPROGRAMMING TUMOR-ASSOCIATED DENDRITIC CELLS IN VIVO USING MICRORNA MIMETICS TRIGGERS PROTECTIVE IMMUNITY AGAINST OVARIAN CANCER. *Cancer Research* **72,** 1683–1693 (Apr. 2012).

333. Chakraborty, C., Sharma, A. R., Sharma, G., Doss, C. G. P. & Lee, S.-S. Therapeutic miRNA and siRNA: Moving from Bench to Clinic as Next Generation Medicine. *Molecular Therapy - Nucleic Acids* **8,** 132 –143. ISSN: 2162-2531 (2017).

334. Martin, D., Kelnar, K. & Bader, A. G. In vivo localization of miR-34 delivered via liposomal MRX34: chromogenic in situ hybridization (CISH) results in a preclinical model and liver biopsies from phase I patients. *Journal of Clinical Oncology* **34,** e14074–e14074 (2016).

335. Bader, A. miR-34 a microRNA replacement therapy is headed to the clinic. *Frontiers in Genetics* **3,** 120. ISSN: 1664-8021 (2012).

336. Farooqi, A. A., Tabassum, S & Ahmad, A. MicroRNA-34a: A Versatile Regulator of Myriads of Targets in Different Cancers. *Int. J. Mol. Sci* **18** (2017).

337. Khan, A., Mudassir, J, Mohtar, N & Darwis, Y. Advanced drug delivery to the lymphatic system: lipid-based nanoformulations. *Int J Nanomedicine* **8,** 2733–44 (2013).

338. Li, Z. & Rana, T. M. Therapeutic targeting of microRNAs: current status and future challenges. *Nature Reviews Drug Discovery* **13,** 622 EP – (July 2014).

339. Lindow, M. & Kauppinen, S. Discovering the first microRNA-targeted drug. *The Journal of Cell Biology* **199,** 407–412. ISSN: 0021-9525 (2012).

340. Carow, K. *et al.* A comparative study of digital PCR and real-time qPCR for the detection and quantification of HPV mRNA in sentinel lymph nodes of cervical cancer patients. *BMC research notes* **10,** 532–532 (Oct. 2017).

341. Schindelin, J. *et al.* Fiji: an open-source platform for biological-image analysis. *Nature Methods* **9,** 676 EP – (June 2012).

342. Vandesompele, J. *et al.* Accurate normalization of real-time quantitative RT-PCR data by geometric averaging of multiple internal control genes. *Genome Biology* **3,** research0034.1–research0034.11 (2002).

343. Andersen, C. L., Jensen, J. L. & Ørntoft, T. F. Normalization of Real-Time Quantitative Reverse Transcription-PCR Data: A Model-Based Variance Estimation Approach to Identify Genes Suited for Normalization, Applied

to Bladder and Colon Cancer Data Sets. *Cancer Research* **64,** 5245–5250. ISSN: 0008-5472 (2004).

344. Metsalu, T. & Vilo, J. ClustVis: a web tool for visualizing clustering of multivariate data using Principal Component Analysis and heatmap. *Nucleic Acids Research* **43,** W566–W570. ISSN: 0305-1048 (May 2015).

345. Johnson, S. M. *et al.* RAS Is Regulated by the let-7 MicroRNA Family. *Cell* **120,** 635 –647. ISSN: 0092-8674 (2005).

346. Park, S.-M. *et al.* Let-7 Prevents Early Cancer Progression by Suppressing Expression of the Embryonic Gene HMGA2. *Cell Cycle* **6.** PMID: 17957144, 2585–2590 (2007).

347. Lin, Z. *et al.* Let-7e modulates the inflammatory response in vascular endothelial cells through ceRNA crosstalk. *Scientific Reports* **7,** 42498 EP – (Feb. 2017).

348. Chen, W. *et al.* miRNA expression profile in primary gastric cancers and paired lymph node metastases indicates that miR-10a plays a role in metastasis from primary gastric cancer to lymph nodes. *Experimental and Therapeutic Medicine* **3,** 351–356 (Feb. 2012).

349. Kagawa, T. *et al.* Increases of microRNA let-7e in peripheral blood mononuclear cells in Hashimotorsquos disease. *Endocrine Journal* **63,** 375–380 (2016).

350. Guan, H. *et al.* MicroRNA let-7e is associated with the pathogenesis of experimental autoimmune encephalomyelitis. *European journal of immunology* **43.** doi:10.1002/eji.201242702 (Jan. 2013).

351. Kumar, M. *et al.* Let-7 microRNA-mediated regulation of IL-13 and allergic airway inflammation. *Journal of Allergy and Clinical Immunology* **128,** 1077–1085.e10 (Feb. 2011).

352. Johnson, N. C. *et al.* Lymphatic endothelial cell identity is reversible and its maintenance requires Prox1 activity. *Genes and Development* **22,** 3282–3291 (Dec. 2008).

353. Parikh, A. *et al.* microRNA-181a has a critical role in ovarian cancer progression through the regulation of the epithelial-mesenchymal transition. *Nature communications* **5,** 2977; 2977–2977 (Jan. 2014).

354. Tominaga, N. *et al.* Brain metastatic cancer cells release microRNA-181c-containing extracellular vesicles capable of destructing blood–brain barrier. *Nature Communications* **6,** 6716 EP – (Apr. 2015).

355. Boscolo, E. *et al.* AKT hyper-phosphorylation associated with PI3K mutations in lymphatic endothelial cells from a patient with lymphatic malformation. *Angiogenesis* **18,** 151–162 (Apr. 2015).

356. Yin, K.-J. *et al.* Vascular endothelial cell-specific microRNA-15a inhibits angiogenesis in hindlimb ischemia. *The Journal of biological chemistry* **287,** 27055–27064 (Aug. 2012).

357. Chen, L. *et al.* miR-15a and miR-16 affect the angiogenesis of multiple myeloma by targeting VEGF. *Carcinogenesis* **34,** 426–435. ISSN: 0143-3334 (Oct. 2012).

358. Ye, E.-A., Liu, L. & Steinle, J. J. miR-15a/16 inhibits TGF-beta3/VEGF signaling and increases retinal endothelial cell barrier proteins. *Vision Research* **139.** Diabetic Retinopathy - an Overview, 23 –29. ISSN: 0042-6989 (2017).

359. Bhattacharya, R. *et al.* MiR-15a and MiR-16 Control Bmi-1 Expression in Ovarian Cancer. *Cancer Research* **69,** 9090–9095. ISSN: 0008-5472 (2009).

360. Schwarzenbach, H. Clinical significance of miR-15 and miR-16 in ovarian cancer. *Translational Cancer Research* **5.** ISSN: 2219-6803. `http://tcr.amegroups.com/article/view/7660` (2016).

361. Cimmino, A. *et al.* miR-15 and miR-16 induce apoptosis by targeting BCL2. *Proceedings of the National Academy of Sciences of the United States of America* **102,** 13944–13949 (Sept. 2005).

362. Tzeng, H.-E., Chang, A.-C., Tsai, C.-H., Wang, S.-W. & Tang, C.-H. Basic fibroblast growth factor promotes VEGF-C-dependent lymphangiogenesis via inhibition of miR-381 in human chondrosarcoma cells. *Oncotarget* **7,** 38566–38578 (May 2016).

363. Xia, B., Li, H., Yang, S., Liu, T. & Lou, G. MiR-381 inhibits epithelial ovarian cancer malignancy via YY1 suppression. *Tumor Biology* **37,** 9157–9167. ISSN: 1423-0380 (July 2016).

364. Wu, R. *et al.* MicroRNA-497 Induces Apoptosis and Suppresses Proliferation via the Bcl-2/Bax-Caspase9-Caspase3 Pathway and Cyclin D2 Protein in HUVECs. *PLOS ONE* **11,** 1–15 (Dec. 2016).

365. Yang, G. *et al.* miR-497 expression, function and clinical application in cancer. *Oncotarget* **7,** 55900–55911 (June 2016).

366. Liang, L. *et al.* MiR-93-5p enhances growth and angiogenesis capacity of HUVECs by down-regulating EPLIN. *Oncotarget* **8,** 107033–107043 (Nov. 2017).

367. Metsalu, T. & Vilo, J. MicroRNA miR-93-5p regulates expression of IL-8 and VEGF in neuroblastoma SK-N-AS cells. *Oncol Rep* **35,** 2866–72 (May 2016).

368. Fu, X., Tian, J., Zhang, L., Chen, Y. & Hao, Q. Involvement of microRNA-93, a new regulator of PTEN/Akt signaling pathway, in regulation of chemotherapeutic drug cisplatin chemosensitivity in ovarian cancer cells. *FEBS Letters* **586,** 1279–1286.

369. Chen, X. *et al.* RhoC is a major target of microRNA-93-5P in epithelial ovarian carcinoma tumorigenesis and progression. *Molecular cancer* **14,** 31; 31–31 (Feb. 2015).

370. Widlansky, M. E. *et al.* miR-29 contributes to normal endothelial function and can restore it in cardiometabolic disorders. *EMBO molecular medicine* **10,** e8046 (Mar. 2018).

371. Yuan, H., Ma, J., Li, T. & Han, X. MiR-29b aggravates lipopolysaccharide-induced endothelial cells inflammatory damage by regulation of NF-IB and JNK signaling pathways. *Biomedicine and Pharmacotherapy* **99,** 451–461. ISSN: 0753-3322 (2018).

372. Teng, Y. *et al.* MicroRNA-29B (miR-29b) regulates the Warburg effect in ovarian cancer by targeting AKT2 and AKT3. *Oncotarget* **6.** doi:10.18632/oncotarget.5695 (Oct. 2015).

373. Minli, Y. *et al.* microRNA-29a repressed epithelial ovarian cancer progression by directly targeting SIRT1. *The Journal of Immunology.* ISSN: 0022-1767. doi:10.4049/jimmunol.1200728. eprint: http://www.jimmunol.

org/content/early/2013/03/20/jimmunol.1200728.full.pdf. http://www.jimmunol.org/content/early/2013/03/20/jimmunol.1200728 (2013).

374. Kuhnert, F. & Kuo, C. J. miR-17-92 angiogenesis micromanagement. *Blood* **115,** 4631–4632. ISSN: 0006-4971 (2010).

375. Doebele, C. *et al.* Members of the microRNA-17-92 cluster exhibit a cell-intrinsic antiangiogenic function in endothelial cells. *Blood* **115,** 4944–4950. ISSN: 0006-4971 (2010).

376. Philippe, L., Alsaleh, G., Bahram, S., Pfeffer, S. & Georgel, P. The miR-17 92 Cluster: A Key Player in the Control of Inflammation during Rheumatoid Arthritis. *Frontiers in immunology* **4,** 70; 70–70 (Mar. 2013).

377. Tang, Y. *et al.* The role of miR-19b in the inhibition of endothelial cell apoptosis and its relationship with coronary artery disease. *Scientific Reports* **5,** 15132 EP – (Oct. 2015).

378. Xu, Y.-L. *et al.* MicroRNA-19 restores vascular endothelial cell function in lower limb ischemia-reperfusion injury through the KLF10-dependent TGF-I21/Smad signaling pathway in rats. *Journal of Cellular Biochemistry* **119,** 9303–9315 (2018).

379. Wang, Y., Zhao, S., Zhu, L., Zhang, Q. & Ren, Y. MiR-19a negatively regulated the expression of PTEN and promoted the growth of ovarian cancer cells. *Gene* **670,** 166 –173. ISSN: 0378-1119 (2018).

380. Ding, Z. *et al.* Regulation of autophagy and apoptosis in response to ox-LDL in vascular smooth muscle cells, and the modulatory effects of the microRNA hsa-let-7g. *International Journal of Cardiology* **168,** 1378 – 1385. ISSN: 0167-5273 (2013).

381. Swaminathan, S. *et al.* Differential Regulation of the Let-7 Family of MicroRNAs in CD4+ T Cells Alters IL-10 Expression. *The Journal of Immunology* **188,** 6238–6246. ISSN: 0022-1767 (2012).

382. Meng, F. *et al.* The MicroRNA let-7a Modulates Interleukin-6-dependent STAT-3 Survival Signaling in Malignant Human Cholangiocytes. *Journal of Biological Chemistry* **282,** 8256–8264 (2007).

383. Aqeilan, R. I., Calin, G. A. & Croce, C. M. miR-15a and miR-16-1 in cancer: discovery, function and future perspectives. *Cell Death And Differentiation* **17,** 215 EP – (June 2009).

384. Yi, D., Xu, L., Wang, R., Lu, X. & Sang, J. miR-381 overcomes cisplatin resistance in breast cancer by targeting MDR1. *Cell Biology International* **43,** 12–21 (2019).

385. Mi, H. *et al.* miR-381 induces sensitivity of breast cancer cells to doxorubicin by inactivation of MAPK signaling via FYN. *European Journal of Pharmacology* **839,** 66 –75. ISSN: 0014-2999 (2018).

386. Wang, Y *et al.* MicroRNA-381 suppresses the proliferation of osteosarcoma cells through LRH-1/Wnt/beta-catenin signaling pathway. *Oncology Reports* **39,** 589–596 (Feb. 2018).

387. Nijhuis, A. *et al.* MCL-1 is modulated in Crohn's disease fibrosis by miR-29b via IL-6 and IL-8. *Cell and Tissue Research* **368,** 325–335. ISSN: 1432-0878 (May 2017).

388. Yu, P.-N. *et al.* Downregulation of miR-29 contributes to cisplatin resistance of ovarian cancer cells. *International journal of cancer. Journal international du cancer* **134.** doi:10.1002/ijc.28399 (Feb. 2014).

389. Su, Z. *et al.* MiR-144 regulates hematopoiesis and vascular development by targeting meis1 during zebrafish development. *The International Journal of Biochemistry and Cell Biology* **49,** 53 –63. ISSN: 1357-2725 (2014).

390. Honglei, Y., Lihua, Z., Junbiao, Z. & Yan, Z. miR-144 regulates the proliferation of human vascular endothelial cells through targeting SRF. *Int J Clin Exp Pathol* **9,** 3357–3364. ISSN: 1936-2625/IJCEP0020189 (2016).

391. Han, S., Zhu, J. & Zhang, Y. miR-144 Potentially Suppresses Proliferation and Migration of Ovarian Cancer Cells by Targeting RUNX1. *Medical science monitor basic research* **24,** 40–46 (Feb. 2018).

392. Chang, R. K. *et al.* MicroRNA expression profiles in non-epithelial ovarian tumors. *International journal of oncology* **52,** 55–66 (Nov. 2017).

393. Li, J. *et al.* The Poly-cistronic miR-23-27-24 Complexes Target Endothelial Cell Junctions: Differential Functional and Molecular Effects of miR-23a and miR-23b. *Molecular Therapy - Nucleic Acids* **5,** e354. ISSN: 2162-2531 (2016).

394. Wynn, T. A. Cellular and molecular mechanisms of fibrosis. *The Journal of pathology* **214,** 199–210 (Jan. 2008).

395. J, D. Pathology of lymphedema. *Clin Dermatol,* 433–444 (1995).

396. Talarico, F, Brunetto, D & Scialabba, M. Fibrosclerotic lymphedema: Pathophysiology and therapy. *Lymphology,* 11—15 (1991).

397. Avraham, T. *et al.* Blockade of transforming growth factor-beta1 accelerates lymphatic regeneration during wound repair. *The American journal of pathology* **177,** 3202–3214 (Dec. 2010).

398. Savetsky, I. L. *et al.* Pirfenidone decreases fibrosis and improves lymphatic function in mouse models of lymphedema. *Journal of the American College of Surgeons* **221,** e121–e122 (Mar. 2015).

399. Cai, X. *et al.* Mesenchymal status of lymphatic endothelial cell: enlightening treatment of lymphatic malformation. *International journal of clinical and experimental medicine* **8,** 12239–12251 (Aug. 2015).

400. Jen-Liang, S., Pai-Sheng, C., Gunnar, J. & Min-Liang, K. Function and Regulation of Let-7 Family microRNAs. *MicroRNA* **1,** 34–39. ISSN: 2211-5366/2211-5374 DOI = 10.2174/2211536611201010034 (2012).

401. Zhang, C., Li, Z, Liu, Y., Y, W. & Qu, X. Prognostic role of the let-7 family in various carcinomas: A meta-analysis update. *Journal of Balkan Union of Oncology* **20,** 631–44 (2015).

402. Cromer, W. E. *et al.* The effects of inflammatory cytokines on lymphatic endothelial barrier function. *Angiogenesis* **17,** 395–406 (Apr. 2014).

403. Aldrich, M. B. & Sevick-Muraca, E. M. Cytokines are systemic effectors of lymphatic function in acute inflammation. *Cytokine* **64,** 362–369 (Oct. 2013).

404. Flister, M. J. *et al.* Inflammation induces lymphangiogenesis through up-regulation of VEGFR-3 mediated by NF-IB and Prox1. *Blood* **115,** 418–429. ISSN: 0006-4971 (2010).

405. Mäkinen, T., Norrmén, C. & Petrova, T. V. Molecular mechanisms of lymphatic vascular development. *Cellular and Molecular Life Sciences* **64,** 1915–1929 (2007).

406. Yang, Y. & Oliver, G. Development of the mammalian lymphatic vasculature. *The Journal of clinical investigation* **124,** 888–897 (Mar. 2014).

407. Schmid-Schönbein, G. W. Nitric oxide (NO) side of lymphatic flow and immune surveillance. *Proceedings of the National Academy of Sciences* **109,** 3–4. ISSN: 0027-8424 (2012).

408. Liao, S. *et al.* Impaired lymphatic contraction associated with immunosuppression. *Proceedings of the National Academy of Sciences* **108,** 18784–18789. ISSN: 0027-8424 (2011).

409. Scallan, J. P., Hill, M. A. & Davis, M. J. Lymphatic vascular integrity is disrupted in type 2 diabetes due to impaired nitric oxide signalling. *Cardiovascular research* **107,** 89–97 (July 2015).

410. Roderburg, C. *et al.* Micro-RNA profiling reveals a role for miR-29 in human and murine liver fibrosis. *Hepatology* **53,** 209–218 (2011).

411. Xiao, J. *et al.* miR-29 inhibits bleomycin-induced pulmonary fibrosis in mice. *Molecular therapy : the journal of the American Society of Gene Therapy* **20,** 1251–1260 (June 2012).

412. Guo, J., Lin, Q., Shao, Y., Rong, L. & Zhang, D. miR-29b promotes skin wound healing and reduces excessive scar formation by inhibition of the TGF-beta1/Smad/CTGF signaling pathway. *Canadian Journal of Physiology and Pharmacology* **95,** 437–442 (2017).

413. Dakhlallah, D. *et al.* Epigenetic Regulation of miR-1792 Contributes to the Pathogenesis of Pulmonary Fibrosis. *American Journal of Respiratory and Critical Care Medicine* **187.** PMID: 23306545, 397–405 (2013).

414. Ichise, T., Yoshida, N. & Ichise, H. FGF2-induced Ras–MAPK signalling maintains lymphatic endothelial cell identity by upregulating endothelial-cell-specific gene expression and suppressing TGFI2 signalling through Smad2. *Journal of Cell Science* **127,** 845–857. ISSN: 0021-9533 (2014).

415. Dadras, S. S. *et al.* Tumor lymphangiogenesis predicts melanoma metastasis to sentinel lymph nodes. *Modern Pathology* **18,** 1232 EP – (Apr. 2005).

416. Breslin, J. *et al.* Vascular endothelial growth factor-C stimulates the lymphatic pump by a VEGF receptor-3-dependent mechanism. *American journal of physiology. Heart and circulatory physiology* **293,** H709–18 (July 2007).

417. Breslin, J. W., Yuan, S. Y. & Wu, M. H. VEGF-C alters barrier function of cultured lymphatic endothelial cells through a VEGFR-3-dependent mechanism. *Lymphatic research and biology* **5,** 105–113 (2007).

418. Shi, J., Li, Y.-J., Yan, B. & Wei, P.-K. Interleukin-8: A potent promoter of human lymphatic endothelial cell growth in gastric cancer. *Oncology reports* **33,** 2703–2710 (June 2015).

419. Anderson, N. S. *et al.* Bcl-2 expression is altered with ovarian tumor progression: an immunohistochemical evaluation. *Journal of Ovarian Research* **2,** 16 (2009).

420. Zaitoun, I. S. *et al.* Endothelium Expression of Bcl-2 Is Essential for Normal and Pathological Ocular Vascularization. *PloS one* **10,** e0139994; e0139994–e0139994 (Oct. 2015).

421. Grutzmacher, C. *et al.* Opposing effects of bim and bcl-2 on lung endothelial cell migration. *American journal of physiology. Lung cellular and molecular physiology* **299,** L607–L620 (Nov. 2010).

422. Kondo, S., Tang, Y., Scheef, E. A., Sheibani, N. & Sorenson, C. M. Attenuation of retinal endothelial cell migration and capillary morphogenesis in the absence of bcl-2. *American Journal of Physiology-Cell Physiology* **294.** PMID: 18417716, C1521–C1530 (2008).

423. IERVOLINO, A. *et al.* Bcl-2 overexpression in human melanoma cells increases angiogenesis through VEGF mRNA stabilization and HIF-1-mediated transcriptional activity. *The FASEB Journal* **16.** PMID: 12205045, 1453–1455 (2002).

424. Trisciuoglio, D *et al.* Involvement of BH4 domain of bcl-2 in the regulation of HIF-1-mediated VEGF expression in hypoxic tumor cells. *Cell Death And Differentiation* **18,** 1024 EP – (Jan. 2011).

425. Giancotti, F. G. & Ruoslahti, E. Integrin Signaling. *Science* **285,** 1028–1033. ISSN: 0036-8075 (1999).

426. Dias, S., Shmelkov, S. V., Lam, G. & Rafii, S. VEGF165 promotes survival of leukemic cells by Hsp90-mediated induction of Bcl-2 expression and apoptosis inhibition. *Blood* **99,** 2532–2540. ISSN: 0006-4971 (2002).

427. Meda, B. *et al.* BCL-2 Is Consistently Expressed in Hyperplastic Marginal Zones of the Spleen, Abdominal Lymph Nodes, and Ileal Lymphoid Tissue. *Am J Surg Pathol* **27,** 888–894 (2003).

428. Levick, J. R. & Michel, C. C. Microvascular fluid exchange and the revised Starling principle. *Cardiovascular Research* **87,** 198–210. ISSN: 0008-6363 (Mar. 2010).

429. Liu, N., Zhou, C., Zhao, J. & Chen, Y. Reversal of Paclitaxel Resistance in Epithelial Ovarian Carcinoma Cells by a MUC1 Aptamer-let-7i Chimera. *Cancer Investigation* **30.** PMID: 22812695, 577–582 (2012).

430. Young, E. W. K., Watson, M. W. L., Srigunapalan, S., Wheeler, A. R. & Simmons, C. A. Technique for Real-Time Measurements of Endothelial Permeability in a Microfluidic Membrane Chip Using Laser-Induced Fluorescence Detection. *Analytical Chemistry* **82,** 808–816 (Feb. 2010).

431. Shrestha, B. *et al.* B Cell-Derived Vascular Endothelial Growth Factor A Promotes Lymphangiogenesis and High Endothelial Venule Expansion in Lymph Nodes. *The Journal of Immunology* **184,** 4819–4826. ISSN: 0022-1767 (2010).

432. Yang, J., Yan, J. & Liu, B. Targeting VEGF/VEGFR to Modulate Antitumor Immunity. *Frontiers in Immunology* **9,** 978. ISSN: 1664-3224 (2018).

433. Chooi, K. Y., Comerford, A., Sherwin, S. J. & Weinberg, P. D. Intimal and medial contributions to the hydraulic resistance of the arterial wall at different pressures: a combined computational and experimental study. *Journal of The Royal Society Interface* **13,** 20160234 (2016).

434. Athanasiou, D. *et al.* The passive biomechanics of human pelvic collecting lymphatic vessels. *PLOS ONE* **12,** 1–12 (Aug. 2017).

435. Wilson, J. T. *et al.* A fully coupled fluid-structure interaction model of the secondary lymphatic valve. *Computer Methods in Biomechanics and Biomedical Engineering* **21.** PMID: 30398077, 813–823 (2018).

436. Maruyama, Y. *et al.* The Effect of Podoplanin Inhibition on Lymphangiogenesis Under Pathological ConditionsPodoplanin Effect on Lymphangiogenesis. *Investigative Ophthalmology and Visual Science* **55,** 4813–4822. ISSN: 1552-5783 (Aug. 2014).

437. Kedl, R. M. *et al.* Migratory dendritic cells acquire and present lymphatic endothelial cell-archived antigens during lymph node contraction. *Nature Communications* **8,** 2034 (2017).

438. Kinjyo, I. *et al.* Real-time tracking of cell cycle progression during CD8+ effector and memory T-cell differentiation. *Nature Communications* **6,** 6301 EP – (Feb. 2015).

439. Pham, T. H. M., Okada, T., Matloubian, M., Lo, C. G. & Cyster, J. G. S1P1 receptor signaling overrides retention mediated by G alpha i-coupled receptors to promote T cell egress. *Immunity* **28,** 122–133 (Jan. 2008).

440. Chun, J. & Brinkmann, V. A mechanistically novel, first oral therapy for multiple sclerosis: the development of fingolimod (FTY720, Gilenya). *Discovery medicine* **12,** 213–228 (Sept. 2011).

441. Wang, Y. *et al.* In vivo albumin labeling and lymphatic imaging. *Proceedings of the National Academy of Sciences* **112,** 208–213. ISSN: 0027-8424 (2015).

442. Kim, H. *et al.* Fluorescent Iodized Emulsion for Pre- and Intraoperative Sentinel Lymph Node Imaging: Validation in a Preclinical Model. *Radiology* **275,** 141159 (Dec. 2014).

Permissions Documents

Journalpermissions <journalpermissions@springernature.com>
Fri 21/12/2018, 14:02
Johnson, Sarah

Reply

Inbox

Dear Sarah,

Thank you for your email. This article is distributed under the terms of the Creative Commons Attribution Noncommercial License which permits any noncommercial use, distribution, and reproduction in any medium, provided the original author(s) and source are credited. https://creativecommons.org/licenses/by-nc/2.0/

If you thesis is only to be made public through print versions and the university repository, then you do not need any permission from us to use the material. Just make sure to cite the original properly and the CC license.

If you thesis is to be published with an ISBN then please let us know as you will need a license to reuse the material.

Best wishes and Happy Holidays!
Oda

Oda Siqveland
Permissions Assistant

SpringerNature
The Campus, 4 Crinan Street, London N1 9XW,
United Kingdom
T +44 (0) 207 014 6851

http://www.nature.com
http://www.springer.com
http://www.palgrave.com

Johnson, Sarah
Fri 21/12/2018, 13:47

Dear Permission teams

I would like to use Figure two of article PMID: 22101807 (Significance of vascular endothelial growth factor in growth and peritoneal disseminations) in my PhD thesis.

FIGURE B.13: Permission for reprint of Figure 2 in Chapter 3.

ELSEVIER LICENSE
TERMS AND CONDITIONS

Mar 25, 2019

This Agreement between Miss. Sarah Johnson ("You") and Elsevier ("Elsevier") consists of your license details and the terms and conditions provided by Elsevier and Copyright Clearance Center.

License Number	4556061439105
License date	Mar 25, 2019
Licensed Content Publisher	Elsevier
Licensed Content Publication	Immunity
Licensed Content Title	Endogenous Naive CD8+ T Cell Precursor Frequency Regulates Primary and Memory Responses to Infection
Licensed Content Author	Joshua J. Obar,Kamal M. Khanna,Leo Lefrançois
Licensed Content Date	Jun 13, 2008
Licensed Content Volume	28
Licensed Content Issue	6
Licensed Content Pages	11
Start Page	859
End Page	869
Type of Use	reuse in a thesis/dissertation
Portion	figures/tables/illustrations
Number of figures/tables/illustrations	1
Format	both print and electronic
Are you the author of this Elsevier article?	No
Will you be translating?	No
Original figure numbers	Data from Figure 4
Title of your thesis/dissertation	Immune Reactions in Lymph Nodes and Ovarian Cancer
Expected completion date	Mar 2019
Estimated size (number of pages)	300
Requestor Location	Miss. Sarah Johnson 64 Park Drive Barlaston Stoke-On-Trent, ST12 9DP United Kingdom Attn: Miss. Sarah Johnson
Publisher Tax ID	GB 494 6272 12
Total	0.00 GBP

FIGURE B.14: Permission for use of data for Fig 1.24 in Chapter 2.

ELSEVIER LICENSE
TERMS AND CONDITIONS

Mar 25, 2019

This Agreement between Miss. Sarah Johnson ("You") and Elsevier ("Elsevier") consists of your license details and the terms and conditions provided by Elsevier and Copyright Clearance Center.

License Number	4556070637546
License date	Mar 25, 2019
Licensed Content Publisher	Elsevier
Licensed Content Publication	Immunity
Licensed Content Title	Naive CD4+ T Cell Frequency Varies for Different Epitopes and Predicts Repertoire Diversity and Response Magnitude
Licensed Content Author	James J. Moon,H. Hamlet Chu,Marion Pepper,Stephen J. McSorley,Stephen C. Jameson,Ross M. Kedl,Marc K. Jenkins
Licensed Content Date	Aug 24, 2007
Licensed Content Volume	27
Licensed Content Issue	2
Licensed Content Pages	11
Start Page	203
End Page	213
Type of Use	reuse in a thesis/dissertation
Intended publisher of new work	other
Portion	figures/tables/illustrations
Number of figures/tables/illustrations	1
Format	both print and electronic
Are you the author of this Elsevier article?	No
Will you be translating?	No
Original figure numbers	Data from Figure 1
Title of your thesis/dissertation	Immune Reactions in Lymph Nodes and Ovarian Cancer
Expected completion date	Mar 2019
Estimated size (number of pages)	300
Requestor Location	Miss. Sarah Johnson 64 Park Drive Barlaston

FIGURE B.15: Permission for use of data for Figure in Chapter 2.

SPRINGER NATURE LICENSE
TERMS AND CONDITIONS

Mar 25, 2019

This Agreement between Miss. Sarah Johnson ("You") and Springer Nature ("Springer Nature") consists of your license details and the terms and conditions provided by Springer Nature and Copyright Clearance Center.

License Number	4556090131367
License date	Mar 25, 2019
Licensed Content Publisher	Springer Nature
Licensed Content Publication	Nature Immunology
Licensed Content Title	Memory CD8 T cell differentiation: initial antigen encounter triggers a developmental program in naïve cells
Licensed Content Author	Susan M. Kaech, Rafi Ahmed
Licensed Content Date	May 1, 2001
Licensed Content Volume	2
Licensed Content Issue	5
Type of Use	Thesis/Dissertation
Requestor type	academic/university or research institute
Format	print and electronic
Portion	figures/tables/illustrations
Number of figures/tables/illustrations	2
Will you be translating?	no
Circulation/distribution	<501
Author of this Springer Nature content	no
Title	Immune Reactions in Lymph Nodes and Ovarian Cancer
Institution name	n/a
Expected presentation date	Mar 2019
Portions	Data from Figure 1
Requestor Location	Miss. Sarah Johnson 64 Park Drive Barlaston Stoke-On-Trent, ST12 9DP United Kingdom Attn: Miss. Sarah Johnson
Total	0.00 GBP

Terms and Conditions

Springer Nature Terms and Conditions for RightsLink Permissions
Springer Nature Customer Service Centre GmbH (the Licensor) hereby grants you a non-exclusive, world-wide licence to reproduce the material and for the purpose and

FIGURE B.16: Permission for use of data for Fig 1.25 in Chapter 2.

Regulation of Dendritic Cell Migration to the Draining Lymph Node
Impact on T Lymphocyte Traffic and Priming

Alfonso Martín-Fontecha,[1] Silvia Sebastiani,[1] Uta E. Höpken,[2] Mariagrazia Uguccioni,[1] Martin Lipp,[2] Antonio Lanzavecchia,[1] and Federica Sallusto[1]

Author information Article notes Copyright and License information Disclaimer

Copyright © 2003, The Rockefeller University Press

This article is distributed under the terms of an Attribution–Noncommercial–Share Alike–No Mirror Sites license for the fir six months after the publication date (see http://www.rupress.org/terms). After six months it is available under a Creative Commons License (Attribution–Noncommercial–Share Alike 4.0 Unported license, as described at http://creativecommons.org/licenses/by-nc-sa/4.0/).

FIGURE B.17: Permission for use of data from Figure 1.25 in Chapter 2.

J Exp Med

Duration of the initial TCR stimulus controls the magnitude but not functionality of the CD8$^+$ T cell response

Martin Prlic, Gabriela Hernandez-Hoyos, and Michael J. Bevan

Author information Article notes Copyright and License information Disclaimer

Copyright © 2006, The Rockefeller University Press

This article is distributed under the terms of an Attribution–Noncommercial–Share Alike–No Mirror Sites license for the first six months after the publication date (see http://www.rupress.org/terms). After six months it is available under a Creative Commons License (Attribution–Noncommercial–Share Alike 4.0 Unported license, as described at http://creativecommons.org/licenses/by-nc-sa/4.0/).

FIGURE B.18: Permission for use of data for Fig 1.26 in Chapter 2.

Cyclical modulation of sphingosine-1-phosphate receptor 1 surface expression during lymphocyte recirculation and relationship to lymphoid organ transit

Charles G. Lo,[1] Ying Xu,[1] Richard L. Proia,[2] and Jason G. Cyster[1]

Author information Article notes Copyright and License information Disclaimer

Copyright © 2005, The Rockefeller University Press

This article is distributed under the terms of an Attribution–Noncommercial–Share Alike–No Mirror Sites license for the first six months after the publication date (see http://www.rupress.org/terms). After six months it is available under a Creative Commons License (Attribution–Noncommercial–Share Alike 4.0 Unported license, as described at http://creativecommons.org/licenses/by-nc-sa/4.0/).

FIGURE B.19: Permission for use of data from Figure 1.27 in Chapter 2.